RARE EARTH CONTAINING MULTI-COMPONENT METALLIC GLASSES

Luka Kelhar

Doctoral Dissertation
Jožef Stefan International Postgraduate School
Ljubljana, Slovenia

Supervisor: Prof. Dr. Jean-Marie Dubois, Institut Jean Lamour and University of Lorraine, Nancy, France, and Jožef Stefan Institute, Ljubljana, Slovenia
Co-Supervisor: Prof. Dr. Spomenka Kobe, Jožef Stefan Institute, Ljubljana, Slovenia

Evaluation Board:
Assoc. Prof. Sašo Šturm, Chair, Jožef Stefan Institute, Ljubljana, Slovenia
Prof. Dr. Boštjan Markoli, Member, Faculty of Natural Sciences and Engineering, University of Ljubljana, Slovenia
Prof. Dr. Dragoljub Mirjanić, Member, Academy of Sciences and Arts of the Republic of Srpska, Banja Luka, Republic of Srpska, Bosnia and Herzegovina.

MEDNARODNA PODIPLOMSKA ŠOLA JOŽEFA STEFANA
JOŽEF STEFAN INTERNATIONAL POSTGRADUATE SCHOOL

Luka Kelhar

RARE EARTH CONTAINING MULTI-COMPONENT METALLIC GLASSES

Doctoral Dissertation

Večkomponentna kovinska stekla z vsebnostjo redkih zemelj

Doktorska disertacija

Supervisor: Prof. Dr. Jean-Marie Dubois

Co-Supervisor: Prof. Dr. Spomenka Kobe

Ljubljana, Slovenia, December, 2018

Acknowledgements

Firstly, I would gratefully like to thank my supervisor Professor Dr Jean-Marie Dubois who guided me in the past three years through the process of my PhD. He taught me discipline, accuracy and consistency (or at least he tried). His uncompromising views dramatically influenced my perception of how scientific work should be carried out. No doubt there is room to improve these skills; nonetheless, the last three years will be remembered as the most enlightening in my period of formal education.

I would also like to thank Professor Dr. Spomenka Kobe, as she assured the financial means for my PhD study and taught me lessons about my (sometimes) unknown flaws. This process did not always consist of gentle words; nevertheless, I am indebted to her for she built my resilience.

The topic of this PhD was placed within the bilateral International Associated Laboratory (LIA) collaboration between the French "Centre National de la Recherche Scientifique" (CNRS) and Slovene "Jožef Stefan Institute" (JSI) in the project Push-Pull Alloys and Complex CompoundS ($PACS_2$), which covered some of the expenses. In this respect, I am grateful to the countries of France and Slovenia and to all project members that contributed in any way to this research.

In connection with experimental work, there are numerous people that I am grateful to. In the first year Božo Skela, then pursuing his M.Sc. unselfishly helped me with sample preparation in the lab, while Jana Ferčič performed XRD measurements on my samples and later trained me for independent XRD use. Fabian Burkhardt assisted me with experimental work when I was abroad. Marjeta Maček-Kržmanc is an indispensable expert for thermal analysis, who contributed immensely to my PhD with DSC measurements. We strived to better the DSC procedure for the given metallic glasses, which resulted in improved accuracy and repeatability of the measurements. Janez Zavašnik, Sašo Šturm, Sandra Drev, Andreja Šestan and Bojan Ambrožič helped me with TEM characterization of metallic glasses on the nanometre scale. Collaboration with Janez was particularly valuable, since he provided assistance with TEM sample characterisation and its interpretation at the Centre for Electron Microscopy and Microanalysis (CEMM), as well as the "Max-Planck-Institut für Eisenforschung" (MPIE) in Düsseldorf during his postdoctoral stay. Regarding microscopy, Zoran Samardžija is a valuable specialist for SEM analysis, who helped me obtain reliable and trustworthy results of glasses' microstructures. Maja Češarek is appreciated for training me for independent use of SEM. Regarding magnetic characterisation, there are multiple people at K7 and F5 that need mentioning. Benjamin Podmiljšak taught me VSM measurements and assisted with day-to-day questions that occurred during the use of VSM. With regards to the elucidation of the physical principles governing the magnetic measurements, the aid of Matej Komelj is gratefully acknowledged. Sharing the E33 office during the first two years with Benjamin and Matej is highly appreciated. F5 department of the JSI offered me immense assistance with cryogenic measurements on SQUID. Primož Koželj and Zvonko Jagličič (affiliated to the Faculty of Mathematics and Physics) performed the measurements and helped me consolidate the results. Aside from Primož, I am also grateful to Prof. Dr. Janez Dolinšek,

who explained the magnetic transitions for metallic glasses with complex magnetic behaviour. I was lucky enough to get a series of synchrotron diffraction data from the European Synchrotron Radiation Facility (ESRF) in Grenoble, for which, the cooperation with Petra Jenuš is highly appreciated.

In the last quarter of 2016, I was given an opportunity to spend three months at Institut Jean Lamour (IJL), in Nancy, France, for which I am grateful to my supervisors, the French government for providing the scholarship and to the people at IJL who made my stay unforgettable. An excellent research practice of IJL has been introduced firstly by Marie-Cécile de Weerd, with whom we grew several monocrystals and who kindly explained to me many of the occurring questions and ambiguities. Julian Ledieu coordinated the research flow and helped me with formalities. For XRD analysis, the assistance of Pascal Boulet is kindly appreciated, as well as useful discussions with Vincent Fournée and Émilie Gaudry. Assistance from Sylvie Migot with FIB preparation and Jaafar Ghanbaja with TEM characterisation is greatly acknowledged.

I also recognise valuable discussions and collaboration with Prof. Dr. Boštjan Markoli and mechanical properties measurements by Martin Lamut, both affiliated to the Faculty of Natural Sciences and Engineering (NTF). Prof. Dr. Anton Meden from the Faculty of Chemistry and Chemical Technology (FKKT) is kindly acknowledged for consultations about the elucidation of the crystalline structure.

Gratefulness also goes to our weekly group meetings, which sometimes resulted in constructive criticism and from which good ideas have emerged. All the members of K7 that helped me in any way are highly appreciated. I especially enjoyed the social environment that surrounded me during the writing of this PhD dissertation. Our “lunch group”, consisting of Špela Trafela, Anja Drame, Nina Kostevšek, Matic Korent, Matej Kocen, and other sporadically attending members was truly a great company. Another group of people that I would like to acknowledge are my E51 roommates. Luka Suhadolnik, Monika Kušter, Živa Marinko and Matic Korent maintained a calm atmosphere when needed, but they were also chatty at times, thus supporting a healthy office mood.

Towards the end, I wish to express the highest gratitude to my cheerleader Teja, to my mother Ana, father Marjan, brother Miha and uncle Ivan for their encouragements throughout the course of this PhD study.

Luka Kelhar

Abstract

The following manuscript discusses the fundamentals of glassy metallic alloys comprising Ce and Gd rare earth (RE) elements. It is of interest to observe to which extent the RE-based alloys inherit the behaviour of the respective RE and how the properties change with the variation between Al and RE. The core of this study lies in the characterisation of structure and magnetic behaviour since the former detrimentally affects the latter.

Besides containing one RE, the composition of quaternary alloys is made of Al, Fe and Cu in order for the general stoichiometry to read $(Al_{1-x}RE_x)_{62}Fe_{13}Cu_{25}$. Alloy design is based on the variation of Al and RE contents, whereas x=RE/(RE+Al), in order to test the impact of RE on the structure, microstructure, thermal behaviour and magnetic properties. A range of glassy alloys is found throughout the composition landscape, but they differ in the ability to hinder crystallisation, because some specimens are fully glassy whereas others contain crystallites, concurrently with a glassy matrix.

A set of Ce-based glasses exhibits a completely glassy structure when ratio x corresponds to the region of deep eutectics in the Al-Ce phase diagram. Microstructural investigation confirms this with the lack of crystallites in transmission electron microscopy (TEM) micrographs and the presence of diffuse rings in the selected area electron diffraction (SAED). The lowest temperature of glass transition (T_g) in Ce-based glasses appears already at 350 K, which, in general, is one of the lowest values for metallic glasses. Afterwards, crystallisation (T_x) appears with a lag of 10-50 K. The magnetic behaviour of Ce-based alloys is paramagnetic (PM) at room temperature (RT), whereas their local structure, crystallite content and composition do not significantly influence the magnetisation, which falls in the range 0.3-0.5 emu/g. Low-temperature magnetism of Ce-based x=0.75 alloys displays a shift from PM to antiferromagnetic (AFM) state, with a spin glass behaviour.

The structure of Gd-based alloys manifests a more reduced vitrification ability than that of Ce-based counterparts, which is consistent with a 300 K higher liquidus line in Al-Gd diagram. TEM observation of microstructure at atomic scale shows crystallites within the glassy matrix. The temperatures T_g and T_x are higher compared to the Ce-based system, which coincides with the higher melting point of Gd. Magnetic behaviour of Gd-based glasses at RT changes from PM to ferromagnetic (FM) and magnetisation increases from 4 to 16 emu/g. Below the blocking temperature, PM is replaced by AFM state. The evidence of spin glass behaviour appears as well. Local atomic structure of the glasses imparts a hybridisation effect, which couples the adjacent magnetic moments of the constitutive elements.

In addition to the variation of x, the ratio y=Fe/(Fe+Cu) between the immiscible Fe and Cu was altered, resulting in strong glasses for Cu-rich compositions. The glasses' magnetisation, however, is higher in the case of Fe-rich alloys.

The ribbons of Ce- and Gd-based metallic glasses were consolidated into cylinders in the range between T_g and T_x, via pulsed electric current sintering, while maintaining a glassy structure. The diffuse hump in XRD pattern of a composite is broadened due to

overlapping of Ce- and Gd-based ribbons, while thermal analysis and magnetisation preferentially follow the behaviour of Gd-based glass.

Povzetek

Doktorska disertacija obravnava temeljne lastnosti kovinskih stekel (KS) z vsebnostjo redkih zemelj (RZ) Ce in Gd, ki sicer pripadata isti skupini RZ kemijskih elementov, vendar pa se njune elektronske in magnetne lastnosti močno razlikujejo. S tem osnovnim vedenjem je bil namen doktorske disertacije študij vpliva količine dodatkov Ce oz. Gd na spremenjene lastnosti osnovnih zlitin, ki smo jih obravnavali. Pri tem je bil pomemben vpliv medsebojnega razmerja med Al in RZ v kovinskem steklu, ki smo ga raziskovali. Bistven del doktorskega dela je bila karakterizacija strukture in magnetnih lastnosti, saj struktura ključno vpliva na lastnosti novega materiala.

Sestava kvartarnih struktur KS, poleg Ce ali Gd, vsebuje tudi Al, Fe in Cu. Tvorba novih zlitin temelji na spreminjanju deleža x med Al in RZ, kjer je x=RZ/(RZ+Al). Vpliv tega deleža se odraža na spremenjeni strukturi in mikrostrukturi, spremenijo se toplotne in magnetne lastnosti. Zlitine s steklasto strukturo nastanejo v vseh preiskovanih vzorcih, kljub temu pa obstaja razlika v zmožnosti vitrifikacije med posameznimi sestavami zlitin. Nekateri vzorci so popolnoma steklasti, medtem ko drugi predstavljajo kompozit v matrici kovinskega stekla.

S prilagajanjem deleža x k sestavi, bližji evtektiku v binarnem diagramu Al-Ce, se sposobnost vitrifikacije Ce zlitin močno poveča. Popolnoma steklasto mikrostrukturo smo potrdili z uporabo transmisijske elektronske mikroskopije (TEM). Posnetek mikrostrukture brez opaznih kristalitov in difuzni SAED obroč dokazujeta popolno amorfnost dobljene zlitine. Temperatura steklastega prehoda (T_g) v Ce zlitinah se pojavi že pri 350 K, kar predstavlja eno najnižjih T_g v KS nasploh. Z zamikom 10–50 K nastopi še temperatura kristalizacije (T_x). Magnetizem Ce zlitin pri sobni temperaturi kaže paramagnetno stanje. Lokalna atomska struktura, pojav kristalitov in pripadajoča sestava nimajo močnega vpliva na magnetizacijo, ki se giblje v območju 0,3–0,5 emu/g. Pri nizkih temperaturah kaže magnetizem Ce-zlitine z x=0,75 prehod iz paramagnetnega (PM) v antiferomagnetno (AFM) stanje, opažamo tudi lastnosti, ki so značilne za spinska stekla.

Pri zlitinah, ki vsebujejo Gd, smo v primerjavi s Ce zlitinami opazili strukture z manjšo vsebnostjo steklaste faze. Razlog za to je ≈300 K višja temperatura taline v diagramu Al-Gd. Opazovanje mikrostrukture s TEM na atomski ravni potrjuje prisotnost kristalov v steklasti matrici. Temperaturi T_g in T_x sta v primerjavi s Ce zlitinami višji, kar sovpada z višjim tališčem Gd. Magnetne lastnosti Gd zlitin pri sobni temperaturi se spremenijo iz PM v feromagnetno ali tudi superparamagnetno stanje, magnetizacija pa se poveča s ≈4 emu/g na ≈16 emu/g. Magnetno obnašanje PM vzorcev pri nizkih temperaturah se spremeni v AFM, prav tako pa se pojavljajo posebnosti, značilne za spinska stekla. Vzrok za te spremembe je lokalna atomska struktura stekla z redom kratkega dosega, kjer pride do izrazite magnetne sklopitve med magnetnimi momenti.

Poleg spremembe deleža x smo v Ce zlitinah spreminjali tudi delež y=Fe/(Fe+Cu) med kovinama. ki se ne mešata. Izrazito steklasto strukturo smo opazili v zlitinah, bogatih s Cu. Magnetizacija zlitin je bila bolj izrazita v primeru zlitin z več Fe.

Steklaste trakce Ce in Gd zlitin smo konsolidirali oz. zgostili v cilindrične vzorce s tehniko sintranja s pulzirajočim tokom v temperaturnem območju steklastega stanja. Pri

tem se je struktura stekla ohranila, difuzen vrh v XRD posnetku pa se je razširil zaradi prispevka s strani Ce in Gd trakcev. Tako pripravljeni kompoziti izkazujejo lastnosti obeh osnovnih KS, toplotna analiza in magnetne meritve pa so pokazali, da stekla močneje sledijo obnašanju Gd zlitin.

Contents

List of Figures

List of Tables

Abbreviations

AFM ... antiferromagnetism/antiferromagnetic
AP ... atmospheric pressure
bcc ... body centred cubic
BF ... bright field
BMG ... bulk metallic glass
DF ... dark field
dhcp ... double hexagonal close packed
DSC ... differential scanning calorimetry
DRP ... dense random packing
DRPHS ... dense randomly packed hard spheres
DTA ... differential thermal analysis
EC ... electronic configuration
EDS ... energy-dispersive X-ray spectroscopy
FC ... field cooled
fcc ... face centred cubic
FFT ... fast Fourier transform
FJC ... free jet casting
FM ... ferromagnetism/ferromagnetic
FS ... free side of the ribbon
FSDP ... first sharp diffraction peak
FWHM ... full width at half maximum
GDA ... glass devitrification ability
GFA ... glass forming ability
HAADF ... high-angle annular dark-field
hcp ... hexagonal close-packed
HRE ... heavy rare earth
IFFT ... inverse fast Fourier transform
LRE ... light rare earth
LRO ... long-range order
MG ... metallic glass
MRO ... medium-range order
PD ... penetration depth
PDF ... pair distribution function or pattern diffraction file
PECS ... pulsed electric current sintering
PFC ... planar-flow cooling
PM ... paramagnetism/paramagnetic
RE ... rare earth
RF ... radio-frequency
RMA ... random magnetic anisotropy
RS ... rapid solidification
RT ... room temperature

SAED ... selected area electron diffraction
SC ... strip casting
SCL ... supercooled liquid
SG ... spin glass
SPM ... superparamagnetic/superparamagnetism
SQUID ... superconducting quantum interference device
SRO ... short-range order
STEM ... scanning transmission electron microscopy
TEM ... transmission electron microscopy
TG ... thermogravimetry
TM ... thermal method
VSM ... vibrating sample magnetometry
WS ... wheel side of the ribbon
XRD ... X-ray diffraction
ZFC ... zero field cooled

Symbols

α	... solute site
β	... secondary solute site
δ	... difference between the heat flux of the baseline and heat flux of the SCL region
δH_{mix}	... mixing enthalpy
δT_g	... temperature range of a supercooled liquid
γ	... tertiary site
η	... viscosity
θ	... Bragg angle between incident or diffracted beam and fixed crystal plane
λ	... radiation wavelength
μ_0	... permeability of free space
μ_B	... Bohr magneton (effective magnetic moment per atom)
χ_{mass}	... mass susceptibility
ϕ	... heat flux
ϕ_0	... one flux quantum
Ω	... solvent site
B	... magnetic induction
C_{min}	... minimum solute concentration
D	... size of the MRO structure/particle/precipitate
D_c	... critical diameter
d_{hkl}	... interplanar distance
d_{max}	... 2θ angle of the maximum of the glassy hump
E_b	... binding energy for bringing the electrons from a core level to Fermi level
H_{max}	... maximum applied magnetic field
I	... current flowing through the long wire/intensity
I_i	... integrated intensity
M	... magnetisation
M at H_{max}	... magnetisation at the maximum magnetic field
M_s	... magnetisation at saturation
Q	... momentum transfer vector
Q_M	... maximum of the Q peak
R	... atomic radius
T	... temperature
T_b	... blocking/Néel temperature
T_c	... Curie temperature
T_{cr}	... critical temperature
T_f	... fictive temperature
T_g	... glass transition temperature
T_l	... liquidus temperature
T_m	... melting temperature
T_N	... Néel temperature

T_{rg} . . . reduced glass transition temperature
T_x . . . crystallisation temperature
V . . . cooling rate/growth rate
Z . . . coordination number

Chapter 1

Introduction

1.1 Glassy State of Matter

In equilibrium conditions, thermodynamically stable liquids are found above the liquidus temperature (T_l). Typical viscosities of the liquid metals are found around 10^{-2} Poise (P) and increase slowly on cooling, with the activation energy $\approx 3\ kT_m$, whereas k is the Boltzmann constant and T_m stands for the melting temperature [1]. When the liquid is cooled, one of two things can occur. Firstly, the formation of crystalline solids can take place, which completes at T_m, and is reflected by an abrupt change of volume, as illustrated by the vertical drop of the volume of crystal in Figure 1 [2]. Crystals are long-range ordered (LRO) solids and they are stable when kept below T_m. If, on the other hand, cooling from liquid does not lead to crystallisation at T_m, liquid's viscosity (η) increases with lowering of the temperature, which is demonstrated with the continuous trend of the slope in Figure 1. In this state, the liquid can be referred to as the supercooled liquid (SCL), since it is undercooled below T_m and still pertains liquid-like characteristics. As the temperature is further reduced, at the break of the slope we detect the glass transition temperature T_g [2], marking the formation of a glass [3].

At this point, it is reasonable to define a glassy and an amorphous solid. A recent (in 2017) suggestion by Zanotto and Mauro [3] describes both these states of matter as non-crystalline solids, however, glass exhibits T_g, while amorphous solid does not. The latter also cannot be produced with quenching, since this would result in glass transition [3]. Since some of the publications included in this PhD dissertation have been produced prior to this definition, amorphous and glassy state are used as synonyms in the present context, except when explicitly stated otherwise. It is, however, more accurate to name the majority of the alloys in this dissertation glasses.

A characteristic property of a glass is the absence of LRO, which means the lack of translational periodicity in 3-dimensional space for crystals and in dimensions higher than 3 for quasicrystals. For the sake of brevity in this work, we will use the word crystal to refer to any kind of LRO solid (crystal or quasicrystal). The resistance of a glass towards crystallisation is based on the transient bonding in the viscous melt, which restricts the formation of crystals, even when the temperature is brought down to a degree, where the free energy of the crystalline phase would be lower than that of the glassy phase [4]. In this respect, high η of the liquid is crucial in defying crystallisation, and in the SCL state it is described by the empirical Fulcher's expression [1]:

$$\eta \approx \eta_0 exp[B/(T - T_0)] \tag{1.1}$$

Where η_0 and B are material's connected constants and T_0 is the ideal glass transition temperature [1]. Spatial atomic configurations of a liquid and a glassy phase do not differ significantly, hence a glass can be regarded as a solid with a frozen-in liquid structure [1]. According to the current and revised definition by Zanotto and Mauro [3], glass is a non-equilibrium, non-crystalline state of condensed matter that exhibits a glass transition and whose structure is similar to that of SCL. With time, glasses spontaneously relax towards the SCL state. Due to structural entropy, glasses readily exhibit 0.5-3% lower densities [5] compared to crystalline materials. In view of their long-term stability, glasses are prone to produce crystals, which stay in equilibrium up to T_m.

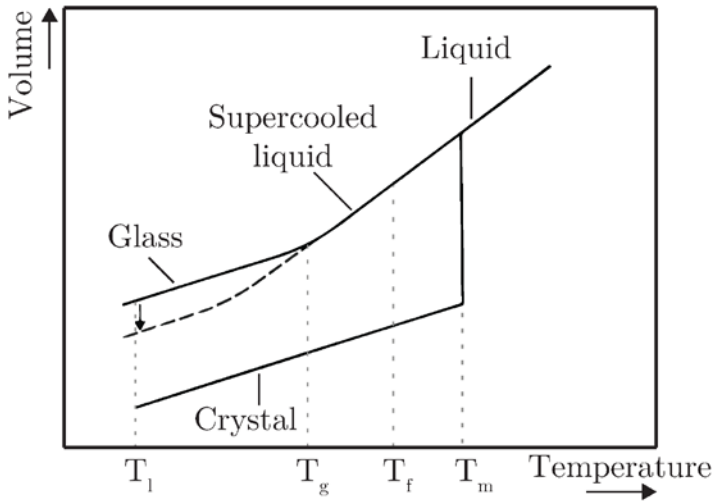

Figure 1: Schematic of the volume vs. temperature change. The change is less intense when the SCL is cooled through T_g into the glass. On the other hand, an abrupt volume change is displayed for crystalline solids. Reproduced from ref. [2].

For a cooling rate different from the equilibrium conditions, such as in the process of rapid solidification, the system becomes kinetically frozen above T_g, at the fictive temperature T_f (Figure 1). In such an event, the pertained glassy structure is frustrated and exhibits a lower density than that of the equilibrium structure. The difference between the density of metastable and equilibrium structure is known as the free volume. Subsequent annealing below T_g decreases this frustration by inducing atomic rearrangements. This process is known as structural relaxation [6] and the theory describing it as the free-volume theory [7], [8]. It describes the distribution of the excess volume, which can be carried out without energy change and is random within the glassy phase [7].

1.2 Historical Development and Properties of Metallic Glasses

The discovery of metallic glasses (MGs) dates back to 1960 when the group of Pol Duwez at Caltech accidentally found a material whose structure did not exhibit crystallinity [9]. While studying solid solubility limits, they quenched a thin foil of $Au_{75}Si_{25}$ at a rate of $\approx 10^6$ K/s and produced an alloy with a glassy structure. This discovery represented an immense scientific novelty, and already in the following years, experimental work expanded the series of alloys that were capable of vitrification [10], [11]. From that point on, efforts were

put in understanding the properties and formation mechanism of MGs [10]. This led to the development of the first bulk metallic glass (BMG) by Cu mould casting, which preserved the glassy nature even in samples with a thickness of 10 mm [12], [13]. Since the casting technique uses a much lower cooling rate of ≈100 K/s, this implies that the chemical composition of those alloys had to be adapted so as to reduce the atomic mobility [14]. Glass forming ability (GFA) of the alloys became a measure of their resistance towards crystallisation, given by the critical diameter (Dc) to yield a completely glassy specimen [6]. The diameters of Pd-containing glassy cylinders have pushed the GFA limit up to an astonishing 72 mm in diameter, which to date stays the maximum attainable thickness of BMG [15]. Determination of GFA, however, was not limited to dimensional measurements, although these indeed are the most definite. Empirically derived GFA measures have been proposed, and these rely on the thermal analysis in order to be associated with the ability of the glass to resist devitrification.

Advantages and drawbacks of MGs stem from the lack of crystalline boundaries and their monolithic microstructure. Due to their absence, mechanical properties (strength, elastic limit, hardness) of MGs are higher compared to crystalline materials [16]. A disadvantage, however, is their limited ductility and thereby increased probability of catastrophic failure in load-bearing condition [17]. Corrosion resistance of MG outperforms that of its crystalline equivalents, in which the corrosion process tends to propagate along the grain boundaries. A very useful property of MGs is the formation of SCL within a temperature region $\delta T_g = T_x - T_g$. It enables thermoplastic forming of glassy alloys and in its principle, it is very similar to the processing of polymers. The gains of processing in the SCL region are the ability to produce parts of intricate shape and tight tolerance [18] through the Newtonian flow of material while preserving the glassy structure and its peculiar characteristics. Alloys containing magnetic transition elements (Fe, Co, Ni) possess excellent soft-magnetic properties [19], which are useful for the construction of highly efficient power transformer cores, data communication interference components, magnetic sensors, magnetic shielding, etc. [20]. Characteristic of MG is an atomically smooth surface finish [21], which can be obtained via direct casting or subsequent thermoplastic forming. The surface smoothness originates from the lack of microstructural features, i.e. lack of grains and grain boundaries.

At present, MGs represent a vibrant and exciting field of scientific research, due to potential advantages that this class of alloys has to offer [22]. The room for improvement remains in the fundamental aspects i.e. understanding of the correlation between microstructure and mechanical properties and the ability to accurately predict glass formation [23], so as to design MGs with superior properties and affordable cost.

Even more anticipated, meanwhile, is the commercialization of MGs. There have been several target-aimed approaches in the past, but the majority of them failed due to problems with inconsistency in manufacturing and insufficient knowledge of materials' properties in the long term [22].

1.3 Structure of MG

1.3.1 Short-range order

In order to understand the structure of multicomponent MGs at atomic level, it is essential to introduce the concepts of atomic organisation on the level of several neighbouring distances. In this respect, short-range order (SRO) and medium-range order (MRO) will be introduced. As depicted in Figure 2, SRO (in a binary MG) can be regarded as the assembly of atoms, where the scarce solute atoms are surrounded by more numerous solvent species [24] and the size scale features up to 0.5 nm in length [2]. Central solute atom and its nearest neighbours in the first and second coordination shell have several topological configurations, of which the most frequent is either one of Kasper's polyhedra (tetrahedron, octahedron, etc.) [25] or icosahedron [26], [27]. As shown in Figure 2a packing efficiency of SRO cluster depends on the ratio R=Rα/RΩ between the radius of the solute atom (Rα) and the radius of the solvent atom (RΩ) [28]. There exist specific R, which result in efficiently packed clusters of spheres, as shown by the histogram in Figure 2b. In order for the spheres in the first coordination shell to yield integer coordination numbers, the radius of the central solute sphere Rα needs to be [29]:

$$R_\alpha = \left\lfloor \frac{1}{\sin \pi/Z} \right\rfloor - 1 \tag{1.2}$$

where Z stands for the integer number of neighbouring (solvent) spheres in the first coordination shell. As per the histogram in Figure 2b, metallic glasses most commonly feature a value of R=0.799, which indicates a cluster with Z=10 [28]. Additional frequent values are R=0.710 for Z=9, R=0.902 for Z=12, R=1.116 for Z=15 and R=1.248 for Z=17 [28]. This indicates that MGs with these particular R ratios and Z values tend to form the most stable glassy structures. Strong preference for these R values is in line with the model of efficiently packed atomic clusters and outlines its importance in the description of the structure of MG [5], [29], [30].

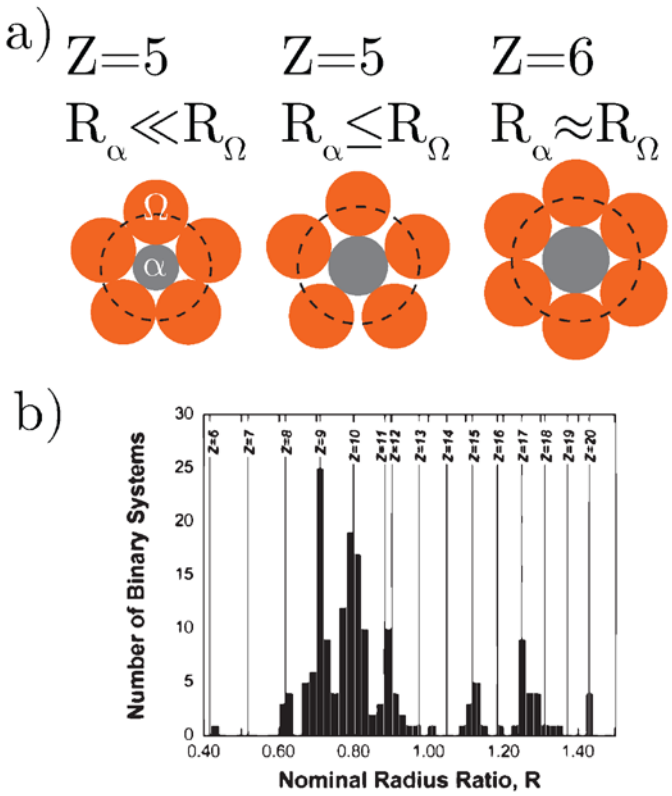

Figure 2: a) Atomic packing in SRO illustrated in two dimensions, depending on the ratio of solute (α)/solvent (Ω) spheres. Designations Rα and RΩ mark the diameter of the solute and solvent sphere, respectively. Z is the number of neighbouring Ω spheres. Reproduced from [28], [29]. b) The frequency of binary systems in three dimensions, where vertical bars predict the number of binary systems that exhibit a certain ratio R. Cluster coordination number of the particular R-value is denoted with Z values above the bars. Reproduced from [28].

1.3.2 Medium-range order

Medium range order is in comparison with SRO much more difficult to define. According to the textbook of Elliot [2], the size scale of MRO is in the range 0.5-2 nm and spans beyond the first and second coordination shells [2], [31]. Representative structural elements of MRO (according to the currently most suitable efficient close packing model [29]) are clusters with distorted fcc-like lattice (Figure 3), arranged over a distance of several cluster diameters [2]. Adjacent clusters exhibit no sign of orientational order, making the atomic positions in the first coordination shell (β spheres in Figure 3a) completely random. There are four distinctive structural sites in MRO structure, some of which are analogous to SRO. The first one is a central, cluster-forming atom α (solute), which is surrounded by Ω atoms (solvent). Secondary solute atoms β occupy octahedral sites of the cluster and tertiary γ sites (shown with orange spheres in Figure 3b) are located in tetrahedral interstices, in the first shell of the clusters [29].

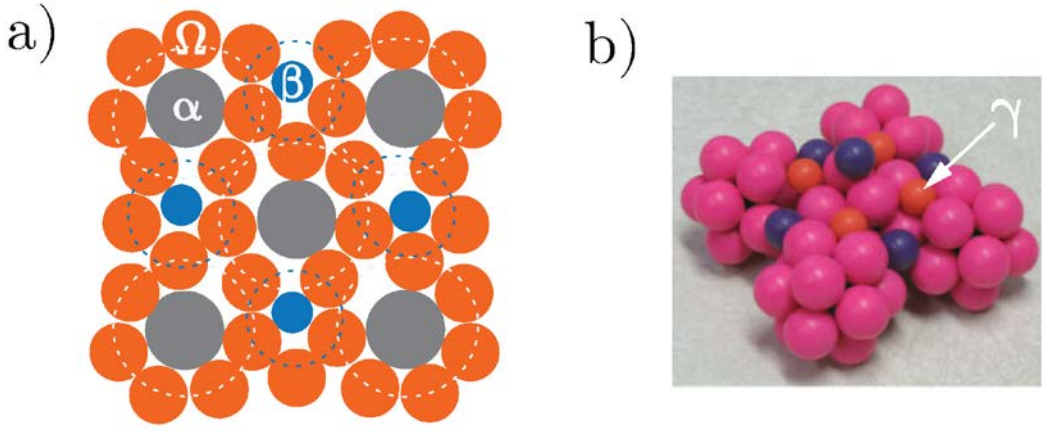

Figure 3: a) MRO of several clusters in two-dimensions, where α designates the solute atom, Ω stands for solvent atoms and β labels a secondary solute. Reproduced from [32]. b) Three-dimensional representation of MRO clusters, with tertiary solute atom γ, represented by orange spheres [32].

MRO structure is influenced by features such as the spatial correlation of voids, large ring structure and "quasi-lattice planes", which distort the crystallographic arrangement of atomic species [31]. To characterize the MRO structure, the region of the first sharp diffraction peak (FSDP) or low-Q structure (LQS) is frequently used. Here, Q stands for the magnitude of the scattering vector [33], while LQS is found in reciprocal space within 5-20 nm^{-1} [31]. Parameter Q connects to the real space θ values with the scale $Q=4\pi\sin(\theta)/\lambda$ [31], where λ marks the wavelength of the utilized radiation. For some cases, it is possible to describe the structure factor solely via interatomic potential with the treatment of pairwise interactions, which works for dense randomly packed hard spheres (DRPHS) with simple interatomic potential.

A small peak which precedes the FSDP in the structure factor plot (shown in Figure 17b) is also one of the strong indications of MRO in MG [2], [31]. It is often termed as a "pre-peak", while its position in the structure plot is located at $Q\approx0.1$ nm^{-1} [2]. The expression that links the diffraction line profile with the size of the MRO structure (D) indicated by a pre-peak can be gauged by considering the Scherrer equation [2]:

$$D = \frac{K\lambda}{\beta cos\Theta} \tag{1.3}$$

whereas K equals a constant of ≈0.9, and β is the half-width of the diffraction line in radians. Values of D for a series of Ge-chalcogenide glasses in real space are found to be ≈1.5 nm [2].

1.4 Modelling of the Glassy Structure

First attempts to describe the structure of MGs in the 1960s by Bernal [34] and Scott [35] were based on the dense random packing (DRP) model. This model assumes randomly packed hard spheres, as in the structure of a liquid. It can satisfactorily describe monoatomic metallic systems as well as those in which multiple constituents have comparable atomic sizes and insignificant chemical SRO. The packing of larger solvent atoms is dense and random, while the solute atoms are jammed into the cavities left by the former [36].

Since the DRP model could not account for solvent atoms smaller than the solutes, another one, named stereochemical model was developed [37], [38]. Local atomic arrangements are here constrained by the positions of atomic species (positional order) and their chemical distribution, i.e. positions of the respective atomic species (chemical order) [37]. SRO is similar to the structure of crystalline compounds, having the same composition, however, with shifted positions of the atoms [37], [38]. Despite notable progress in the determination of the MG structure, the description of MRO was still not tackled. In 1985, Dubois, Gaskell and Le Caër proposed a model to describe metal-metalloid glassy structures via the concept of chemical twining [39]. Structural units, made of triangular prisms, are linked via vertex atoms, representing an organisation that extends into MRO. This way, a homogeneous structure capable of describing the metal-metalloid glasses is obtained.

Theory of Miracle from the beginning of the 2000s proposed a "sphere-packing scheme", i.e. dense packings of overlapping atomic clusters [5], [30], [32], [40]. In this model (visualized in Figure 3), an arbitrary fcc or most efficiently packed [41] hcp lattice of clusters is taken and distorted with a strain factor, so as to diminish the LRO. In metal-metal MGs, such as $Zr_{65}Ni_{35}$, this model can account for MRO up to a radial distance of 0.7–1 nm [32]. Vitreous compositions of a wide array of simple and complex alloys [30], including an extensive series of eutectic MGs [42]–[44], can be predicted in this manner.

To cross-check the theory developed by Miracle, Sheng et al. set out to solve the three-dimensional structure of MG without the use of a predetermined structural model [25]. By implementing reverse Monte Carlo simulations of experimental X-ray diffraction data, coupled with ab-initio simulations of molecular dynamics in Ni-based binary MG, they reconstruct the atomic positions, describe the topological entities of clusters and propose their assembly into MRO range [25]. A very good match is found between the experiments and the reconstructed atomic-level structure of MG, pointing out at the superior ability of this technique in MG structure determination.

1.5 Requirements for Metallic Glass Formation

Formation of glasses is alleviated by a number of factors. Among crucial parameters are the properties of the atomic species, such as their atomic size mismatch [23], electron configuration [45], immiscibility [46], mixing enthalpy [47] and their amounts in a multicomponent glassy alloy [48]. The composition of the alloy close to eutectic is also one of the prominent glass forming stimulators [49].

1.5.1 Influence of atomic size

The influence of atomic size with regards to diffusion and alloying has been studied since the first half of the 20th century [50]. First criterions that facilitate the formation of solid solution phases, i.e. Hume-Rothery rules have been given more than six decades ago in the form of three empirically derived rules [51]. Several years later, Egami and Waseda [52] proposed a similar set of criterions to explain the formation of MG. They say that when the size difference of solute and solvent atom reaches a critical limit, atomic strains are generated. These strains lead to topological instability of the crystalline lattice and vitrification takes place. To determine the minimum solute concentration (C_{min}) for glass formation and the size of atomic size mismatch, Egami and Waseda proposed an expression to determine C_{min} [52], [53]:

$$C_{min} = \frac{0.1}{|(R_\alpha/R_\Omega)^3 - 1|} \tag{1.4}$$

where R_α and $R\Omega$ have the same meaning as above. By increasing the difference between R_α and $R\Omega$, the critical concentration of solute species decreases [53]. Since solute atoms solely occupy substitutional sites, the probability of giving rise to internal stresses increases, and with it, the ease of vitrification increases as well.

Topological theory of glass formation by Egami and Waseda was further evolved by Miracle and Senkov at the beginning of 2000s. They postulate that increasing the difference of the atomic sizes R_α and $R\Omega$, decreases C_{min} in the range $R_\alpha > 0.82R\Omega$ [54], where α atoms are substitutional. When $R_\alpha < 0.8R\Omega$, critical concentration of solute α species features a decrease and their position is entirely interstitial, which was not proposed by the previous theory. At present, one of the proposed and agreed topological parameters for obtaining a glassy material in binary or higher order systems is the atomic size difference between the constituent atoms [48]. It should amount to at least 12% [55].

1.5.2 Formation of metallic glasses at eutectic compositions

Another possibility of how to stabilize a glassy structure during the transition from a liquid to a glassy state is to design a suitable composition. As it was found experimentally more than half a century ago [56], eutectics greatly aid in the formation of a glassy structure. Although not all eutectic compositions are found to form glassy alloys upon rapid cooling, many of them feature a stoichiometry that corresponds to near-eutectic regions [42]. A reason for the stabilisation of the glassy phase in the vicinity of eutectics is the shift of the liquidus temperature (T_l) to temperatures, which are much lower than that of the pure metals' melting points. This is shown in Figure 4, with the binary diagrams of Al-Ce and Al-Gd, featuring a significant decrease of the liquidus line around the eutectic compositions. During non-equilibrium solidification, (such as planar flow casting) processing in the region with lower T_l gives the liquid an extended range of undercooling. Liquid phase is stable over a much larger temperature span, which favours vitrification of the alloy before solidification can take place. The decrease in T_l brought about with the discovery of multicomponent eutectic MGs, enabled the fabrication of BMGs using the cooling rate of the order $\approx 10^2$ K/s (mould casting), instead of previously required $\approx 10^5$ K/s achieved with RS techniques [57].

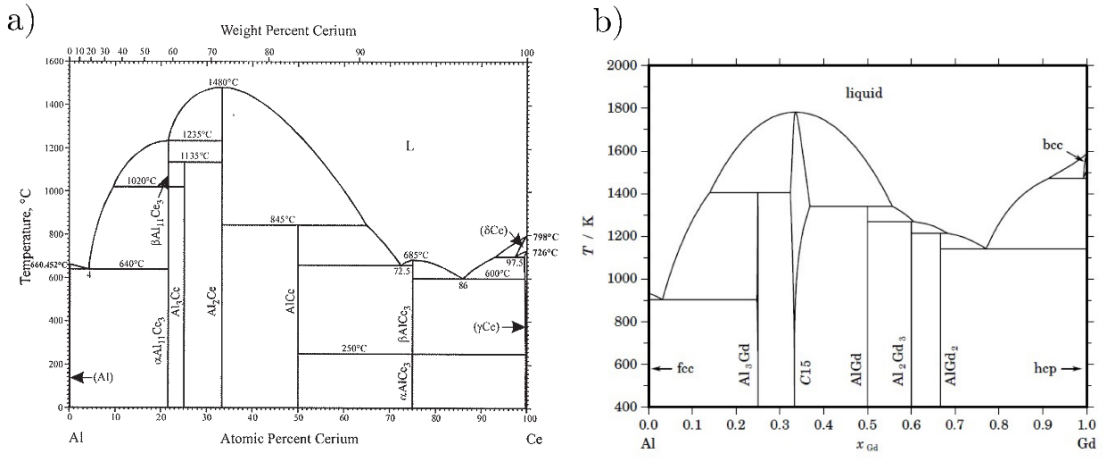

Figure 4: Binary alloy phase diagrams of a) Al-Ce [58] and b) Al-Gd [59] systems.

Al-Ce and Al-Gd belong to the series of phase diagrams with an asymmetric eutectic coupled zone at $\approx 2/3$ of RE, as depicted in Figure 4. The composition of eutectics is governed by the atomic structure of a liquid, made of two different atomic species. According to a recent theoretical suggestion, eutectic liquids comprise of primary and secondary SRO clusters, connected with 2, 4 or 6 glue atoms, which compensate for the compositions in the vicinity of the eutectic point [60]. The most common coordination numbers of the clusters equal Z=9, Z=10, Z=12 and Z=14, and they structurally correspond to the relevant eutectic phases. Factors that influence the overall cluster-glue structure of the liquid include atomic size, atomic concentration and the discrepancy between the different cluster sizes and geometries [60].

The growth of the glassy phase from the liquid in the binary system competes with eutectic and primary crystallites α and β, as seen in Figure 5. For low cooling rate (V) and eutectic composition, the growth temperature (thick solid line in Figure 5b) of the eutectic is above that of α or β, Figure 5b. This implies that the microstructure with such V is eutectic. If V is increased, precipitates α or β are formed along with a eutectic. Glass transition temperature T_g does not depend on the cooling rate, thus appearing with a straight line in Figure 5b and d. A further increase of the cooling rate between V_c and V_a, causes precipitates α to coexist with a glass. When $V>V_a$ the growth temperature is reduced below that of the flat-line T_g, and complete alloy vitrification takes place [61].

Off-eutectic compositions will be fully eutectic at low V (thick solid line in Figure 5d), whereas an intermediate V will produce dendrites and eutectic. Further augmentation of V will again yield a microstructure consisting of the eutectic. For V higher than V'_a the resulting alloy will be completely glassy [61].

The comparison between eutectic and off-eutectic alloys outlines different minimum V values to yield a glass. In the case of a eutectic alloy, cooling rate V_a needed to completely vitrify the alloy is higher than the same rate for off-eutectic alloy, Figure 5b and d. Consequently, for the asymmetric eutectic coupled zone, off-eutectic alloys can yield stronger glasses than strictly eutectic alloys [61], [62].

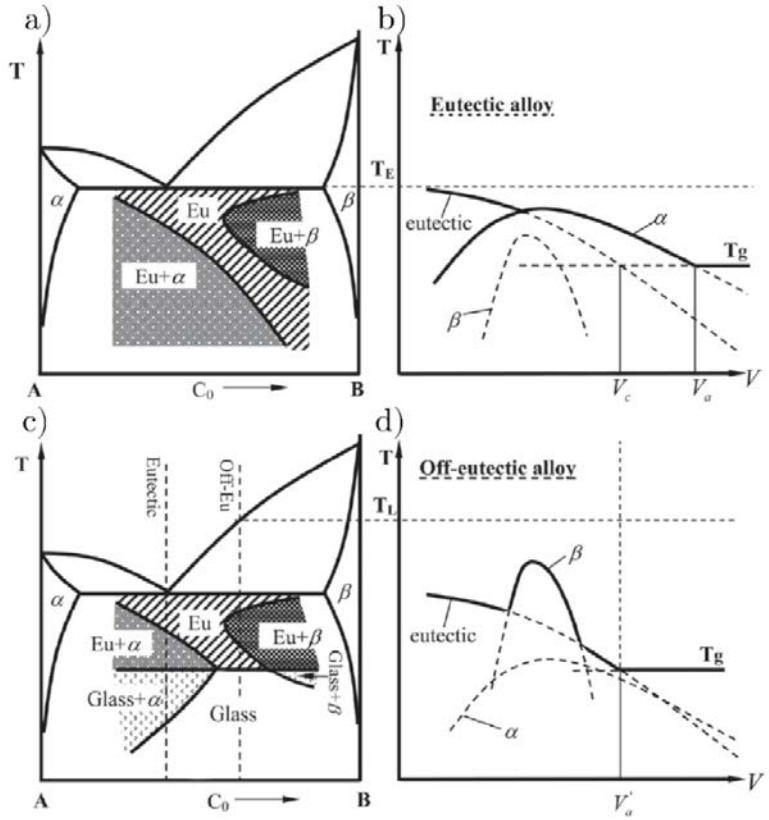

Figure 5: Diagrams of an asymmetric eutectic coupled zone and its connection with the glass-forming ability. (a) A eutectic system with an asymmetrically coupled zone. (b) The growth temperature of the phases as a function of growth rate V for the eutectic alloy. (c) Different phase regions related to the asymmetrically coupled zone, whereas eu labels eutectic, glass is the glassy phase and α and β are the precipitate phases. (d) The growth temperature of the phases as a function of V for an off-eutectic alloy. Diagrams originate from ref. [61].

The majority of binary eutectics in metallic systems appear at discrete composition ratios in the phase diagram, as depicted in Figure 6. First observation of this order dates back to 1935 when Stockdale suggested that the compositions of A_xB_y eutectics are in very good correspondence with simple whole-number ratios of the constituent atoms A and B [63]. A few decades later, these postulations were confirmed by Hume-Rothery and Anderson [64], by outlining several maximums in the occurrence of eutectics. They were found at A/B ratios of 8/1, 5/1, 3/1, 2/1 and 3/2. The latter authors [64] proposed that eutectics are likely to form when interatomic interactions are such that B–B nearest neighbours are avoided and instead, the structure of eutectic liquid features an icosahedral motif [64]. More recently, it was suggested that the remaining ambiguities in the theory of Hume-Rothery and Anderson can be resolved with structural models of Miracle glasses [42]. The reason for peculiar ratios of eutectics is connected with the characteristic cluster packings, which are found in $A_6B_1C_1D_2$ and $A_8B_1C_1$ compositions [5], [32]. Replacing the sites of C and D atoms with B species in different proportions results in the ratios given by Hume-Rothery and Anderson. The most frequently encountered ratios are then found to be A_2B_1 and A_3B_2 [42]. In the Ce-Al system, eutectics are located around the ratio 5/1 ($\approx Ce_{86}Al_{14}$), at a temperature of 600°C, and around the ratio 3/1 ($\approx Ce_{72.5}Al_{27.5}$) and a temperature of 685°C [65], which conforms to the Stockdale/Hume-Rothery's eutectic puzzle. In the Gd-Al system, the eutectic appears at higher amounts of Al, around the ratio 3/1 ($\approx Gd_{77}Al_{23}$) [66], [67], whereas the equilibrium eutectic temperature is 875°C. The latter is due to the Gd metal having a higher melting point than Ce.

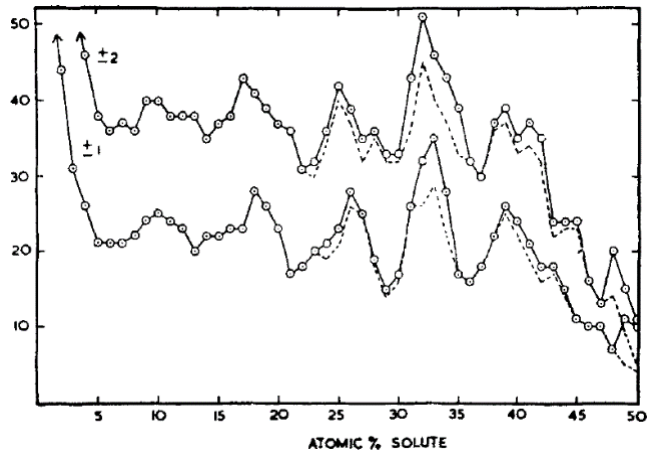

Figure 6: The frequencies of eutectics according to the Stockdale/Hume-Rothery eutectic puzzle. Notations ±1 and ±2 reflect the composition range, from which the plotted eutectic points are taken. To explain, composition at 20 at% corresponds to the values on the ordinate of 23 and 37 for the ±1 and ±2 curve, respectively. The curve marked with ±1 thus includes 23 eutectic points in the range 19-20-21 at%, while the curve marked with ±2 covers 37 compositions and features a broader composition range of 18-19-20-21-22 at% [64].

Another way to comprehend the improvement of glass formation at eutectic compositions is through the difference in the lengths of diffusive paths. For pure metals, the diffusive motion to crystallize is smaller than a single atomic diameter. In contrast, eutectic compositions require a chemical diffusivity path of several atomic diameters to facilitate crystallisation [56]. In turn, a higher amount of energy is required to trigger the crystallisation of eutectic melts, which preserves the glassy nature of such alloys.

1.5.3 Influence of formation enthalpy

Phase-formation requires a suitable formation or mixing enthalpy (δH_{mix}) between the constituent species in order to guarantee thermodynamic stability. Negative δH_{mix} promotes the formation of stable crystalline phases. Meanwhile, positive δH_{mix} imparts repulsive interactions between the atomic species, which hinders the formation of stable phases and facilitates immiscibility of the elements [68]. For $\delta H_{mix} \approx 0$, the mixture resembles an ideal gas, whereas the mean contribution of the multiple substances is the same as that of the final mixture.

The empirical rule for the formation of MGs, which was postulated nearly two decades ago by Inoue [18], says that stabilisation of MGs requires negative heats of mixing among the constituents. Nevertheless, there are several departures from this rule, which outline the complexity of MG modelling. Some Zr-, Cu-, Fe- and Ni-based MGs were stabilised with additions of alloying elements, which have a positive δH_{mix} with the main element [69].

In order to demonstrate the discrepancy in δH_{mix} between the crystalline and the glassy phases, Figure 7 depicts the calculated δH_{mix} diagrams of the glassy and crystalline phase in the Al-Ce system. As observed, δH_{mix} of the glassy phase is more negative than that of the crystalline phase in the range 20-80 at% Ce [70], implying that in this composition range, the formation of glassy phase is favoured against crystalline phase. Experimental evidence suggests that the rapidly quenched ribbons exhibit predominately glassy [71], [72] or fully glassy [73], [74] microstructure for compositions in the range 70-80 at% Ce. This region is in close vicinity of the eutectic in Al-Ce at 72.5 at% Ce [75]. These near-eutectic compositions turn glassy when quenched to thin-foils [73] or when synthesized in the form of thin films [72].

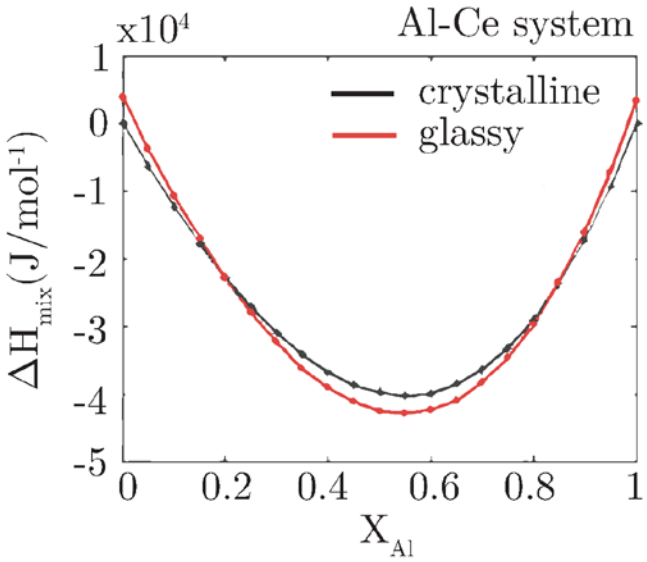

Figure 7: Mixing enthalpy-composition diagram of Al-Ce system. Reproduced after [70].

1.6 Fundamental Properties of Rare Earth Elements

Rare earths (REs) or lanthanides are a family of 15 elements spanning from La with atomic number Z=57 to Lu with Z=71. Due to specific electronic and physical behaviour of the RE group, two other elements are frequently counted as REs. These two metals are Sc, Z=21 and Y, Z=39. According to the geochemical nomenclature, REs are subdivided into light rare earth (LRE) subgroup, comprising La-Sm, and heavy rare earth (HRE) subgroup, spanning from Gd to Lu. Element Eu represents a breaking point in this classification, due to its anomalous behaviour [76].

In this classification, Ce belongs to the group of LRE and Gd is regarded as HRE. In a chemical sense, REs are very similar, which explains their troublesome separation. The first successful isolation of RE was accomplished in 1827 when Ce was reduced to metallic form from $CeCl_3$, [77]. At that time, the produced metal was heavily contaminated with impurities and thus inappropriate for structural and physical properties characterisation. It took another hundred years to produce Ce in a form pure enough to be used for diffraction experiments [78]. First achievements in the isolation of RE to pure metallic form were accomplished by Spedding and co-workers in 1952. They used a metallothermic process to reduce the chloride compounds (containing RE) with Ca, which worked for LRE compounds with low melting points. For HREs with higher melting points reduction of chlorides with Li [79], [80] and reduction of fluorides with Ca [81] have been developed in the 1960s. Even today, the method of reduction remains the utmost efficient method to produce pure RE.

Despite its name, REs are contained in a vast majority of ores and their natural abundance in crustal rocks in fact is not as scarce as the name suggests [76]. The second RE which will be addressed in this work, Gd, is about ten times scarcer than Ce, with 6.2 ppm [82] in the Earth's crust. Natural abundances of REs, lined up with those of other elements are given in Figure 8. REs are located somewhere in the middle of the plot with regards to the abundance. It is seen that some more common elements, i.e. precious metals, are significantly scarcer than REs.

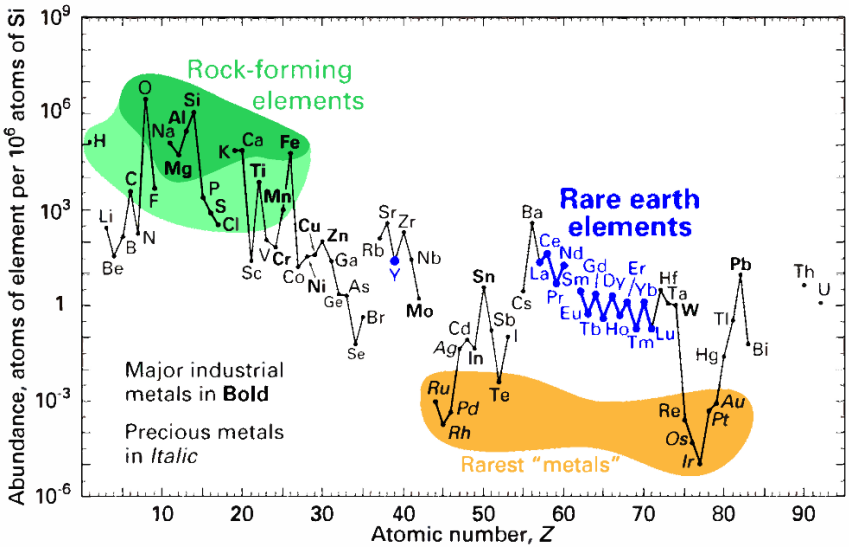

Figure 8: Abundance of chemical elements in the Earth's upper continental crust as a function of atomic number. RE from La–Lu and Y are labelled in blue. Diagram reproduced after [83].

1.6.1 Physical, electronic and magnetic properties of cerium

It can be claimed that Ce was discovered simultaneously by Hisinger, Berzelius and Klaproth in 1803 [84], although in that time Ce was intermixed in the mineral called "cerite" [85]. It took several decades to prepare the metallic Ce, but even those pieces were contaminated with oxychlorides [84]. The first significant advance in purifying Ce was accomplished by the Swedish chemist Mosander. Following slow but steady steps, the next achievement in isolation of Ce was electrolytic preparation by Hillebrand and Norton in 1875 [86] and in 1911 Hirsch obtained Ce, which only contained 2 % of impurities. On a large scale, Ce is nowadays produced with metallothermic reduction or via electrolysis of molten salt [85], [87].

The element features the highest abundance of all REs [83], and 27th [76] highest abundancy with 66.5 ppm [88] in the Earth's crust. It is also one of the cheapest REs. In the periodic table, Ce is located in period six, with Z=58 and belongs to LREs. The density of Ce at room temperature is 6.77 g/cm^3, while its melting point is set at 799°C [87]. Its atomic diameter according to Pauling amounts to 0.1818 nm [89].

Ce features an electronic configuration (EC), based on the core of Xe, and supplemented by the valence electrons placed into the 6s orbital. With the appropriate denomination, its EC is written as [Xe] 4f^1 5d^1 6s^2. Ce is the first RE to have one electron in the 4f shell, and this configuration is responsible for many fundamental peculiarities of Ce, one of which is the previously mentioned fluctuation between 3$^+$ and 4$^+$ valence. The valence of 3$^+$ (found for most REs) is characteristic of pure Ce at RT, whereas delocalized 3.5$^+$ or 4$^+$ state is found in Ce-containing alloys or aqueous solutions. The basis for strong electron delocalization in Ce is that the energy of the inner 4f electron is very similar to that of the valence electrons [87]. Thus, only minor amounts of energy are needed to move this electron from inner to outer levels [87]. The manifestation of this transition is a volume change of 14% when the metal is exposed to pressure [90] or cooled to cryogenic temperatures [91]. This change is not constrained only to Ce metal but also appears in Ce-alloys. Eutectic glassy alloy $Al_{25}Ce_{75}$ exhibits a pressure-induced transition from low density to high-density glassy state, resembling the behaviour of the base RE [92].

Regarding the allotropic modifications, Ce is unique among REs, since its temperature and pressure alterations do not conform to the rest of REs. At room temperature (RT) and atmospheric pressure (AP), the stable variant of Ce is face centred cubic (fcc) γ Ce [87]. If the pressure is increased to 1.9 GPa, an isostructural transition to α Ce occurs, which is accompanied by the previously mentioned decrease of volume by 14 % [93]. The first-order transition line between these phases ends at a critical point with p_c=1.75-2 GPa and T_c=550-630 K [93]. As the temperature is elevated, at 999 K, the fcc γ Ce with lattice parameter a=0.5161 nm [94] changes to body centred cubic (bcc) δ Ce, while at 1071 K [95], δ Ce transforms to liquid state [95]. At AP and in the vicinity of solidus temperature, the density of liquid Ce is higher than that of its solid form. Below ≈260 K [94], γ Ce transforms into hexagonal close-packed (hcp) β Ce (lattice parameter a=0.3673 nm, c=0.1180 nm [94]), which is stable down to 77 K [95]. The low-temperature form α Ce (lattice parameter a=0.485 nm [94]) is then stable at T<77 K. Ce in fcc α form structurally resembles the variant encountered at high pressure, which is 16% denser than γ Ce [96].

The magnetic behaviour of Ce is paramagnetic (PM) [97] in the region RT-110 K [98], where Ce obeys a Curie-Weiss law χ=C/(T-θ), explained in the second publication [99] contained in this dissertation. Effective magnetic moment per atom (μ_B) of free Ce^{3+} ion, according to the calculation is 2.54 μ_B, whereas experimentally observed μ_B of Ce in RT-110 K range is 2.51 μ_B, conforming well with the predicted value [98]. Néel temperature of magnetic ordering (T_N), which marks the transition from antiferromagnetic (AFM) to PM state, is 13.7 K for β Ce and 12.5 K for γ Ce phase [97]. Applications of Ce are numerous

and stem from the fact that it is the most abundant RE. It is used as a polishing compound for efficient polishing of glass screens of mobile phones, and as a fluid catalyst for converting the crude oil into gasoline [85]. Ce is used in catalytic converters together with Pt-group materials, as well as a pyrophoric "misch metal" alloy, utilized as the ignition device in lighters and torches [100]. It is also used as a special additive for glasses and pigment for colouring toys, containers and household wares [101]. Due to the large unbalance in the production of REs [102], efforts were recently put in more effective use of Ce, with the aim to stabilize the global RE market. In this respect, new promising application of Ce is Al-Ce based alloy [103] with excellent castability and improved high-temperature stability compared to conventional Al alloys.

1.6.2 Physical, electronic and magnetic properties of gadolinium

Gadolinium was first detected in 1880 by Marignac, a Swiss scientist [87]. Through communication with Lecoq de Boisbaudran, they coined the name gadolinium, after the Finish scientist Gadolin, who discovered yttria in 1794 [104]. He found that the latter is a mixture of oxides, containing seven unknown metals, but could not separate them [105]. This reasoning was deduced from a set of characteristic spectroscopic lines in samples of didymium and gadolinite [106]. Six years later, Marignac and Lecoq de Boisbaudran isolated Gd in its metallic form.

One way to produce pure Gd is via metallothermic reduction. Gd oxide is converted to fluoride using ammonium bifluoride, followed by a reduction with metallic Ca, yielding a crude RE [107]. This procedure was first accomplished in 1942 at Ames Laboratory [108]. Another route to prepare the metal is by solid-state electrolysis, as an additional means of purification. With this step, the concentrations of non-metallic impurities can be reduced. Oxygen impurities can on average be reduced down to 0.5 at% [109].

Natural abundance of Gd is about 10 times less than that of Ce, with up to 6.4 ppm in the Earth's crust [110]. In the periodic table, Gd features Z=64 and its density is higher than that of Ce, amounting to 7.9 g/cm^3, while its melting point is 1313°C [87]. Due to the latter properties, Gd is sorted into the HRE group. Atomic diameter according to Pauling [111] amounts to 0.1795 nm, which is just slightly less than that of Ce.

Gadolinium is the first RE to exhibit a heavy-lanthanide crystal structure sequence [95]. Two allotropic modifications of Gd exist at AP. At RT, Gd is stable in hcp form [95], (a=0.361 nm; c = 2.603 nm [112]) and with the rise of temperature, transition to a bcc phase (a=0.406 nm) is observed at 1263°C [113], [114]. Atomic volume shrinks for 2 % on hcp to bcc phase transition. With the increase of pressure, hcp phase, stable at RT, changes to rhombohedral or "Sm-type" phase with a=0.892±0.001 nm and α=2.33±0.003° [112]. Further elevation of pressure to 6.5 GPa [115] results in a transition to double hexagonal close-packed (dhcp) phase, which is stable up to 24 GPa and then replaced by fcc above. At pressures higher than 33 GPa, a phase change of fcc to distorted fcc takes place [115]–[117]. The given phase-change-sequence conforms very well to the generalized phase changes in RE with pressure; namely, the majority of REs except Eu and Yb [116] follow an array: hcp → Sm-type → dhcp → fcc → distorted fcc [118].

Ground state EC of Gd, based on the core configuration of Xe is [Xe] 4f^7 5d^1 6s^2. It is the half-filled 4f electron shell, containing seven unpaired 4f electrons that gives Gd its spherical 4f shell and with it some prominent characteristics. The 5d and 6s conduction bands jointly contain three electrons per site, however, they are not responsible for the magnetism of Gd. These electrons are polarized by an exchange interaction with 4f electrons, which results in the temperature dependence of the band structure [119].

Gadolinium is one of four elements (in addition to Fe, Co and Ni) considered to be a classical Heisenberg ferromagnet around room temperature [120]. This is due to half-filled

4f-shell, with seven unpaired electrons giving rise to localized magnetic moments [119], [120]. Total magnetic moment per atom amounts to 7.63 μB [121]. Curie temperature (T_c), which marks the second-order paramagnetic-ferromagnetic transition is detected at ≈293 K, and below that temperature, Gd remains ferromagnetic (FM) down to liquid He temperature [122]. Easy magnetisation axis coincides with the c-axis in hcp, which is also [0001] direction, from TC down to the spin reorientation temperature, TSR>230 K [120]. Magnetic phase transitions of Gd are not only intriguing for its fundamental aspect, but also in a technological sense. Gd exhibits large magnetic entropy change near RT when the magnetic field is applied and removed. This can be used as an effective mean of magnetocaloric cooling since the piece warms up with the application of magnetic field and cools down with its removal. Under varying magnetic fields and isothermal conditions, Gd and its alloys can release 4 kJ/kg of heat, meaning that the achieved temperature difference (under adiabatic conditions) can be up to 14 K [123].

From the application side, there is no major consumer of Gd, but it is rather scattered through many different fields. An important application is that for Gd:YAG garnets used in microwave and laser devices [87]. Another emerging use for Gd, which was introduced in the previous paragraph, is magnetic refrigeration. Although its potential is not fully exploited yet, Gd metal is known to possess excellent near room temperature magnetocaloric properties [124]. The use of Gd-based alloys for heat exchange presents a clean, energy conservative and low maintenance solution [125], which could be the next-generation refrigerant technology [126]. A peculiar application of Gd derives from its characteristic of having the highest thermal neutron capture cross-section of any known element with a value of 49,000 barns [87], [127]. For this reason, Gd is used as a burnable poison in the fuel pin or moderator in the reactor core [127]. A minor quantity of 1% of Gd has been found to improve the workability and resistance of Fe- and Cr-containing alloys to high temperatures and oxidation [87]. For magnetic resonance imaging, Gd3+ ions are bound to organic ligands, oxide nanoparticles and similar structures, in order to serve as highly effective contrast agents [128].

1.7 Fundamentals of Magnetism

Magnetism represents the cornerstone of our modern society, with its ubiquitous role in the way we communicate, transport and produce. Some of the most important breakthroughs in magnetism occurred in the first half of the 19th century by a handful of discoverers. Hans Cristian Oersted in Denmark showed in 1820 that current carrying wire produces a field, which is capable of deflecting a compass needle [129]. With that, he demonstrated that an electric field generates a magnetic field. Months after Oersted's discovery André-Marie Ampère and Dominique-François Arago showed that current-carrying-coil is behaving like a magnet [130], laying the foundations of electromagnetism. A year later, Michael Faraday discovered the electromagnetic induction and demonstrated the principle of electric motor [129]. In 1827, Hungarian Istvan Jedlik was the first to put magnetism to use by constructing the world's first rotary machine with electromagnets [131]. The basic quantity in magnetism is the magnetic moment m. It originates from atomic structure, through the electron spin and electron orbital motion around the nucleus. The density of the local magnetic moment varies intensively on the scale of nanometres. On the macro scale, the time varied magnetic moment δm corresponds to homogeneous magnetisation M in a given volume δV [129]:

$$\delta m = M \delta V \tag{1.5}$$

and the theoretical outline of smooth variation in m is known as a continuous medium approximation [129]. Next, if we represent m with a small current loop (as seen from Figure 9a), it can be connected with the circulating electric current as postulated by Ampère. The current flowing on a long straight wire (shown in Figure 9b) is known as the Ampère's law. The expression used to calculate the magnetic flux field B is [129]:

$$\oint B\delta l = \mu_0 I \tag{1.6}$$

where δl is a small section of the wire, μ_0 the permeability of free space, corresponding to $4\pi 10^{-7}$ H/m and I is the sum of currents threading the path.

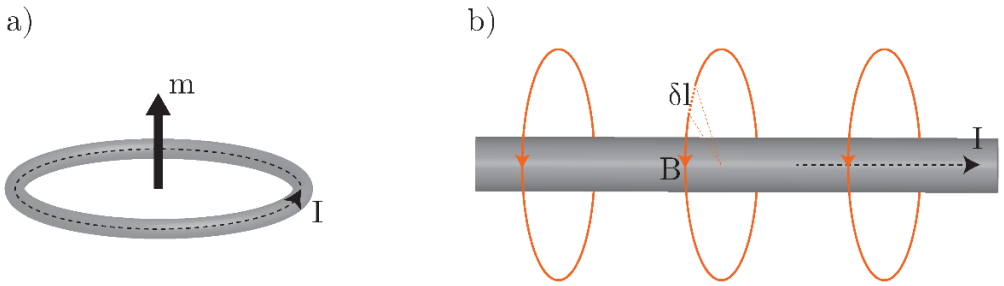

Figure 9: a) Magnetic moment m (axial vector) which appears due to the electric current I. b) Illustration of Ampère's law, where the current I flowing through the long wire is proportional to the induced magnetic flux B.

To further the understanding of magnetism, Jean-Baptiste Biot and Felix Savart proposed a rule to determine the magnetic field strength around a current conducting wire [132]:

$$\delta H = \frac{1}{4\pi a^2} I\delta l \times u \tag{1.7}$$

where δH marks the magnetic field strength generated by the current I, of infinitesimal length δl, set at a radial distance labelled with a. The letter u is a unit vector along the radial direction.

About a decade later, Michael Faraday postulated another vital law of electromagnetics. He found that changing the magnetic flux ϕ in the electrical circuit, in turn, changes the electromotive force, i.e. voltage V. Variation of the voltage with time follows an expression:

$$V = -\frac{\delta\phi}{\delta t} \tag{1.8}$$

whereas negative notation stands for the voltage being induced in the direction different than the flux change which produces it. This effect is known as electromagnetic induction. A set of great achievements in magnetics was crowned with James Clerk Maxwell's formulation of theory on electricity, magnetism and light in 1864, with four equations connecting the electric and magnetic fields [129]. They provide a concise concept for the understanding of electromagnetism.

1.7.1 Magnetic moment and its ordering

In the previous section, the evolution of the magnetic moment from purely a physics point of view was given. In the next lines, a connection with the material's atomic structure, the behaviour of atomic moments and evolution of magnetic order will be established.

The origin of magnetic properties lies in the motion of electrons, consisting of electron spin and electron circling around the nucleus and the explanation of this phenomena demands quantum physics. Electron motion results in an electronic magnetic moment akin to the schematic in Figure 9a. Further, the evolution of bulk magnetic moment can be explained with the models of atomic theory and band theory. While the former considers the electronic magnetic moment to be bound to the ionic core, the latter is due to conduction band electrons, which, when the atoms are joined in solid, start to move throughout the material. The first theory suits the behaviour of RE elements, while the second one is more appropriate for ferromagnetic 3d metals Fe, Co and Ni [133].

The emergence of bulk magnetisation, though, is bound to the collective aligning of the electronic magnetic moments. In this respect, several different magnetic moment interactions, meaningful for this PhD dissertation, are given in Figure 10.

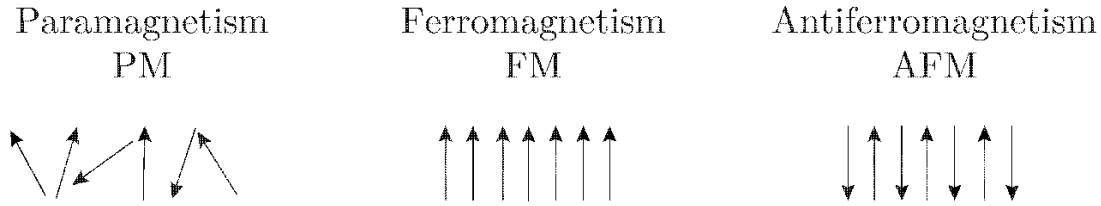

Figure 10: Schematics of paramagnetic, ferromagnetic and antiferromagnetic ordering.

Paramagnetism (PM) describes the degenerate nature of magnetic moment interactions, with spin-up and spin-down states being equivalent in size and direction. In the absence of an external applied field, this cancels out the net magnetisation [133]. On application of the external magnetic field, the spin-down states acquire additional energy that changes them to spin-up states and net magnetisation is obtained. Magnetic behaviour of Ce and Gd REs is PM at RT.

Ferromagnetism (FM) at RT appears only in 3d metals Fe, Co and Ni. An exchange interaction between the electrons aligns them in a co-operative manner to yield an effective magnetic field without the application of the external field, as opposed to PM behaviour. The outer electron band that determines the magnetic order is the 3d band being able to contain up to 10 electrons. Partial occupancy of the spin-down and spin up electron states invokes (via quantum mechanical phenomena) the parallel alignment of the spins, favouring the spin-up state. The result of this unbalance, determined quantitatively by the discrepancy in the energy of spin-down and spin-up states is net magnetisation of the material [133]. With a higher temperature, thermal fluctuations try to randomise the directions of magnetic moments. After exceeding the Curie temperature T_c, the material undergoes order-disorder transition and it becomes paramagnetic, thus loosing its net magnetisation.

Antiferromagnetism (AFM) is described as magnetic ordering where the nearest-neighbouring moments are aligned antiparallel, as shown graphically in Figure 10. On each sublattice, the electron coupling is positive, however, the coupling between the moments on the neighbouring sublattices is negative [134]. When the AFM material is brought to its Néel temperature, it obeys the Curie-Weiss law: $\chi = C/(T-\theta)$, where C is a constant and θ the value where χ intersects the temperature axis.

1.7.2 Magnetic hysteresis loop

In order to describe the behaviour of materials in the magnetic field, it is essential to understand the magnetic hysteresis loop and its characteristic features. The loop contains information which is intrinsic or extrinsic in its nature. Intrinsic information is independent of the material's shape and quantity, whereas extrinsic information depends on the shape of the sample, surface roughness, defects in the microstructure, history of thermal processing, magnetic field sweep rate, etc. [135].

When a magnetic signal of the sample needs to be determined, two different kinds of hysteresis loops need discerning. These two are B(H) (induction-field) and M(H) (magnetisation-field) hysteresis loops. The expression connecting the quantity B to M is [134]:

$$B = \mu_0(H + M) \tag{1.9}$$

B(H) loop shows the magnetic field as a sum of the material's magnetic field and external magnetic field, creating a curve with a steeper slope, as depicted in Figure 11. Such a curve needs to be considered for the construction of magnet-powered machines. For material's science though, M(H) loop is more convenient, since it only carries the magnetic signal of the sample, without the contribution of the external magnetic field.

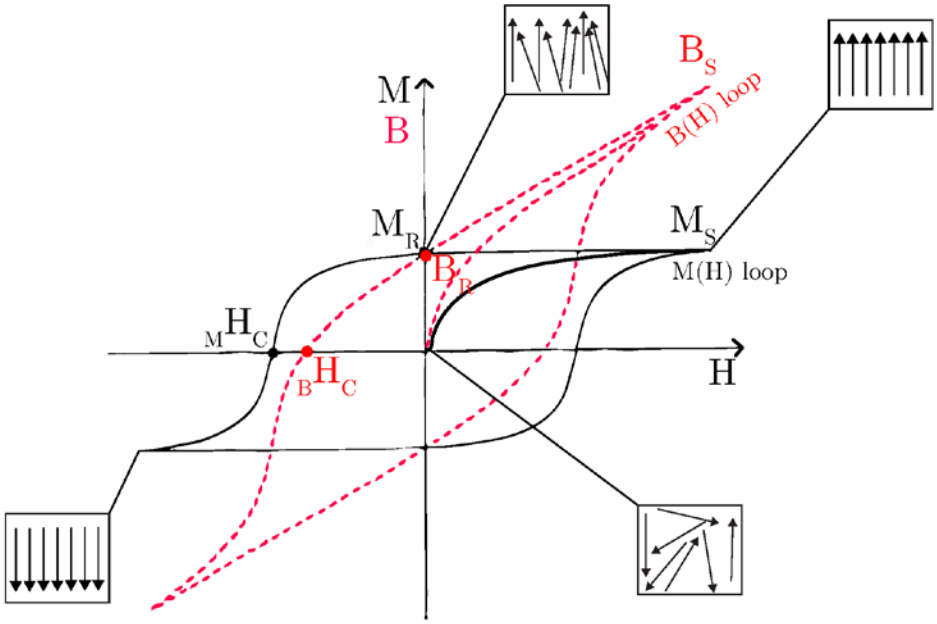

Figure 11: Magnetic hysteresis M(H) loop (black solid line) and B(H) loop (red dashed line). M_S stands for saturation magnetisation, B_S is saturation induction, M_R is remanent magnetisation, B_R is remanent induction, intrinsic coercivity is labelled with $_MH_C$ and normal coercivity is $_BH_C$. Rectangles containing the arrows outline the direction of magnetic moment vectors at a particular point in the hysteresis loop.

Magnetic hysteresis loop (in case of FM material) usually begins at the intersection of the horizontal and vertical axis, where the magnetic field and magnetisation equal zero and magnetic moments (within magnetic domains) are oriented randomly. As the field increases, so does the magnetisation, which occurs due to aligning randomly oriented magnetic moments in a parallel direction. In the state of full alignment, shown by an unidirectional set of arrows in the upper-right corner of Figure 11, saturation magnetisation

(M_S) is reached. The process is analogous on the B(H) curve; except that the final point is denominated saturation induction (B_S) and it is located at a higher ordinate, due to the addition of an external magnetic field. At M_S or B_S all the magnetic moments are pointing to one direction, i.e. the material has reached full magnetisation/induction. This first magnetisation sequence of the previously unmagnetized sample is referred to as the "virgin curve". As the field changes towards lower values, M or B are lowered until at H=0 some residual magnetisation remains and it is named remanent magnetisation M_R or analogously, remanent induction B_R. According to the amount of M_R and the shape of the hysteresis loop, materials can be characterised as ferromagnetic, paramagnetic, and diamagnetic. When the field's direction is inverted, i.e. goes to negative values, the next point on the loop is intrinsic coercivity (denoted ${}_MH_C$ or H_{CJ} or H_{Ci}) in the case of M(H) loop and normal coercivity (${}_BH_C$ or H_{cB}) in the case of B(H) loop. Their discrepancy is a consequence of non-inclusion or inclusion of external magnetic field, respectively. At the point of H_{Ci}, the sum of magnetic moments exhibits random orientation and the material is demagnetized. Coercivity defines the material as soft magnetic, hard magnetic or in between. In practice, the coercivity field can be viewed as the external field, needed to demagnetize the specimen. If we continue further along the hysteresis loop towards more negative fields, the point of M_S or B_S is reached once again, however, the direction of magnetic moments is now turned by 180°, as shown in Figure 11. As the hysteresis loop returns to positive H values, M(H) and B(H) loops are symmetrical to the shapes in the first three quadrants.

1.8 Summary of the Introduction

With the magnetic section, the introductory part of the dissertation is coming towards the end. Description of the glassy state, central to this PhD, was given. It was followed by the explanation of glass forming parameters and illustration of Ce and Gd, the two most important alloy constituents. The representation of magnetic phenomena aimed to introduce the reader to the concepts of magnetism, useful for the understanding of results in Chapter 4.

In the following Chapter 3, the utilized methods will be presented. The functional principles needed to understand the production of glasses via strip casting, as well as characterisation techniques of X-ray diffraction, thermal analysis, microstructure examination and magnetic measurements, will be introduced. With this knowledge, the transition to results-containing Chapter 4 will be more fluent and comprehensible.

Chapter 2

Methods

2.1 Rapid Solidification

The field of rapidly quenched metals opened up in 1960, with the discovery of the first metallic glass, obtained by quenching the Au-Si alloy from the molten state [9]. Rapid solidification (RS) or rapid quenching is defined as the fast extraction of thermal energy, during the transition from liquid state at high temperature to a solid state at ambient temperature. For the solidification to be considered "rapid", the cooling rate should be of an order greater than 10^4 K/s [136]. An important benefit of RS compared to equilibrium cooling (cooling rate to obtain the phases with minimum energy state) is higher control over the kinetics of crystallisation. This can be used in a way to avoid crystallisation and yield a fine-grained, nanocrystalline or glassy microstructure. By offsetting the cooling rate away from equilibrium conditions, RS permits extension of the solid solubility range. It can produce metastable phases and refine the grain size, which is difficult to achieve using conventional solidification techniques. For many alloys, use of RS is obligatory for the production of glasses, since it enables high cooling rates, essential for many glassy compositions.

2.1.1 Strip-casting technique

First achievements in continuous strip casting (SC) or melt-spinning date back to 1857 when Sir Henry Bessemer invented the process of twin-roll casting of steel [137]. There were, however, some serious problems with the control of fluid flow, melt distribution, refractory material and similar parameters. Bessemer's ideas were then revived in the 20$^{\text{th}}$ century by American engineer Clarence W. Hazelett who improved the technique and established the first commercial continuous metals casting company in 1924 [138].

In its fundamentals, SC involves the formation of a molten stream of alloy, which impinges onto a rotating disk to produce rapidly quenched ribbon in a continuous manner. Several different variants of SC exist, namely: chill block melt-spinning, planar flow casting, melt drag casting and twin-roll quenching.

The principal difference between these techniques lies in the way how melt is supplied to the cooling wheel, how it contacts it and the number of wheels in the SC system [137]. In respect of the first two points, SC is divided into free jet casting (FJC), also known as chill block melt spinning and planar flow casting (PFC), shown schematically in Figure 12. In FJC (Figure 12a), a molten jet of alloy impinges onto the surface of rotating wheel [139], while not being constrained from the top, but solely from the bottom by the wheel itself. The free falling of the melt makes the quench rate depend primarily on the characteristics of the melt puddle. Surface-controlled oscillation of the melt is a dominant factor for the unsteady thermal conditions and it also controls the crystallisation from the melt [140]. In PFC, the melt is constricted between the wheel and the nozzle [137], [141] (Figure 12b), meaning that the nozzle is set closer to the wheel, in comparison with FJC [141]. Such positioning minimizes the perturbations of the melt flow [142], resulting in ribbons of larger width and more consistent thickness (within 8%) [143]. Ribbons with the thickness of 10-

50 μm and width of up to 10 mm can be readily produced [144]. In an industrial environment, a width of 200-300 mm and length of some kilometres can be obtained [145].

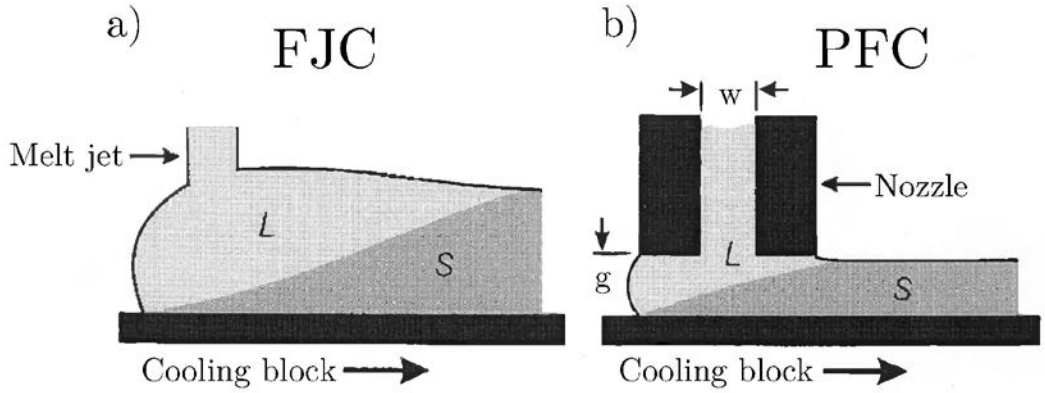

Figure 12: Schematics of a) free jet casting and b) planar flow casting. Reproduced after [137].

In the following, explanation of the PFC technique will be given with more details, since it is used throughout the experimental work of this dissertation. The similarities between PFC and FJC are very pronounced, meaning that most of the parts are used in both techniques. An integral part of PFC setup is the crucible, responsible for containing and properly distributing the alloy on the wheel. An appropriate crucible should be selected upon its chemical compatibility, temperature resistance, resistance to thermal shocks, thermal conductivity and porosity [146]. Materials that are commonly used for PFC include alumina (Al_2O_3), quartz (SiO_2), graphite and boron-nitride (BN) crucibles [146]. A batch of material is heated via radio-frequency (RF) induction coil, made of several windings of Cu tube. The temperature of the alloy is monitored with a pyrometer, positioned above the crucible so as to have a direct visual contact with the alloy. An alternative method is a measurement with a thermocouple, positioned inside the crucible. In order for this setup to work, the thickness of thermocouple wire must not exceed the critical diameter, so as to prevent the RF heating the wire [146]. At the bottom of the crucible is the nozzle, which allows the ejection of the molten alloy. Different nozzle shapes are possible, thus determining the stream volume and the width of the ribbons.

Another part of the PFC apparatus is the cooling wheel (or the drum), whose task is to dissipate the heat, introduced by the molten alloy. Usually, the cooling wheel is made of Cu or stainless steel with coatings to ensure sufficient removal of heat [146]. The wheel, RF coils and other structural parts are water-cooled in order to prevent overheating. System for the PFC can be installed in a chamber with an inert gas atmosphere that enables the processing of oxygen sensitive materials, such as titanium alloys or RE-containing alloys. For the processing of melts, which are stable in the atmosphere (Fe, Co and Ni alloys), PFC can be carried out without a protecting chamber [144].

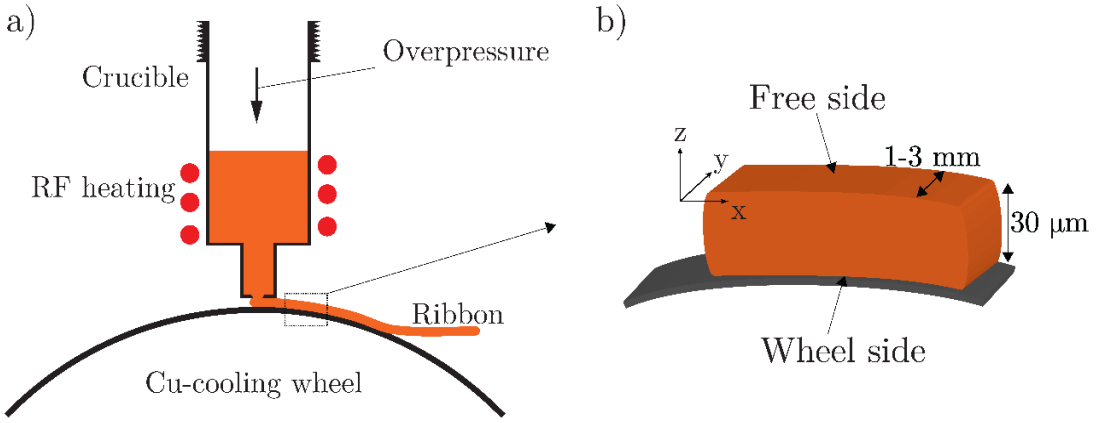

Figure 13: a) Schematic of the laboratory planar flow casting system used in the present experimental work. b) The denomination of the ribbon's geometry, wheel side WS and free side FS ribbon surfaces.

The process of PFC starts with the evacuation of the chamber in order to ensure the appropriate atmosphere, i.e. a minimum amount of oxygen. Then, the alloy is induction heated to result in a viscous melt. A stream of liquid is then ejected through the nozzle by applying overpressure. The melt drops onto the cooling wheel, which rotates at high circumferential speed. The wheel, made of a highly conductive material (usually Cu), extracts the heat, causing the melt to solidify in the form of ribbons. Upon leaving the Cu wheel, cooling continues via convective heat transfer [147]. The thickness (z-axis in Figure 13b) and the width (y-axis) of the obtained ribbons can be controlled by controlling the nozzle-to-wheel distance, the geometry of the nozzle and the circumferential speed. SC ribbons exhibit two distinctive sides, i.e. a wheel side (WS) and a free side (FS), as depicted from Figure 13b. WS features higher cooling rate V due to direct contact with the wheel, while FS experiences lower V, due to the contact with the inert gas (Ar, N, He), whose heat conductivity is much lower compared to Cu. Generally, the cooling rate can reach up to 10^6 K/s [148] and depends on parameters such as wheel speed, ribbon side, gas overpressure, nozzle diameter and thermal conductivity of the wheel [136], [143], [146].

2.2 X-Ray Diffraction

More than a century has passed since the discovery of X-rays by Röntgen in 1895 [149]. Unique properties of X-rays were immediately recognized and implemented in the characterisation of materials by Friedrich, Knipping and Laue in a manner to study the diffraction of crystalline materials [150]. Their efforts were crowned with Nobel Prize for physics in 1914, which was awarded to Laue for the elucidation of crystalline scattering due to X-ray irradiation [151]. Throughout the 20th century, X-ray diffraction (XRD) was studied as a physical phenomenon and introduced into experimental work, as a technique to study the structure of materials [74].

Nowadays, XRD is a well-established and one of the most frequently used methods for materials characterization. It enables the determination of crystalline nature, chemical composition, particle size, distortions of the crystalline lattice, etc. [152]. With its sensitivity down to 0.001 nm, it is well-suited for accurate determination of crystalline lattice constants [152].

In XRD characterisation, materials being crystalline or glassy/amorphous in terms of structure are irradiated with X-ray waves of monochromatic or white radiation. While the latter is made of a wide spectrum of wavelengths (advantageous for the characterisation of monocrystals), for the present case, we will only consider monochromatic radiation of a narrow wavelength. When the incident beam of parallel X-rays reaches a material, interaction with the atoms in the unit cell (for the crystalline matter) or with the SRO and MRO structures (in the glassy matter) occurs. Interaction can be constructive or destructive. When two parallel X-ray waves interfere constructively, the resulting X-ray exhibits an increased amplitude of the wave and for the case of destructive interference, the two waves distinguish each other. Constructive interference is the key phenomenon that governs the diffraction. For it to occur, the path difference 2δ between the two X-ray waves (shown in Figure 14) must conform to the relation: $2\delta=n\lambda$, where λ corresponds to the wavelength and n is the order-of-reflection integer, exhibiting orders $n>1$, but can always be represented with first-order reflections, i.e. $n=1$ [33]. To establish the characteristic relationship between the diffraction or Bragg angle θ, wavelength λ and interplanar spacing d_{hkl}, William Henry Bragg and his son William Lawrence Bragg have set a law [153]:

$$n\lambda = 2d_{hkl}sin\theta_{hkl} \tag{2.1}$$

which determines the characteristic angles where diffraction occurs, when an incident front of waves with parallel propagation vectors interacts with the given matter. The order of reflection integer n is taken as 1. This means that each hkl plane (in the case of crystalline matter) is considered as an individual scattering object, being periodic in the direction, perpendicular to the planes. The distance d_{hkl} between the two neighbouring planes (illustrated in Figure 14) depends on the crystallographic system.

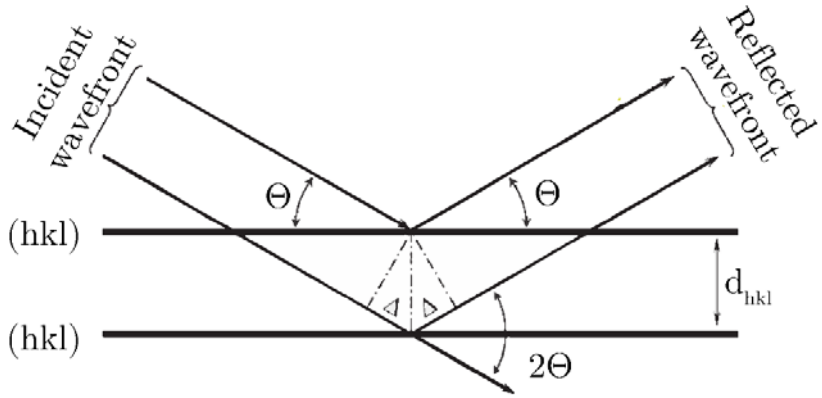

Figure 14: Schematic of the Braggs' law reproduced after [33].

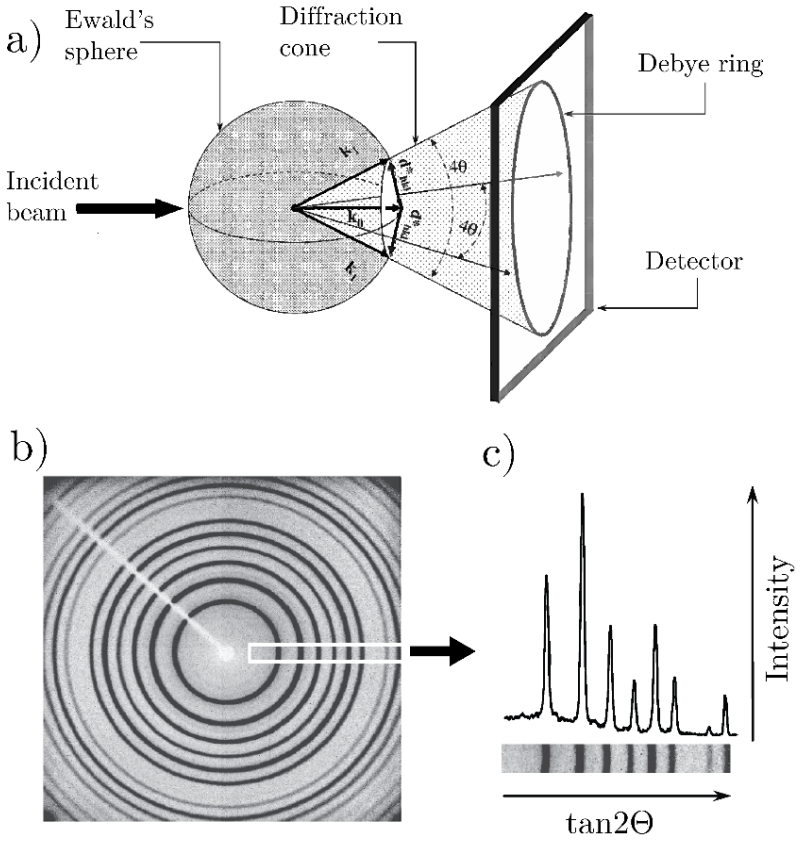

Figure 15: a) The origin of powder diffraction, via a representation of Ewald's sphere [33]. b) The X-ray diffraction pattern of a polycrystalline LaB_6 showing the measured intensity, which is proportional to the degree of darkening [33]. c) The resulting intensity plotted as a function of tan2θ. Below the diffracted peaks is the pattern from part b) on which the integration has been performed [33].

The fulfilment of Braggs' law at a certain 2θ angle yields a peak on the diffraction pattern, corresponding to crystallographic plane denoted with hkl indices. In order to illustrate this phenomenon more accurately, Figure 15 outlines some fundamental principles governing the scattering event. In Figure 15a incident beam of X-rays interacts with crystallites of random orientations, thus generating a random distribution of scattered X–rays with reciprocal lattice vectors, d^*_{hkl}. The ends of identical reciprocal vectors arrange along the surface of Ewald's sphere, perpendicular to the incident wavevector k_0, and these are known as Debye rings [33]. They are visualized in Figure 15b. The rings of different diameters correspond to different hkl Miller indices of the crystalline unit cell. Their distance from the centre is marked as the interplanar distance (d–value). Diffraction rings appear at certain angles due to scattering by periodic planes, which fulfil Braggs' law for different parallel and equally spaced hkl planes. By integration of the intensity of the rings in a given range (rectangular shaped area), as shown in Figure 15c, the intensity is plotted against Bragg angle and diffraction peaks are obtained. This represents the process of information retrieval from an XRD experiment. Commonly, XRD data is represented with the ordinate axis being the intensity in linear, logarithmic or square root scale, while abscissa is plotted in a variant of theta θ, 2θ, 4θ, sine square θ or d–value. Here, θ corresponds to the angle between the incident or diffracted beam with regards to the horizontal plane and d is the interplanar distance.

Peak positions, given as the inverse square of the interplanar distance ($1/d^2$), are a function of unit cell parameters (a, b, c and α, β, γ) and hkl indices. For systems with high symmetry, such as the cubic system, the formula is quite simple [33]:

$$\frac{1}{d^2} = \frac{h^2 + k^2 + l^2}{a^2} \tag{2.2}$$

but for more complicated crystallographic arrangements with lower symmetry, like that of the monoclinic system, the expression becomes more challenging:

$$\frac{1}{d^2} = \frac{h^2}{a^2 sin^2\beta} + \frac{k^2}{b^2} + \frac{l^2}{c^2 sin^2\beta} + \frac{2hl\cos\beta}{acsin^2\beta} \tag{2.3}$$

This demonstrates the influence of atomic structure (comprising the unit cell content and the spatial distribution of atoms) and the dimensions of the unit cell on the diffraction pattern. The features of diffraction peaks that are subjected to significant changes are peak's position, intensity and shape. They can be influenced by material- or instrument-governed variables [33].

When the incident beam of X-rays propagates through the material, it coherently scatters on the crystalline lattice. In order to decipher the characteristics of the scattered beam, it is essential to understand the penetration of X-rays into the matter. The wavelength of the scattered beam is identical to that of the incident beam, which preserves the photon energy and enables the construction of a diffraction pattern. Scattered beam exhibits an intensity (I) which decreases exponentially with penetration depth (x), according to the Beer-Lambert law [154]:

$$I = I_0 \exp(-Ax) \tag{2.4}$$

where I_0 is the initial intensity of the beam and A is linear absorption coefficient. The latter can be determined as $A=\mu\rho$, where μ is the mass absorption coefficient and ρ is the density [154]. The irradiated volume depends on the radiation wavelength, materials' density, attenuation coefficient of the atomic species and incident angle θ.

In order to describe the peak in more detail, parameters like full width at half maximum (FWHM) or integrated intensity have been developed. The schematic of FWHM determination is shown in Figure 16a. It is sensitive to the changes in microstructure and the accumulations of stress and it is also indicative of crystal size and strain. In Scherrer equation [155], FWHM (referred to as h) is used to approximate the mean, volume averaged [156] crystallite size D, according to the relation [157]:

$$D = \frac{K\lambda}{h\cos\theta} \tag{2.5}$$

where λ is the utilized wavelength and K is the crystallite shape factor that depends on the shape of the crystallites [158].

The intensity of the peak can be represented in two ways. The first and most straightforward path is to determine the peak, where the maximum of relative intensity I_{max} (highest signal count) is reached, Figure 16b. Reading I_{max} is simple, but it is only suitable for quantitative data acquisition, e.g. to search for a similar pattern. If, on the other hand, qualitative information is sought, this method is inadequate, since peak broadening can change the I_{max} [33].

For qualitative analysis, integrated intensity (I_i) is more appropriate, since it covers the area under the peak, which remains unchanged even when peak broadening occurs. Graphically, I_i is shown with the orange hatched area in Figure 16. It is constituted of intensities at different 2θ angles, denominated profile intensity (I_n), where n represents the sequential number of data points beginning with n=1 and having a total number of m data points. The observed I_i obtained by summing I_n in all the data points and stripping off the background b_n is then [33]:

$$I_i = \sum_{n=1}^{m} (I_n - b_n) \tag{2.6}$$

The contribution to I_i is mainly from atomic structure, however, the influence of specimen and instrumental parameters is also present. These include the input from scale factor K, which compares the observed I_i with the theoretical I_i, multiplicity factor p_{hkl} accounting for the number of symmetrically equivalent reflections, preferred orientation factor T_{hkl} which accounts for deviations of grain orientations from a complete randomness and other parameters [33].

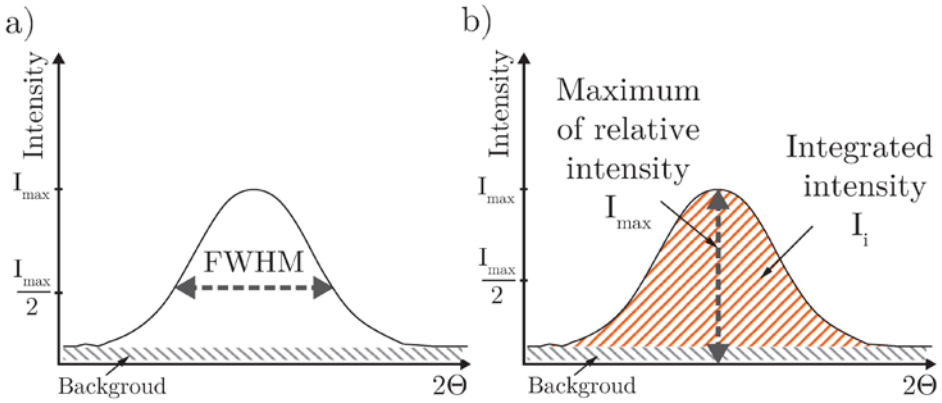

Figure 16: a) Representation of the FWHM. b) Illustration of the maximum of relative intensity I_{max} and the integrated intensity I_i (orange hatched area).

2.2.1 X-ray diffraction of glassy matter

In amorphous or glassy materials, diffraction pattern does not consist of well-defined Bragg peaks as for the crystalline materials. Rather, it is made of diffuse halos, because of the absence of LRO in MG. The fingerprint of a glassy solid is its SRO, which was introduced in Section 1.3.1. SRO in glasses is intuitively visualized as a random distribution of atomic species, as shown by the 3D representation of MG structure in Figure 17a. On the atomic scale, however, arrangements of atoms are not random. They form clusters (as illustrated in Figure 2 and Figure 3) and constitute the central building blocks of MG structure. Structural arrangements between the central and the surrounding atoms in a cluster can be described SRO and MRO. These interatomic arrangements are reflected via multiple diffuse halos in diffraction experiment, as shown on an example in Figure 17b [25]. To yield this information, characterisation with X-ray diffraction or more preferably synchrotron light diffraction is used.

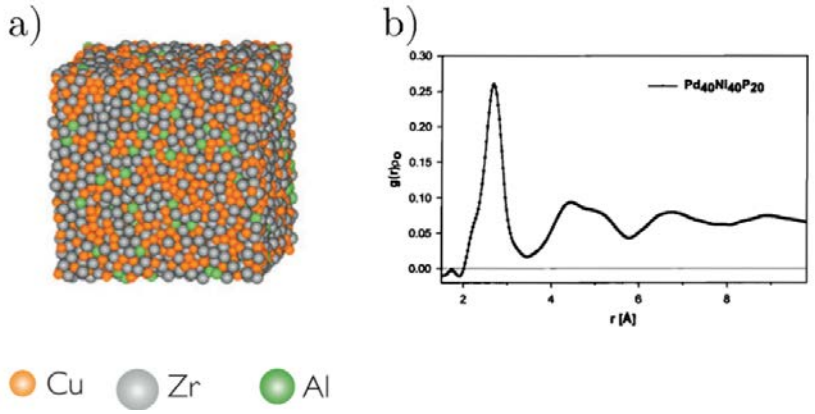

Figure 17: a) 3D representation of the glassy structure, made of constituents Cu, Zr and Al [159]. b) Atomic pair density function ρ(r) of $Pd_{40}Ni_{40}P_{20}$ alloy, indicating the frequency of interatomic distances in metallic glass [160].

Analysis of diffraction patterns with the method of "total scattering analysis" known as pair distribution function (PDF) provides detailed structural information about the glassy solid [33]. Denomination "pair distribution" emphasizes the distribution of interatomic distances, which exist within SRO arrangement. Different functions exist, carrying the same structural information of a material, such as G(r), g(r) and ρ(r) just to name a few. Their meanings will be given in the following paragraphs.

Any PDF method starts from a diffraction experiment that, after carrying out the appropriate corrections for experimental artefacts, delivers a pattern, with an intensity I on the ordinate scale, and on the abscissa, 2θ diffraction angles are converted to wavelength-free $|\mathbf{Q}|=4\pi\sin(\theta)/\lambda$, the magnitude of the scattering vector. In order to show the intensity on a scale from zero to unity in Q-space, structure function S(Q) reads [160]:

$$S(Q) = \frac{\mathrm{I}(Q)}{\langle b \rangle^2} \tag{2.7}$$

where $\langle b \rangle^2$ is the Laue term, which ensures that S(Q) approaches unity at large Q [160]. From positions and shapes of the peaks in the S(Q) function, SRO and MRO of MG can be deduced.

Frequently, though, instead of S(Q), which is easily obtained from diffraction data, reduced pair distribution function G(r) is employed. The latter can be calculated by Fourier transforming S(Q), yielding G(r) in direct space [160]:

$$G(r) = \frac{2}{\pi}\int_0^\infty Q[S(Q) - 1]\sin(qr)\,dQ \tag{2.8}$$

where r is the distance separating two atoms. If r is large, the function oscillates around zero and if it r→0, G(r) is a straight line that goes through zero with a slope proportional to the average atomic number density ρ_0. The advantage of G(r) compared to g(r) or ρ(r), which are the next to be discussed, is the fact that it does not require the assumption of ρ_0, making it less likely to give an erroneous information.

The atomic pair distribution function g(r) is more intuitive than G(r), caused by its ability to emphasize the SRO at low r values. When r→0 (for r shorter than the closest distance between two atoms), g(r) becomes zero and for r→∞, g(r) approaches unity [160]:

$$g(r) = 4\pi r[\rho(r) - \rho_0] \tag{2.9}$$

where ρ(r) is the pair density function. The function g(r) gives the probability of finding two atoms on a distance r.

The atomic pair density function ρ(r) closely resembles g(r), since they are only distinguished by factor ρ_0 [160]:

$$\rho(r) = \rho_0 g(r) \tag{2.10}$$

Due to the inclusion of ρ_0 factor, the difference of ρ(r) with respect to g(r) is that it oscillates about and converges to ρ_0 at high r. When r→0, it becomes zero. Similarly as g(r), it can accent low-r SRO, however, this comes with a trade-off, since the uncertainty of ρ(r) follows 1/r. Both g(r) and ρ(r) give information about deviations from average behaviour of pairs of atoms. This comes about useful for finding the local environment of atoms, i.e. the number of neighbours and their separating distance [160].

2.3 Thermal Analysis

Heating of the glasses imparts changes in their structure, phase, density, electronic and magnetic properties, and many more. If we are able to quantitatively asses the observed changes, a large amount of useful information can be obtained. Methods of measuring the heat changes are known as calorimetric techniques or thermal methods (TM) and they enable the detection of physical transformations (melting, crystalline transitions, vaporisation, etc.) and chemical transformations [161]. TMs can be sorted by the principle of measurement (heat compensation or accumulation), by the method of operation (static, flow, scanning) or by the construction principle (single or twin cell) [161]. Techniques frequently used in TM include differential scanning calorimetry (DSC), differential thermal analysis (DTA) and thermogravimetry (TG). They characterise the differences in heat flow, temperature gradients, and mass, respectively [161]. Determination of material's mechanical behaviour is carried out via thermomechanical analysis (TMA) and dynamic mechanical analysis (DMA).

2.3.1 Differential thermal analysis and differential scanning calorimetry

Differential scanning calorimetry (DSC) and differential thermal analysis (DTA) are the most widely used thermal techniques. In many scientific reports, the difference between DSC and DTA is not so obvious; therefore, I will shortly outline it in order to avoid ambiguities. DTA is used to measure the temperature difference between the investigated sample and the reference as a function of time or temperature. The difference in temperature provides a qualitative assessment of heat exchange [162]. DTA functions in dynamic mode, meaning that it can perform temperature scans of the processes. This is useful for the determination of characteristic temperatures and assessment of qualitative properties [162], such as heats of formation, melting enthalpies etc.

DSC, in contrast, is an evolution of DTA, since it is upgraded with features, enabling the characterization of heat flux ϕ. Instruments used for DSC are divided into heat-flux DSC and power-compensated DSC [162]. Their common point is the differential method of measurement, which measures the unknown quantity and compares it with the known value [162]. Power-compensated DSC maintains the same temperature of the sample and the reference, while the supplied power is varied to maintain the homogeneous heating of sample and reference.

Heat-flux DSC measures the temperature difference between the sample and the reference in order to determine the intensity of the heat exchange. The latter is then proportional to the heat exchange [162]. In this respect, heat-flux DSC is more comparable to DTA than it is to power-compensation DSC. The important property of heat-flux DSC is that it contains only a single furnace with two crucibles, whereas one crucible contains the sample and the other contains the reference (Al_2O_3 powder). Under a sample and a reference is a thermocouple, which measures the temperature variation. Accurate control of the heating rate is achieved by an additional thermocouple or via reference thermocouple, which controls the amount of power delivered to the furnace. Schematics of the two setups are shown in Figure 18. In DTA, the difference signal is obtained by shorting the B legs and measuring the voltage between A legs. In heat-flux DSC, the connecting metal strip (shown between the crucibles in Figure 18b) is used to provide the ϕ path q between the sample and the reference. Thus, the minimization of temperature difference and proportionality of the signal (measured between the legs B) is obtained [163].

The accuracy of heat-flux DSC is inferior to that of power-compensated DSC, but the attainable temperature range is higher, with the ability to operate up to 1600°C [162], [163].

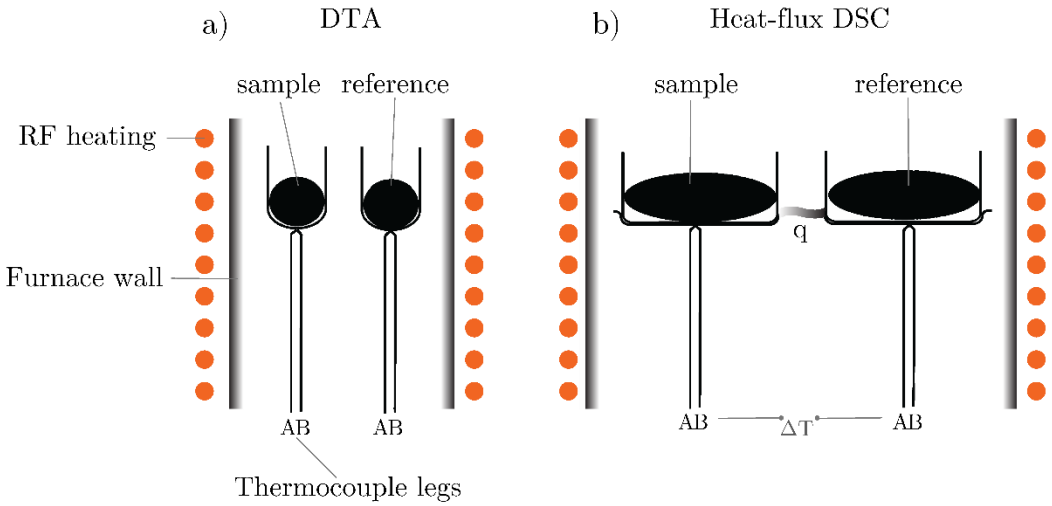

Figure 18: Schematic of a) DTA and b) heat-flux DSC apparatuses. A and B mark the legs of thermocouples and q designates the thermal bridge connecting the sample and the reference. Reproduced after [162]–[164].

The signal in a DSC scan is shown as the difference in voltage or temperature between the sample and the reference thermocouples. In order to show this difference with temperature, voltage data (source values) is treated with a reference table or an equation [163]. A common practice in the heat-flux representation is to divide the values of voltage (usually in millivolts with the sample mass (commonly in milligram). By its qualitative manner, the signal on the y-axis can be endothermic or exothermic, indicating heat into or out of the sample, respectively. There is, unfortunately, no agreement on the direction of the endothermic and exothermic signal. Most of the established researchers working with heat-flux DSCs, however, use the marking where a positive change of signal on the y-axis stands for the exothermic event [161], [163]. On the x-axis, it is common to plot temperature or time scale. The first is useful for the reading of characteristic temperatures of thermal events, while the second option is convenient for the determination of peak area, i.e. enthalpy change.

Parameters that govern the shape, quality and reproducibility of a DSC measurement can be specimen- and instrument-governed. Overall, some 16 variables [165] are known to have an influence on the DSC output. Differences that might occur due to specimen-related inputs are unequal sample mass and unequal sample shape [163]. Instrument-brought parameters are different heating/cooling rate, selection of crucible, atmosphere, reference, etc. [161], [163], [166]. Figure 19 outlines the impact of sample mass and heating rate on the shape and the position of a peak corresponding to a thermal event. Larger sample results in a more pronounced peak (Figure 19a), however, it also retards the return of a signal to a baseline, which can lead to smearing of the transition. A similar effect appears with the increase in heating rate. As depicted in Figure 19b, the higher the rate, the more pronounced the shift towards higher temperatures. Return to the baseline is stretched along a larger temperature range.

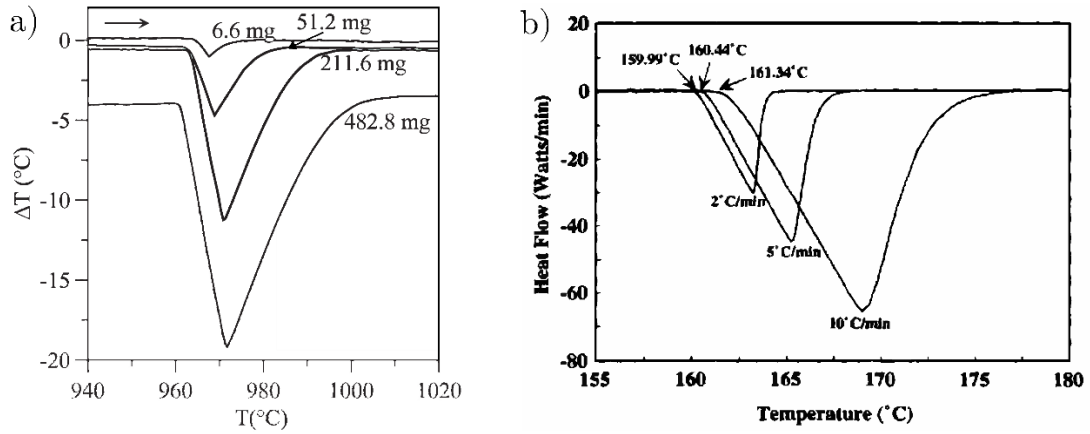

Figure 19: Influence of a) sample mass (reproduced after [163]) and b) heating rate (reproduced after [161]) on shape and position of the thermal event in a DSC measurement.

2.3.2 Characteristic DSC temperatures of metallic glasses

Formation of MG is a process that consists of cooling the alloy from a liquid state with a sufficiently high cooling rate to restrain the formation of crystalline phases. The latter includes thermal events such as glass transition, crystallisation, melting and solidification. Temperature, at which thermal transitions are detected, depends on specimen and instrument governed variables. Accurate determination of the transition temperature is an arduous task, which demands calibrations in different temperature ranges. In addition to thermal lags, caused by the above-mentioned variables, there is also an ambiguity of accurately determining the start and the end of a process [163]. Figure 20 shows different paths to analyse a thermal event. Denomination T_o marks the onset temperature and can be defined as the first departure of the signal from the baseline. If the baseline is further extrapolated and the peak in its steady state is drawn a tangent (Figure 20), then the intersection of the two lines is the extrapolated onset temperature (T_{eo}). Maximum of the peak designates the highest offset of ϕ signal (for this peak) from the baseline and can be labelled with T_p. Towards the end of the peak, the process is analogous to the start, the intersection of the auxiliary line (tangent on the steady state of the peak) and the baseline is the extrapolated endset temperature (T_{ee}), and the last detected point, before the signal returns to the baseline is marked as the endset or final temperature (T_e) [162]. In order to eliminate the asymmetries of ϕ, caused by the daily-changing state of the apparatus, the zero line (Figure 20) must be subtracted from the measured curve. This yields a true sample ϕ and a curve, which is almost straight and horizontal [162]. In the following section about the determination of characteristic temperatures, T_o and T_e will be used to represent the beginning and the end of a thermal event.

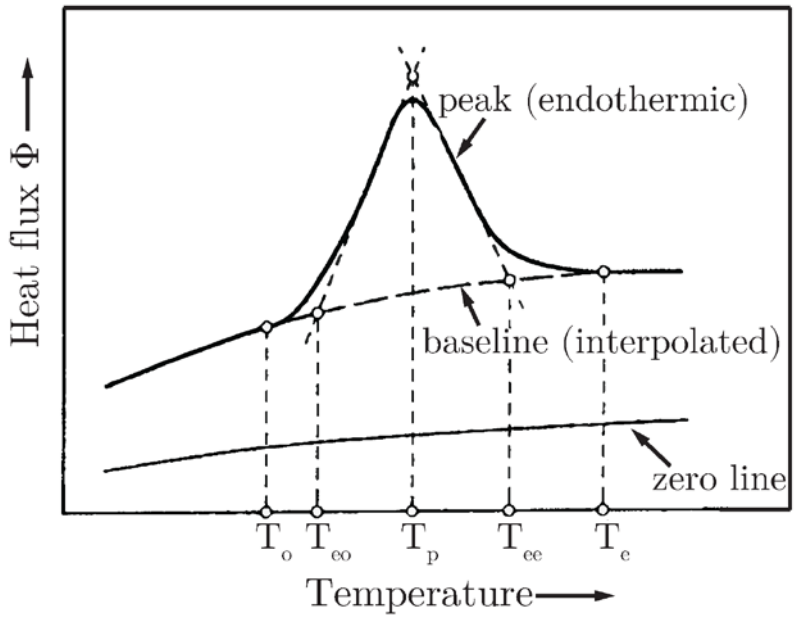

Figure 20: Definition of baseline, zero line and transition temperatures. Reproduced after [162].

A typical DSC measurement of a metal or an alloy contains multiple peaks, indicating first- or second-order phase transitions. First-order transitions have no discontinuity in the first derivative of Gibbs free energy and involve a release or intake of latent heat to facilitate the transition. Examples of first-order phase transitions are melting and solidification. Second-order phase transitions occur on the discontinuity of the second derivative of the Gibbs free energy, and the examples are glass transition and order-disorder transitions [167]. This explanation sets foundations for the description of phase changes, shown in Figure 21. Glass transition (T_g), being the transformation of the second order, does not exhibit a sharp peak in the DSC scan. A rather indistinct and subtle change of signal from the baseline is a consequence of atomic relaxation, imposed by a metastable processing route. T_g depends on atomic frustration within the material [168], but also on thermal history [162]. Cooling rate used to vitrify the alloy affects the T_g by as much as 10-20% [2], which can explain spurious results in the case of different cooling rates.

The region from T_g up to crystallisation temperature T_x is known as the SCL. When the material is brought to this temperature range, it exhibits malleable behaviour due to a drop in viscosity [169], [170]. The crystallisation of MG is usually hindered (on a time scale of several hours) if the temperature is kept within the SCL range. This property offers an immense applicative potential for MGs. In one single process, the material can be heated to its T_g, to facilitate liquid-like flow, and then mechanically deformed to yield a specimen with nanometre-sized smooth surface [171].

Further up the temperature scale, T_x marks the beginning of crystallisation, which is observed via intense exothermic event (Figure 21). In the DSC scan, several exothermic peaks can coexist, indicating multiple crystallisations or phase transitions. When the temperature is elevated, so as to yield an endothermic event, the first liquid is obtained and this point is labelled the temperature of melting (T_m). The initial state of this process, i.e. the endothermic deviation of the signal from the baseline, is shown by the inset in Figure 21. The final event in a thermal scan of a glassy alloy is the liquidus temperature (T_l), which marks the complete liquid state. This temperature is determined as the endset

of the last endothermic peak. The procedure of T_g, δT_g, T_x, T_m and T_l, determination as described in the latter section is applied in the experimental section of the thesis.

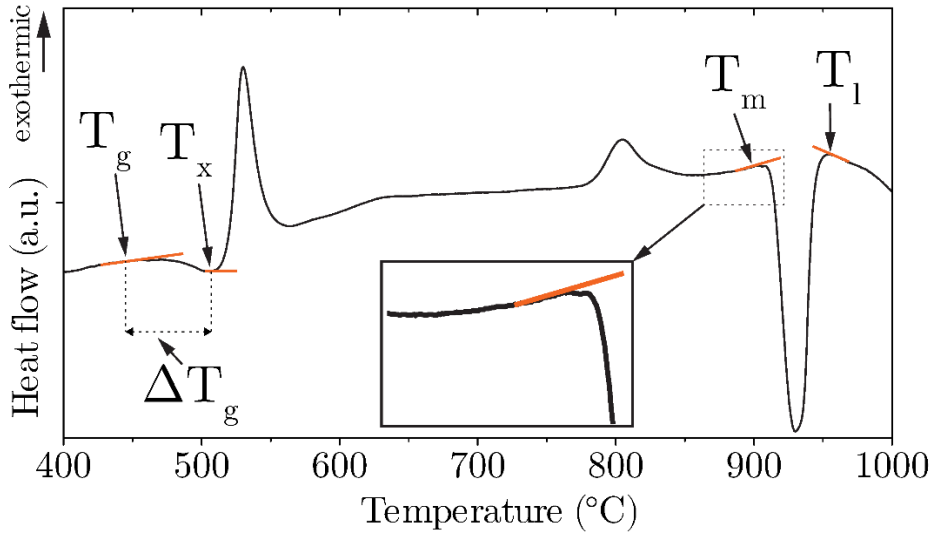

Figure 21: Characteristic temperatures of glass transition T_g, supercooled liquid region δT_g, crystallisation T_x, melting T_m and liquidus T_l in a DSC scan of a glassy alloy. The inset shows a zoomed-in part, where the signal departs from the baseline.

2.3.3 Glass formation parameters

To describe the tendency of alloy towards the formation of the glassy state, several empirically derived parameters have been proposed [172]–[174]. One of such is the parameter of reduced glass transition temperature T_{rg} [174], which is defined as $T_{rg}=T_g/T_l$. It represents a well-established indicator of GFA of glassy alloys [174], although there are exceptions, where T_{rg} cannot predict the glassy structure [175]. As the alloy concentration changes, T_g often exhibits a weak dependence on composition, while T_l often changes more intensively. Accordingly, the interval between T_l and T_g substantially increases around eutectic, where T_l is very large and thus this parameter can be used to predict the increased glass-forming tendency.

Another characteristic parameter is the temperature interval of SCL or δT_g but it will not be dealt with in detail since it has already been described several paragraphs earlier. GFA describes the ease of glass formation and helps to outline the origin of glass formation. Different analytical parameters of vitrification have been developed to date [176], but the most common parameter for BMG is still the maximum attainable size of the MG [6].

GFA does not only relate to the stability of the liquid phase, but also to resistance towards crystallisation [177] and in this respect, it is addressed as the glass devitrification ability (GDA). To determine it, one can use the characteristic temperatures from thermal analysis. By assuming that GDA ≡ GFA, the expression reads [177]:

$$\mathrm{GFA} = \frac{(2T_X - T_g)}{T_l} \tag{2.11}$$

and it reflects the stability of SCL region (from T_g to T_x) versus T_l.

2.4 Transmission Electron Microscopy

Modern transmission electron microscope (TEM) is a highly complex, but a versatile instrument, which enables atomic-level microstructural characterisation [178]. It uses the techniques of electron and X-ray scattering to reconstruct the image and produce diffraction data. Most common imaging modes include imaging of different types of contrasts (diffraction, mass-thickness, phase), obtaining diffraction patterns by means of selected area electron diffraction (SAED), or performing electron-energy-loss spectroscopy (EELS) and energy-dispersive X-ray spectroscopy (EDS). More advanced options of microstructural characterisation, include nanobeam diffraction [179] or fluctuation electron microscopy [180], which are suited for studies of glassy materials.

The process of obtaining an electron micrograph or diffraction pattern can be divided into several sections, as it is schematically shown in Figure 22. The first part comprises an illumination stage, where the electrons are accelerated by means of the electron gun and directed towards the sample. The voltage for electron excitation of a common medium-voltage instrument varies from 200-500 kV, whereas in dedicated high-voltage TEM setups, it can go all the way up to 3 MV [181].

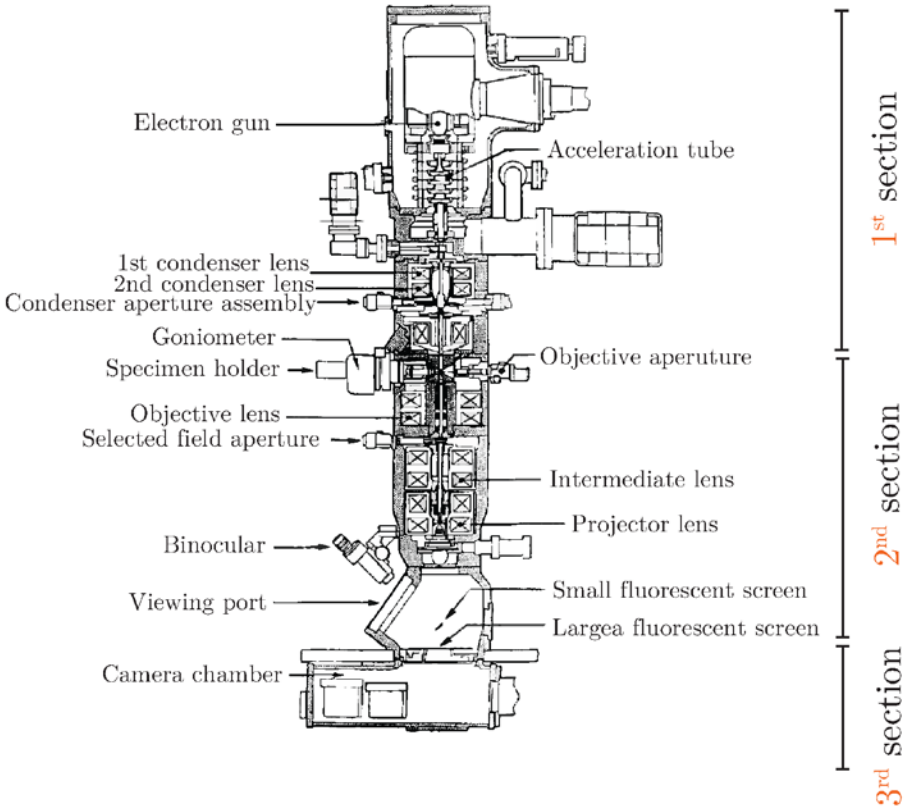

Figure 22: Layout of a typical TEM instrument. After [178].

In the second section of the TEM layout, electrons reach the specimen stage and interact with the observed material. Herein, the thickness of the sample must be appropriate so as to permit electron transparency. Depending on the accelerating voltage, a suitable thickness of the samples for electron-transparency varies from several 10 nm at 200 kV to 1 μm or more at 1 MV [181].

In the last-third section of the electron path in the TEM, an electron micrograph or diffraction pattern is observed. Imaging stage consists of the electronic camera system, which is used for the generation of micrograph or SAED pattern [182]. The first type of contrast, which can be obtained in TEM, is diffraction or Bragg contrast, and it represents the variations in the intensity of electron diffraction. It appears due to the crystallographic orientation of the specimen and is pronounced if the crystal is oriented along the zone axis with low indices, which will yield dark contrast in bright field image [183]. Diffraction contrast can be used to image features such as interfaces, multiple phases and dislocations [178]. Secondly, differences in intensity can also arise due to the mass-thickness contrast. The latter originates from the difference in mass (atomic mass of the species) and thickness of the specimen, whereas higher atomic mass and thicker regions will appear darker in the bright field image [183]. Origin of this effect lies in the Coulomb interaction, which deflects the incident electron beam that passes through the atom [178]. Another type of contrast, which arises in high-resolution transmission electron microscopy (HRTEM) is phase contrast. It appears due to the phase of the diffracted electron interacting with the phase of the transmitted wave. This technique is utilized to image columns of atoms. Two of its variants include imaging with nanobeam (for local probing of atomic arrangements) and with electrons scattered at a high angle to prevent interference. The latter is known as high-angle annular dark-field (HAADF) imaging [178].

In view of diffraction (via SAED), qualitative data retrieved by TEM is comparable with the one from the conventional XRD method. Both unveil the structural data, however, the former has an advantage of being able to focus the electron beam, which is accomplished via precise controlling of the electromagnetic lenses. This enables sampling from microscopic regions of the specimen, yielding information about the local structure with the highest spatial resolution of ≈0.08 nm [178].

Modes of TEM operation depend on the position of the objective aperture and the direction of the incident and diffracted beam. Outline of different configurations is given in Figure 23. Bright field (BF) mode is obtained with an objective aperture positioned in the centre of the back focal plane. This allows the direct (un-diffracted) beam to pass through, while diffracted beams are stopped [178], [183]. Dark field (DF) mode features objective aperture shifted to one side, which only allows some of the diffracted beams to pass through [178]. Due to the highly scattered nature of these beams, information about particle size and defects is generated [183]. A difference between BF and DF imaging is shown by the micrographs (in one-to-one correspondence) in Figure 23a and b, respectively. In the case of BF, contribution to contrast from the direct beam is prevalent and the precipitates are visualized dark. When DF is used (Figure 23b) with the objective aperture around (001) diffraction spot, the contribution from diffraction contrast is dominant and the particles appear bright. The discrepancy between the contrast in BF and DF mode indicates that the particles exhibit uniform crystallographic orientation, caused by a constructive interference of electrons.

By tilting the angle of the incident beam (α), as shown in Figure 23c, the direct beam is stopped, while the diffracted beam passes through the objective aperture. The diffracted lines lie on the optic axis, which reduces the blurring from lens defects [178].

To retrieve a diffraction pattern from an area of a specimen, SAED is used. An intermediate aperture is positioned in front of an intermediate lens (Figure 23d) to restrict the area illuminated by the electron beam. The result is a series of diffraction spots in case

of the nanocrystalline specimen (pattern i in Figure 23d) and diffuse glassy rings (pattern ii in Figure 23d), a fingerprint of a glassy/amorphous structure.

The accuracy of SAED is hindered by distortions of lenses and specimen height drifts. Error in electron diffraction is around 1%, which is substantially higher compared to a few parts-per-million uncertainties that can be obtained with X-ray diffraction.

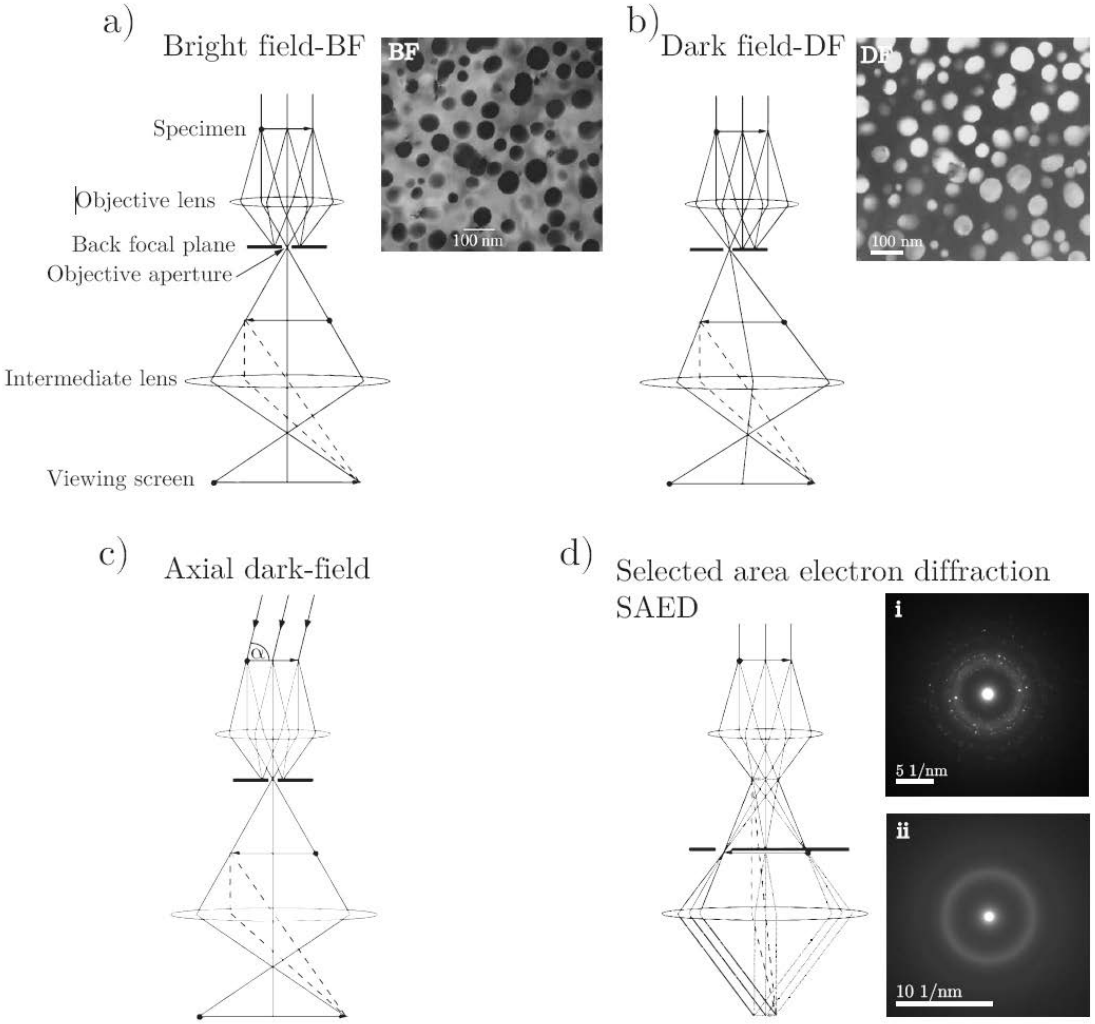

Figure 23: a) Schematic of electron path in bright field (BF) mode and on the right, the corresponding micrograph. b) Dark field (DF) mode and the corresponding micrograph on the right. c) Axial dark-field mode with α being the angle of the incident electron beam. d) Electron path in selected area electron diffraction (SAED) and SAED patterns of i nanocrystalline and ii glassy sample. Reproduced from [178].

2.5 Magnetic Measurements

The first magnetic measurements were conducted in the middle of the 18th century when the studies of atmospheric electricity and earth's magnetism commenced [184]. The first instruments capable of characterising the magnetism of materials were constructed about a century later, following Oersted's discovery of the connection between magnetic and electric field. The first magnetic measurements were based on the attraction of magnets towards ferrous objects and used force to evaluate the strength of the magnetic pull [184].

2.5.1 Vibrating sample magnetometer

First vibrating sample magnetometer (VSM) was constructed by Simon Foner in 1959 [185]. The first version was made using simple components such as loudspeaker magnet and a paper cup, nevertheless, it provided a validation of its principle [186]. Through the following years, VSM evolved into a reliable and sensitive method for measuring the material's magnetic hysteretic loops. Working principle of the VSM is such that it measures the magnetic moment m and with it the magnetic dipole moment $j=\mu_0 m$ in the presence of static or slowly changing external magnetic field. Schematic of the setup is shown in Figure 24a. A specimen to be measured is suspended between two poles of the electromagnet. To generate a uniform magnetic field, a strong electromagnet is used. Its ends are usually made of Fe-Co alloy and tapered at 54° in order to maximize the magnetic field strength and homogeneity [187]. Space between the pick-up coils (air gap) amounts to several centimetres and is used to accommodate the oscillating specimen rod. When the external magnetic field is turned on, the vibrating sample produces an oscillating magnetic dipole, inducing a proportional voltage in the pick-up coils. To deduce the amplitude and phase, a permanent magnet is attached at a higher section of the rod. As the magnet vibrates with the sample, the auxiliary signal is produced which is synchronous with the signal of the sample. The known portion of the voltage from the reference coil is then balanced (via lock-in-amplifier) with the voltage from the specimen coils. The magnetic moment of the sample is proportional to the obtained voltage [187]. By having the sinusoidal vibration of the signal $x(t)=X_0 \sin\omega t$, the equation for induced voltage e can be written as [132]:

$$e(x,t) = \mathrm{mS(x)}\omega X_0 cos\omega \mathrm{t} \tag{2.12}$$

where m represents the magnetic moment, S(x) is the sensitivity factor, which depends on sample geometry, coil arrangement and electromagnet geometry, ω is the oscillating frequency and X_0 is the amplitude [132], [188]. In order to minimize the fluctuation of the sine function and maximize the intensity of the signal, i.e. improve the S(x) function, the sample needs to be centred between the pickup coils, which is achieved by positioning it, so as to minimize or maximize the signal in x-, y- and z-direction. Factor S(x) can be determined theoretically, according to the following expression, which is valid for a magnetic moment in x-direction (m_x):

$$S(x) = \frac{dk_x(x)}{dx} \tag{2.13}$$

where $k_x(x)=B(x)$ corresponds to the current circulating in the coil. Most often, however, calibration of S(x) is achieved experimentally, using a standard magnetic moment. Pure Ni sphere is commonly used for this purpose since Ni provides high moment and stability in atmospheric conditions. The peak in S(x) is achieved when pick-up coil geometry exhibits a radius of the coil (a) equal to the distance (d) between them, d=a (as

illustrated in Figure 24d), which is known as inverse Helmholtz pair. Other configurations include $d = \sqrt{3}a$, which ascertains maximum homogeneity of S(x) and d=1.848a [187]. Pick-up coils can be arranged so as to measure m_x only, by two- and four-coil configuration (known as Mallinson set) in Figure 24a and b. Measurement of the components m_y and m_z is possible, as depicted by four- and eight-coil setups in Figure 24b and c, respectively [189]. Sensitivity of a commercial VSM apparatus is around 10^{-6} emu, making this method suitable not only for measurements of FM, but also weakly magnetic and PM materials [187].

Reproducibility of VSM measurements was tested with permanent magnet samples. A series of 3 mm sized Ni spheres circulated among 24 European laboratories, which performed the measurements under the same conditions and using the same parameters. As it was found, the relative standard deviation of remanence B_r was 1.0%, whereas that of H_{ci} was 3.7% [190]. Deviation of energy product BH_{max}, which represents a figure-of-merit for energy-related applications was 2.3% [190].

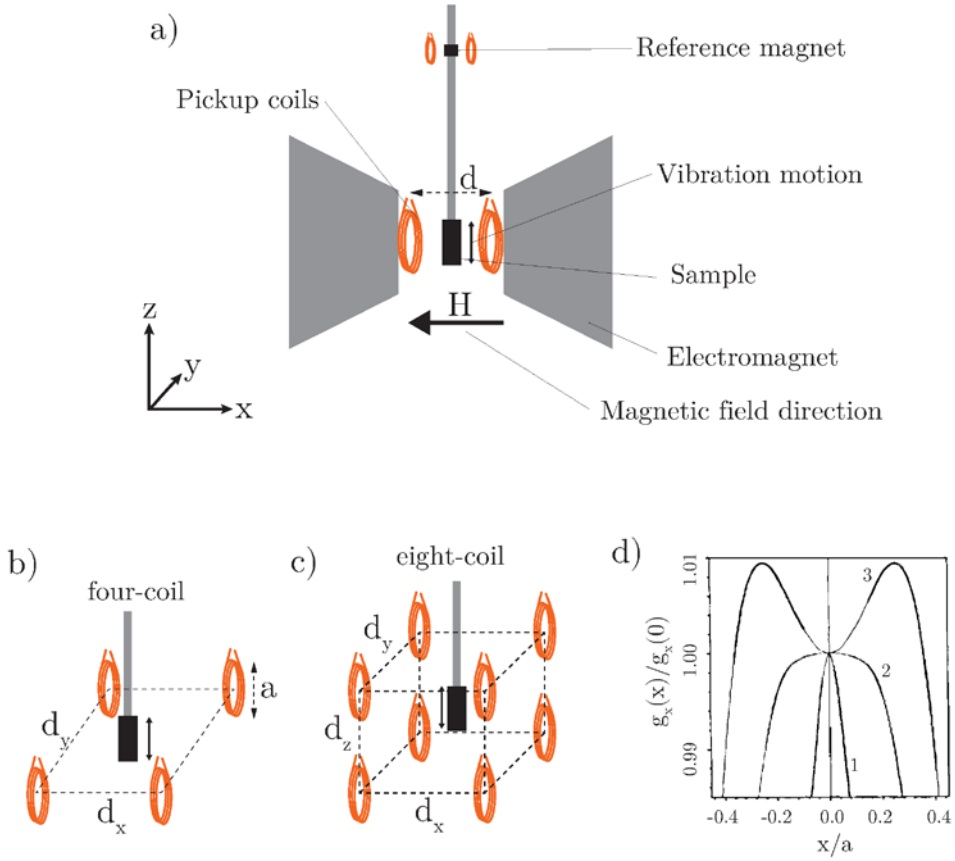

Figure 24: Schematics of VSM apparatus. a) Measuring part of VSM, comprising a two-coil setup. Parts b) and c) denote variations of the pickup coils using four- and eight-coil assembly, respectively. d) Different S(x) functions; 1: d=a, 2: $d = \sqrt{3}a$, 3: d=1.848a [187].

2.5.2 Superconducting quantum interference device magnetometer

A method which provides the most sensitive way of measuring the magnetic flux is a superconducting quantum interference device (SQUID) magnetometer. In part, it consists of similar components as a VSM, but with some alterations, which facilitate extremely low magnetic noise. The advantage of SQUID is the ability to attain higher magnetic fields (compared with VSM) and the ability to measure signal on the level of femto-tesla, 10^{-15} T, [132], owing to a different design of a sensing element.

SQUID instrument (Figure 25a) features a central sample tube, which houses the specimen and is surrounded by liquid He containing cooling annulus. Measurement is performed by moving the sample through the field, provided by superconducting magnet and measuring its response by a set of pick-up coils [191]. To enable the achievement of a high-enough magnetic field, the magnet needs cooling below the critical superconducting temperature, which is achieved with liquid He.

Fundamentally, two types of SQUID instruments exist; rf SQUID and dc SQUID, depending on whether they contain one or two Josephson junctions, respectively. Latter variant was the first to be developed and will be described in greater detail. Dc SQUID is a complex device, which enables fundamentally different flux sensing (compared to VSM) and achieving of higher magnetic fields. The most significant piece of SQUID is a sensing element in the form of a superconducting coil, being a flux-to-voltage transducer that traces the variation in magnetic field flux. A layout of the sensing coil is shown in Figure 25b. In 1962, Josephson predicted [192] that interrupting a toroidal coil with a narrow metallic section (Pd or Nb metal), i.e. a Josephson junction barrier shown in Figure 25b, causes the so-called supercurrent in the junction, with no fluctuations and the current is increased steadily from zero [192], [193]. The voltage across the junction will remain zero until the current I will exceed the critical current I_0 [194]:

$$I = I_0 \sin \delta \tag{2.14}$$

and a difference $\delta=\phi_1-\phi_2$ between the phases ϕ_1 and ϕ_2 of the two superconducting electrodes [194], will vary rapidly over the barrier causing the maximum supercurrent to drop with increasing field [192]. Josephson's prediction was experimentally confirmed a year later by Anderson and Rowell using superconducting Pb and Sn, separated by a thin barrier of Sn-oxide [195].

One or two Josephson junctions can be present, which alter the nature of the current, being the ac or dc type, respectively. The observed supercurrents alter the resonant frequency, thus yielding an oscillating function of the magnetic field, which is visualized as a series of peaks, shown in Figure 25c. The phase of this periodic variation corresponds to an increase of one flux quantum-ϕ_0 given by the expression [196]:

$$\phi_0 = \frac{2\pi\hbar}{2e} \cong 2.0678 \times 10^{-15}\ tesla\, m^2 \tag{2.15}$$

where $\hbar$ is reduced Planck constant, connecting to Planck constant h with the expression $h=2\pi\hbar$ [196]. In Eq. (2.15), e is the magnitude of the electric charge. Induced magnetic flux ϕ quantization arises from the fact that the number of ϕ_0 oscillations must conform to the integer values of $\pm$ 1, 2, 3, ... n, so as to result in $\phi=n\phi_0$ [194]. Then, the induced flux ϕ can be written as:

$$\phi = B\omega(d + \lambda_1 + \lambda_2) \tag{2.16}$$

Where B is induced magnetic field, ω corresponds to the width of the barrier, d is the barrier thickness, while λ_1 and λ_2 are London penetration depths into the superconductors, amounting to 100-300 nm [194]. In order to maximize the sensitivity of SQUID, another superconducting ring is placed around the first one with one or two Josephson junctions, but without the separating metallic weak link. This acts as a dc search coil, gathering flux from the area of several square centimetres and improving the measuring precision [193].

According to the measured frequency, SQUID instruments are divided into three ranges. The first is the measurement of quasistatic voltages and up to the frequency of 10 Hz, which is utilized to determine the thermoelectric voltage or the voltage generated by the quasiparticle charge imbalance [197]. Measurements of brain activity are also conducted with this type of SQUID. The second division of SQUID sensors (in the range 10 Hz-100 kHz) finds use in imaging methods such as nuclear quadrupole resonance and magnetic resonance imaging. Magnetic properties measurements in this PhD dissertation were carried out using SQUID in this range [198]. The third type of SQUID instruments operate via a flux-locked loop in the frequency range of up to several MHz and above they function via open-loop configuration. The SQUIDs used in experimental physics exhibit modulation frequencies of 150 MHz [197].

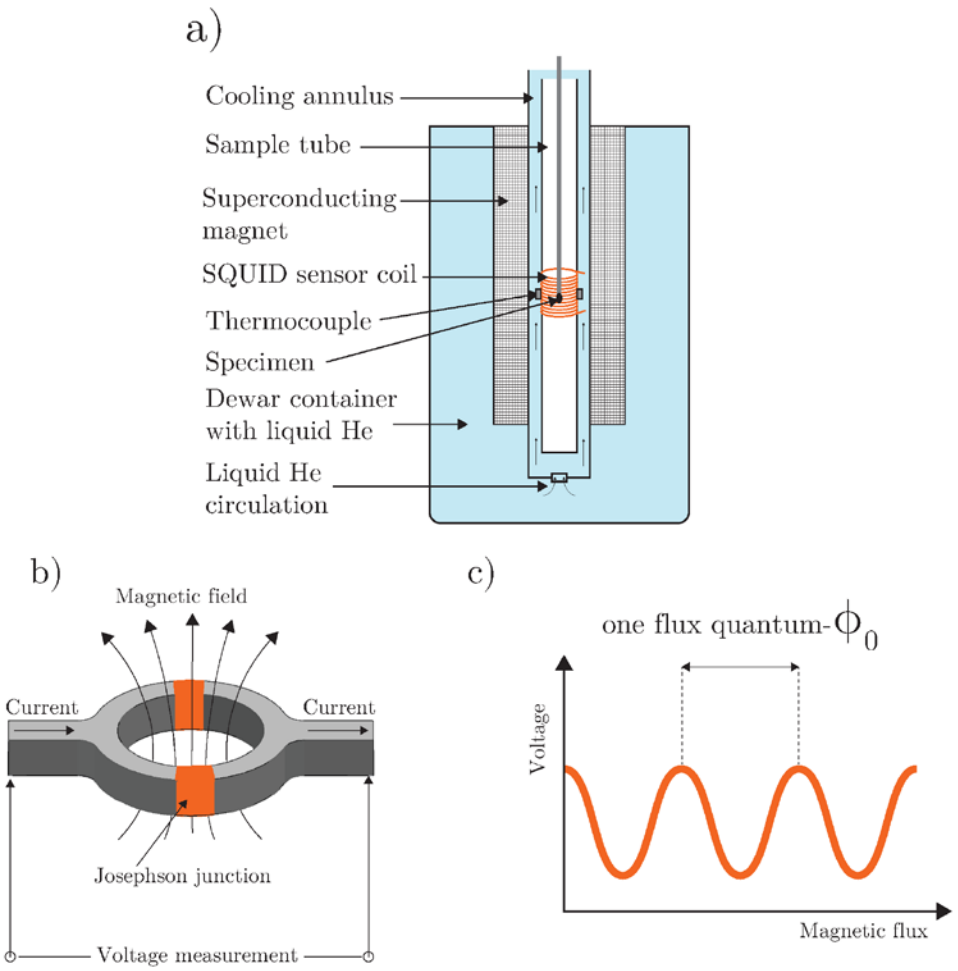

Figure 25: a) Schematic of the SQUID instrument. b) The layout of dc SQUID setup, featuring two Josephson junctions, reproduced after [196]. c) Oscillations of the induced voltage and depiction of one flux quantum ϕ_0, reproduced after [196].

2.6 Pulsed Electric Current Sintering

Methods of densification with electric current have a rich history since the early patents go back to the beginning of the 1900s. The first commercial machines, meanwhile, appeared when the filed patents have expired, towards the end of the 1980s [199].

The foundation of this type of sintering is the use of electric current, utilized in conjunction with applied pressure to consolidate the powder into bulk shape. Denominations of this technique have several variants. Pulsed electric current sintering (PECS), field assisted sintering technique (FAST), spark plasma sintering (SPS) and current-activated, pressure-assisted densification (CAPAD) all label the same process [200]. The positive effects are energy efficiency (due to short processing time) and the ability to consolidate materials with advanced properties. The layout of PECS (this name will be used through the rest of the section) setup is shown in Figure 26.

In the PECS process, powders are filled into a mould and confined by the upper and lower punch. After applying the pressure, DC current is sent through the setup and electric current heats the powder. The fundamental mechanism of heat formation in PECS is not resolved at present [201], [202], justifying numerous names of the technique. Nonetheless, a widely accepted mechanism of heating and sintering in PECS is based on the principle of Joule heating [203], [204]. The generation of heat H is proportional to the following expression:

$$H \propto I^2 R \tag{2.17}$$

where I represents the electric current and R is the electrical resistance. Currents are dissipated through the network of percolating current paths (as shown in Figure 26b), and their distribution depends on powder's packing. This induces electrical discharges at the edges of particles, causing high-temperature gradients [200]. In addition to heat, another important parameter in PECS is pressure. Uniaxial pressure is applied simultaneously with heating, raising the effectiveness of consolidation. The maximum temperature to reach a full density of the samples can be decreased, due to the lower contact resistance of the powder-tool surface [205]. This results in a few important advantages of PECS, such as heating rates as high as several hundred degrees Celsius per minute [200], preservation of powder's microstructure [206] and dramatically shorter sintering times [207]. The material, which is subjected to PECS can be either electrically conductive or non-conductive. In the former case, Joule heating principle is at work, while for non-conductive (e.g. ceramic powders) materials, the heat (Joule heat) is dissipated in the tooling (punches and mould) and is later transferred to the sample via conduction. Materials suitable for moulds include graphite, SiC and WC-Co composite, which have good electrical and thermal conductivity.

The use of PECS technique is feasible in cases, where material's performance is ahead of its price. Industries such as biomedical [204], tooling [208] and military [209] are using PECS since it can preserve nanocrystalline and glassy microstructure and with it some of the superior qualities.

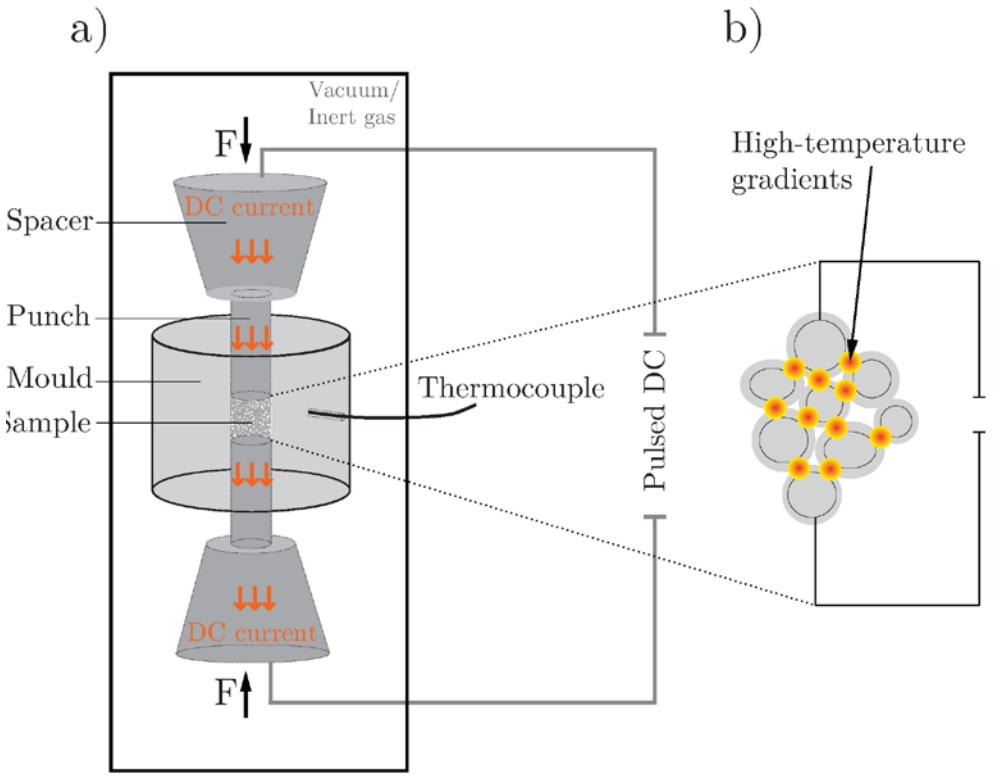

Figure 26: a) Layout of the PECS device, delineating the main components. b) Illustration of the percolating current paths that form high-temperature gradients on the edges of the particles.

Chapter 3

Aims and Hypothesis

3.1 Objectives of the Research

This PhD dissertation is envisioned as a systematic comparison of $(Al_{1-x}RE_x)_{62}Fe_{13}Cu_{25}$ quaternary alloys, where the RE element is either Ce or Gd. Structure, thermal behaviour, microstructure and magnetic properties of the alloys are studied. The peculiar stoichiometry originates from $Al_{62}Fe_{13}Cu_{25}$, which form an icosahedral quasicrystal [210]. In our set of alloys, Al is partially or completely replaced by RE, according to the relation x=RE/(RE+Al), whereas RE can take seven equally distant x values within the range $0.5 \leq x \leq 1$. Cerium and gadolinium are selected for their contrasting electronic properties and structure, but above all for their differing magnetic properties. Ce appears in 3^+ but also up to $\approx 3.5^+$ valence state [211] as a low-temperature phase, while Gd is found in 3^+ state [212]. Regarding the magnetic properties, Ce and Gd differ significantly, whereby their magnetic moments amount to 2.54 μ_B for Ce and 7.63 μ_B for Gd. It is expected that these fundamental differences will dictate the magnetic properties of the respective families of alloys. In addition, the influence of possible crystalline precipitates on the magnetic properties of the alloys will be interesting to observe.

The rule of deep eutectics [49] and the confusion principle [48] will be used to formulate alloys' compositions in order to yield strong MGs. Firstly, the eutectic ratio between the elements lowers the liquidus line. Since the melting points of two REs differ significantly, the temperature of the liquidus line will differ as well, which has an impact on the MG formation. If the difference between the T_l and the quenching temperature is not large enough, the formation of glass can be impaired and crystallites can emerge. Secondly, the composition of the alloy with four distinct atomic species exhibiting different atomic sizes decreases the probability of crystallisation. The increase of packing density in a liquid state and less viable initiation of the primary crystallisation should frustrate the structure, so as to result in metallic glass [48].

In the first instance, Ce will be replacing Al, while the amounts of Fe and Cu will be constant. Since the liquidus line in Al-Ce diagram is lowered down to ≈600°C [213] for eutectic composition, the probability of MG formation should be the largest, when the ratio x is near the binary eutectic. Ce-based glasses hold the world's lowest T_g among all MG systems [214], amounting to ≈80°C, implying that Ce-rich MGs with high ratio x should display very low T_g. Thermoplastic consolidation of MG ribbons can be accomplished with PECS, by means of turning crushed ribbons into dense, millimetre-sized BMG. The process is carried out with a rapid heat-up to around T_g and simultaneous application of pressure, which hinders the crystallisation while densifying the material.

Ce belongs to the group of PM metals and exhibits a fluctuating valence, depending on the temperature and the atomic environment. In the given series of MGs, Ce will be surrounded with three distinct atomic species, giving rise to the potential coupling of the electron spins. Hybridization effects should differ according to the structure in which the constituent elements are placed, meaning that spin coupling in a glassy phase without LRO should be different compared to crystalline phase with well-defined LRO. Ce-based glasses

are anticipated to result in lower magnetisation when set against Gd-based counterparts, due to the lower magnetic moment of Ce.

In addition to the variation of x, the ratio y=Fe/(Fe+Cu) between the two immiscible metals is studied as well. The ratio x is fixed to x=0.67 so as to result in good vitrification ability of the starting composition, followed by changing the fractions of Fe and Cu, according to the ratio y. Fe and Cu metals do not mix in solid [68] nor in the liquid state [215], which brings about the questions of whether the ratio y controls the stability of the glassy phase and if and how it alters the physical properties.

In the case of Gd-based alloys, a variation of the amounts of Al and Gd follows the same, above-stated expression for x, while fractions of Fe and Cu are fixed. It is expected that MG formation will be more difficult since the liquidus line in Al-Gd diagram is some 300°C higher than that of Al-Ce. In turn, precipitation of crystallites can occur over a wider composition range. A higher T_g is anticipated in comparison with Ce-based MGs, because similar Gd-rich MGs exhibit higher T_g as well [216]. In contrast to Ce, the magnetic moment of Gd is three times larger, which is, in connection with hybridization, expected to yield a higher magnetisation of the alloys. Since the threshold temperature for Gd to become FM is just slightly below RT, the possibility of crossing this boundary in the vicinity of RT with compositions containing higher amounts of Gd is a viable option.

The idea of composite MG will be tested using the consolidation of Ce- and Gd-based ribbons into a BMG. The added value of this process is a fabrication of BMG, containing two different MGs, which can, in comparison with MG ribbons, enable broader functionality for potential applications. Combination of powders aims at unusual magnetic properties originating from the mixed microstructure. Due to the higher magnetic moment of Gd, the magnetisation of the composite is expected to arise from the Gd-based constituents.

3.2 Methods to be Used

Rapid solidification by means of PFC is a metallurgical processing route, distinguished by its ability to impart metastable, nanocrystalline or glassy structure of the alloy. Many variables can detrimentally affect the repeatability of the results, hence, all the alloys will be produced by using a constant set of parameters. Experiments will be carried out on the Edmund Bühler GmbH single-roller melt spinning device, model SC. The diameter of Cu spinning wheel amounts to 200 mm and it is encased in a high-vacuum chamber. A maximum mass of the sample is 10 g per batch, melted using 6 kW Himmel HIT 6 radio frequency inductor. All the alloys will be produced in 700 mbar atmosphere of 99.999% Ar, at a wheel frequency of 40 Hz (circumferential speed of 25 m/s), with a nozzle-to-wheel distance of 400 μm. The utilized crucibles will be made of graphite, have a nozzle with a diameter of 1.5 mm and will be coated with boron nitride layer to prevent the reaction of the alloy with carbon. Quenching temperatures will be in the range 1300-1400°C.

Structure of the ribbons will be determined with XRD measurements, firstly on a powdered sample delivering an averaged information. For the cooling profile of a melt spun ribbon is not homogeneous through its cross-section, it is reasonable to determine its structure on wheel side (WS) and a free side (FS) as well. A property of limited PD of X-rays will be used, allowing partial reconstruction of the ribbon's cross-section and approximation of the thickness of the crystalline layer. PANalytical Empyrean XRD instrument in Bragg-Brentano geometry, with Cu wavelength λ=0.15406 nm, will be used for structural characterisation. Silicon zero-background sample holders, producing no diffraction in the range 0 to 120° of 2θ, will be employed. Background subtraction will be performed to emphasize the halo-containing signal of the glassy specimens.

Thermal characterisation of the glasses will be carried out with DSC measurements, aimed at determining T_g, T_x, T_m, T_l and analysing the variation of these temperatures with respect to different compositions. An instrument for simultaneous thermal analysis by Netzsch, model Jupiter 449, will be employed. The samples will be measured in highly conductive Pt crucibles with Al_2O_3 insets in one instance. Secondly, standard Al_2O_3 crucibles with thicker walls and lower thermal conductivity will also be used for temperatures exceeding ≈900°C. The samples to be loaded into the crucibles will be melt spun ribbons, cut to size in order to fit the crucible. The heating rate will be 20 K/min for heating and cooling. A set of glass forming parameters will be introduced as well, in order to describe the vitrification tendency and compare it against the eutectic compositions.

For microstructural examination down to atomic-scale, TEM technique will be used. Sample preparation for TEM will be carried out with both, focused ion beam FIB preparation (FEI Helios NanoLab 650) and precision ion polishing system PIPS (Gatan, model 691), using Ar gas. Three different TEM instruments will be used, firstly Jeol ARM 200 CF, with up to 200 kV of acceleration voltage, located at the National Institute of Chemistry KI, Ljubljana, Slovenia, for the study of Ce-based MGs with variable x=Ce/(Ce+Al). Secondly, for the study of Ce-based MGs with variable ratio y=Fe/(Fe+Cu), Jeol JEM-2100, 200 kV of maximum beam energy, located at the Centre for Electron Microscopy and Microanalysis, Ljubljana, Slovenia, will be used. For the characterisation of Gd-based MGs with variable x=Gd/(Gd+Al), FEI Titan Themis, with 300 kV of beam energy will be utilized, located at Max-Planck-Institut für Eisenforschung GmbH in Düsseldorf, Germany.

Magnetic properties will be studied primarily through M(H) loops using the open-loop technique of VSM at RT, which is expected to yield general information about the magnetic behaviour of the studied alloys. Here, the utilized VSM instrument will be Microsense EZ9 with 1.8 T of maximum applied field (at 18 mm of pole face distance) and ≈0.5 μT of noise. Samples will be prepared in the form of powder, encapsulated in a plastic holder.

Further, magnetic ZFC-FC measurements at cryogenic temperatures will be conducted on MGs with the most intriguing behaviour via SQUID measurements. Magnetic property measurement system MPMS3, made by Quantum Design, Inc. will be used for this purpose. An instrument incorporates 7 T magnetic field, operates in VSM mode (AC option as well) functions within the temperature range 1.8-400 K and features a sensitivity of $\leq 10^{-8}$ emu.

3.3 Outline of the Experimental Section

The first part of the third chapter will present a peer-reviewed article where Ce-based glassy alloys are obtained through the variation of ratio x between Al and Ce contents [206]. Structural, thermal, and mechanical properties are measured and microstructure of the alloys is characterised. Consolidation of powders into BMG is described as well.
Further on, additional results regarding Ce-based alloys are presented, which were not included in the article. An analysis of the ribbon's structure on FS and WS, crystallisation of the glass as observed with synchrotron light, and magnetic properties of Ce-based ribbons are presented.

The following section presents the article about Ce-based alloys with variable ratio y of immiscible Fe and Cu metals [99]. Structure, thermal properties, microstructure and magnetic properties are studied to deliver the information about glass formation tendency, characteristic temperatures, the microstructure of the glass at the atomic level and magnetic behaviour.

In the next section, results on Gd-based alloys are presented in the form of so far unpublished data. The alloys contain variable amounts of Al and Gd (x), whereas their composition is analogous to the family of Ce-based alloys with variable amounts of Al and Ce. Experimental techniques include a structural determination on powder, FS and WS of the ribbon, thermal analysis, microstructural investigation with TEM and measurements of magnetic properties. In addition to RT VSM magnetic measurements, cryogenic SQUID measurements are performed on some specimens, in order to give insight into the glasses' phase transitions.

The latter topic considers the synthesis of composite BMG formed with the thermoplastic consolidation of glassy Ce- and Gd-based ribbons with the use of PECS technique. Its ability to restrain crystallisation and yield a composite glass is probed with the structural examination, thermal measurements, microstructural study and determination of magnetic hysteresis loops. The effect of two distinct RE-based glasses on the combined properties of a BMG is depicted.

Discussion of the properties of Ce- and Gd-bearing MGs is given in the final section of the third chapter. It is viewed in terms of different valence and magnetic moment of the two REs, as well as discrepant binary diagrams of Al-Ce and Al-Gd, influencing the ease of glass formation. The quantity of RE can be strongly correlated with the characteristic transition temperatures in thermal analysis, while the implications of RE content on magnetisation and magnetic behaviour of the studied alloys are not straightforward, but can in part be explained with their structure.

Chapter 4

Results and Discussion

4.1 Ce-Based Alloys

4.1.1 Paper "Stabilisation of Ce-Cu-Fe glassy alloys by addition of Al"

The following section presents a paper entitled "Stabilisation of Ce-Cu-Fe amorphous alloys by addition of Al", written by Luka Kelhar, Jana Ferčič, Pascal Boulet, Marjeta Maček-Kržmanc, Sašo Šturm, Martin Lamut, Boštjan Markoli, Spomenka Kobe and Jean-Marie Dubois, which appeared in Philosophical Magazine, Vol. 96, No. 30, in 2016 on pages 3143-3158.

This article describes the formation of a family of glassy $(Al_{1-x}Ce_x)_{62}Fe_{13}Cu_{25}$ alloys, developed from $Al_{62}Fe_{13}Cu_{25}$ quasicrystalline alloy by replacing Al with Ce. It is aimed at investigating the composition range which yields alloys with a pronounced glassy structure. It is found that the stability range of these MGs correlates with the occurrence of eutectic compositions between Al and Ce. In the Al-Ce binary diagram, the region of deep eutectics appears around 70 at% Ce, corresponding with the formation of strong glasses for the corresponding ratio x in a series of quaternary glassy alloys.

The crystallisation temperature of the studied alloys highly depends on the amount of Ce. With higher additions of the latter element, it moves towards lower temperatures. A range of strong glass forming alloys that possess an extensive range of supercooled liquid prior to crystallisation is found. This temperature region enables the consolidation of bulk MGs via thermoplastic forming of MG powders with the PECS technique. An advantage of this process is the possibility to achieve a BMG with several millimetres in size by avoiding crystallisation. Consolidation temperature that exceeds the crystallisation temperature results in primary $AlCe_3$ phase.

Mechanical properties of $(Al_{1-x}Ce_x)_{62}Fe_{13}Cu_{25}$ ribbons were tested using the nanoindentation technique. They strongly depend on the ratio x=Ce/(Ce+Al), whereas more Al increases the elastic modulus and hardness.

PHILOSOPHICAL MAGAZINE, 2016
VOL. 96, NO. 30, 3143–3158
http://dx.doi.org/10.1080/14786435.2016.1229062

Taylor & Francis
Taylor & Francis Group

Stabilisation of Ce-Cu-Fe amorphous alloys by addition of Al

Luka Kelhar[a,b,e], Jana Ferčič[a,e], Pascal Boulet[a,d,e], Marjeta Maček-Kržmanc[a], Sašo Šturm[a,e], Martin Lamut[c], Boštjan Markoli[c,e], Spomenka Kobe[a,b,e] and Jean-Marie Dubois[a,b,d,e]

[a]Jožef Stefan Institute, Ljubljana, Slovenia; [b]International Postgraduate School 'Jožef Stefan', Ljubljana, Slovenia; [c]Faculty of Natural Sciences and Engineering, University of Ljubljana, Ljubljana, Slovenia; [d]Institut Jean Lamour (UMR 7198 CNRS-Université de Lorraine), Parc de Saurupt, Nancy Cedex, France; [e]International Associated Laboratory PACS2, CNRS–Nancy, France and JSI-Ljubljana, Slovenia

ABSTRACT

The present work describes the formation of amorphous alloys in the $(Al_{1-x}Ce_x)_{62}Cu_{25}Fe_{13}$ quaternary system ($0 \le x \le 1$). When the amount of Ce falls in the range $0.67 \le x \le 0.83$, the alloys obtained exhibit a completely amorphous structure confirmed by powder X-ray diffraction. Otherwise, at compositions $x = 0.5$, 0.58, 0.92 and 1, a primary crystalline phase forms together with an amorphous matrix. The crystallisation temperature (T_x) decreases with increasing Ce content, varying from 593 K for $x = 0.5$–383 K for $x = 1$. Composition $x = 0.75$ is considered as the best glass former, exhibiting a large supercooled liquid region of 40 K width that precedes crystallisation. In order to form bulk amorphous alloys, ribbons with this later composition were consolidated into few millimetre thick discs using pulsed electric current sintering at different temperatures, yet preserving the amorphous structure. Meanwhile, increasing temperature above 483 K triggers crystallisation of a primary phase isostructural to $AlCe_3$. Further increase in the temperature up to 573 K yields a higher fraction of the crystalline phase. Testing mechanical properties, using nanoindentation, revealed that both elastic modulus (E) and hardness (H) depend on the Al content, ranging from $E = 85.6 \pm 3.7$ GPa and $H = 6.2 \pm 0.7$ GPa for $x = 0.5$ down to $E = 39.8 \pm 1.0$ GPa and $H = 3.1 \pm 0.2$ GPa for $x = 0.92$.

ARTICLE HISTORY
Received 8 April 2016
Accepted 22 August 2016

KEYWORDS
Metallic glasses; rare-earths; sintering; stability; crystallisation

1. Introduction

It is commonly understood that the formation of amorphous alloys is due to frustration of the structure that forms a disordered state [1–3] in addition to a proper design of the chemical composition [4]. Amorphous alloys, or metallic glasses, are therefore always trapped in a metastable state that may be achieved when certain conditions are fulfilled. Three empirical rules govern the formation of a disordered metallic lattice. First, it must be made of a variety of chemical species, so that crystallisation of a stable phase is more difficult. The tendency towards suppressed crystallisation arises from packing constraints that vary

CONTACT Luka Kelhar luka.kelhar@ijs.si

with the size of the different atoms [5]. This means that in order to form a glass, one should combine elements with differing atomic sizes and valences, thus reducing the possibility to form ordered intermetallic phases. Recently, Laws et al. have proposed a topological model to describe the superior glass-forming ability (GFA) of particular alloys [6]. They showed that efficient local packing around every constituent atom species is needed to form bulk glasses. Formation enthalpy between the constitutive elements determines whether the phase is thermodynamically favoured or not [7]. If it is negative, then the formation of a stable phase is favoured, and this interaction becomes useful in forming a metastable glass. Several additional criteria such as ion mixing [8,9] and minor additions of alloying elements [10,11] are also known to influence the glass formability of the alloy, although it is obvious that all those conditions may not be sufficient to predict glass formation in every possible system.

The GFA of a given alloy characterises the ability of a molten alloy to remain stable in the disordered state when its viscosity exceeds a very large value typical of a solid. There exist various definitions of this criterion, the most straightforward, being the inverse liquidus temperature T_l^{-1} that stresses the tendency of the liquid to sustain cooling without the formation of a crystal. In the present context, we refer to the criterion introduced by Du et al. [12], which reads:

$$\mathrm{GFA} = \left(2\,T_x - T_g\right) / \,T_l \tag{1}$$

where T_x is the temperature of the onset of crystallisation, T_g is the temperature of the glass transition and T_l is the liquidus temperature, ll of which aredetermined experimentally by thermal analysis. Conversely, it was postulated by Turnbull [13] that GFA is related to the reduced glass transition temperature, T_{rg}, which is defined as $T_{rg} = T_g/T_l$. As T_{rg} increases from 1/2 to 2/3, it becomes more likely that a certain alloy will forms a glass [14]. In order to increase T_{rg}, either the glass transition temperature or liquidus temperature should be changed (or both). Whereas T_g is found difficult to adjust via composition, the liquidus temperature is more easily lowered by designing eutectic alloys [14]. With this approach, the homogeneous crystallisation in the undercooled liquid supressed, because the eutectic features an undercooling, which is deeper in temperature than the surrounding compositions. Consequently, due to high GFA, such alloys are produced using lower solidification rates and still preserve their amorphous structure.

Yet, it is important to stress that we do not study GFA in the present context since we process heating experiments: the amorphous solid undergoes a glass transition at $T = T_g$ upon continuous heating, which therefore is different from the one addressed above due to temperature hysteresis effects, before crystallisation takes place at T_x. We therefore assessed the glass devitrification ability (GDA) rather than GFA. This later GFA is addressed via experiments performed on the cooling liquid: critical size of the volume that is vitrified using a given method (cylindrical mould, or wedge shaped mould), which we could not perform in the present study. In view of the consolidation experiments, which are an essential part of it, we are however in need of information regarding the resistance to crystallisation that our samples may offer as a function of composition. To this end, and in a first-order approximation, we consider that:

$$\mathrm{GDA} \approx \mathrm{GFA}$$

With all restrictions set forth above in mind, we proceed with data gained from (continuous) heating experiments to get insight in the alloys ability to retain an amorphous state when approaching the temperature of the onset of crystallisation.

Amorphous alloys based on Ce are interesting, both for their fundamental significance and potential usefulness [15]. Several Ce-rich alloys are known to form glasses in combination with metals like Fe, Cu, Ni, Al and Ga, and minor additions of alloying elements like Si, Co and Nb [15–20]. While rapid quenching produce some glassy alloys, others can also be made into bulk glasses by means of mould casting. Compositions with high amounts of Ce exhibit low T_g [21], reminiscent of that of polymers, which is of peculiar interest for the fundamental studies of the supercooled liquid region ($T_g \leq T \leq T_x$). Properties like viscosity, thermodynamic and kinetic behaviour [22] are studied in the temperature range 100–200 °C, which is generally rather low for amorphous alloys. A salient characteristic of Ce-based glasses is their very low elastic modulus and hardness [23, 24], which places these alloys between metals and polymers with respect to mechanical properties.

In this paper, we study the influence of Al additions in the system $(Al_{1-x}Ce_x)_{62}Cu_{25}Fe_{13}$ in terms of composition–structure–properties relationship. We report on the GDA, thermal stability and mechanical properties of amorphous samples prepared by melt spinning in the shape of ribbons as well as hot consolidated to form bulk amorphous ingots. The alloy system is selected from the composition of the stable icosahedral quasicrystal $Al_{62}Cu_{25}Fe_{13}$ discovered by Tsai et al. [25]. In this quasicrystal, the contribution of each Al atom to the valence band is equal to e/a = 3.01 el/at, that of Cu is 1 el/at and that of Fe is e/a = 1.05 el/at [26]. While e/a for cerium atoms is equal to 4 el/at in the dioxide CeO_2, its contribution in metals is more difficult to assess since this element is known to exhibit a fluctuating valence. Based on X-ray absorption spectroscopy, Wohlleben and Röhler showed that it decrease down to e/a = 3.25 el/at in Ce intermetallics and diluted alloys [27]. The case of cerium was recently reconsidered by Mizutani, using the same method as in [26]. Application to magnetic rare-earth elements is however by far not straightforward, and correlation energy and many-body effects are explicitly taken into account. This point explains why the study is still going on and its results were not published so far. The main results were sent to us by Mizutani nevertheless, showing that e/a = 3.1 el/at for the pure element [28]. We use this value in the present study.

The atomic radii of Al and Ce are quite different: goldschmidt radii are R_{Al} = 143 pm and R_{Ce} = 182 pm, respectively. Substituting Ce for Al atoms in the quasicrystal offers thus an opportunity to test the stability of the quasicrystalline lattice upon size mismatch effects as well as against variation of the type of electronic contributions: Al has a 3s2 3p1 contribution to the valence band, whereas Ce brings 5d1 6s2 electronic states. As we show in the following, the quasicrystalline state disappears with very little Ce substituting for Al. A broad range of glassy alloys is found instead, which is the focus of the present study.

2. Experimental details

Starting ingots of an $(Al_{1-x}Ce_x)_{62}Cu_{25}Fe_{13}$ alloy were prepared from pure elements of 99.9% Al (Sigma Aldrich), 99.9% Ce (Pi-Kem), 99.99% Cu (Sigma Aldrich) and 99% Fe (Pi-Kem). Non-consumable arc-melting was used to melt the high-purity elements into bulk ingots. Homogeneity of the specimens was achieved by several remelting cycles and turning around the pieces. The weight loss upon arc melting was measured to be less than 0.1%, which

excludes any significant shift in the composition. Bulk pieces were later on induction-melted and rapidly quenched by melt spinning in Ar gas. To this end, we used a copper wheel of 20 cm in diameter that was rotating at a frequency of 40 Hz. To comminute the ribbons into an amorphous powder, we used a blade grinder, rotating at high circumferential speeds of up to 18,000 rpm. The size distribution of the particles, in fact their lateral extension since the ribbon thickness was not affected, was reduced to a maximum of 315 μm by mechanical sieving.

After differential thermal calorimetry (DSC) analysis, we selected the melt-spun ribbons that showed the widest ΔT range and highest T_{rg}, which were then consolidated into bulk discs by pulsed electric current sintering (PECS) with DR. SINTER SPS-615 (Fuji). We used the amorphous powder, with concentration ratio $x = Ce/(Ce + Al) = 0.75$ and particle size smaller than 315 μm. PECS sintering was used to compact the ribbons by simultaneous application of heat and pressure into the shape of a disc with diameter of 10 mm and height of 4 mm. A hard-metal die was used for high pressure sintering at 500 MPa. Heating rate in the PECS was kept around 150 °C/min and temperature was measured with a K-type thermocouple placed in the wall of the die. Sintering was conducted at temperatures selected between 453 and 573 K, with steps of 20 K. The sintering programme featured 3 min heat-up time and 1 min of sintering at the pre-determined temperature, followed by furnace cooling.

Powder X-ray diffractometry (PXRD) with Bragg-Brentano geometry was used to assess the amorphous state of the ribbons and sintered discs. We present in the following conventional diffraction patterns, with intensity vs. twice the Bragg angle θ, as well as the interference function I(q) where the modulus of the transfer momentum is $q = 4\pi\sin\theta/\lambda$ with λ the wavelength. Details about these measurements given elsewhere [29]. Conventional PXRD patterns and the interference function were obtained using a Cu anode (λ = KαCu = 0.154 nm). DSC using Netzsch 204 F1 was used to determine the thermal changes, i.e. the characteristic temperatures of glass transition T_g, crystallisation T_x, supercooled liquid region $\Delta T = T_x - T_g$, reduced glass transition temperature $T_{rg} = T_g/T_l$, melting temperature T_m and liquidus temperature T_l. The heating programme featured a 303–1073-303 K sequence and heating/cooling steps of 20 K/min. The samples were placed in an Al_2O_3 crucible covered with a lid. A flow of Ar (99.999%) was used as inert atmosphere.

Microstructure was studied using scanning electron microscope (FE-SEM, Jeol JSM-7600F). For transmission electron microscopy (TEM) analysis, the specimens were prepared using dual-focused ion beam system (FIB, FEI Helios NanoLab 650). TEM and STEM imaging were performed on a JEOL JEM-ARM 200 CF using the cold field emission source, equipped with EDXS (Centurio 100 mm^2, JEOL) and EELS (QuantumGIF, Gatan) system. The probe size was 0.12 nm. The energy-dispersive X-ray spectroscopy (EDXS) and electron energy loss spectroscopy (EELS) were performed using probe currents of 250 pA, thereby degrading the spatial resolution approaching the values of 0.2 nm. For nanoindentation, we used a Keysight Nano Indenter G200 with a three-sided Berkovich pyramid. Cross sections of the ribbons were placed in metallographic resin and polished. The nanoindentation was performed on 10 different spots. Elastic modulus and hardness were quantified via electromagnetic tracking of force and displacement.

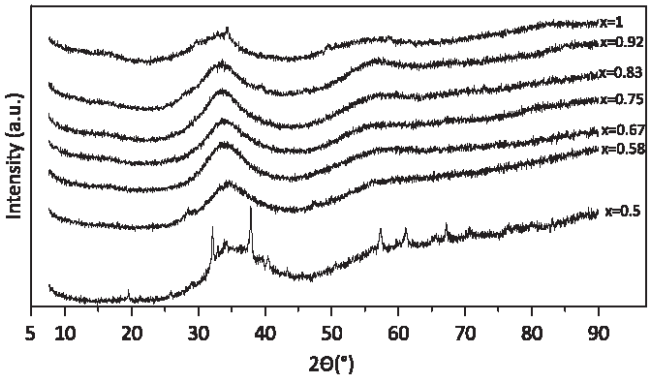

Figure 1. Powder X-ray diffraction (λ = K∝Cu) data of melt-spun $(Al_{1-x}Ce_x)_{62}Cu_{25}Fe_{13}$ alloys in the Ce-rich region ($0.5 \leq x \leq 1$).

3. Experimental results

3.1. Powder X-ray diffraction and TEM

By varying the ratio between Ce and Ce + Al in $(Al_{1-x}Ce_x)_{62}Cu_{25}Fe_{13}$ alloys (x), we found that the quaternary compositions with $0.67 \leq x \leq 0.83$ form completely amorphous alloys upon rapid quenching at 40 Hz (Figure 1). Ribbons with $x = 0.5$ exhibit sharp peaks that point out the existence of crystallites within an amorphous matrix, itself characterised by a pronounced hump at $2\theta = 35°$. This result indicates that the Ce/(Ce + Al) ratio at this composition is not sufficient to completely frustrate the structure and hinder crystallisation. The position in reciprocal space of the diffraction peaks shows that a primary crystallisation of a phase isostructural with cubic $Al_{1.2}CeFe_{0.8}$ has occurred.

Increasing the concentration of Ce above $x = 0.58$, the ribbons turn amorphous. A structure exhibiting complete disorder is found for $x = 0.67$ and 0.75. These compositions correspond to a deep eutectic region in the Al–Ce binary phase diagram [30]. The formation of two eutectics at 72.5 and 86 at.% Ce [30, 31] correlates with the formation of completely amorphous ribbons in the composition range from $x = 0.67$ to $x = 0.83$. This suggests that the most stable glasses lie in the vicinity of $x = 0.75$. The interference function (Figure 2), where intensity is plotted vs. momentum transfer indicates the occurrence of complex short and medium-range orders. The main peak, located around $q_1 = 23$–25 nm^{-1} is dissymmetric and contains at least two components, which is consistent with the large difference in atomic radii of the elemental constituents. A pre-peak is clearly visible around $q_0 = 12$ nm^{-1}. Its presence is a signature for some medium range order between constituents having the largest scattering power for X-rays, although it is not possible to separate transition metals and the rare earth with this simple experiment. At larger q values, a broad, nearly split peak appears with a main component at $q_2 = 37$–39 nm^{-1} and a shoulder around $q_3 = 46$ nm^{-1}. The occurrence of the set of halos at positions in reciprocal space $q = \{q_0, q_1, q_2, q_3\}$ is a clear indication of pronounced medium range order, going beyond at least second neighbours. It is furthermore expected that the type of medium range order is close to icosahedral ordering if $q_1/q_0 = \tau^{-1} \approx 0.618$ and $q_2/q_1 = \tau \approx 1.618$ while $q_3 = 2q_1$ [32]. In the present case, the distribution of atomic sizes and hybridisation effects does not allow for a sharp correspondence to the theoretical values predicted for medium range icosahedral order. It is

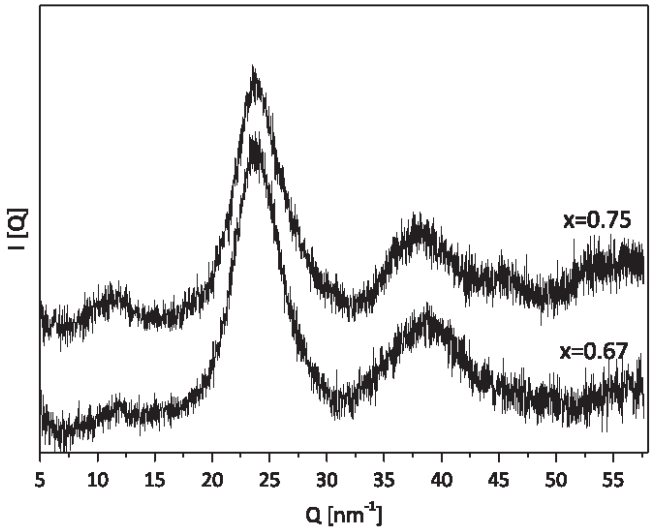

Figure 2. Interference function recorded for amorphous samples of composition $(Al_{0.25}Ce_{0.75})_{62}Cu_{25}Fe_{13}$ (top curve) and $(Al_{0.33}Ce_{0.67})_{62}Cu_{25}Fe_{13}$ (bottom curve).

observed however from Figure 2 that $q_1/q_0 = 0.5$, $q_2/q_1 = 1.6$ and $q_3/q_1 = 1.9$ is in reasonable agreement with the ratios predicted by Sachdev and Nelson [32].

The PXRD diffraction pattern of the ternary alloy $Ce_{62}Cu_{25}Fe_{13}$ shows nanocrystallites embedded in an amorphous matrix, with a broad hump at 33° (Figure 1). The intensity of the peaks is very low however, making assessment of the correct phase difficult. The shift towards lower 2θ angles of the broad hallo corresponding to the amorphous matrix is consistent with a larger Ce concentration, which in average increases interatomic distances compared to the previous alloy with $x = 0.5$.

To elucidate the completely amorphous nature of the ribbons and the occurrence of nanocrystallites in the microstructure, we employed TEM analysis of thin lamellae produced from representative regions of the ribbons (Figure 3). An indication of the amorphous nature of the melt-spun alloy with composition $(Al_{0.25}Ce_{0.75})_{62}Cu_{25}Fe_{13}$ is given by the TEM image shown in Figure 3(a). The SAED pattern presented in the inset, as well as observation of the structure at a local scale do not reveal any order feature.

TEM micrographs of a sample with composition $Ce_{62}Cu_{25}Fe_{13}$ reveal a significant number of nanocrystals embedded in an amorphous matrix, as seen in Figure 3(b). It should be noted that the lamella was cut from the central part of the ribbon, to average out the effect of wheel side and free side. The distribution of nanocrystals in amorphous matrix is homogeneous and from the micrographs, their estimated size is ≈ 5–30 nm.

Crystals that form in the sample $Ce_{62}Cu_{25}Fe_{13}$ are rich in Ce, which we confirmed by the EDXS analysis. To eliminate possible errors in interpretation, we only analysed the concentration of Ce and Fe, since the lamella is attached on a Cu-grid, which contributes to the overall Cu intensity. In order to deduce the composition of the crystallites, two EDXS measurements were performed, one from the amorphous matrix of the specimen (marked 'amorphous' in Figure 3(c)) and the second from the specimen region containing crystalline particles (labelled with 'crystalline' in Figure 3(c)). Results of the EDXS analysis are shown in Table 1. It should be mentioned that according to the number of counts in the

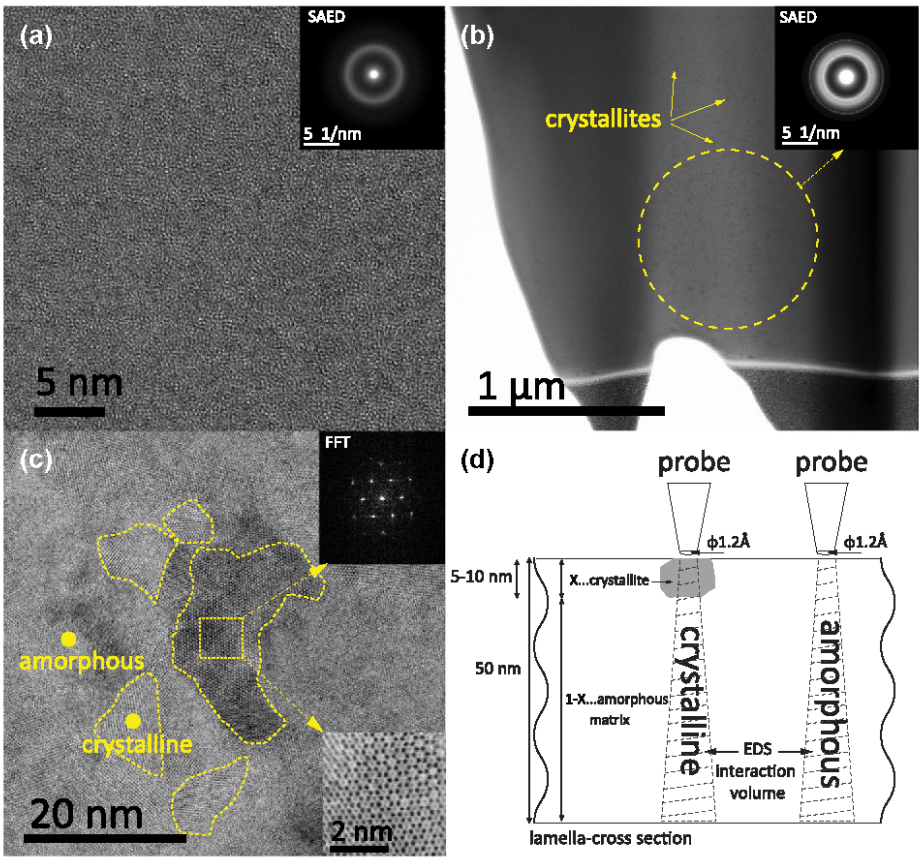

Figure 3. (colour online) (a) TEM micrograph of melt-spun $(Al_{0.25}Ce_{0.75})_{62}Cu_{25}Fe_{13}$ ($x = 0.75$) sample. Inset shows the SAED pattern of the observed area. (b) TEM micrograph of the melt-spun $Ce_{62}Cu_{25}Fe_{13}$ ($x = 1$) lamella, containing crystallites (marked by arrows). Inset belongs to the SAED of the marked circular area. (c) Micrograph of the same sample with several crystalline regions outlined. The two insets show the atomic resolution bright-field STEM image (bottom) and the corresponding FFT (top) and of the marked square-shaped area of interest. (d) Schematics of the EDXS data acquisition process used to analytically evaluate the composition of the crystallite embedded in the amorphous matrix.

Table 1. EDXS analysis of the two regions in Figure 3(c), marked with amorphous and crystalline.

Region	Ce (at.%)	Fe (at.%)	Error bar (%)
Amorphous	85	15	±3
Crystalline	87	13	±3

EDXS spectrums, the error bar is ±3%. Nevertheless, the repeatability of the measurements indicates the compositions in Table 1. In the amorphous matrix, the EDXS analysis yielded a Ce/(Ce + Fe) composition of 85 at.%. On the other hand, the analysed volume of a region containing a crystalline particle exhibits a Ce concentration of 87 at.%. When repeated on multiple crystallites and amorphous matrixes, these results were consistent throughout the sample. Schematic explanation of the procedure to determine the composition of the crystallite embedded in the amorphous matrix is shown in Figure 3(d). The corresponding equation to describe the composition of the crystallites was deduced from Ref. [33] and modified according to our parameters:

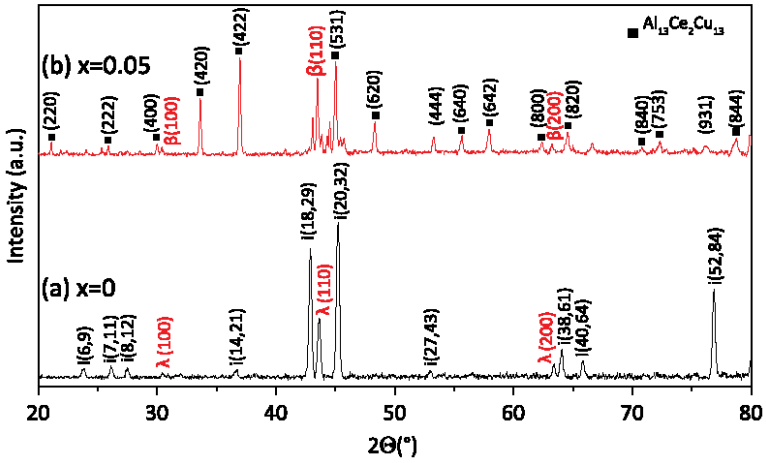

Figure 4. (colour online) Powder X-ray diffraction (λ = KαCu) data of melt-spun $(Al_{1-x}Ce_x)_{62}Cu_{25}Fe_{13}$ alloys for (a) $x = 0$ and (b) $x = 0.05$. Label iQC marks the quasicrystalline $Al_{62}Cu_{25}Fe_{13}$ phase, λ stands for monoclinic $Al_{13}(Fe,Cu)_4$, β represents a cubic AlCu(Fe) phase and black squares belong to cubic $Al_{13}Ce_2Cu_{13}$.

$$C_{Ce} = \left[AvCom_{Ce} - A_{Ce}{}^{*}\,(1 - X)\right]/(X), \tag{2}$$

where C_{Ce} is the concentration of Ce in the crystalline region, $AvCom_{Ce}$ marks the average composition of Ce in the interaction volume, composed of crystallite and amorphous region, and A_{Ce} is the concentration of Ce in the amorphous matrix (Figure 3(d)). X corresponds to the normalised size of the crystallite in the cross section view of the lamella and $1-X$ is the normalised thickness of the remaining amorphous layer in the cross section (Figure 3(d)). We assumed that the size of the crystallite is 5–10 nm, and the thickness of the lamella is 50 nm, which results in $X = 10–20\%$, according to the schematics shown in Figure 3(d). By inserting the value of A_{Ce} 85 at.% and $AvCom_{Ce}$ 87 at.% and normalised thicknesses X and $1-X$, the concentration of the crystallite yields a composition of 100% Ce.

This result is in agreement with the experimental observation (areas of interests shown in Figure 3(c) and Table 1), where 87 at.% of Ce was detected. Therefore, we postulate that the crystallites in the specimen of ternary composition $Ce_{62}Cu_{25}Fe_{13}$ are predominantly composed of Ce. If for example, the crystallites would contain only 50 at.% of Ce, the $AvCom_{Ce}$ would have to be ≈80 at.%, which is significantly lower than our experimental values.

The ternary alloy $Al_{62}Cu_{25}Fe_{13,}$ without Ce, is a well-known stable icosahedral quasicrystal, featuring five-fold symmetry. XRD reveals that besides the i-phase, we also produced the monoclinic λ-phase $Al_{13}(Fe,Cu)_4$ [34], as shown in Figure 4. Upon addition of at most 3 at.% of Ce, the quasiperiodic structure disappears and is mostly replaced by a phase isostructural with cubic $Al_{13}Ce_2Cu_{13}$ [35]. Several additional peaks in the X-ray pattern belong to the cubic phase β-AlCu(Fe) [36]. This result targets the origin of quasiperiodic order in aluminium-based alloys. Addition of 3 at % of Ce changes the Fermi vector only through atomic volume effects since Al and Ce have almost identical valence of 3 and 3.1 el/at, respectively. Considering the Goldschmidt radii quoted above, $x = 0.05$ yields a volume change when substituting Ce for Al of +3%, which in turns leads to shift the amplitude of the Fermi vector by −1%. Such a minute effect cannot account for a breakdown of the Hume-Rothery

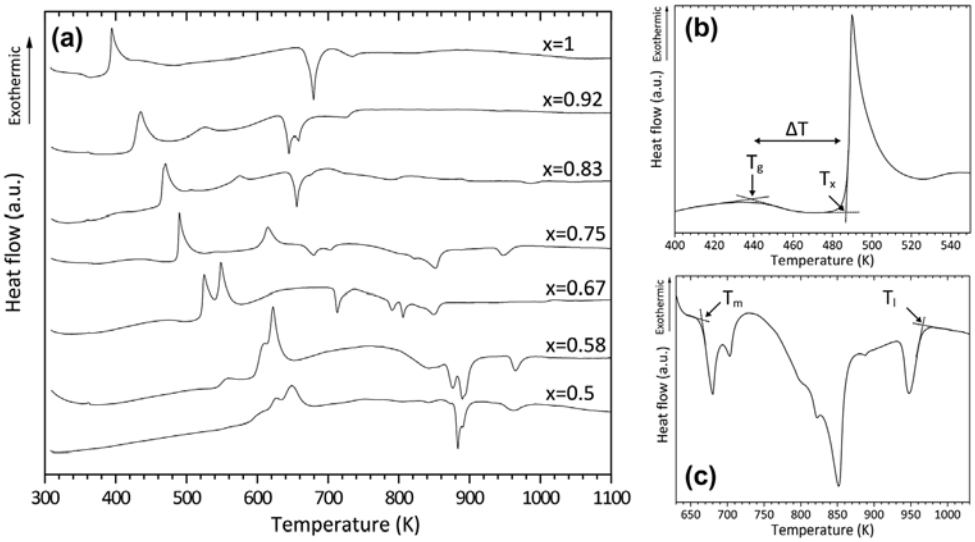

Figure 5. (a) DSC curves recorded at constant heating rate of 20 K/min for a series of melt-spun $(Al_{1-x}Ce_x)_{62}Cu_{25}Fe_{13}$ alloys. (b) Enlargement of the curve for the $Al_{15.5}Ce_{46.5}Cu_{25}Fe_{13}$ glass in the region of the glass transition (T_g) and crystallisation (T_x) temperatures, (c) same, but for the melting temperature (T_m) and liquidus temperature (T_l) of the same alloy. The thin straight lines explain how each characteristic temperature is defined.

rule, namely for any dephasing between Fermi surface and Jones zone. The lack of stability of the Ce-dopped icosahedral compound must therefore arise from another effect, which presumably is related to the different contributions that Al and Ce have, respectively, to the valence band. On the one hand, Al contributes spherically symmetric s and p states while, on the other hand, Ce brings d and s states that are orthogonal and of very different symmetries. This purely experimental conclusion is in line with the results of a study of partial densities of states in complex intermetallic and quasicrystals [37]. Detailed computation of the electronic structure using first principle methods is under way to confirm this point on a large size, yet periodic, approximant.

3.2. Thermal analysis

Representative DSC charts are assembled in Figure 5(a), whereas Figure 5(b) and (c) shows how the characteristic temperatures T_g, T_x, T_m and T_l of interest for the present study were defined. Their numerical values are given in Table 2 for x varying between 0.5 and 1. Figure 6 presents a digest of some of these data for $x \geq 0.5$. It is observed that the most stable glasses are found in the vicinity of $x = 0.7$, which also corresponds to a lowering of the liquidus line due to the formation of a eutectic alloy.

The differential calorimetry scans in Figure 5(a) show the exothermal (towards the top of the figure) and endothermal (towards the bottom of the figure) peaks that sign glass transition, crystallisation, phase transformation in solid state and melting. The multiplicity of those peaks suggests that non-trivial thermal events take place and are governed by the nucleation of multiple crystalline phases. The absence of any significant DSC signal before crystallisation for some compositions ($x \leq 0.58$) indicates that the glass transition proceeds with a very small transformation enthalpy or takes place almost at the same temperature as

Table 2. Thermal analysis data for amorphous $(Al_{1-x}Ce_x)_{62}Cu_{25}Fe_{13}$ alloys with $0.5 \leq x \leq 1$. Symbols are as in text: T_g: glass transition temperature, T_x: temperature of the onset of crystallisation, T_m: melting point, T_l: liquidus temperature, T_{rg}: reduced glass transition temperature. Uncertainties on temperatures are ± 5 K.

x	Composition (at.%)	T_g (K)	T_x (K)	$\Delta T = T_x - T_g$ (K)	T_m (K)	T_l (K)	$T_{rg} = T_g/T_l$	GDA = $(2T_x - T_g)/T_l$
0.5	$Al_{31}Ce_{31}Cu_{25}Fe_{13}$	535	590	55	750	995	0.538	0.648
0.58	$Al_{26}Ce_{36}Cu_{25}Fe_{13}$	515	595	80	755	975	0.528	0.692
0.67	$Al_{20.5}Ce_{41.5}Cu_{25}Fe_{13}$	470	520	50	630	860	0.547	0.663
0.75	$Al_{15.5}Ce_{46.5}Cu_{25}Fe_{13}$	440	490	50	645	965	0.456	0.560
0.83	$Al_{10.5}Ce_{51.5}Cu_{25}Fe_{13}$	405	465	60	645	1010	0.401	0.520
0.92	$Al_5Ce_{57}Cu_{25}Fe_{13}$	365	425	60	635	1060	0.344	0.458
1.0	$Ce_{62}Cu_{25}Fe_{13}$	350	390	40	665	1100	0.318	0.391

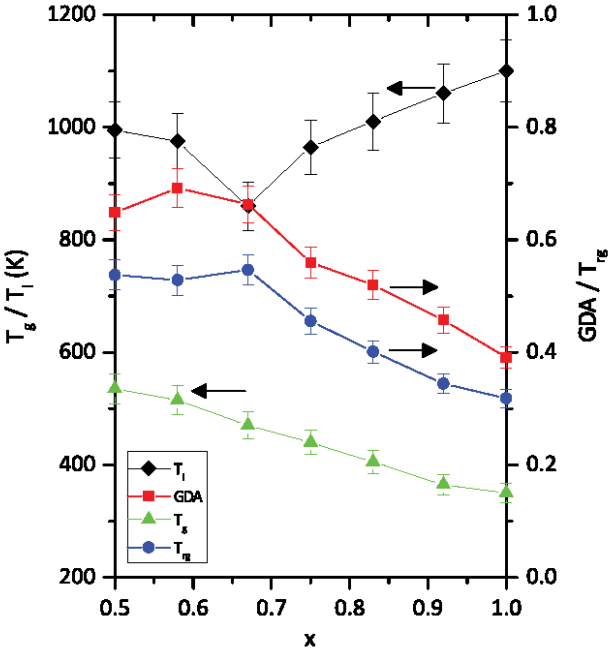

Figure 6. (colour online) Plot of T_g (triangles) and T_l (diamonds) vs. $x \geq 0.5$. Also shown with the right-hand side *y*-axis is the reduced glass transition temperature (dots) and the GDA (squares).

crystallisation sets in. However, for $x = 0.67$ up to 1.0, a slight, but significant, decrease in signal can be observed before the onset of crystallisation. This indicates a reversible transformation, which was associated with no doubt to the glass transition starting at temperature T_g. Hence, the temperature range of amplitude $\Delta T = T_x - T_g$ corresponds to the undercooled liquid region that ends up into crystallisation at $T = T_x$.

As already observed by X-ray diffraction, a majority of the compositions is amorphous and is characterised by a pronounced exothermic peak at $T = T_x$. Meanwhile, the composition $x = 0.5$ consists of nanocrystallites embedded in an amorphous matrix, as revealed by PXRD (Figure 1) and direct microstructural observation. As a consequence, the peak at T_x is less pronounced and shifted to lower temperatures compared to the other alloys with larger x. In contrast, the crystallisation temperature T_x is lower for Ce-rich compositions:

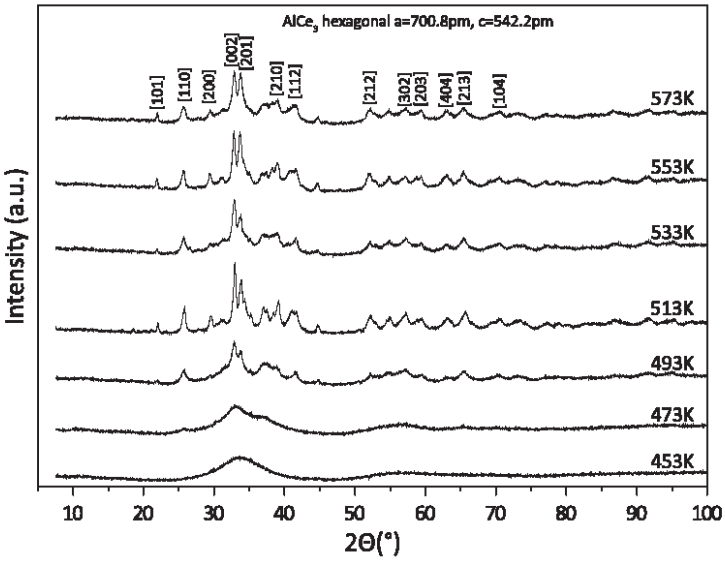

Figure 7. Powder X-ray diffraction patterns (λ = KαCu) of $Al_{15.5}Ce_{46.5}Cu_{25}Fe_{13}$ samples consolidated by PECS at the temperatures indicated in the right-hand side of the figure. Stars mark the presence of a crystalline phase that is isostructural to the hexagonal $AlCe_3$ phase.

for $x = 1$, it amounts to $T_x = 390$ K, which corresponds to the data for similar Ce-rich alloys [18]. With an increased amount of Al, e.g. in the case of $x = 0.58$, T_x increases up to 595 K. The change in T_x as a function of x follows a nearly linear increase (not shown here). Variations in T_m and T_l are also governed by the Ce/(Ce + Al) ratio, but the trend deviates from a linear relationship in consistency with the complexity of the phase diagram.

3.3. PECS consolidation of melt spun ribbons

The alloy with $x = 0.75$ lies among the alloys with the best GDA and shows superior stability in atmosphere, in spite of its high concentration (46.5 at.%) in rare earth element Ce. This property is in agreement with a previous report [17] on Ce-rich amorphous alloys, denoting the good air stability and ageing behaviour of some RE-rich glasses. For this reason, completely amorphous ribbons with $x = 0.75$ were chosen to fabricate a stable bulk amorphous alloy by PECS. Thanks to the existence of a supercooled liquid region as wide as 40 K and therefore, the availability of viscous flow in this temperature range, and the amorphous ribbons were processed into completely dense amorphous ingots. Results of the PECS experiments at different temperatures were studied using PXRD as shown in Figure 7. A fully amorphous structure results from consolidation at a temperature of 453 K without any significant peak showing up in the PXRD pattern. Shallow bumps appear on the diffraction pattern if the consolidation temperature is set at $T = 473$ K. The latter two temperatures are both below the crystallisation temperature (490 K), which explains the preservation of an amorphous structure. With the increase in sintering temperature up to 493 K, the first crystalline phases start to emerge. This observation is in accordance with the DSC result, which shows the onset of crystallisation at 490 K.

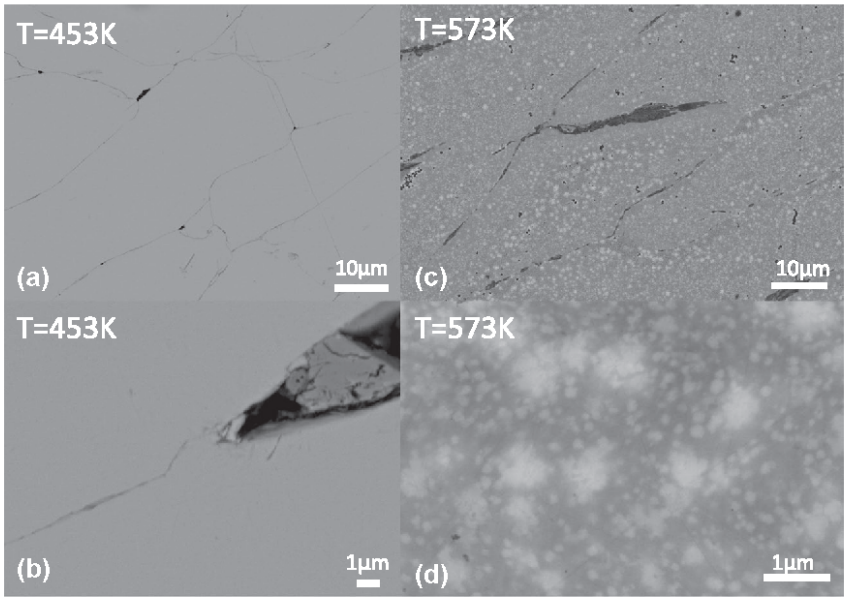

Figure 8. SEM images of bulk amorphous samples at two different magnifications, consolidated at temperatures of 453 K (a and b) and 573 K (c and d).

Increase in the PECS temperature from 493 K up to 573 K does not induce the formation of any additional phase. Hence, it rather results in the increase in the peak intensity. The observed primary phase is isostructural with hexagonal $AlCe_3$, Figure 7. This was the only phase that could be identified throughout the 453–573 K temperatures range. The absence of other intermetallic phases is in accordance with the binary Al–Ce phase diagram [31], which suggests formation of the $AlCe_3$ intermetallic for the concentration ratio 0.25/0.75 between Al/Ce. The microstructure of the samples sintered at 453 and 573 K is visualised in Figure 8. The sintering temperature of 453 K is proven to retain the amorphous structure, which is illustrated in Figure 8(a) and (b). Clearly, the microstructure is featureless, which is characteristic for a metallic glass. The packing of the ribbons is dense, which goes with the observation of thin boundaries between ribbons and an almost complete elimination of porosity. Such an effect is due to sintering with the assistance of plastic flow of the material within the supercooled region, which enables effective consolidation, whereas sintering at a temperature of 573 K, that clearly exceeds the crystallisation threshold, results in the precipitation of a primary phase.

Several authors report about the polymorphous transformation of the $AlCe_3$ phase [31, 38], shifting from a hexagonal to a cubic unit cell. This structural change should occur around 523 K, but it was not observed in our samples. We connect the absence of this phase transition with the rapid sintering in PECS. The process inherently results in metastable conditions, due to short sintering time and non-equilibrium heating and cooling rates.

3.4. Mechanical properties

Room temperature measurements with a nanoindenter enabled us to investigate the mechanical properties of the alloys. The analysis was performed on the cross sections of

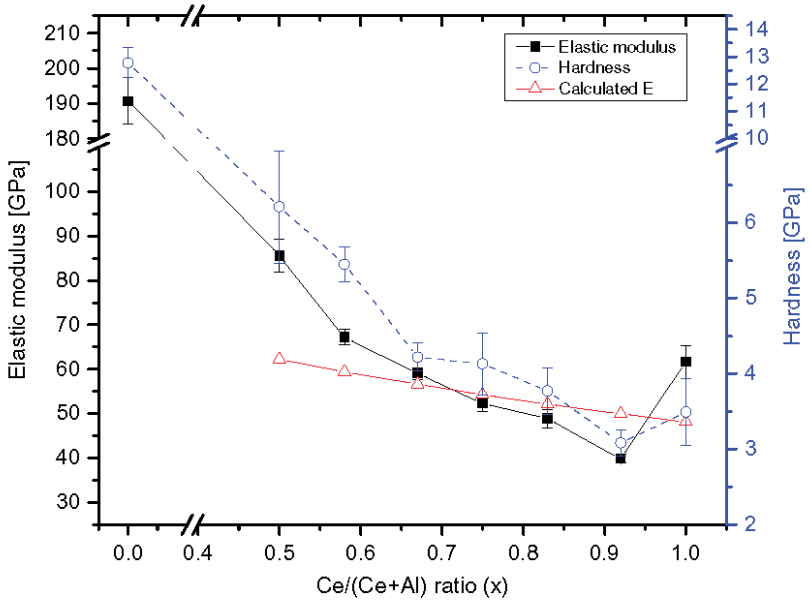

Figure 9. (colour online) Elastic modulus (*E*, black squares), hardness (*H*, open dots) and calculated elastic modulus (red open triangles) for $(Al_{1-x}Ce_x)_{62}Cu_{25}Fe_{13}$.

melt-spun ribbons, embedded in the metallographic resin. Elastic modulus (E) and hardness (H) were determined as functions of the Ce/(Ce + Al) ratio, Figure 9. The initial composition $Al_{62}Fe_{13}Cu_{25}$ yields the highest E and H, amounting to 190.7 ± 6.7 GPa and 12.8 ± 0.5 GPa, respectively. The alloy with $x = 0.5$ yields $E = 85.6 \pm 3.7$ GPa and $H = 6.2 \pm 0.7$ GPa. For higher contents of Ce (i.e. higher x), E and H linearly decrease, reaching a minimum of $E = 39.8 \pm 1.0$ GPa and $H = 3.1 \pm 0.2$ GPa at $x = 0.92$. This observation is in accordance with similar measurements on Ce-rich amorphous alloys [23]. Decrease in mechanical properties with the amount of Ce stops at $x = 1$, where both E and H show a sudden increase in 61.6 ± 3.7 GPa and 3.5 ± 0.4 GPa, respectively. Theoretical predictions of elastic modulus in BMG are based on the expression:

$$M^{-1} = \sum f_i M_i^{-1}, \tag{3}$$

where M stands for any elastic constant, f_i is the atomic percentage of the constituent element and M_i is the elastic modulus of the element [24]. To calculate these values, we took the elemental elastic modulus of Al, Ce, Fe and Cu from Webelements, https://www.webelements.com (accessed 8 July 2016). The results (red triangles in Figure 9) are in quite good agreement for the completely amorphous specimens $0.67 \leq x \leq 0.83$, but for $x = 0.5$ and $x = 1$, the differences are substantial. This outcome is attributed to the occurrence of crystallites, which increase the overall elastic response of the glassy samples, according to the 'rule of volume mixtures' [39]. In the case of $x = 0.5$ and $x = 1$, the crystallites have an elastic modulus and hardness, higher than the surrounding amorphous matrix. In addition, the volume fraction of crystallites is high, and amounts up to 30–40% (determined from the TEM micrographs). A standard deviation for E and H (indicated by the error bars in Figure 9) is higher in the case of samples that are not fully amorphous, i.e. for $x = 0.5$ and 1.

All these indices led to a conclusion that improved mechanical properties are due to crystalline precipitates in the amorphous matrix.

4. Conclusion

We have shown by powder X-ray diffraction that the $(Al_{1-x}Ce_x)_{62}Cu_{25}Fe_{13}$ alloys with composition $0.67 \leq x \leq 0.83$ are completely amorphous. This ratio of constituent elements overlaps with the eutectic compositions in the Al–Ce system. Alloys with more or less Ce, i.e. $x = 0.5$, 0.58, 0.92 and 1 turn to be partially crystallised within an amorphous matrix. The glasses obtained with $x = 0.75$ were chosen for further work, since they show a substantial supercooled liquid region, enabling the fabrication of bulk amorphous alloys via PECS. Variations in sintering temperature around T_x result in different degrees of crystallinity. The samples with $x = 0.75$ that are sintered below the crystallisation temperature of 483 K preserve an amorphous structure, while higher temperatures yield crystalline precipitates that are isostructural with $AlCe_3$. Testing the elastic modulus E and hardness H via nanoindentation reveals that both mechanical properties decrease with increase in the amount of Ce. While Ce-free specimens show $E = 190.7 \pm 6.7$ and $H = 12.8 \pm 0.5$, the composition $x = 0.92$ gives $E = 40.0 \pm 1.0$ GPa and $H = 3.1 \pm 0.2$ GPa, in good agreement with the same characteristics measured in other Ce-based glasses. An increase in E and H occurs at compositions $x = 0.5$ and $x = 1$, both of which contain a significant number of crystallites embedded in the amorphous matrix.

Contributions of the co-authors

LK prepared the samples, JF and PB did the XRD experiments and determined the interference function, SŠ did the TEM analysis, MMK did the DSC experiments and ML did the mechanical testing under the supervision of BM. The study was placed under the supervision of SK in Ljubljana and of JMD in Nancy. LK and JMD wrote the manuscript. All authors agree to co-sign the present article.

Acknowledgements

The present study was performed in the frame of a bilateral French–Slovene collaborative programme financed by CNRS and the Slovenian Research Agency, respectively. B. Skela and B. Ambrožič (Jozef Stefan Institute, Ljubljana) are acknowledged for providing assistance with the experimental part and microstructural analysis, respectively. J. Zavašnik (Jozef Stefan Institute, Ljubljana) is thanked for discussions regarding the principles of TEM analysis.

Disclosure statement

No potential conflict of interest was reported by the authors.

Funding

The work was financed by CNRS and the Slovenian Research Agency.

References

[1] J.F. Sadoc, *Use of regular polytopes for the mathematical description of the order in amorphous structures*, J. Non-Cryst. Solids. 44 (1981), pp. 1–16.
[2] D.R. Nelson and M. Widom, *Symetry, Landau theory and polytope models of glass*, Nucl. Phys. B 240 (1984), pp. 113–139.
[3] J.-M. Dubois, *Topological instability of metallic lattices and glass formation*, J. Less-Common Met. 145 (1988), pp. 309–326.
[4] A.L. Greer, *Confusion by design*, Nature 366 (1993), pp. 303–304.
[5] T. Egami and Y. Waseda, *Atomic size effect on the formability of metallic glasses*, J. Non-Cryst. Solids 64 (1984), pp. 113–134.
[6] K.J. Laws, D.B. Miracle, and M. Ferry, *A predictive structural model for bulk metallic glasses*, Nat. Commun. 6 (2015), pp. 1–10, Article number 8123.
[7] A.I. Akira, *Takeuchi, calculations of mixing enthalpy and mismatch entropy for ternary amorphus alloys*, Mater. Trans. 41 (2000), pp. 1372–1378.
[8] B.-X. Liu, W.L. Johnson, M.-A. Nicolet, and S.S. Lau, *Structural difference rule for amorphous alloy formation by ion mixing*, Appl. Phys. Lett. 42 (1983), pp. 45–47.
[9] J.A. Alonso and S. Simozar, *Prediction of amorphous alloy formation by ion beam mixing*, Solid State Commun. 48 (1983), pp. 765–767.
[10] A. Inoue, T. Shibata, and T. Zhang, *Effect of additional elements on glass transition behavior and glass formation tendency of Zr-Al-Cu-Ni alloys*, Mater. Trans. JIM 36 (1995), pp. 1420–1426.
[11] Z.P. Lu and C.T. Liu, Role of minor alloying additions in formation of bulk metallic glasses: A Review, J. Mater. Sci. 39 (2004), pp. 3965–3974.
[12] X.H. Du, J.C. Huang, C.T. Liu, and Z.P. Lu, *New criterion of glass forming ability for bulk metallic glasses*, J. Appl. Phys. 101 (2007), pp. 1–4.
[13] D. Turnbull, *Under what conditions can a glass be formed*? Contemp. Phys. 10 (1969), pp. 473–488.
[14] R.J. Highmore and A.L. Greer, *Eutectics and the formation of amorphous alloys*, Nature 339 (1989), pp. 363–365.
[15] X. B. Zhang, D.Q. Zhao, M.X. Pan, W.H. Wang, and A.L. Greer, *Amorphous metallic plastic*, Phys. Rev. Lett. 94 (2005), pp. 1–4.
[16] B. Zhang, M.X. Pan, D.Q. Zhao, and W.H. Wang, *'Soft' bulk metallic glasses based on cerium*, Appl. Phys. Lett. 85 (2004), pp. 61–63.
[17] Q. Luo, B. Zhang, D.Q. Zhao, R.J. Wang, M.X. Pan, and W.H. Wang, *Aging and stability of cerium-based bulk metallic glass*, Appl. Phys. Lett. 88 (2006), pp. 4–7.
[18] Z. Bian and A. Inoue, *High glass-forming CeCuFeAlSi bulk metallic glass alloys*, Mater. Sci. Eng. A 449–451 (2007), pp. 114–117.
[19] B.C. Xu, R.J. Xue, and B. Zhang, *Superior glass-forming ability and its correlation with density in Ce-Ga-Cu ternary bulk metallic glasses*, Intermetallics 32 (2013), pp. 1–5.
[20] G. Orveillon, O.N. Senkov, J.L. Soubeyroux, B. Chevalier, and S. Gorsse, Composition selection and glass forming ability of Ce-based amorphous alloys, Adv. Eng. Mater. 9 (2007), pp. 483–486.
[21] Z. Bian and A. Inoue, Ultra-low glass transition temperatures in Ce-based bulk metallic glasses, Mater. Trans. 46 (2005), pp. 1857–1860.
[22] T. Wang, Y.Q. Yang, J.B. Li, and G.H. Rao, *Thermodynamics and structural relaxation in Ce-based bulk metallic glass-forming liquids*, J. Alloys Compd. 509 (2011), pp. 4569–4573.
[23] P. Yu, R.J. Wang, D.Q. Zhao, and H.Y. Bai, *Anomalous temperature dependent elastic moduli of Ce-based bulk metallic glass at low temperatures*, Appl. Phys. Lett. 91 (2007), pp. 1–4.
[24] Y.X. Wei, B. Zhang, R.J. Wang, M.X. Pan, D.Q. Zhao, and W.H. Wang, *Erbium- and cerium-based bulk metallic glasses*, Scr. Mater. 54 (2006), pp. 599–602.
[25] A.-P. Tsai, A. Inoue, and T. Masumoto, *A stable quasicrystal in Al-Cu-Fe system*, Jpn. J. Appl. Phys. 26 (1987), pp. L1505–L1507.
[26] U. Mizutani, H. Sato, M. Inukai, Y. Nishino, and E.S. Zijlstra, *Electrons per atom ratio determination and Hume-Rothery electron concentration rule for P-based polar compounds studied by FLAPW – Fourier calculations*, Inorg. Chem. 54 (2014), pp. 930–946.

[27] D. Wohlleben and J. Röhler, *The valence of cerium in metals (invited)*, J. Appl. Phys. 55 (1984), pp. 1904–1909.
[28] U. Mizutani, Unpublished results, private communication, (2016).
[29] L. Kelhar, J. Ferčič, J.M. Dubois, and S. Kobe, In preparation, n.d.
[30] K.A. Gschneidner and F.W. Calderwood, The Al–Ce (Aluminum–Cerium) system, Bull. Alloy Phase Diagr. 9 (1988), pp. 669–672.
[31] H. Okamoto, Al–Ce (aluminum–cerium), J. Phase Equilib. 19 (1998), pp. 395–396.
[32] S. Sachdev and D.R. Nelson, Theory of the structure factor of metallic glasses, Phys. Rev. Lett. 53 (1984), pp. 1947–1950.
[33] S. Šturm, K.Ž. Rožman, B. Markoli, E. Sarantopoulou, Z. Kollia, A.C. Cefalas, and S. Kobe, *Formation of core-shell and hollow nanospheres through the nanoscale melt-solidification effect in the Sm-Fe(Ta)-N system*, Nanotechnology. 21 (2010), pp. 1–8.
[34] C. Freiburg and B. Grushko, *An Al13Fe4 phase in the Al-Cu-Fe alloy system*, J. Alloys Compd. 210 (1994), pp. 149–152.
[35] I. Felner, *Crystal structures of ternary rare-earth-3d transition metal compounds of the RT6Al6 type*, J. Less Common Met. 72 (1980), pp. 241–249.
[36] F.W. Gayle, *Phase equilibria at 550 ~ in the Al-Cu-Fe system: 50 to 70 at.% AI, 0 to 9 at.% Fe*, J. Phase Equilib. 13 (1992), pp. 619–622.
[37] J.-M. Dubois and E. Belin-Ferré, *Electronic properties and complexity of Al-based complex metallic alloys*, Acta Phys. Pol., A 126 (2014), pp. 453–457.
[38] M.C. Gao, N. Ünlü, G.J. Shiflet, M. Mihalkovic, and M. Widom, *Reassessment of Al-Ce and Al-Nd binary systems supported by critical experiments and first-principles energy calculations*, Metall. Mater. Trans. A 36 (2005), pp. 3269–3279.
[39] D.C. Hofmann, J. Suh, A. Wiest, G. Duan, M. Lind, M.D. Demetriou, and W.L. Johnson, *Designing metallic glass matrix composites with high toughness and tensile ductility*, Nat. Lett. 451 (2008), pp. 1085–1089.

4.1.2 Additional results regarding Ce-based alloys

4.1.2.1 Detailed XRD examination

Penetration depth (PD) of incident X-rays is a function of their intensity and material parameters such as density as well as the corresponding linear attenuation coefficient A explained in Section 2.2 on X-ray diffraction technique. In addition to these parameters, the angle at which the incident X-rays irradiate the sample is vital for PD. The results of PD against different 2θ incident angles are plotted for different x values of $(Al_{1-x}Ce_x)_{62}Fe_{13}Cu_{25}$ alloys in Figure 27a. With higher x=Ce/(Ce+Al) ratio, the density of the alloy increases, leading to more X-rays being attenuated by the material and consequently, PD decreases. It is in the range ≈1-14 μm when 2θ is scanned from 10° to 90° for the alloy designated with x=0.5. When the heavier Ce (compared to Al) is added to the alloy, the attenuation of X-rays elevates. The alloy, marked with x=1 thus features a lower PD of ≈1-9.5 μm, when 2θ is varied from 10° to 90°.

To explore the benefits of known X-ray PD, in conjunction with fixed thickness of the specimens (ribbons of ≈30-50 μm), measurements were conducted on the wheel side (WS) and the free side (FS) of the melt-spun ribbons. The schematic, explaining WS and FS is shown in Figure 13b. Different structures emerge due to different cooling rates on WS and FS. As depicted in Figure 27b, alloys (prepared in powdered form) in the range $0.58 \leq x \leq 0.92$ feature a clean diffraction pattern with a strong diffuse hump at approximately 35° of 2θ. Compositions x=1 (to a minor extent) and especially x=0.5 exhibit several peaks superimposed on top of the main hump. Structural identification of the peaks in specimen x=0.5 indicates a phase isostructural with cubic $Al_{1.2}FeCe_{0.8}$ (PDF number 04-005-2177). XRD patterns of the ribbons measured from their WS (Figure 27c) show no peak in the range $0.58 \leq x \leq 1$. Crystalline reflections, however, are present in the sample denoted with x=0.5, where the same cubic $Al_{1.2}FeCe_{0.8}$ phase can be matched. The absence of crystalline peaks in other compositions can be explained by the fact that WS of the ribbons exhibits a higher cooling rate compared to FS, suppressing the crystallisation. Nevertheless, the removal of heat is not large enough to ensure complete vitrification of WS in the case of specimen x=0.5.

In the measurements of FS (Figure 27d), most of the patterns exhibit weak crystalline reflections. The specimens in the range $0.75 \leq x \leq 1$ have a common peak at 30° and 35° of 2θ, but their structural identification from these two reflections does not yield a viable candidate. Meanwhile, the specimens within $0.58 \leq x \leq 0.67$ display a glassy structure without notable peaks superimposed on top of the glassy hump. Pattern x=0.5, which was found to possess the most intense crystalline reflections on the WS, displays less intense peaks on the FS.

According to the powder XRD measurements and WS and FS XRD measurements, it can be concluded that the glassy state with the least amount of additional crystalline precipitates is obtained in the composition range $0.58 \leq x \leq 0.75$. The latter x ratio coincides with a deep eutectic between Al and Ce, where the liquidus line is much lower compared to the neighbouring compositions. Temperature-stability of the liquid prior to quenching is thus increased, raising the ease of alloy vitrification [49].

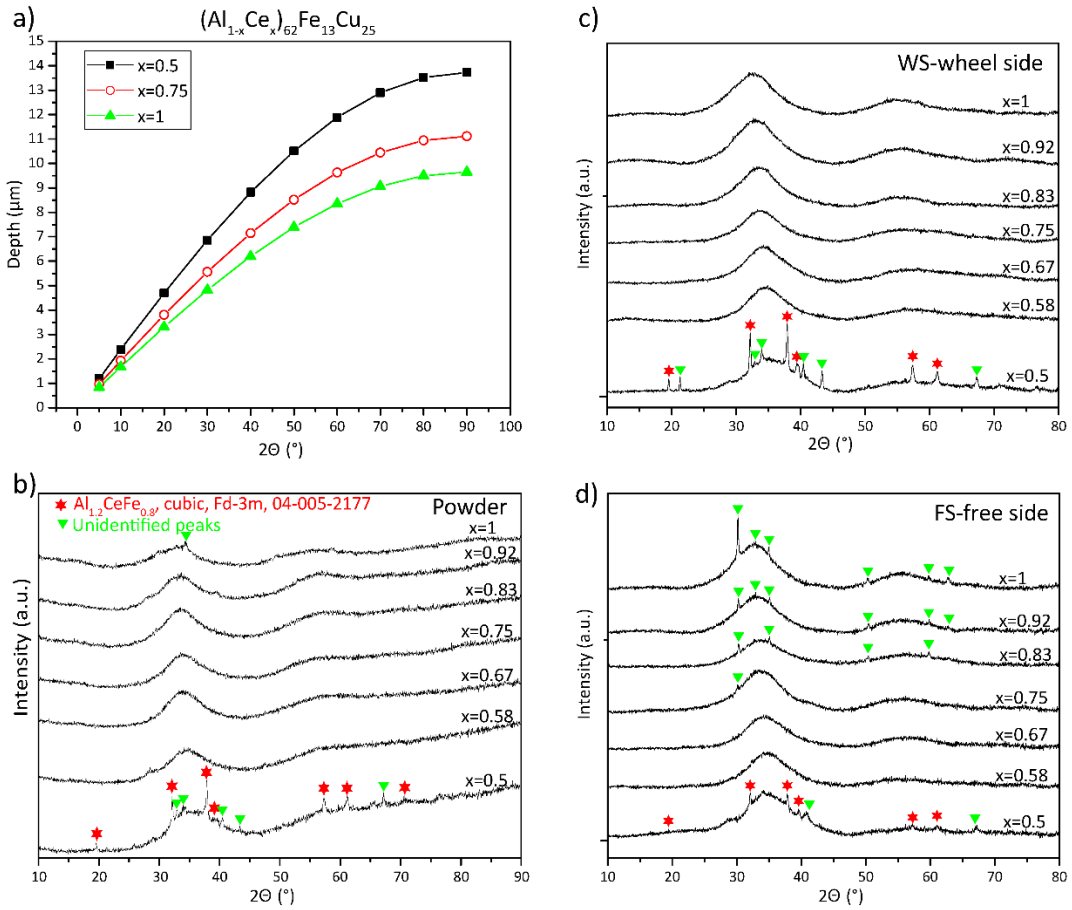

Figure 27: a) Penetration depth of CuK$_\alpha$ X-rays (with wavelength λ=0.15406 nm) against the 2θ angle, for $(Al_{1-x}Ce_x)_{62}Fe_{13}Cu_{25}$ alloys with x=0.5, x=0.75 and x=1. b) XRD patterns of $(Al_{1-x}Ce_x)_{62}Fe_{13}Cu_{25}$ alloys in powder form, whereas $0.5 \leq x \leq 1$. Six-fold red stars indicate the reflections, belonging to the cubic $Al_{1.2}FeCe_{0.8}$ phase (PDF number 04-005-2177). Green flipped triangles indicate the crystalline reflections that could not be indexed. c) XRD patterns of $(Al_{1-x}Ce_x)_{62}Fe_{13}Cu_{25}$ alloys on WS, whereas $0.5 \leq x \leq 1$. d) XRD patterns of $(Al_{1-x}Ce_x)_{62}Fe_{13}Cu_{25}$ alloys on FS, whereas $0.5 \leq x \leq 1$.

4.1.2.2 In-situ synchrotron-light radiation study of Ce-based glass

In order to understand the formation of primary crystallites from the glassy matrix, in-situ synchrotron radiation study was performed on $(Al_{0.25}Ce_{0.75})_{62}Fe_{13}Cu_{25}$ alloy x=0.75. As described in the first article [206], the primary crystallites in this Ce-based MG belong to the hexagonal $AlCe_3$ phase, which grows from a primary glassy matrix and was firstly detected with a laboratory XRD technique.

Synchrotron experiments were conducted at the European Synchrotron Radiation Facility (ESRF) in Grenoble, France, at a Swiss-Norwegian beamline. The samples were prepared by sealing the crushed ribbons in millimetre-sized quartz ampoules and then they were analysed in transmission mode. Diffraction experiment is made of a set of periods, where in the first part (30 s) the detector axis moves clockwise and collects the data according to the given time and step. In the second part (10 s), the axis moves backwards, to its initial position in order to repeat the cycle. Calibration of the apparatus is performed with LaB_6 standard. Radiation with the wavelength λ=0.06973 nm was used and diffraction measurements were performed in the range 5-40° of 2θ and in the temperature range 30-350°C. The heating rate was maintained at 5°C/min.

As seen in Figure 28, the original diffraction pattern at 30°C is predominately glassy. Nevertheless, several crystalline broad peaks appear around 12°, 18°, 25° and 28° of 2θ (Figure 28a), pointing out at crystallites within the glassy matrix. They could, however, not be detected prior to synchrotron light experiments, via laboratory XRD and TEM techniques. Its absence in the XRD patterns is ascribed to a low brilliance of the laboratory XRD instrument. The absence of crystallites in TEM micrographs and SAED patterns is attributed to the local probing nature (compared to the width of the ribbon) of the electron beam, which cannot detect crystalline features if they are present in minute amounts. The reason for the appearance of crystalline broad peaks under synchrotron radiation can be due to crystallisation, induced by the sample preparation with milling of melt-spun ribbons to powder. Because of friction, local heating of the material can occur, and since Ce-based MG with x=0.75 has a low T_x of ≈220°C, this can trigger the crystallisation.

As the temperature elevates, the first peaks that start to grow are the pre-existing ones. The fastest growth is observed for peaks at 12°, 14.5°, 15.5°, 18° and 28° of 2θ, which start to develop at ≈200°C. In Figure 28 they are labelled with inverted red triangles. By structural identification, these reflections can be ascribed to hexagonal $AlCe_3$ phase (PDF number 04-004-840). Another set of reflections, also belonging to $AlCe_3$, starts to emerge at ≈250°C. These peaks are located at 2θ=10°, 18.5°, ≈20°, ≈21°, 23°, 26°, ≈28°, 33°, ≈35° and ≈36°.

Accuracy and precision provided by synchrotron radiation source were able to unravel the emergence of a secondary phase-an information inaccessible via laboratory XRD measurements. In addition to primary $AlCe_3$, the cubic Fe_2Ce phase (ICSD number 657903) was also detected via in-situ experiment. These peaks are marked with green stars in Figure 28 and they are located at 2θ≈9°, ≈18°, ≈22° and ≈31.5°. Since their relative intensity is low, it is assumed that their volume share is low as well. However, they appear from the start in the pattern recorded at 30°C, which means that they are quenched in the ribbon or formed during sample preparation. The most notable peak of Fe_2Ce is the one at ≈18°.

In addition to $AlCe_3$ and Fe_2Ce phases, there are also several crystalline reflections that could not be indexed. These peaks are labelled with a question mark (?) and they are located at ≈8°, ≈11°, 12.5°, ≈17°, ≈20°, 24°, ≈30°, ≈32.5° and ≈38.5°.

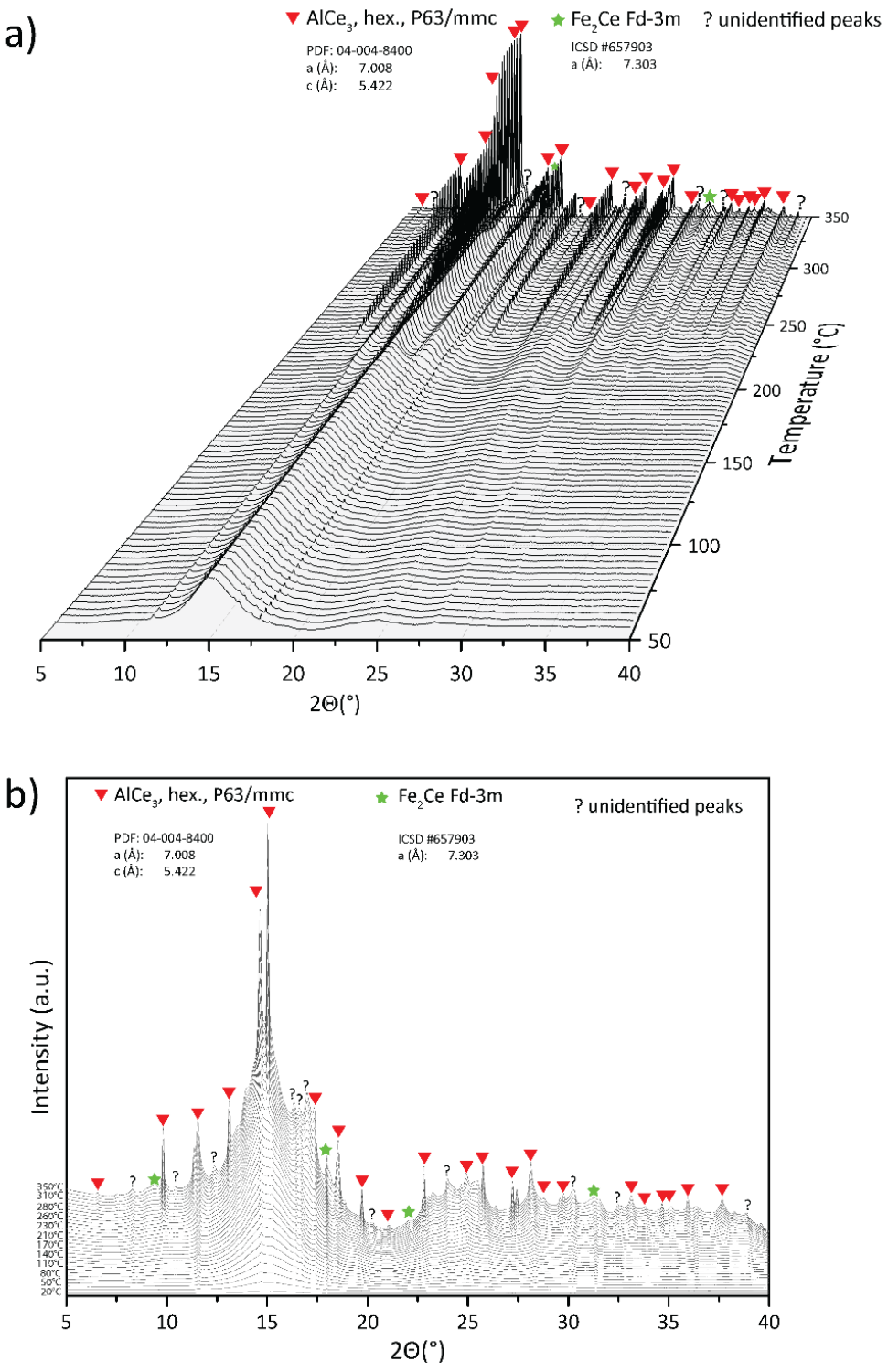

Figure 28: a) Three-dimensional representation of the data obtained with in-situ synchrotron X-ray diffraction (wavelength λ=0.06973 nm), from 5-40° of 2θ and in the temperature range 30-350°C. b) Two-dimensional plot of the selected diffraction patterns, which accurately illustrate the evolution of the structure. The indexed phases of $AlCe_3$, Fe_2Ce and some unidentified reflections are denoted in both a) and b) using the same symbols.

Since $AlCe_3$ is the most widely occurring phase, further quantitative work was pursued to determine its evolution with temperature more accurately. FWHM and I_i (schematically defined in Figure 16) were analysed for a series of 33 selected patterns at different temperatures. The range of 2θ was limited to the glassy hump with $I_{max} \approx 15°$. With a higher temperature, the hump transforms into two separate peaks at ≈14.5° and ≈15.5° of 2θ, ascertained to $AlCe_3$. Figure 29a shows the variation of FWHM for the hump (y-axis on the left side of the diagram) and the two emerging peaks (y-axis on the right side of the diagram). Data indicates that FWHM of the glassy hump (black squares) is kept at the value of 0.48° up to 160°C. It then drops to 0.47° for temperatures between 160-200°C. After that, the hump disappears and is replaced by peaks at ≈14.5° and ≈15.5° of 2θ, which are visualized by red circles and green triangles, respectively. FWHM of the emerging peaks is very large (up to 0.7°) up to 230°C and falls out of scale. In Figure 29b, the data points, which are missing in Figure 29a, are plotted on a larger scale and they are outlined with a dashed black line. The initial increase of the 1st and 2nd peak's FWHM belongs to the transition from glassy to crystalline peak. After 230°C, the two FWHMs feature a subtle decrease, as a consequence of crystal growth. The 1st peak decreases from 0.03° to 0.02° and the 2nd peak decreases from roughly 0.025° to 0.015°. However, there is a discrepancy between the behaviour of the 1st and 2nd peak in the range 300-340°C. The 1st peak exhibits a local maximum in FWHM at ≈320°C, whereas the 2nd peak shows a steady decrease (Figure 29a). The plot of I_i, whose determination is graphically represented in Figure 16b, is shown in Figure 29c and d. I_i of the glassy hump is constant up to ≈160°C, whereas above it starts to decrease gradually. Then, at ≈200°C, the hump evolves into two peaks, resulting in largely different I_i before and after this threshold. The last is plotted in Figure 29d. The emerging 1st and 2nd peak exhibit high values of $\approx 90 \times 10^{-6}$ a.u. (2nd peak) up to ≈230°C, which is shown by the dashed line surrounding the points in Figure 29d. This behaviour in the temperature range 200-220°C of the 2nd peak, is connected with the initial stage of crystallisation. After 230°C, when the growth of crystallites advances, I_i of both 1st and 2nd peak drops to $\approx 1 \times 10^{-6}$ and then increases steadily to $\approx 5 \times 10^{-6}$ a.u. up to 350°C. This result is in accordance with the increase in I_{max}, as seen from Figure 28b. The increment in both I_i and I_{max} indicates a growth of $AlCe_3$ crystalline phase. It is observed that the increase of I_i of the 1st and 2nd peak features a very steep slope from 230°C, and there is no sign of saturation towards 350°C. The available time for crystallisation, given the heating rate of 5°C/min and a temperature range spanning from the emergence of first peaks at 230°C to the final data point at 350°C is 24 min. Still, this time is not sufficient to complete the crystallisation process, which is still ongoing in the last point.

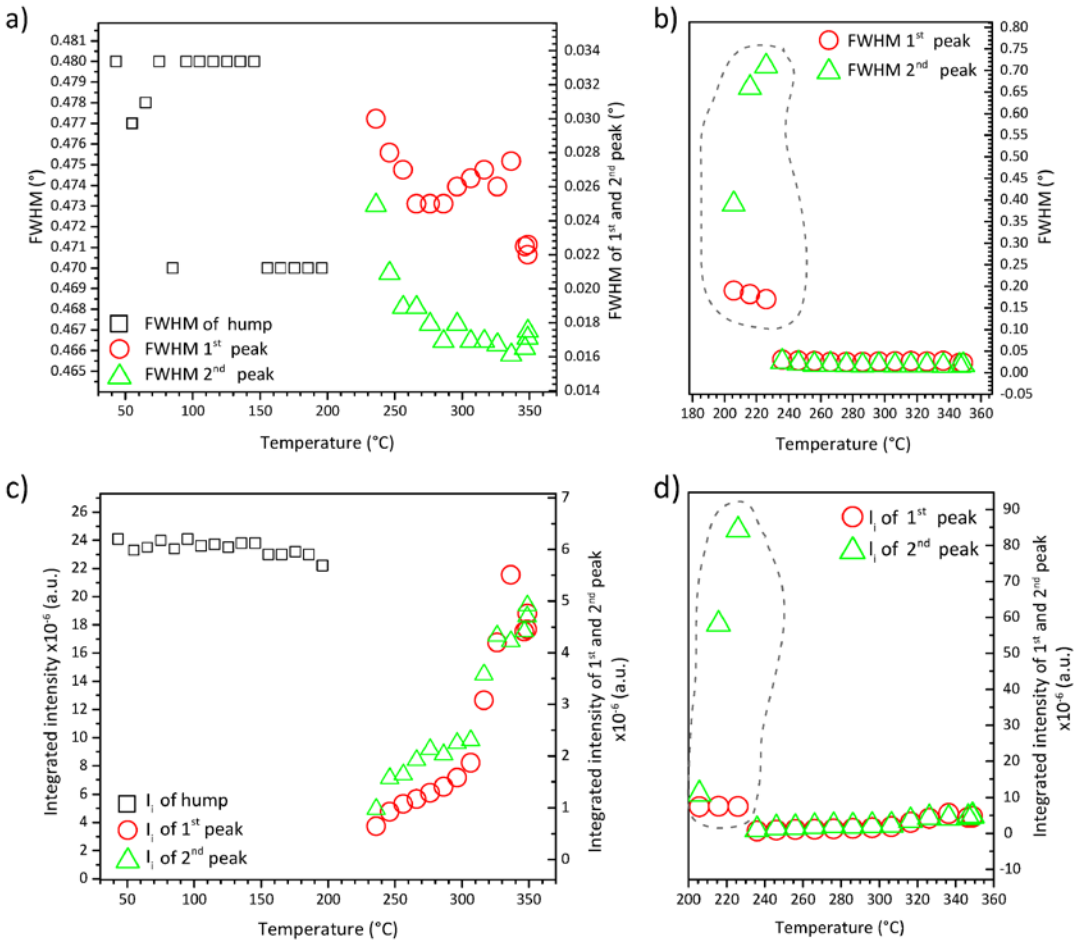

Figure 29: Evolution of the central hump and two crystalline peaks that emerged from it. a) The plot of FWHM. Left-hand side ordinate axis gives FWHM of the hump, while right-hand side gives the FWHM of the 1st and 2nd peak. b) The FWHM of 1st and 2nd peak plotted at a larger scale to visualize all the data. Dashed line surrounds the points, which cannot be observed in part a). c) Evolution of I_i of the hump/peak. Left-hand side ordinate axis gives I_i of the hump, while right-hand side stands for the 1st and 2nd peak. d) I_i of the 1st and 2nd peak, plotted at a larger scale to visualize all the data. Dashed line surrounds the points, which cannot be observed in c).

4.1.2.3 Magnetic properties of Ce-based glasses

Magnetic measurements of Ce-based alloys were conducted using the open-loop VSM method on powder specimens. Magnetic hysteresis loops are demonstrated in Figure 30. Most of the curves exhibit PM behaviour, where magnetisation linearly increases with the external magnetic field. Loops of the specimens x=0.83 and x=0.92 show a slightly S-curved shape. However, the reason for this behaviour is not obvious, moreover because the sample x=1 does not follow this behaviour. From the XRD patterns in Figure 27 it is seen that a similar set of crystalline reflections can be observed in the samples where $0.83 \leq x \leq 1$, which suggests that the FM contribution to the hysteresis loop should continue up to x=1. However, this is not the case. The magnetisation of alloys does not monotonically depend on the content of crystallites nor does it increase linearly with the ratio x. In general it does not vary significantly, for it is kept in the range from 0.3 emu/g to 0.5 emu/g.

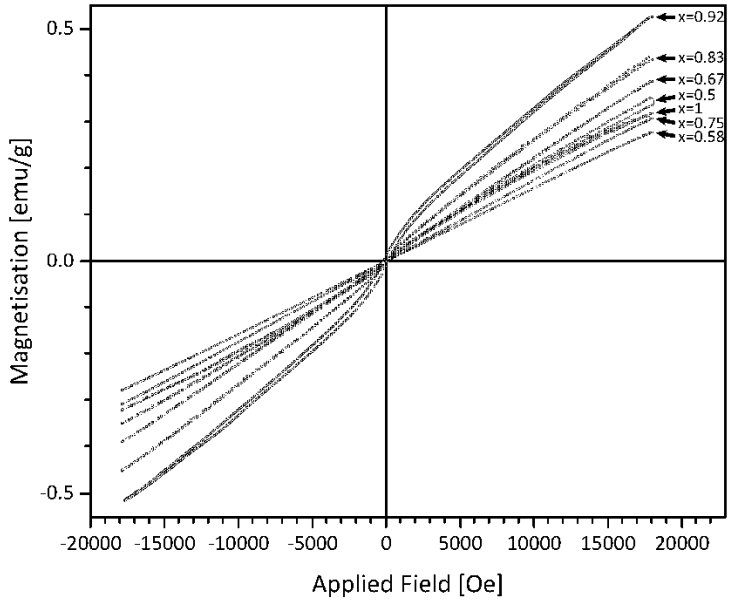

Figure 30: Room temperature VSM measurements of $(Al_{1-x}Ce_x)_{62}Fe_{13}Cu_{25}$ alloys in the range $0.5 \leq x \leq 1$.

Since the quantity of measuring time spent on SQUID apparatus was greatly limited, only one measurement was carried out on the series of Ce-based alloys. The sample with x=0.75 was chosen for this purpose since it is located within the range $0.58 \leq x \leq 0.75$ of good glass formers. The procedure of ZFC-FC measurements was the following. Zero-field cooled (ZFC) curve was obtained by cooling down to 2 K in the absence of an external field, which was followed by a temperature increase up to 300 K and simultaneous data recording. At 300 K the field of 1000 Oe was turned on, the specimen was cooled down to 2 K and the magnetisation was recorded, yielding the field cooled (FC) curve. In Figure 31 the mass susceptibility $\chi_{mass}=dM/dH$ is shown versus temperature T. Its advantage compared to plotting M instead is a clearer representation of phase transitions since it is the first derivative of M. Magnetic behaviour of sample x=0.75 is strongly PM at RT, but with the decrease in temperature, M increases. Critical temperature (T_{cr}) where the PM phase features the most pronounced increase was determined according to the differential method, shown in Figure 31b. First derivative $d\chi_{mass}/dH$ of the FC curve was calculated, where the maximum labels the point (marked with an arrow in Figure 31b) where the slope

is the steepest and it presents a reasonable estimate of T_{cr}. For the Ce-based specimen x=0.75, T_{cr} yielded a value of 212 K. Further down the temperature scale is the point where ZFC and FC curves split. At this point, the ZFC curve exhibits a cusp, while FC curve increases further although with a minor kink at the same abscissa as the cusp. This threshold, where the cusp and the kink appear, is known as the blocking temperature T_b or sometimes also Néel temperature, marking the transition from high-temperature PM phase to low-temperature AFM phase. A kink at T_b should appear in the case of FC curve, but it is very indistinct due to the high field of 1000 Oe, reducing the sharpness of transition. The use of lower field would be advantageous in this respect, but unfortunately, there was not enough time available on the SQUID for this purpose. From ZFC curve, T_b was ascertained to lie at $\approx$118 K.

Below 120 K, a splitting between ZFC and FC appears, whereas the former turns downwards and the latter continues with a similar slope. The cusp-like peak at 120 K and the separation of the ZFC and FC curves are highly reminiscent of spin-glass (SG) behaviour [217]. Unusually wide peak and a steep slope of the FC curve, however, are discrepant with classical spin-glasses, found in dilute alloys [218]. These peculiarities most likely derive from glasses' SRO, influenced strongly by RE atoms that induce random single ion magnetic anisotropy interaction [219]. Solid affirmation of this theory is difficult since SGs and the nature of random anisotropy interactions (RMAs) in MGs are still unsettled questions [219].

Temperature range from 10 K to 2 K features a rapid increase of the FC curve's χ_{mass}. This behaviour is not akin to SG or AFM behaviour. Comparison with low-temperature behaviour of pure Ce indicates that the increase is characteristic of Ce metal itself [98]. Change of the trend in χ_{mass} can also be a consequence of low-temperature PM, stemming from the fundamental behaviour of SRO atomic clusters [220].

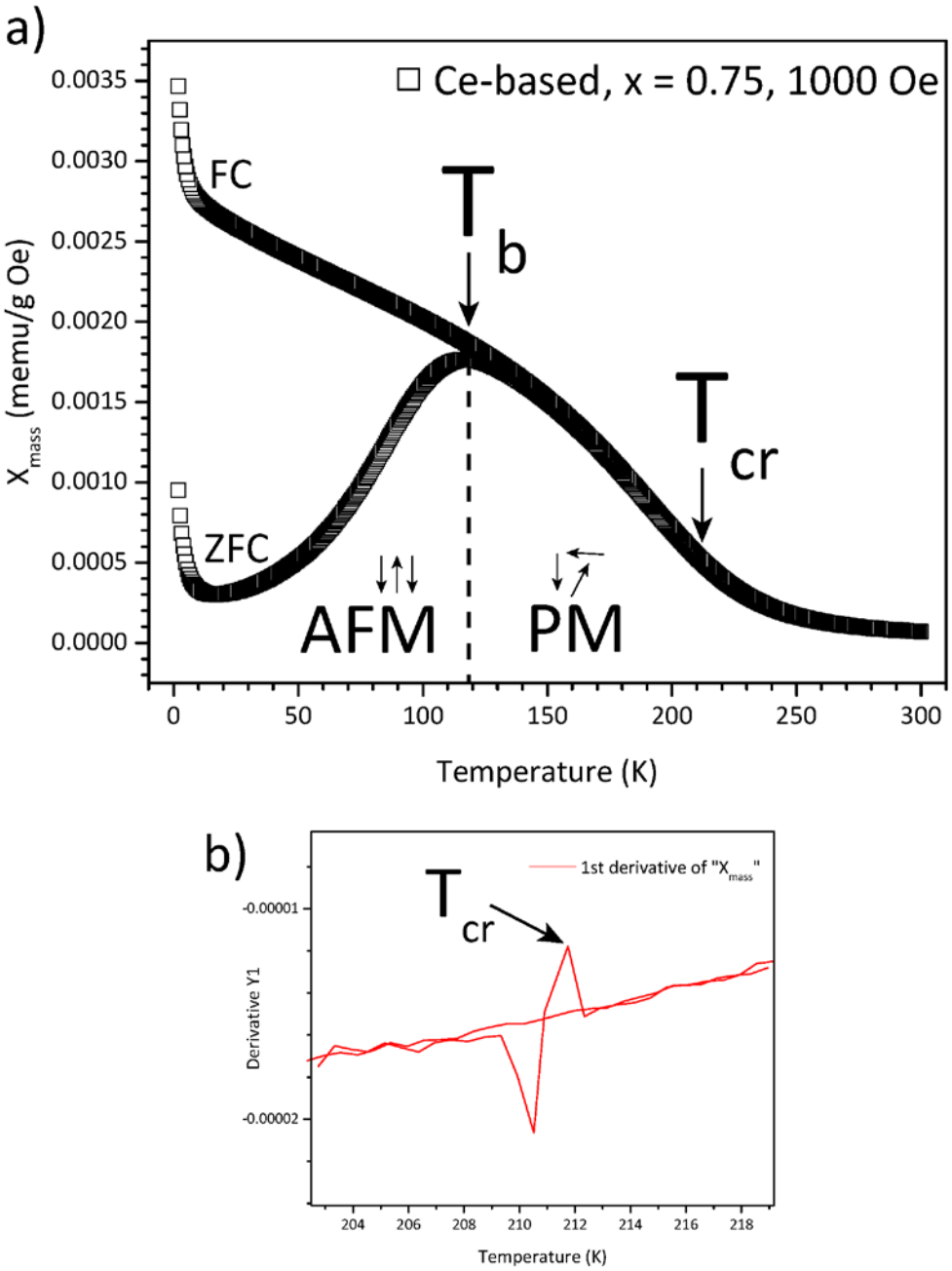

Figure 31: a) ZFC-FC $\chi_{mass}(T)$ curves of Ce-based sample x=0.75 recorded in the magnetic field of 1000 Oe. b) Schematic which shows the plot of the first derivative of χ_{mass} and determination of T_{cr}.

4.1.3 Paper "The role of Fe and Cu additions on the structural, thermal and magnetic properties of amorphous Al-Ce-Fe-Cu alloys"

The succeeding paper, entitled "The role of Fe and Cu additions on the structural, thermal and magnetic properties of amorphous Al-Ce-Fe-Cu alloys" is written by Luka Kelhar, Jana Ferčič, Marjeta Maček-Kržmanc, Janez Zavašnik, Sašo Šturm, Primož Koželj, Spomenka Kobe and Jean-Marie Dubois, and appeared in "Journal of Non-Crystalline Solids", Vol. 483, in 2018 on pages 70-78.

The previous study [206] found that the ratio x=Ce/(Ce+Al)=0.67, corresponding to 20.5 at% Al and 41.5 at% Ce, yields a strong metallic glass. In order for the present study to commence from a strong glass forming composition, the above-mentioned contents of Al and Ce are fixed. Here, the variation of ratio y=Fe/(Fe+Cu) in the series of $Al_{20.5}Ce_{41.5}(Fe_yCu_{1-y})_{38}$ alloys is conducted and it is traced through structure and microstructure analysis, thermal measurements and magnetic properties. A peculiarity, known to influence GFA is immiscibility among constituent elements. In $Al_{20.5}Ce_{41.5}(Fe_yCu_{1-y})_{38}$ alloys, binary pair Fe-Cu is immiscible throughout the composition landscape as well as in solid and liquid state [68], [215].

In the article, it is shown that the additions of Fe in the range $0 \leq y \leq 0.74$ result in alloys with a glassy structure. SRO of the glassy alloy y=0.34 was found to be icosahedral-like, since the ratios $q_2/q_1=1.69$ and $q_3/q_1=2.17$ between the successive humps in I vs. q plot are in close vicinity to those of icosahedral ratios, amounting to $q_2/q_1=1.71$ and $q_3/q_1=2.04$. In contrast, alloys in the range $0.87 \leq y \leq 1$ exhibit a structure made of the glassy matrix and crystalline precipitates.

Thermal analysis shows that T_g, T_x and T_l are lower in the case of Cu-rich alloys. The change of heat flux at T_g (δ) is well in accordance with the formation of strong glasses, providing an original parameter to describe strong MGs. In the case of Cu-rich alloys, a more pronounced δ step correlates with the occurrence of glassy alloys, while for the Fe-rich compositions a minute δ step is connected with the impossibility of hindering crystallisation and occurrence of crystallites.

TEM study shows that Cu-rich alloys are predominately composed of a glassy matrix, but on the nanoscale, they possess trace amounts of CeO_2 crystallites. The latter cannot be observed through X-ray diffraction. These crystallites do not interfere with the glassy matrix on heating.

Measurements of magnetic properties reveal that the magnetisation of the alloys greatly depends on the amount of Fe. Cu-rich alloys in the range $0 \leq y \leq 0.74$ exhibit PM behaviour, while FM is observed for the two Fe-rich compositions.

Magnetic behaviour of Ce-metal is characterised with low-temperature SQUID measurements, which reveal two separate linear regions. Their slopes hint at PM-like behaviour but have a different effective magnetic moment of Ce. In the low-temperature region, effective magnetic moment amounts to 2.2 μ_B, while in the high-temperature region it is 3.0 μ_B. Both magnetic moments slightly deviate from Ce free-ion value of 2.54 μ_B, indicating hybridisation effects. Partial delocalisation of 4f electrons is induced by alloying (3.0 μ_B) but it fluctuates with temperature (2.2 μ_B) as well.

Journal of Non-Crystalline Solids 483 (2018) 70–78

Contents lists available at ScienceDirect

Journal of Non-Crystalline Solids

journal homepage: www.elsevier.com/locate/jnoncrysol

The role of Fe and Cu additions on the structural, thermal and magnetic properties of amorphous Al-Ce-Fe-Cu alloys

Luka Kelhar[a,b,d,*], Jana Ferčič[a,b,d], Marjeta Maček-Kržmanc[a], Janez Zavašnik[a], Sašo Šturm[a,b,d], Primož Koželj[a], Spomenka Kobe[a,b,d], Jean-Marie Dubois[a,c,d]

[a] Jožef Stefan Institute, Jamova cesta 39, 1000 Ljubljana, Slovenia
[b] International Postgraduate School Jožef Stefan, Jamova cesta 39, 1000 Ljubljana, Slovenia
[c] Institut Jean Lamour, UMR 7198 CNRS, Université de Lorraine, 2 Allée André Guinier, BP 50840, 54011 Nancy Cedex, France
[d] International Associated Laboratory PACS 2, CNRS (Centre national de la recherche scientifique) and JSI (Jožef Stefan Institute), Nancy, France

ARTICLE INFO

Keywords:
Metallic glass
Rare earths
Cerium
XRD
DSC
Immiscible metals
Magnetic properties

ABSTRACT

Iron and copper are immiscible elements, but can be combined in the presence of a third element such as aluminium or cerium. We varied the additions of immiscible Fe and Cu (ratio y) in the stoichiometric $Al_{20.5}Ce_{41.5}(Fe_yCu_{1-y})_{38}$ alloys in order to trace their impact on the structure, microstructure, thermal properties and magnetism. By powder X-ray diffraction (PXRD), we found that Fe-rich alloys ($0.87 \leq y \leq 1$) do not completely hinder crystallisation and yield nanocrystalline precipitates. Cu-rich alloys completely vitrify for $0 \leq y \leq 0.74$ and exhibit a characteristic broad hump in PXRD patterns. DSC shows that Cu-rich alloys exhibit a noticeably lower crystallisation temperature T_x of about 510 K, liquidus temperature T_l at approximately 900 K and a more pronounced drop Δ of the heat flux at the glass transition temperature T_g. These criteria indicate that Cu-rich alloys are better glass formers. Transmission electron microscopy (TEM) shows that the specimens with $y = 0$ and $y = 0.34$ are composed of an amorphous matrix with minor impurities of CeO_2 nanocrystals, which can only be observed via transmission electron microscopy. However, these nanocrystals do not interfere with the formation of the glassy phase and are therefore inert. Magnetic measurements show that Fe-rich alloys possess higher magnetisation at maximum field ($M_{max\ H}$), peaking at 3.3 and 3 emu/g for $y = 1$ and $y = 0.87$, respectively. From ferromagnetism in the latter two alloys, the behaviour turns to paramagnetism for $0 \leq y \leq 0.74$. Cryogenic measurements on SQUID show that the sample with $y = 0$ displays two different temperature regions at 2–50 K and 100–300 K. The first one exhibits nearly pure paramagnetic behaviour with $\Theta = -0.7$, while the second one shows a highly negative Weiss constant of $\Theta = -80.6$.

1. Introduction

Formation of metallic glasses (MG) has been under scientific investigation for more than five decades since the pioneering work of Klement, Willens and Duwez [1]. A series of Al-Ce-based MG around the eutectic composition 25:75 in at.%, is interesting due to its unusual physical properties [2–4], and very low glass transition temperature T_g compared to other metallic systems [5]. An intriguing phenomenon is amorphous polymorphism, which manifests with the increase of pressure. Transition from low density amorphous state to high density amorphous state occurs at 2 GPa [6], and can be detected by the shift to higher values of the momentum vector q associated with the maximum diffracted intensity as a result of densification [3]. This effect is ascribed to the delocalization of 4f electrons from 3^+ valence, but only to the extent whereby the energy landscape still remains within the stability range of a glassy structure [3]. A different situation is observed at substantially higher pressures of approximately 25 GPa. Al and Ce containing glassy alloys hereby undergo a devitrification, which results in crystallisation to face-centred cubic $Al_{25}Ce_{75}$ [7]. Pressure-induced delocalization of the 4f electron governs a collapse in the volume of Ce atom [8], which shrinks and thereby its size approaches that of Al. Subsequently, the two metals are brought within the Hume-Rothery limits for substitutional alloy formation [9] and crystalline nucleation occurs. Another peculiarity of Ce based glasses is their thermoplastic behaviour at very low temperatures. Some compositions exhibit a glass transition temperature as low as 80 °C [5,10], with a stable supercooled liquid region (ΔT_x) and with it, the ability of thermoplastic forming. The temperature of glass transition below 100 °C is the lowest among amorphous alloys, and it could turn out as an advantage for fundamental studies or carry significance for future applicative research [11].

* Corresponding author.
E-mail address: luka.kelhar@ijs.si (L. Kelhar).

https://doi.org/10.1016/j.jnoncrysol.2018.01.003
Received 13 November 2017; Received in revised form 28 December 2017; Accepted 1 January 2018
Available online 08 January 2018

In this respect, it has been demonstrated that Ce-based amorphous alloys can be consolidated into centimetre-sized discs via pulsed electric current sintering in ΔT_x region, while still maintaining its glassy structure [12].

The term "immiscibility" can be used to define an effect, where thermodynamic driving forces oppose the intermixing of elements, so that little alloying is possible [13]. Immiscibility of some constitutive elements and its effect on glass formation in a multicomponent glassy alloy is an approach, which is not frequently considered in the literature. Heats of mixing (ΔH) for immiscible systems are positive, which manifests their disability of forming an intermetallic phase. A requirement for glass formation according to the set of empirical rules [14], however, states that ΔH should be negative in order to form strong glasses. Nevertheless, when some immiscible elements are introduced into a multicomponent alloy, these postulations tend to change. Microalloying additions of immiscible Nb to Cu-based glasses [15] provide an evidence that element pairs with positive ΔH in the correct concentration ratio can enhance the formation of glassy structures [15]. This effect is ascribed to a change in the local atomic environment, and is very sensitive to the composition. Fe and Cu exhibit a complete phase separation at room temperature [16], and also in liquid state at 1873 K, where ΔH remains positive with a value of about 10 kJ/mol [17]. Formation of an amorphous structure in binary Fe-Cu was reported via solid state transformation with ion beam mixing [18]. A series of alloys produced via sputter deposition, resulted in an amorphous structure in the ternary alloy of Fe-Cu-Ag as well [19]. Similarly, the combination of immiscible Fe and Cu has an important implication in the formation of aperiodic Al-Cu-Fe quasicrystals [20]. However, a systematic study of multicomponent metallic glasses depicting variable amounts of immiscible Fe and Cu is to the best of our knowledge not present in the literature.

In this work, we fix the concentration ratio $x = Ce/(Ce + Al)$ to 0.67, according to the findings of our previous study [12]. This choice is illustrated in Fig. 1 where we present simultaneously the position q_M of the maximum intensity in reciprocal space of the main diffraction peak, the full width at half maximum (FWHM $= q_R - q_L$, where the indices L and R denote the left and right sides at half maximum intensity of the main peak in q-space) and a measure of the asymmetry of this peak, which is given by $q_B - q_M$, where $q_B = (q_L + q_R)/2$ is the position in q-space of the barycentre of the peak at half maximum. This measure is

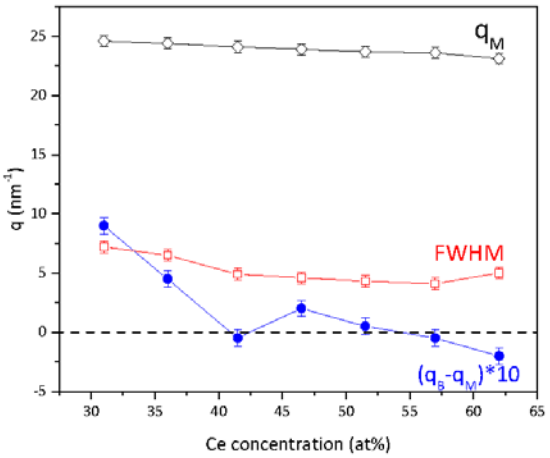

Fig. 1. Variation with Ce concentration of the position in q-space of the maximum diffracted intensity (open lozenges), full width at half-maximum of the most intense diffraction peak (open squares) and symmetry index (solid dots) as defined in text (and multiplied by 10 to make the figure easier to read). Error bars denote the uncertainty of data determination and lines connecting the data points are guide for the eyes only.

equal to 0 for a symmetric peak whereas it yields negative values if the peak is broadened on the side of low q values. It is observed that the position of the peak shifts smoothly towards lower values of q when the concentration of Ce increases from 31 at.% to 62 at.%, which traces the replacement of the smaller aluminium atoms by larger Ce ones. Meanwhile, the peak is broader and significantly less symmetric at low Ce contents (< 40 at.%) whereas it keeps almost unchanged in symmetry from 41.5 at.% and above. This is basically the reason why we have selected this composition or equivalently a ratio $x = 0.67$ for the present study. Henceforth, we start from a composition with good glass forming ability, and extend the investigation to the variation of the $y = Fe/(Fe + Cu)$ ratio. The system $Al_{20.5}Ce_{41.5}(Fe_yCu_{1-y})_{38}$ (at.%) is studied with respect to structure, microstructure, thermal properties and magnetism.

2. Experimental

Specimens were prepared by weighing appropriate amounts of 99.9% Al chunks (Sigma-Aldrich), 99.9% Ce ingot (Aldrich), 99.98% Fe ingot (Pl-KEM) and ≥ 99.9% Cu shots (Sigma-Aldrich). Alloying was performed in an arc-melting furnace (Edmund-Buehler), with multiple turning and melting cycles in order to ensure the alloying of all the pieces. Weight loss after the arc melting never exceeded 1 wt%. Further, the ingots were processed in a single roller melt spinner (Edmund-Buehler). The alloy was inductively melted and ejected onto the surface of a copper cooling wheel, rotating at circumferential speed of 25 m/s. This procedure was accomplished in 700 mbar of 99.999% Ar. For the powder X-ray diffraction (PXRD) characterization, comminuted melt-spun ribbons were used to prepare powder batches by means of crushing in a mortar and manual crushing. PXRD measurements were performed with an Empyrean diffractometer (PANalytical) in Bragg-Brentano geometry, using Cu radiation (wavelength λ = 0.15406 nm). Zero background Si holders were used to load the powdered samples. Analysis of the patterns included background subtraction in order to correct the data for the high background in the case of Cu-rich alloys. Differential scanning calorimetry (DSC) measurements were performed on a Jupiter 449 simultaneous thermal analysis (STA) instrument (Netzsch) using a TG/DSC-cp sample holder and highly conductive Pt crucibles with Al_2O_3 liners. Calibration of temperature and sensitivity was performed with In, Bi, Zn, Al and Au standards. The accuracy in temperature readings is better than 3 K. Specimens for DSC analysis were prepared from crushed ribbons with a mass of ≈ 22 mg stacked into the crucibles to ensure good contact with the bottom of the crucible. Thermal measurements were performed in an inert atmosphere of 99.999% Ar (flow rate 50 ml/min) and in the temperature range from 310 K to 1273 K, with a heating rate of 20 K/min. Magnetic measurements were carried out on a vibrating sample magnetometer (VSM) (MicroSense), up to the maximum applied field of 18 kOe using a step of 100 Oe. We used point-by-point mode, where the field is increased and steadied in one-step, followed by the measurement of magnetisation. Specimens were prepared of crushed ribbons (≈ 100 μg), which were fixed in the plastic holder. For magnetic measurements at cryogenic temperatures, we used a superconducting quantum interference device (SQUID), model MPMS3 (Quantum Design), operated in DC mode. The programme to measure the thermal dependence of magnetisation featured a temperature interval from 2 to 300 K at the applied field of 5 kOe. M(H) loops were measured at a maximum field of 70 kOe and at temperatures of 2 K, 10 K and 100 K. Phase composition and crystallinity of the samples were investigated by transmission electron microscopy (TEM), using a 200 kV JEM-2100 instrument (Jeol), equipped with an energy-dispersive X-ray (EDX) spectrometer (Jeol). Special care was taken to avoid excessive heat evolution during sample preparation: a single ribbon was fixed onto the Mo-support disc with Ag-adhesive paint. Sample prepared this way was further thinned until being transparent for electrons using precision ion polishing system (PIPS, model 691, Gatan). Initially ≈ 30 μm thick

Table 1
Compositions (in at.%) of $Al_{20.5}Ce_{41.5}(Fe_yCu_{1-y})_{38}$ alloys, with y varying from 1 to 0.

y (Fe/(Fe + Cu))	Composition (at.%)
1	$Al_{20.5}Ce_{41.5}Fe_{38}$
0.87	$Al_{20.5}Ce_{41.5}Cu_5Fe_{33}$
0.74	$Al_{20.5}Ce_{41.5}Cu_{10}Fe_{28}$
0.61	$Al_{20.5}Ce_{41.5}Cu_{15}Fe_{23}$
0.47	$Al_{20.5}Ce_{41.5}Cu_{20}Fe_{18}$
0.34	$Al_{20.5}Ce_{41.5}Cu_{25}Fe_{13}$
0.21	$Al_{20.5}Ce_{41.5}Cu_{30}Fe_8$
0.11	$Al_{20.5}Ce_{41.5}Cu_{34}Fe_4$
0	$Al_{20.5}Ce_{41.5}Cu_{38}$

ribbon was bombarded with Ar^+ ions accelerated at 4 keV from top and bottom at an angle of 5°. The latter process reduced the current density and minimized the heating of the sample. The process took several hours to produce a perforation.

3. Results

3.1. Powder X-ray diffraction (PXRD)

To investigate the influence of the y ratio on the structure as well as on the thermal and magnetic properties, we prepared a series of alloys $Al_{20.5}Ce_{41.5}(Fe_yCu_{1-y})_{38}$ with y being varied between 1 and 0. Table 1 reports the values of y and the corresponding nominal compositions (in at.%) of the studied alloys. Results of the PXRD measurements are shown in Fig. 2. For a better comparison between the patterns, they were subjected to background subtraction.

The first indication of an amorphous structure is a strong, diffuse hump, which is present in all the specimens. Cu-rich samples ($0 \le y \le 0.34$) exhibit a symmetric amorphous hump whose barycentre varies from $2\Theta = 35°$ to $2\Theta = 34°$. Increase of y to the value of 0.61 and beyond causes the emergence of an additional broad hump at $2\Theta = 43$–$44°$. When $y = 0.61$ and $y = 0.74$, there is a distinct appearance of a third diffuse hump at $2\Theta = 68°$. The development of these additional peaks suggests a change in the local atomic environment, and the appearance of medium range order, spanning beyond the first neighbours [21]. In the partially crystalline samples, $y = 0.87$ and $y = 1$, amorphous halos present a baseline for several sharply defined Bragg peaks, which superimpose on the top. None of the patterns from

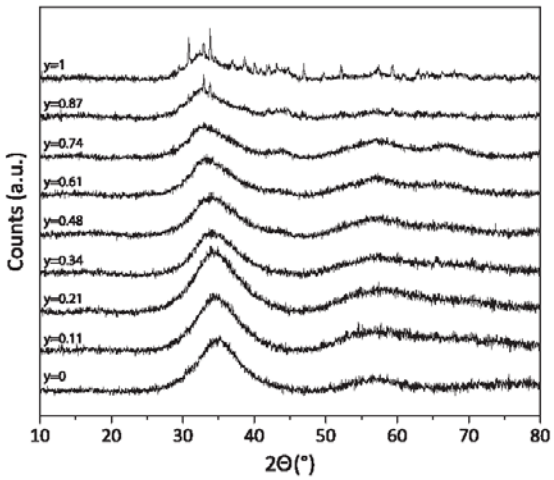

Fig. 2. PXRD patterns of $Al_{20.5}Ce_{41.5}(Fe_yCu_{1-y})_{38}$ alloys, with y varying from 1 to 0.

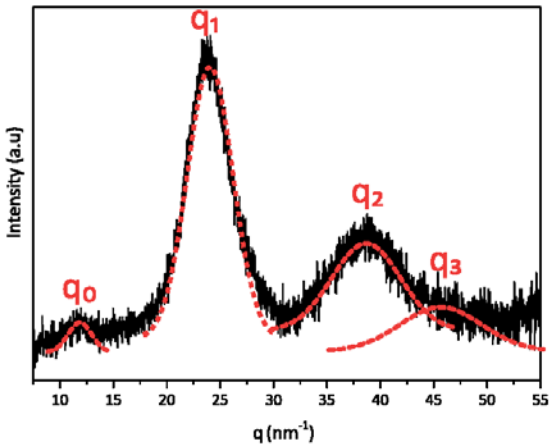

Fig. 3. PXRD pattern of the specimen y = 0.34 in q space. Doted red lines represent Gaussian fits of the observed humps with respective maximum intensity at positions q_0, q_1, q_2, and q_3. (For interpretation of the references to color in this figure legend, the reader is referred to the web version of this article.)

PDF4 + database can be fitted with the observed peaks, however energy dispersive X-ray spectroscopy (EDS) performed with a scanning electron microscope (not shown here), suggests that the crystallites stoichiometry is approximately $Al_{20}Ce_{25}Fe_{55}$. Throughout the composition landscape, the position of the strongest amorphous hump varies from $2\theta = 33°$ (for sample y = 1) to $2\theta = 35°$ (for sample y = 0). The shift correlates with the change of the chemical composition of the amorphous phase. Namely, as the alloy composition varies from Fe- to Cu-rich, the local atomic environment in the glass changes. Additions of Cu shift the position of the strongest amorphous hump towards higher 2Θ angles or lower interatomic d values. This means that the average interatomic distance in Cu-rich alloys is lower than the average interatomic distance in Fe-rich alloys.

The broad humps in the amorphous PXRD pattern for y = 0.34, (shown in Fig. 3) are labelled hereafter q_0, q_1, q_2, and q_3, respectively, along the q axis. Values of q were obtained with a conversion from 2Θ space via the momentum transfer function $q_i = 4\pi\sin\Theta_i / \lambda$. A pre-peak is located at $q_0 = 12\ nm^{-1}$, the main peak at $q_1 = 23\ nm^{-1}$, and the two following peaks at $q_2 = 39\ nm^{-1}$ and $q_3 = 50\ nm^{-1}$. The ratios between the successive positions of the peaks in reciprocal space, are $q_0/q_1 = 0.52$, $q_2/q_1 = 1.69$ and $q_3/q_1 = 2.17$. The ratio between positions of the most intense humps $q_2/q_1 = 1.69$ and $q_3/q_1 = 2.17$ are found in close vicinity of the ratios expected for icosahedral ordering $q_2/q_1 = 1.71$ and $q_3/q_1 = 2.04$ which are predicted according to the work of Sachdev and Nelson [22]. These findings point out the predominance of icosahedral short range order in those glasses, which is not surprising, since it has been previously found that RE-containing metallic glasses exhibit icosahedral ordering without long range periodicity [23]. Moreover, quasicrystals with long range order, albeit aperiodic, have been found in RE-containing binary [24] and higher-component systems [25].

3.2. Transmission electron microscopy (TEM) studies

The study of the present metallic glasses via PXRD reveals that some specimens contain crystallites within the amorphous matrix. For a definite determination of the microstructure, however, it is important to have information on the level of atoms or atomic clusters. With TEM, we investigated few representative samples, whose amorphous structure cannot be confirmed solely via PXRD. Study was performed on ternary $Al_{20.5}Ce_{41.5}Cu_{38}$ (y = 0) and quaternary $Al_{20.5}Ce_{41.5}Cu_{25}Fe_{13}$

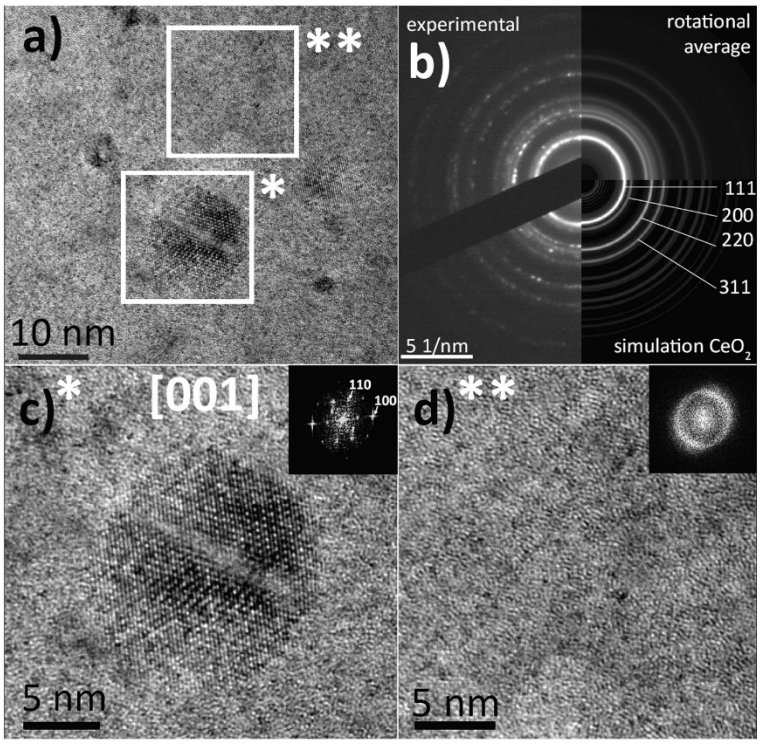

Fig. 4. TEM investigation of the sample y = 0. a) TEM micrograph with marked squares representing the areas * and **. b) Combined SAED pattern of the experimental part (left half), the rotational average [30] (upper-right section) and simulated SAED pattern (bottom-right) of cubic CeO_2 (PDF#: 00-004-0593) structure. c) Area with a crystallite of CeO_2, marked with * in part a. Square brackets outline the view-plane and the inset in the upper right part shows FFT of the crystallite, with labelled lattice planes. d) Amorphous matrix, which corresponds to the square area ** in part a. Inset in the upper right corresponds to the FFT of the amorphous matrix.

(y = 0.34) specimens.

We found that the microstructure of quaternary y = 0.34 specimen is very similar, when compared to the ternary y = 0 specimen. Both of them exhibit a microstructure with crystallites embedded in the amorphous matrix. Structural identification of the crystallites indicates that they match the same crystalline phase.

The TEM micrograph (Fig. 4a) of sample y = 0 shows regions with nanocrystals embedded into the amorphous matrix. As we explain below, we identify these particles to be cubic CeO_2 oxide particles of nanometric size. To determine the overall content of CeO_2 particles, we used the ImageJ software [26] and performed the analysis on different parts of the melt-spun ribbon. Distribution of the crystallites in the melt-spun ribbon is non-homogeneous, although the difference cannot be ascribed to the wheel or off-wheel side of the ribbon. The overall average volume ratio of the crystallites is ≈ 5–6 vol%, while their mean particle size is within the range of 5–10 nm. Both of these parameters influence the sensitivity to detect CeO_2 crystallites, such, that it falls below the detection threshold of the powder diffraction technique. This is manifested by the lack of CeO_2 crystalline reflections in the series of Cu-rich ($0 \leq y \leq 0.34$) PXRD patterns in Fig. 2.

Identification of the CeO_2 particles is based on a representative selected area diffraction pattern (SAED) that was acquired from a region with higher density of nanocrystals to increase the signal-to-noise ratio while acquiring diffraction patterns. In Fig. 4b, the experimental SAED, (left half of the figure), is compared with the rotational average (upper right part) used for de-noising of the experimental spectra, in order to increase the characteristic information originating only from the diffraction rings. Broad diffuse rings in the background of the experimental SAED pattern originate from the electrons scattered in the amorphous matrix, while additional sharp diffraction rings correspond to the electrons scattered from the crystalline lattice of nanocrystallites. Diffraction rings are compared with the simulated pattern of cubic CeO_2 phase, located in the bottom right section of the figure. Four of the strongest crystalline planes of the simulated CeO_2 pattern are marked in the figure. Structural identification of the crystallographic reflections yields a good match with cubic CeO_2 phase, since four of the strongest reflections of the planes (111) with experimental interplanar distance d = 0.30 nm, (200) with d = 0.27 nm, (220) with d = 0.19 nm and (311) with d = 0.16 nm are in good agreement with the literature data [27]. Deviation of the experimental data is within the relative error of ± 3% compared to the reported d-values. First, crystallites morphology features faceted edges, which indicate well-crystallised particles that are less likely to develop during rapid solidification. Secondly, their homogeneous size distribution and the lack of any distinct correlation between the quantities of crystallites on the wheel or off-wheel side of the ribbon, imply that the crystallisation of CeO_2 is not governed by the rapid extraction of heat. High-magnification TEM micrograph of CeO_2 crystallite labelled with * in Fig. 4a, is shown in more detail in Fig. 4c. Inset of the same figure shows the fast Fourier transform (FFT) analysis. Via this procedure, we confirm that the crystallite exhibits lattice reflections and, with it, long-range order. Lattice planes in the FFT inset correspond to (110) and (100) planes and the crystallite view-plane was calculated to be [001]. In Fig. 4d, we show a high-magnification TEM micrograph depicting the amorphous matrix, that corresponds to an area labelled with ** in Fig. 4a. A broad diffuse ring in the inset of the figure (FFT) confirms the amorphous structure of this specimen area. The lack of any long-range order is visualized on the micrograph via random positions of the atomic species, which pack in short range order configurations.

The occurrence of CeO_2 crystallites in both y = 0 and y = 0.34 samples is due to the strong affinity of Ce-based alloys towards oxidation. In melt spinning, we use radio frequency (RF) heating to melt and vigorously stir the alloy [28] before being ejected onto the surface of cooling wheel. RF stirring disperses the CeO_2 oxide particles throughout

the metallic melt. In addition, when melt impinges onto the surface of the cooling wheel, flow of the liquid is not laminar, but heavily turbulent [29]. This aids in mixing the particles and the remaining liquid at the front of the solid ribbon and results in more or a less random dispersion of the solid particles with no tendency to the occurrence of crystallites on the wheel or off-wheel side of the Cu-cooling wheel.

Approximately 1 at.% of Ce from the amorphous matrix was consumed for the formation of CeO_2 nanocrystals, given that their share is 5 vol%. This does not greatly change the composition of the amorphous phase nor does it hinder the formation of the glass upon solidification. We find that the behaviour of embedded CeO_2 particles in the amorphous matrix is inert at room temperature and that they are stable at the temperature of melt quenching. If crystallisation would be nucleated on those crystals during melt spinning, the crystallites would grow differently upon quenching according to the cooling rate experienced locally. Therefore, we would observe different quantities of crystallised material on the wheel and off-wheel sides of the ribbon, which is not the case. The microstructure of sample y = 0 is therefore a two-component system, whereas there is no mutual influence between the oxide crystalline particles and the metallic amorphous matrix.

3.3. Thermal analysis

In Fig. 5b.

Fig. 5 a) Schematics, which show the determination of the characteristic temperatures. b) DSC records of the $Al_{20.5}Ce_{41.5}(Fe_yCu_{1-y})_{38}$ alloys, with y varying from 1 to 0. Zoomed-in part on the right shows the alloys with large change in Δ. c) Plot of Δ vs. y, the experimental data are shown by the red squares and the fit is represented with a black solid line., thermal analysis measurements are displayed for the temperature region from 310 K to 1273 K. Characteristic temperatures for glass transition T_g, crystallisation T_x, melting T_m, and onset of liquidus state T_l were determined according to Fig. 5a. These temperatures, along with the calculated glass forming parameters of glass devitrification ability GDA, reduced glass temperature T_{rg} and width of the supercooled liquid region ΔT_x are plotted in Fig. 6. (For interpretation of the references to color in this figure legend, the reader is referred to the web version of this article.)

Fig. 5c shows the qualitative assessment of T_g and its dependence on composition (y values). T_g of the given series of alloys decreases with the addition of Fe. On the other hand, it should be noted that the baseline signal change at T_g of Fe-rich samples is much less pronounced

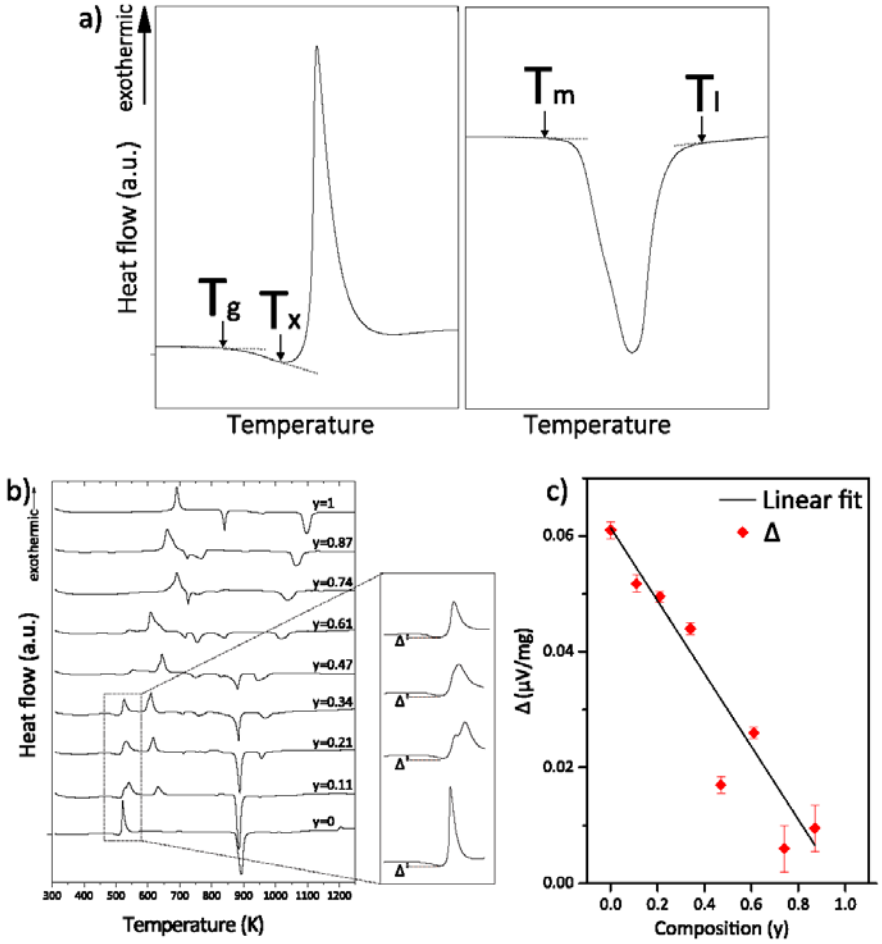

Fig. 5. a) Schematics, which show the determination of the characteristic temperatures. b) DSC records of the $Al_{20.5}Ce_{41.5}(Fe_yCu_{1-y})_{38}$ alloys, with y varying from 1 to 0. Zoomed-in part on the right shows the alloys with large change in Δ. c) Plot of Δ vs. y, the experimental data are shown by the red squares and the fit is represented with a black solid line.

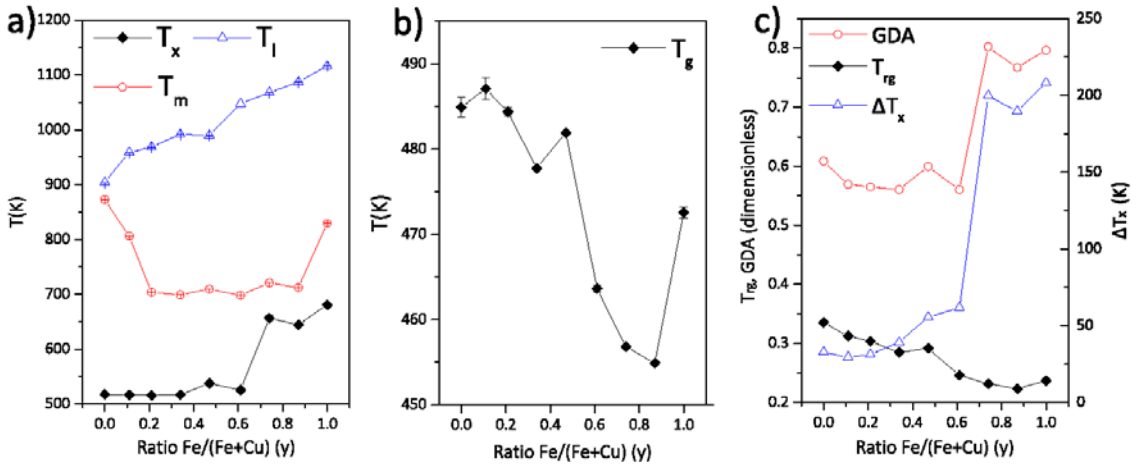

Fig. 6. Plots of a) T_x, T_m, T_l temperatures, b) T_g temperature and c) GDA, T_{rg} and ΔT_x criterions as functions of the ratio y. Error bars are significant in the case of T_g, for the other parameters they are within the size of the data point. Lines connecting the data points are guides for the eyes only.

than that of Cu-rich samples. In this manner, it is useful to show the change Δ of the heat flux at T_g against the sample composition, which is plotted in Fig. 5c. Schematics of the determination of Δ are shown in the zoomed-in part of Fig. 5b. Error bars reflect the uncertainty of finding the minimum and maximum of the baseline around T_g, and they correspond to approximately 2%. These results provide an indirect measurement of the change in specific heat. Direct determination of the latter was not possible, because to this end, the alloys would have to be measured in Pt-crucibles, which would cause a reaction between sample and crucible. The sharpness of Δ step decreases with higher additions of Fe, and for the specimen $y = 1$, this change is so minute that it cannot be separated from the baseline. Fit of the experimental data was performed with a linear function, and it offers a good match for the compositions that fall within the range $0 \leq y \leq 0.34$. For higher concentrations of Fe, T_g becomes more difficult to determine because the signal is much less pronounced. Consequently, the uncertainty increases, and this is reflected in larger deviations from linearity for $0.47 \leq y \leq 1$. The proposed thermal analysis suggests different amounts of heat needed for the transition from solid glass to supercooled liquid state. This difference is clearly introduced with the change in composition, since Cu-rich alloys exhibit larger Δ compared to Fe-rich alloys. The latter suggests that Cu-rich alloys are trapped in a more stable amorphous state, which is supported also by the complementary findings with PXRD and TEM. The complete absence of T_g at $y = 1$ indicates that the crystallisation occurs directly from the solid amorphous state, without a transition to supercooled liquid state, i.e. is a growth process from already existing crystal nuclei.

With increasing the amount of Cu, the crystallisation temperature T_x decreases. T_x exhibits a pronounced jump between $y = 0.61$ and $y = 0.74$. For the Cu-rich compositions $0 \leq y \leq 0.34$, (Fig. 5b), it settles at ≈ 510 K. Specimens with $0.11 \leq y \leq 0.61$, exhibit a T_x of around 500–550 K, while having at least two crystallisation peaks. In the case when $0.74 \leq y \leq 1$, crystallisation is evidenced by a pronounced single peak. With higher addition of Fe in the range $0.74 \leq y \leq 0.87$, this peak is convoluted to at least two components. The complex sequence of exothermic peaks indicates the existence of multiple crystallisation phases and a non-trivial crystallisation sequence of the quaternary amorphous alloys. A clear difference between the ternary alloys $y = 0$ and $y = 1$ and the quaternary compositions in-between, can be observed from the number of exothermic crystallisation peaks. The former two samples only exhibit a single crystallisation peak, whereas quaternary alloys $0.11 \leq y \leq 0.87$ exhibit at least two peaks.

Melting temperature T_m exhibits maximum values of 870 K and 820 K for the ternary compositions of $y = 0$ and $y = 1$, respectively. For the intermediate quaternary compositions, T_m is around 700–720 K, as depicted in Fig. 6a. An exception from this trend is the Cu-rich $y = 0.11$ sample, which shows a T_m of ≈ 800 K. The pronounced endothermal peak around 890 K is always present when $0 \leq y \leq 0.48$, but tends to be less pronounced with higher additions of Fe, until it totally disappears at $y = 0.61$. Liquidus temperature T_l features the steadiest variation of all the characteristic temperatures. It increases almost linearly with the increasing y values, from 900 K for $y = 0$ to 1110 K for $y = 1$.

To evaluate the amorphousness of the alloys, we show in Fig. 6c plots of the glass devitrification ability (GDA), reduced glass transition (T_{rg}) and width of supercooled liquid region (ΔT_x), which we all define below. It should be mentioned that GDA was determined by the characteristic temperatures given by differential scanning calorimetry (DSC). On the other hand, glass-forming ability (GFA) exhibits a tendency of vitrification upon cooling, whereas GDA points to the ability of the glass to resist crystallisation upon heating. In the present study, we have thus assumed that both GDA and GFA are identical [31], which simplifies the relations in order to postulate the following equation:

$$\mathrm{GDA} \equiv \mathrm{GFA} = (2T_x - T_g)/T_l, \tag{1}$$

Additionally, T_{rg} and ΔT_x were implemented to describe the tendency for glass formation by the following equations [32,14]:

$$T_{rg} = T_g/T_l \tag{2}$$

$$\Delta T_x = T_x - T_g \tag{3}$$

Coefficient T_{rg} features a steady decrease with higher y values (Fig. 6c), spanning from 0.34 for $y = 0$, to 0.23 for $y = 1$. This can be an indicator of a decrease in the tendency to form a glass. The lowest value is reached when the amorphous alloys exhibit crystalline peaks (near $y = 1$). The GDA on the other hand exhibits a more diverse behaviour. It is quite stable for $0 \leq y \leq 0.61$, ranging between 0.4 and 0.45. Then, it increases to around 0.7–0.8 in the range $0.74 \leq y \leq 1$. This jump in GDA is in line with the appearance of sharp diffraction peaks in the PXRD pattern when $y \geq 0.87$. With lowering of y, T_g is increasing while T_x decreases. Result of these variations is a greater difference in the coefficient ΔT_x, which marks the temperature interval between the glass transition and crystallisation. ΔT_x features a step-like

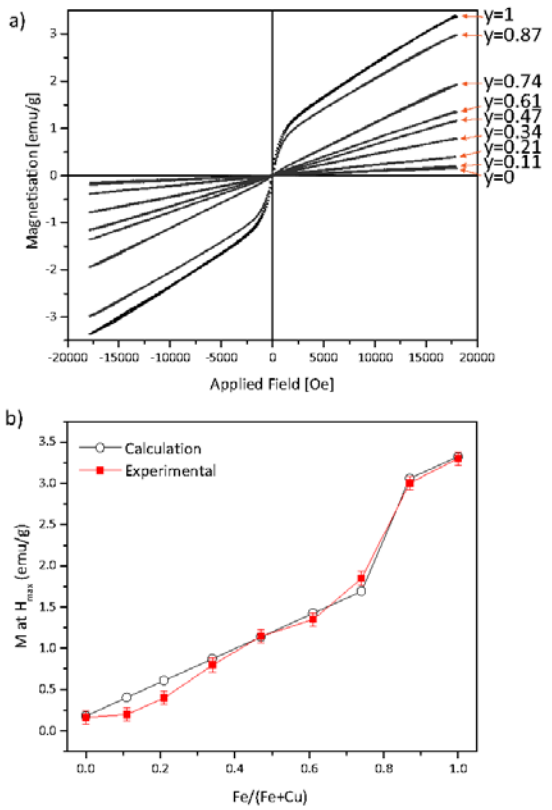

Fig. 7. a) Solid squares: M(H) measurements of studied alloys showing the magnetisation in dependence of the applied field. b) Magnetisation at the maximum field ($M_{max\ H}$) vs. Fe/(Fe + Cu) content. Solid squares are experimental data points and open dots represent the magnetization calculated using Eq. (4). Solid lines guide the eye.

increase, (Fig. 6c) when $0.74 \leq y \leq 1$. Behaviour of ΔT_x is very similar to the GDA in the sense that it features a pronounced jump in the given range. Discontinuous change in ΔT_x can be correlated with the pronounced occurrence of crystallites in the amorphous matrix, as it is visible from the PXRD patterns.

3.4. Magnetic properties

Magnetic hysteresis loops in Fig. 7a show the series of alloys within the $0 \leq y \leq 1$ range. First, it is evident that the samples $y = 0.87$ and $y = 1$ exhibit a ferromagnetic response, which greatly differs from that of the rest of the specimens. In the first part of the curve, for the fields between 18 kOe and 3 kOe, these two samples exhibit a paramagnetic behaviour, where magnetisation (M) linearly increases with the field (H). This is ascribed to the magnetic response of the amorphous matrix. Linear, Curie-Weiss dependence of M(H) is not unusual for an amorphous alloy based on rare earth [33]. The second part, which characterises a ferromagnetic contribution, occurs in the range 3 kOe to − 3 kOe. This effect can be ascribed to the crystalline precipitates, which are also observed on the PXRD patterns in Fig. 2. As we state in the PXRD section, the crystallites in $y = 1$ contain approximately 55 at. % of Fe, which explains the ferromagnetic behaviour of these two M(H) curves. Owing to these crystallites, samples $y = 1$ and $y = 0.87$ show an increase in magnetisation at maximum external field ($M_{max\ H}$), which deviates from linearity as shown in Fig. 7b. $M_{max\ H}$ is equal to 3.3 and 3 emu/g for $y = 1$ and $y = 0.87$, respectively. Hysteresis loops of the samples where $0 \leq y \leq 0.74$, show a paramagnetic response with magnetisation linearly following field according to Curie-Weiss law. A structure exhibiting amorphous nature (in Fig. 2), is thus in line with paramagnetism. The $M_{max\ H}$ of these amorphous specimens linearly decreases with lower concentration of Fe. This change is plotted in Fig. 7b. Here, it is visible that net magnetisation of the amorphous alloys is predominately dependent on the variation of Fe content.

Whereas the Al and Ce contents are invariant, it is interesting to see how magnetization evolves with increasing Fe concentration. Due to its 3d electrons, Fe carries a net magnetic moment, which may be altered by its neighbourhood in an alloy if chemical bonding, more specifically hybridization, takes place. To see to which extent the magnetism of Fe is responding to composition changes in our alloys, we have first measured M(H) of each constituent in its allotropic form at room temperature. $M_{max\ H}$ of the elements at 18 kOe yielded values of 0.08, 0.03 and 0.37 emu/g for paramagnetic fcc Al, fcc Cu, and close-packed Ce. The value of $M_{max\ H}$ for ferromagnetic bcc Fe, however, is nearly three orders of magnitude higher than that of Ce, amounting to ≈ 200 emu/g. The change in $M_{max\ H}$ in the paramagnetic state cannot be accounted for by such a high value of the magnetization of iron. Therefore, we assume that $M_{max\ H}$ as a function of y is given by a concentration weighted average of the $M_{max\ H}$ values measured for the Al, Cu and Ce elemental constituents, one fitted for Fe in the glass and an effective magnetization of the impurity crystals formed at high y:

$$M_{max\,H\ calculated} = \sum_{i=1}^{4} x_i m_i + z m_{Al_{20}Ce_{25}Fe_{55}} \quad (4)$$

where x_i denotes the concentration in constituent i and m_i its contribution to $M_{max\ H}$ and z is the weight fraction of $Al_{20}Ce_{25}Fe_{55}$ crystals that are ferromagnetic and contribute for a net magnetization $m_{Al20Ce25Fe55} = 0.2 \times 0.08 + 0.25 \times 0.37 + 0.55 \times 200 = 110$ emu/g, assuming for simplicity that the moment carried by each species is identical to the one in the pure metal.

Sample $y = 0$ ($Al_{20.5}Ce_{41.5}Cu_{38}$) does not contain any Fe, and exhibits a value of $M_{max\ H}$ of 0.16 emu/g, in very good correspondence with its composition. Introducing iron leads first to an almost linear increase of $M_{max\ H}$, roughly in proportion to the Fe/(Fe + Cu) content until a significant increase of $M_{max\ H}$ is observed at $y = 0.87$ and 1. The two later data points fit with the ferromagnetic behaviour of those samples already observed in Fig. 7a. They sign the formation of a very small amount of ferromagnetic $Al_{20}Ce_{25}Fe_{55}$. Assuming that the contribution of Al, Fe and Ce is identical to that found in the pure elements gives an approximate amount of $z = 1$ wt% for those crystals in the samples with $y = 0.87$ and 1 (Fig. 7b). At lower Fe-contents, the $M_{max\ H}$ follows the one expected from Ce contributing 0.37, Al 0.08, Cu 0.03 emu/g and Fe contributing only 5.5 emu/g. Such a low value is consistent with a complete filling of the 3d-band due to hybridization effects [34].

In order to describe the magnetic behaviour at cryogenic temperatures we conducted magnetisation vs. temperature M(T) measurements on the sample with $y = 0$, using SQUID. The plot shown in Fig. 8a depicts the inverse susceptibility ($1/\chi$) vs. temperature (T) resulting from the fc (field cooled) measurement. In order to describe the observed behaviour in terms of the Curie C and Weiss Θ constants appearing in the Curie-Weiss law: $1/\chi = (T - \Theta) / C$, we distinguish between the two linear-dependence regions: 2–50 K and 100–300 K. A linear fit was ascribed to both temperature ranges shown with the black solid lines in Fig. 8a. Θ was retrieved from the intersection of the linear fit with the x-axis. For a correct calculation, C was converted from mass to molar units. The specimen exhibits a paramagnetic behaviour in both temperature regions, with a monotonic increase in magnetisation down to the temperature of ≈ 50 K. In the range from 50 K to 2 K, magnetisation rapidly increases, from 0.4 emu/g to 5 emu/g, respectively. C is related to the effective magnetic moment of Ce atoms (μ_{eff}) according to

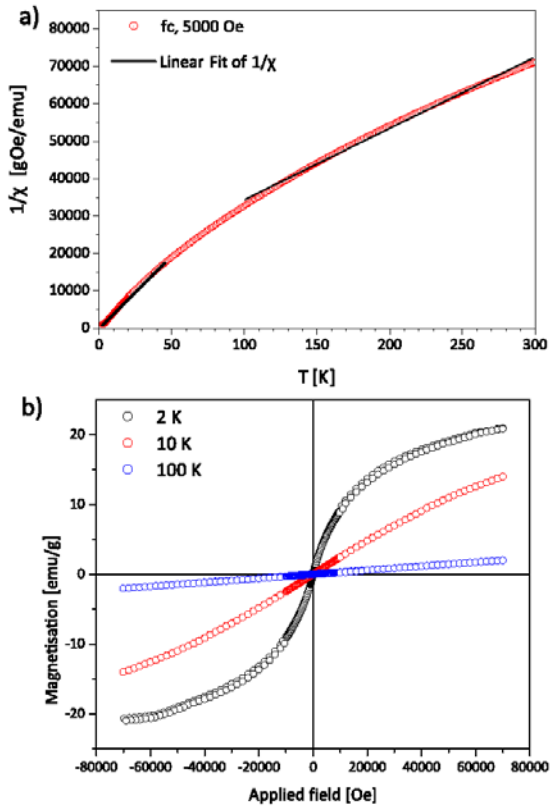

Fig. 8. a) Fc (field cooled) measurement of $1/\chi$ vs T of sample $y = 0$, from 2 K to 300 K in 5 kOe field. Black lines correspond to a linear fit in the ranges 2–50 K and 100–300 K. b) M(H) loops of the sample $y = 0$ measured at 2 K, 10 K, and 100 K.

the equation: $\mu_{eff} = (3k_B * C / n_{Ce} * N_A * \mu_B^2)^{1/2}$, with k_B being the Boltzmann constant, n_{Ce} the proportion of Ce atoms in the alloy $y = 0$, N_A Avogadro constant and μ_B the Bohr magneton. In the region from 100 to 300 K, the μ_{eff} of Ce is 3.0 μ_B, a value higher than that of free Ce ion − 2.54 μ_B. Magnetic ordering in this range exhibits strongly negative fitted Θ of ≈ − 80.6. In the range 2–50 K, μ_{eff} was found to be 2.2 μ_B, which is lower than the moment of free Ce ions. Here, the magnetic response was found to be very close to paramagnetic with $\Theta \approx -0.7$. Effective magnetic moments different from that of the free Ce ion, indicate a delocalization of Ce 4f electrons and thus a shift from its initial 3^+ valence. Measurements of M(H) at temperatures of 2 K, 10 K and 100 K, Fig. 8b, all indicate a paramagnetic response with a higher value of magnetisation at lower temperature. It is also noticeable that the Brillouin function, describing a paramagnetic curve, changes with the temperature. This occurs below 50 K and the observed increase in M is in accordance with the measured $1/\chi$(T), Fig. 8a. Lower temperature reduces the thermal fluctuations of magnetic spins, therefore locking them in place, which in turn elevates M.

Similar observations concerning thermal dependence of $1/\chi$ were found also for the binary Ce-Al metallic glass [16], which points at a dominant role of Ce in the magnetic behaviour of these alloys. The study of this binary glass shows that the increase in magnetisation at $T < 50$ K similarly does not change the magnetic order. One of the previous investigations demonstrated the temperature independence of M(H) curves of CeO_2 nanoparticles [35], suggesting that the increase in magnetisation below 50 K cannot be associated with a potential change of the magnetic state of CeO_2. This postulation is based on the hysteresis loops, recorded at 4 K, 295 K and 380 K [35], which do not exhibit any measurable difference. In contrast, our measurements at 2 K, 10 K, and 100 K demonstrate a substantial change in M. With this, we rule out the effect of CeO_2 and postulate that the main contributor to the behaviour of M(H) loops of the sample $y = 0$ is Ce.

4. Conclusions

In summary, the present work shows the impact of replacing Fe for Cu in the $Al_{20.5}Ce_{41.5}(Fe_yCu_{1-y})_{38}$ alloys, which influences the structure, thermal properties, magnetism and microstructure of glasses formed thereof by rapid solidification. Amorphousness was evaluated with PXRD patterns, which demonstrate that the structure turns from amorphous in the case of Cu-rich alloys, to partially nanocrystalline in the case of Fe-rich alloys. With TEM, we found that the specimen $y = 0$ mostly contains an amorphous matrix with ≈ 5–6 vol% of CeO_2 particles, whose size is in the range 5–10 nm. However, the latter do not influence the glass forming ability nor the stability of the glassy phase on heating. Thermal measurements outline the best glass formers, which are located around Cu-rich compositions whereas the intensity of the heat flux drop at T_g is correlated with the tendency for glass formation. Magnetic properties show that magnetisation at maximum field is strongly dependent on the amount of Fe and varies from paramagnetic in samples with < 30 at.% Fe ($y < 0.8$) to ferromagnetic when $Al_{20}Ce_{25}Fe_{55}$ nanocrystals form, although in very small weight fraction (≈ 1%). The effective magnetic moment of Ce in the specimen $y = 0$ was found to be 3.0 μ_B and 2.2 μ_B for the temperature regions of 100–300 K and 2–50 K, respectively, which is in close vicinity of the free Ce ion with 2.54 μ_B.

Acknowledgments

The assistance in sample preparation by B. Skela and TEM sample preparation by A. Šestan and EDS analysis by Z. Samardžija is gratefully thanked. We gratefully acknowledge discussions and manuscript revisions by J. Dolinšek and M. Komelj regarding the magnetic properties. The research was financed by CNRS and the Slovenian Research Agency (P2-0084-0106/04).

References

[1] W. Klement, R.H. Willens, P. Duwez, Non-crystalline structure in solidified gold—silicon alloys, Nature 187 (4740) (1960) 869–870.
[2] M.J. Duarte, P. Bruna, E. Pineda, D. Crespo, G. Garbarino, R. Verbeni, K. Zhao, W.H. Wang, A.H. Romero, J. Serrano, Polyamorphic transitions in Ce-based metallic glasses by synchrotron radiation, Phys. Rev. B: Condens. Matter Mater. Phys. 84 (22) (2011) 1–7.
[3] Q.S. Zeng, Y. Ding, W.L. Mao, W. Yang, S.V. Sinogeikin, J. Shu, H.K. Mao, J.Z. Jiang, Origin of pressure-induced polyamorphism in $Ce_{75}Al_{25}$ metallic glass, Phys. Rev. Lett. 104 (10) (2010) 1–4.
[4] Q.S. Zeng, V.V. Struzhkin, Y.Z. Fang, C.X. Gao, H.B. Luo, X.D. Wang, C. Lathe, W.L. Mao, F.M. Wu, H.-K. Mao, J.Z. Jiang, Properties of polyamorphous $Ce_{75}Al_{25}$ metallic glasses, Phys. Rev. B 82 (5) (2010) 54111.
[5] Z. Bian, A. Inoue, Ultra-low glass transition temperatures in Ce-based bulk metallic glasses, Mater. Trans. 46 (8) (2005) 1857–1860.
[6] Q.S. Zeng, Y.Z. Fang, H.B. Lou, Y. Gong, X.D. Wang, K. Yang, A.G. Li, S. Yan, C. Lathe, F.M. Wu, X.H. Yu, J.Z. Jiang, Low-density to high-density transition in $Ce_{75}Al_{25}Si_2$ metallic glass, J. Phys. Condens. Matter 22 (37) (2010) 375404.
[7] Q. Zeng, H. Sheng, Y. Ding, L. Wang, W. Yang, J.-Z. Jiang, W.L. Mao, H.-K. Mao, Long-range topological order in metallic glass, Science 332 (6036) (2011) 1404–1406.
[8] Q. Zeng, W.L. Mao, H. Sheng, Z. Zeng, Q. Hu, Y. Meng, H. Lou, F. Peng, W. Yang, S.V. Sinogeikin, J.Z. Jiang, The effect of composition on pressure-induced devitrification in metallic glasses, Appl. Phys. Lett. 102 (17) (2013).
[9] Q.-S. Zeng, Y. Ding, W.L. Mao, W. Luo, A. Blomqvist, R. Ahuja, W. Yang, J. Shu, S.V. Sinogeikin, Y. Meng, D.L. Brewe, J.-Z. Jiang, H.-K. Mao, Substitutional alloy of Ce and Al, Proc. Natl. Acad. Sci. 106 (8) (2009) 2515–2518.
[10] B. Zhang, D.Q. Zhao, M.X. Pan, W.H. Wang, A.L. Greer, Amorphous metallic plastic, Phys. Rev. Lett. 94 (20) (2005) 1–4.
[11] Q. Luo, W.H. Wang, Rare earth based bulk metallic glasses, J. Non-Cryst. Solids 355 (13) (2009) 759–775.
[12] L. Kelhar, J. Ferčič, P. Boulet, M. Maček-Kržmanc, S. Šturm, M. Lamut, B. Markoli,

S. Kobe, J.-M. Dubois, Stabilisation of Ce-Cu-Fe amorphous alloys by addition of Al, Philos. Mag. (Sep. 2016) 1–16.
[13] E. Ma, Alloys created between immiscible elements, Prog. Mater. Sci. 50 (2005) (2004) 413–509.
[14] A. Inoue, Stabilization of metallic supercooled liquid and bulk amorphous alloys, Acta Mater. 48 (1) (2000) 279–306.
[15] S.Y. Wu, S.H. Wei, G.Q. Guo, J.G. Wang, L. Yang, Structural mechanism of the enhanced glass-forming ability in multicomponent alloys with positive heat of mixing, Sci. Rep. 6 (November) (2016) 38098.
[16] Q. Chen, Z. Jin, The Fe-Cu System: A Thermodynamic Evaluation, February (1995).
[17] I.V. Nikolaenko, M.A. Turchanin, Enthalpies of formation of liquid binary (copper + iron, cobalt, and nickel) alloys, Metall. Mater. Trans. B Process Metall. Mater. Process. Sci. 28 (6) (1997) 1119–1130.
[18] L.J. Huang, B.X. Liu, Spontaneous vitrification in an immiscible Fe-Cu system, Appl. Phys. Lett. 57 (14) (1990) 1401–1403.
[19] K. Sumiyama, K. Nishi, M. Shiga, M. Sakurai, K. Suzuki, The amorphous structure of immiscible Fe-Cu-Ag alloys, J. Non-Cryst. Solids 150 (1992) 391–395.
[20] J.-M. Dubois, E. Belin-Ferré, A.P. Tsai, J. Dubois, E. Belin-Ferré, A.P. Tsai, Quasicrystals and complex metallic alloys, Kirk-Othmer Encyclopedia of Chemical Technology, John Wiley & Sons, Inc., Hoboken, NJ, USA, 2016, pp. 1–19.
[21] N.C. Wu, M. Yan, L. Zuo, J.Q. Wang, Correlation between medium-range order structure and glass-forming ability for Al-based metallic glasses, J. Appl. Phys. 115 (4) (2014).
[22] S. Sachdev, D.R. Nelson, Theory of the structure factor of metallic glasses, Phys. Rev. Lett. 53 (20) (1984) 1947–1950.
[23] T. Chiang, M. Ohta, A. Fujita, K. Fukamichi, E. Mastubara, Formation of icosahedral clusters and spin freezing in RE $(Fe_{1-x}Al_x)_{13}$ amorphous alloys, Mater. Trans. 45 (1) (2004) 149–156.
[24] A.I. Goldman, T. Kong, A. Kreyssig, A. Jesche, M. Ramazanoglu, K.W. Dennis, S.L. Bud'ko, P.C. Canfield, A family of binary magnetic icosahedral quasicrystals based on rare earths and cadmium, Nat. Mater. 12 (8) (Aug. 2013) 714–718.
[25] J.G. Uo, E.A. Be, A.T. Sai, Stable icosahedral quasicrystals in the Cd–Mg–RE (RE = rare earth element) systems, Jpn. J. Appl. Phys. 39 (8) (2000) 770–771.
[26] C.A. Schneider, W.S. Rasband, K.W. Eliceiri, NIH image to ImageJ: 25 years of image analysis, Nat. Methods 9 (7) (2012) 671–675.
[27] Tatge, Swanson, PDF 00-004-0593, From PDF + 2015 Database, The International Centre for Diffraction Data, 2015.
[28] M. Ferry, M. Institute of Materials, CRC Press LLC, Direct Strip Casting of Metals and Alloys: Processing, Microstructure and Properties, Woodhead Pub. and Maney Pub. on behalf of The Institute of Materials, Minerals & Mining, 2006.
[29] C.J. Byrne, S.J. Weinstein, P.H. Steen, Capillary stability limits for liquid metal in melt spinning, Chem. Eng. Sci. 61 (24) (2006) 8004–8009.
[30] D.R.G. Mitchell, Circular Hough transform diffraction analysis: a software tool for automated measurement of selected area electron diffraction patterns within Digital Micrograph™, Ultramicroscopy 108 (4) (Mar. 2008) 367–374.
[31] X.H. Du, J.C. Huang, C.T. Liu, Z.P. Lu, New criterion of glass forming ability for bulk metallic glasses, J. Appl. Phys. 101 (8) (2007) 1–4.
[32] D. Turnbull, Under what conditions can a glass be formed? Contemp. Phys. 10 (5) (1969) 473–488.
[33] Q.S. Zeng, Y.C. Li, C.M. Feng, P. Liermann, M. Somayazulu, G.Y. Shen, H.-K. Mao, R. Yang, J. Liu, T.D. Hu, J.Z. Jiang, Anomalous compression behavior in lanthanum/cerium-based metallic glass under high pressure, Proc. Natl. Acad. Sci. U. S. A. 104 (34) (Aug. 2007) 13565–13568.
[34] D. Plusa, Effect of aluminium on magnetic properties of $DyFe_3$ compounds, J. Magn. Magn. Mater. 51 (1985) (1985) 331–336.
[35] M. Coey, K. Ackland, M. Venkatesan, S. Sen, Collective magnetic response of CeO_2 nanoparticles, Nat. Phys. 12 (7) (2016) 694–699.

4.2 Gd-Based Alloys

4.2.1 Variation of the amounts of Al and Gd

The succeeding section examines Gd-based alloys $(Al_{1-x}Gd_x)_{62}Fe_{13}Cu_{25}$, where x=Gd/(Gd+Al) and it is located within the range $0.5 \leq x \leq 1$. These alloys are analogous to the previously studied Ce-based alloys in terms of stoichiometry, which will allow the comparison of physical properties.

The replacement of Al with Gd is intriguing since it displays properties, significantly different from those of Ce. Melting point, electronic structure and magnetic moment of the two REs show dissimilar values and their integration into the quaternary alloys is expected to yield different properties.

4.2.1.1 XRD characterisation

Structural characterisation of Gd-based alloys was performed on powdered samples as well as on the WS and FS of the ribbons. Together with PD calculation, these results are presented in Figure 32. PD of X-rays is calculated for three different x values; x=0.5, x=0.75 and x=1 (Figure 32a). It can be observed that in composition x=0.5, PD ranges from 1.5-10 μm, for incident 2θ angles from 10° to 90°, respectively. For composition x=1, PD is within 1.5-8.5 μm for the same range of incident angles. Higher amounts of heavy Gd attenuate more X-rays and PD is less significant. An important data that can be retrieved from these results is the scale of PD, relative to the size of the melt-spun ribbon. It is within 1/3 of the thickness of a melt-spun ribbon (≈30 μm) for the entire range of x-ratios from x=0.5 to x=1.

Figure 32b shows the XRD patterns within the composition range $0.5 \leq x \leq 1$, taken in powder form. Such specimens result in an averaged structural information since the orientations of the particles are randomized. Diffractograms in Figure 32b show an intense hump at approximately 35° of 2θ, indicating pronounced SRO. Samples in the range $0.58 \leq x \leq 0.75$ exhibit a completely glassy structure, without the occurrence of crystalline reflections. Compositions outside this range, on the contrary, display peaks that belong to crystalline precipitates. In the specimen x=0.5, a majority of these peaks can be indexed to a hexagonal phase of composition $Al_{1.2}Fe_{1.8}Gd$ (PDF number 01-082-5084). Tiny crystalline bumps appearing in Gd-rich samples where $0.83 \leq x \leq 1$ are too minute to be indexed. XRD patterns of ribbons in the as-melt-spun state are shown in Figure 32c and d, where WS and FS surfaces were characterized. According to WS measurements, the range of completely glassy structure is enhanced with respect to the one deduced from diffractograms on powder. Even the sample x=0.83 shows a completely glassy structure, without the occurrence of crystalline peaks. The ease of vitrification on WS is because of higher dissipation of heat, compared to FS. Namely, WS is in direct contact with the Cu cooling wheel. Considering the PD of X-rays, which at its maximum value amounts to 10 μm, a completely glassy structure is obtained down to at least 10 μm below the WS surface of the ribbon within the range $0.58 \leq x \leq 0.83$.

XRD measurements on FS of the ribbons, however, show that these patterns exhibit a series of crystalline reflections, superimposed on top of the glassy humps. Even the specimens, which did not show any sign of crystalline order on powder or WS of the ribbons ($0.58 \leq x \leq 0.75$), exhibit minute crystalline reflections, albeit the signal is very weak compared to the intensity of the wide glassy hump. The latter indicates that their share is very low. Some reflections in Gd-rich samples ($0.67 \leq x \leq 1$), for instance at 2θ angles of ≈31°, ≈35.5°, ≈36° and ≈60°, but also in x=0.5 and x=0.58, could not be indexed. They are labelled with green flipped triangles in Figure 32b, c and d. Since the crystalline

reflections at ≈31° and ≈36° occur for the entire span of x ratios within 0.67≤x≤1, it can be deduced that they are structurally identical. Two Gd-poor samples within the range 0.5≤x≤0.58 display a set of distinct crystalline reflections, whereas x=0.5 exhibits a higher number of peaks than x=0.58 and they are more intense as well. The peaks are located at positions corresponding to those of the crystalline reflections on powder specimens in Figure 32b. A match with hexagonal $Al_{1.2}Fe_{1.8}Gd$ phase, PDF number 01-082-5084 is found and it is shown for the sample denoted x=0.5. The strongest reflections from hexagonal $Al_{1.2}Fe_{1.8}Gd$ phase are also observed in x=0.58.

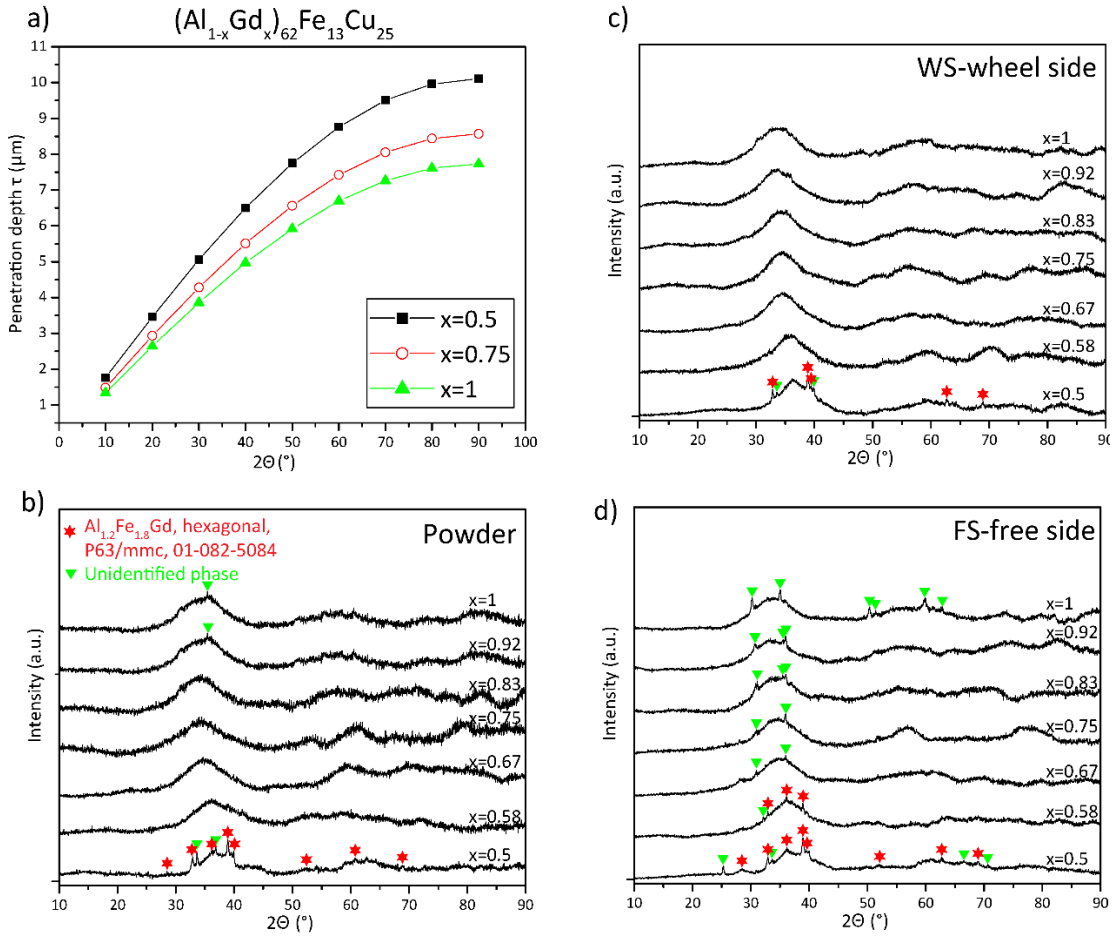

Figure 32: a) Penetration depth of CuK_α X-rays (with wavelength λ=0.15406 nm) against 2θ angle, for three distinctive compositions of $(Al_{1-x}Gd_x)_{62}Fe_{13}Cu_{25}$ alloys. b) XRD patterns of $(Al_{1-x}Gd_x)_{62}Fe_{13}Cu_{25}$ alloys in powder form, whereas 0.5≤x≤1. Six-fold red stars label the hexagonal $Al_{1.2}Fe_{1.8}Gd$ phase (PDF number 01-082-5084). Green flipped triangles label the peaks that could not be matched. c) XRD patterns of $(Al_{1-x}Gd_x)_{62}Fe_{13}Cu_{25}$ alloys on WS, whereas 0.5≤x≤1. d) XRD patterns of $(Al_{1-x}Gd_x)_{62}Fe_{13}Cu_{25}$ alloys on FS, whereas 0.5≤x≤1.

Figure 33 depicts a shift in the position of the main glassy hump and outlines the change of peak symmetry on FS and WS of the ribbon. Data is contained in reciprocal, wavelength-independent Q space, which connects to θ space via $Q=4\pi\sin(\theta)/\lambda$. In Figure 33a parameters Q_M, Q_L, Q_R, and FWHM are graphically presented. Here, FWHM stands for the full peak width at half-maximum intensity of the main peak, Q_M labels the maximum intensity of the main glassy peak, Q_L is the left-hand side of the main peak's FWHM and Q_R is the right-hand side of the main peak's FWHM. In Figure 33b, parameter $Q_S=(Q_B-Q_M)*10$ is additionally introduced. It is multiplied with a factor of 10 to fit on the same scale with the other parameters. In the last expression, $Q_B=(Q_L+Q_R)/2$ and represents a measure of peak's asymmetry. When $Q_B=0$, the peak is symmetric, while negative values indicate peak broadening towards lower Q and positive values convey peak broadening towards higher Q.

The position of the main peak's maximum intensity on the FS exhibits higher Q compared to WS. This comes about due to higher susceptibility to crystallisation on the FS as a consequence of lower heat dissipation. The result is a different composition of the glassy phase on FS and WS, which is reflected in different Q. The emerging crystals also influence the size of the error bars, the latter being higher for FS. It is due to peaks superimposed on top of the main glassy hump, which blur the top of the glassy hump and make Q_M less definite. For the alloys within $0.67\leq x\leq 0.83$, containing less crystalline peaks in the XRD pattern on FS and WS, the error bars are much lower. Similar can be claimed for Gd-rich alloys x=0.92 and x=1, which exhibit several crystalline reflections, yet they do not alter significantly the shape of the glassy hump at its top. Variation in Q_M follows a decreasing trend with higher contents of Gd, descending from 26.4 nm^{-1} for x=0.5 to 23.8 nm^{-1} for x=1. This can be explained with the altered local environment in a glass. As more Gd atoms (0.1795 nm) are added, the mean interatomic distance in the alloy elevates, since Al (0.1429 nm), Fe (0.1260 nm) and Cu (0.1276 nm) are all significantly smaller compared to the RE [111].

Next, FWHM is plotted according to the relation $FWHM=Q_R-Q_L$. Overall, the FWHMs of FS and WS increase with more Gd. FS curve features an augmentation from 5.5 nm^{-1} to 6.1 nm^{-1}, whereas WS climbs from 4.4 nm^{-1} to 5.6 nm^{-1}. This change implies that the glassy hump becomes wider with higher content of Gd.

The last parameter given in Figure 33b is Q_S. It outlines the asymmetry of the glassy hump according to the difference of Q_S from zero. In the two samples within $0.5\leq x\leq 0.58$, the parameter Q_S is strongly positive and strongly negative for WS and FS, respectively. This means that the glassy hump is broadened towards higher Q for WS and broadened towards lower Q for FS. In contrast, alloys within composition range $0.67\leq x\leq 0.83$ have a much lower discrepancy of WS and FS from zero. Their structure does not exhibit the same amount of crystallinity, as is the case for x=0.5. With this reasoning, it is reasonably safe to find that the formation of strong glasses is predominant in the composition range within $0.67\leq x\leq 0.83$.

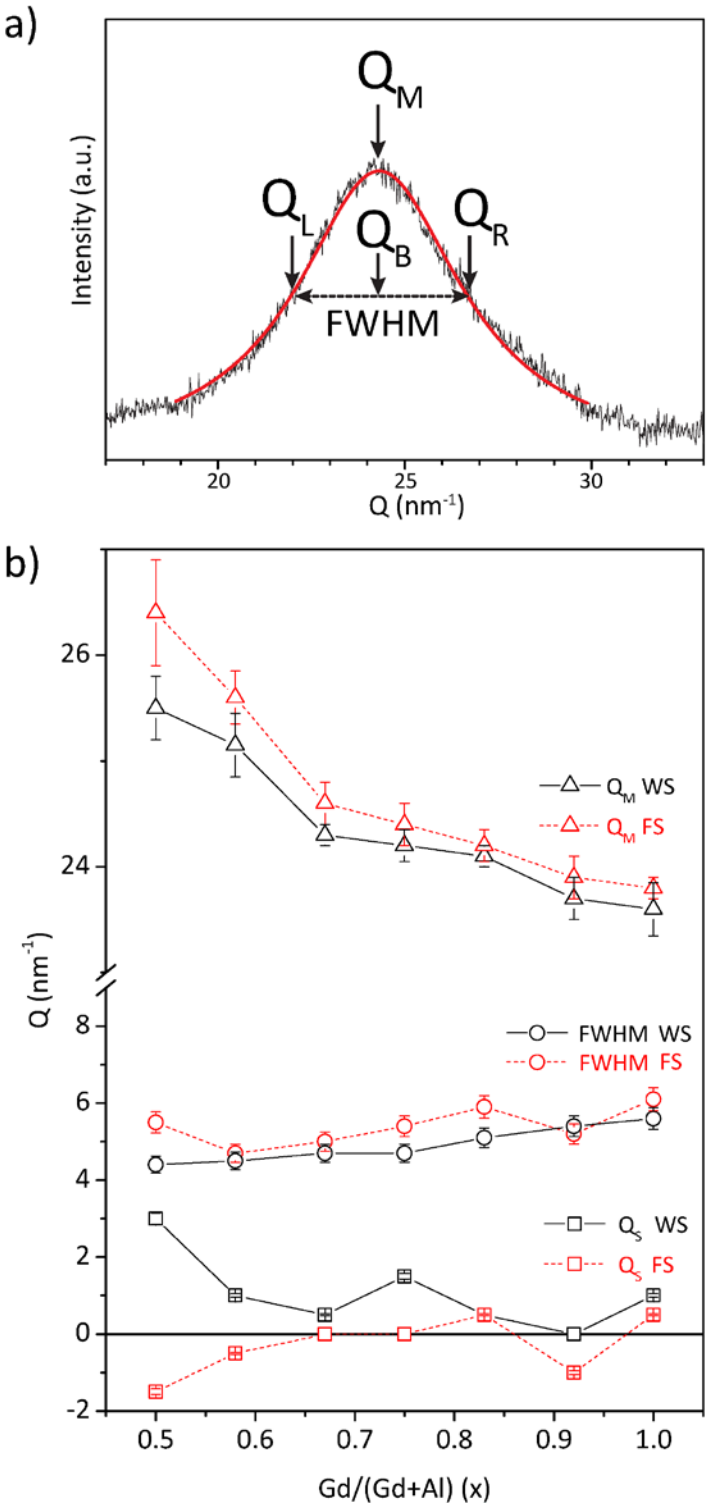

Figure 33: a) Illustration of Q_M, Q_L, Q_R, Q_B and FWHM. b) Plots of Q_M, FWHM, and $Q_S=(Q_B-Q_M)*10$ (definition of Q_B is given in the text), against alloy composition given with the ratio x=Gd/(Gd+Al). Data is shown for WS and FS of the ribbon. Error bars represent the uncertainty of the maximum of Q (for Q_M), the uncertainty of FWHM width (for FWHM curves) originates from the breadth of diffraction line profile and a mix of both these uncertainties for the determination of Q_S.

4.2.1.2 TEM study

Results in Figure 34 show the microstructural study of Gd-based glass labelled with x=0.75. They were conducted on a probe corrected microscope FEI Titan Themis IC, using 300 kV of acceleration voltage.

In general, the microstructure of melt-spun ribbons is made of regions that show a fully glassy phase and regions made of glassy phase with crystalline precipitates. In the former region, observed on TEM micrograph in Figure 34a, the glassy structure is recognised by the absence of LRO, meaning that the positions of atomic species are not rigorously defined and do not feature translational periodicity. Rather, they are organised into SRO clusters with relaxed atomic positions. Figure 34b displays the SAED pattern of the corresponding glassy matrix from Figure 34a, albeit, taken at lower magnification, to provide an average structural information from $\approx$100 nm^2 of the area. A diffuse ring (shown with the red arrow in Figure 34b) is characteristic of SRO in MG ref. [221]. It is smeared out over distances 0.27-0.37 nm, whereas its maximum is located at d$\approx$0.30 nm.

Micrograph in Figure 34c shows a region made of glassy phase and crystallites. It was processed by Fast Fourier Transform (FFT) into the frequency domain, bandpass filtered to eliminate the noise and then converted back into real space domain via Inverse Fast Fourier Transform (IFFT). This process accentuated the crystalline columns inside the glassy matrix. Crystallite fraction, determined by measuring their area in Figure 34c with ImageJ software ref. [222] is $\approx$7 % of the area. As noted in the figure, the viewing direction of the crystallites is [440]. SAED pattern in Figure 34d depicts the diffraction from a region made of glassy phase and crystalline precipitates. The diffuse ring appears together with several bright spots, hinting at LRO structures. The first set of spots (from the centre of the pattern outwards) is located within the diffuse ring. A close inspection delineates a set of sharp white specks at interplanar distance d$\approx$0.31 nm. Clarity-wise, a pair of red arrows in the upper-right hand corner of Figure 34d shows some of the most intense reflections. Additional two sets of crystalline reflections occur at lower real space distance and outside the diffuse ring. Their d values amount to d$\approx$0.20 nm and d$\approx$0.16 nm, whereas the former set of spots is much more intense than the latter set. Structurally, these reflections can be matched with cubic Gd_2O_3 (PDF 00-012-0797) ref. [223], whereas specks having d$\approx$0.31 nm belong to (222) plane, those with d$\approx$0.20 nm match with (440) plane and the ones with d$\approx$0.16 nm correspond to (622) plane ref. [223]. The mismatch of experimental and theoretical values is within $\pm$0.1 nm.

In the region containing the glassy phase and crystallites (Figure 34d), the position of the diffuse hump is shifted with respect to the hump from Figure 34b. In Figure 34d, the diffuse halo spans from 0.24-0.33 nm and has a maximum at d$\approx$0.28 nm. This suggests an alteration of the MG's local environment. Gd metal, used for the formation of Gd_2O_3 crystallites, is supplied from a glassy phase, in turn reducing the amount of Gd in the glassy phase. Due to the significantly larger size of the Gd atom, a decrease of mean interatomic distances in the glassy phase is anticipated. A decrease of diffuse hump's d from d$\approx$0.30 for the fully glassy region to d$\approx$0.28 for the partly crystalline counterpart is in reasonable agreement with the above-given interpretation.

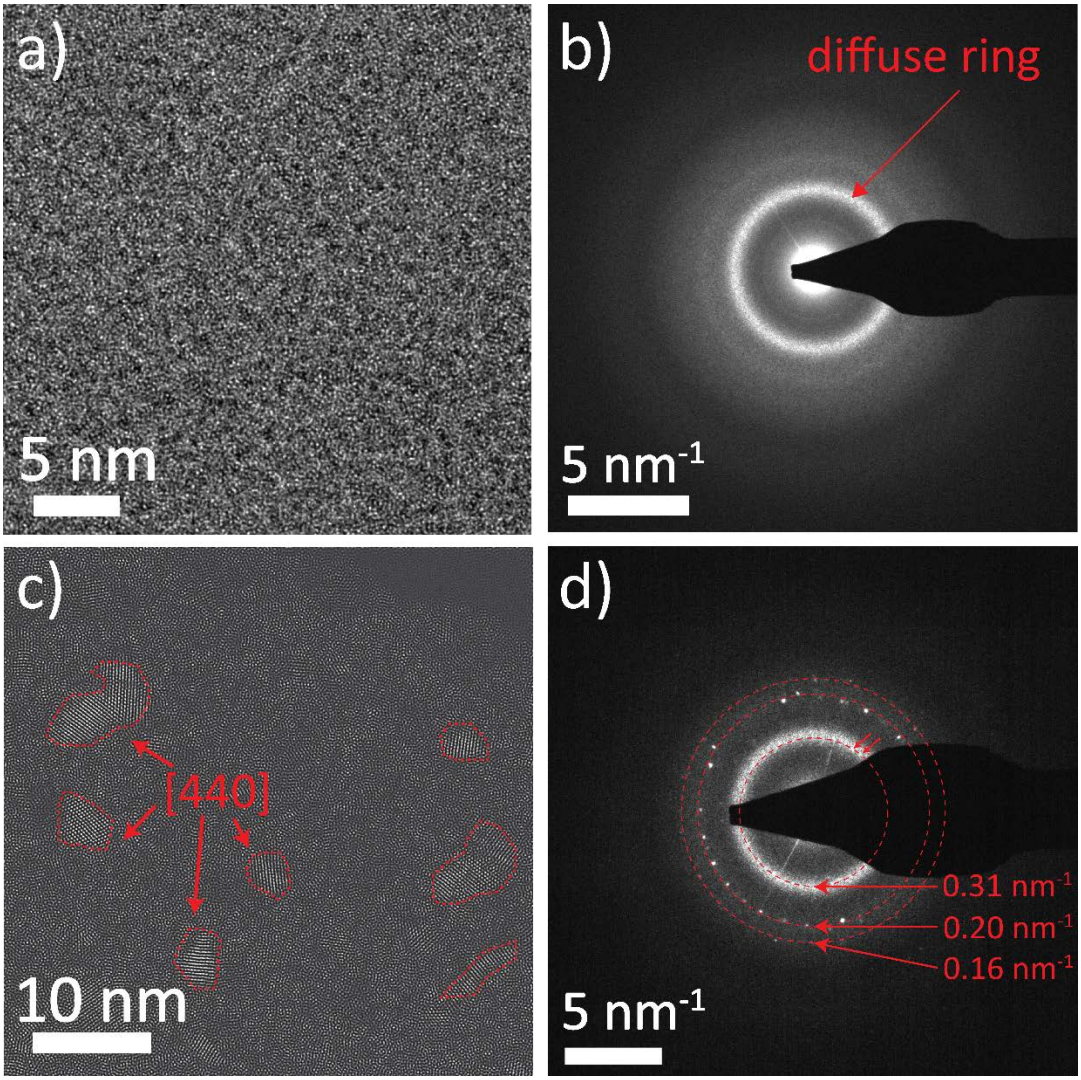

Figure 34: a) HR-TEM micrograph of a region in the sample x=0.75 comprised solely of the glassy matrix and b) SAED of the glassy matrix, with indicated diffuse ring. c) Micrograph from a region (in the sample x=0.75) that contains a glassy matrix and crystallites, processed with FFT, bandpass filtered and transferred back to real space via IFFT to visualize crystallites (dashed line) more clearly. The noted crystallites belong to Gd_2O_3 and are viewed in [440] direction. d) SAED of the representative region in c, showing three sets of crystalline spots. The innermost dashed circle represents several specks (indicated by two red arrows), with d≈0.31 nm, that coincide with the diffuse ring. Two other sets of crystalline spots are located at d≈0.20 nm and d≈0.16 nm.

4.2.1.3 Thermal analysis

Figure 35 outlines the results of the thermal analysis conducted with DSC on a series of Gd-based alloys in the range $0.5 \leq x \leq 1$. The first set of results shown in Figure 35a and b shows the heat-up and cool-down measurements, respectively, recorded in the temperature range 300-1250 K and with a heating rate of 20 K/min. Two-part crucibles were used, where the inner part is made of thin Al_2O_3 inset and the outer crucible is made of Pt to enable excellent heat conductivity. This set of results will be addressed as the ones using Pt crucibles. The second part of the results shown in Figure 35c and d was performed on the same set of alloys, but using an instrument capable of higher temperatures, in the range 300-1450 K and with the same heating rate of 20 K/min. Crucibles used herein were monolithic Al_2O_3, which results in lower heat conductivity and lower stability of the baseline. These measurements will be addressed as the ones performed in Al_2O_3 crucibles. Superior heat conductivity of the Pt+Al_2O_3 crucibles is demonstrated (in Figure 35a and b) via the existence of a very flat baseline, which enables more accurate determination of changes and characteristic temperatures. Error bars in the plots of characteristic temperatures (in Figure 36) correspond to the difference in measurements with and without the Pt crucibles. The only exception to this is the temperature T_l, where the data points were taken solely from measurements up to 1450 K since T_l was found to be above 1250 K for all the alloys. Alloys in the range $0.67 \leq x \leq 1$ exhibit glass transition prior to crystallisation, which holds true for measurements in both, Figure 35a and c. T_g varies from about 560 K for x=0.67 to 480 K for x=1, as depicted by the plot in Figure 36a. The lack of data points in samples x=0.5 and x=0.58 indicates an absence of glass transition. It is because the crystallisation proceeds from crystalline precipitates, already present in the alloys (XRD patterns of x=0.5 and x=0.58 in Figure 32d), whereas the crystallisation from the glassy state is preceded by nucleation and growth of crystallites.

The crystallisation of the glassy matrix occurs in all samples within $0.5 \leq x \leq 1$ and follows after the glass transition. It is recognised by the exothermic nature of the peak. An evidence that these peaks belong to crystallisation are the cooling curves in Figure 35b and d, demonstrating that these peaks arise from an irreversible transition, which we can safely assign to crystallisation. In general, T_x decreases with higher additions of Gd, and changes from 670 K at x=0.5 to 500 K at x=1, which is depicted in Figure 36b. Melting temperature T_m is also reduced with higher additions of Gd, which can be seen clearly from Figure 36c. It changes from 1125 K at x=0.5 to 925 K at x=1. Liquidus temperature T_l, on the other hand, does not exhibit a pronounced trend with the variation in ratio x. Its value fluctuates between 1300 K and 1375 K for x=0.5 and x=1, respectively. Due to the high value of T_l, this data is solely based on high-temperature experiments (up to 1450 K) using Al_2O_3 crucibles and is not averaged out with the measurements using Pt crucibles.

Parameters of glass formation δT_g, GDA and T_{rg} are shown in Figure 36d. They were determined according to the expressions, described in the Section 2.3.3. Their retrieval requires T_g, and since the latter is missing for x=0.5 and x=0.58, this explains the lack of data points for the two Gd-poor compositions. Parameter δT_g shows its highest values in the range $0.67 \leq x \leq 0.75$, implying that these samples form the strongest glasses, which is complemented by the findings of XRD measurements in Figure 32. This result is in accordance with the generally accepted rule [18] that stabilisation of MG is related to a large SCL region. The line connecting data points of GDA and T_{rg} exhibits a slope similar to that of δT_g. The maximum values are obtained for the composition range $0.67 \leq x \leq 0.75$, followed by a steady decrease with higher amounts of Gd. The highest values of GDA and T_{rg} correspond to the vicinity of the eutectic composition (at 77 at% Gd) [224] in the binary Al-Gd system. The tendency towards the formation of strongest Gd-glasses conforms to

the maximum values of GDA and T_{rg}, which are the highest in the vicinity of eutectics [225].

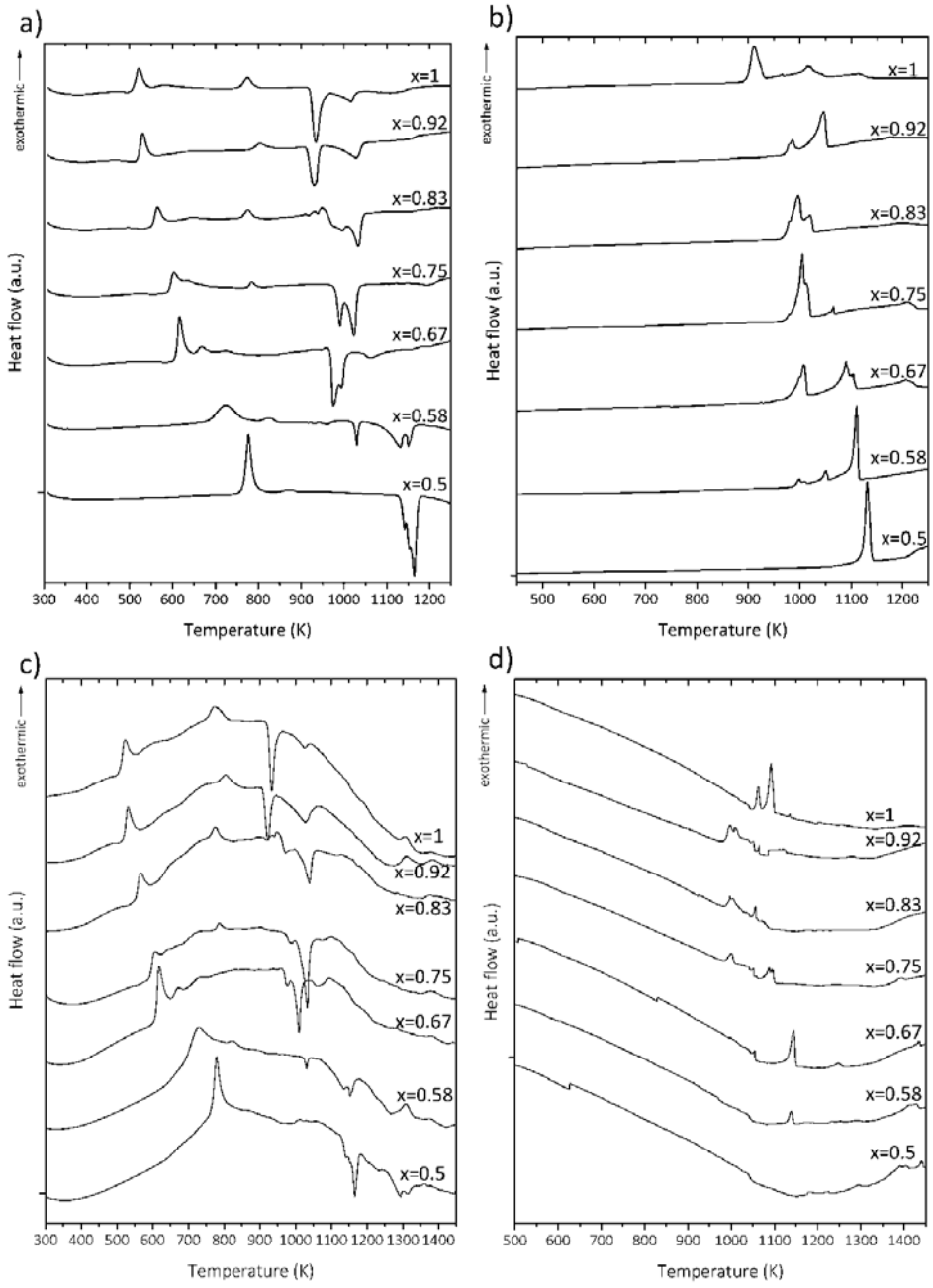

Figure 35: DSC measurements of $(Al_{1-x}Gd_x)_{62}Fe_{13}Cu_{25}$ alloys in the range $0.5 \leq x \leq 1$. Datasets a) and b) were measured up to 1250 K and using Pt crucibles with Al_2O_3 insets. Series c) and d) were measured up to 1450 K, using Al_2O_3 crucibles. Plots a) and c) show the heat-up, while b) and d) show the cool-down.

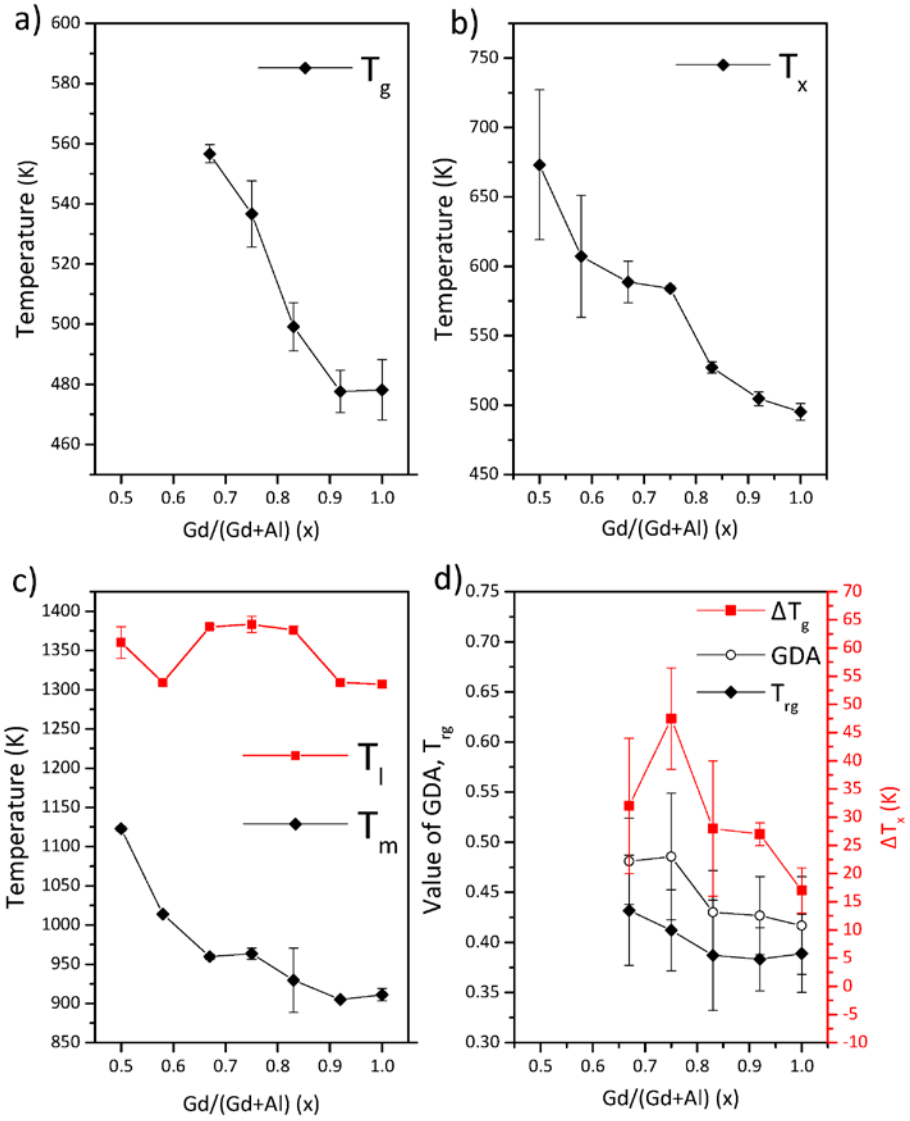

Figure 36: Plots of characteristic temperatures a) T_g, b) T_x and c) T_m, T_l. The plot in d) shows the glass forming parameters δT_g, GDA and T_{rg}. The error bars derive from 4-8 measurements of the characteristic temperatures, and they are influenced by the sharpness of the thermal event.

4.2.1.4 Magnetic properties

4.2.1.4.1 Measurements at room temperature

Magnetic properties of Gd-based MGs were primarily characterised with VSM on powdered samples prepared by crushing the PFC ribbons. M(H) hysteresis loops with the maximum applied field (H_{max}) up to 18 kOe are displayed in Figure 37. Magnetisation shown on the plot is normalized with respect to the mass of powders, yielding mass magnetisation. It can be seen from the hysteresis loops that the shape of the curves within $0.5 \leq x \leq 0.67$ is PM, i.e. M features linear dependence on the applied field. On the other hand, alloys in the range $0.75 \leq x \leq 1$ exhibit S-shaped curve, characteristic of FM-like or SPM-like magnetic behaviour.

The magnetisation of Gd-alloys varies substantially with the ratio x. For Gd-poor specimen x=0.5 it amounts to 3.6 emu/g, while for higher additions of Gd, the magnetisation increases. The variation of magnetisation at the maximum applied field (M at H_{max}) is plotted in Figure 37b. Sample x=1 containing the highest amount of Gd exhibits magnetisation of 15.8 emu/g. According to the theory of random magnetic anisotropy (RMA) [226], magnetic behaviour of the glassy alloys derives from SRO clusters, where exchange interactions among constitutive species result in the magnetic spin of the individual cluster. Interaction of the clusters yields either an anisotropic easy magnetisation direction or a random easy magnetisation direction and governs the appearance of coercivity or its absence, respectively [227]. In the case of Gd-based alloys, the shape of the curves (from linear to S-shaped) as well as the rise in M at H_{max} (shown in Figure 37b) suggest that the atomic environment and magnetic behaviour in SRO clusters changes with altering the composition. The strength of Zeeman interaction, orienting the magnetic dipoles in SRO clusters in the direction of the applied field, becomes more intense for higher amounts of Gd in the alloy. This is observed through a steeper M slope for higher ratios x, meaning that a higher number of dipoles exist with stronger magnetic coupling between them. Since the latter holds, the achieved M at H_{max} is higher in the case of alloys with a higher ratio x, due to a higher quantity of strongly magnetic Gd atoms in the SRO clusters increasing the inter-cluster magnetic interactions. When the field is removed, however, easy magnetisation directions of the clusters orient randomly, which is reflected in zero or negligible coercivity of all the measured Gd-based MGs at zero applied field (see Figure 37a).

As shown in the M(H) loops measured at RT, PM-FM-like boundary appears between x=0.67 and x=0.75, respectively. Crystallites that emerge in x=0.5 do not contribute to FM-like behaviour since there is no sign of M departing from the linear relation. With 46.5 at% of Gd (x=0.75), though, FM order appears. As observed from the XRD patterns on FS, crystalline reflections in the alloys where $0.67 \leq x \leq 1$ appear at identical positions of $\approx 31°$ and $\approx 36°$ of 2θ, albeit with slightly different relative intensities. On one hand, the magnetic behaviour of x=0.75 containing these precipitates is FM, while on the other hand, the presence of identical precipitates in x=0.67 yields PM. With this reasoning, the contribution of crystallites in the alloys with $0.67 \leq x \leq 1$ to FM-like behaviour can be ruled out.

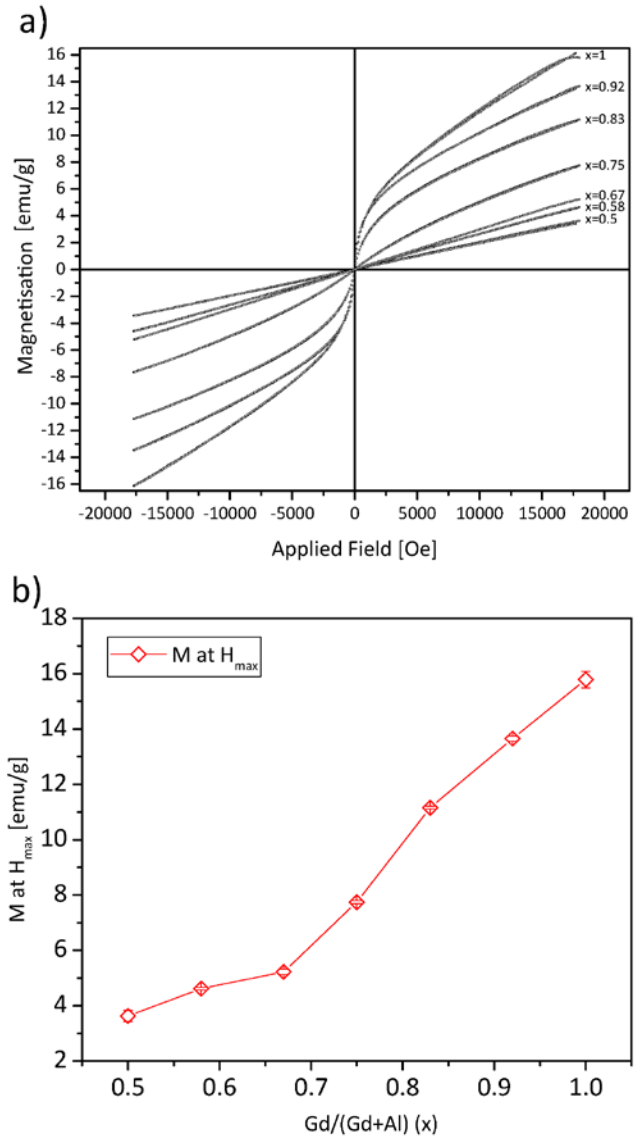

Figure 37: a) Room temperature VSM hysteresis loops of $(Al_{1-x}Gd_x)_{62}Fe_{13}Cu_{25}$ alloys in the range $0.5 \leq x \leq 1$. b) The plot of M at H_{max} vs. ratio x, Gd/(Gd+Al). Error bars are limited to the size of the data point, except for x=1, where they reach beyond the size of the lozenge-like data point.

4.2.1.4.2 Measurements at cryogenic temperature

In order to understand the magnetic behaviour of MGs within the range $0.5 \leq x \leq 0.67$ in more detail, additional magnetic measurements were conducted at cryogenic temperatures (Figure 38) with a SQUID magnetometer. The measuring procedure was performed with continuous variation of temperature and in constant magnetic fields. Two distinct types of curves have been retrieved, namely ZFC and FC curves. Specimens were cooled down to 2 K without the applied magnetic field, followed by temperature increase up to 300 K and simultaneous data recording. This section is regarded as ZFC. At 300 K the field was turned on and the specimen was cooled downwards to 2 K, which resulted in an FC curve.

Results in Figure 38a, b and c show the ZFC and FC measurements of the specimen denoted with x=0.67 performed in fields of 5 Oe, 100 Oe and 10000 Oe (FC only), respectively. With the decrease in temperature, glass x=0.67 features an increase in χ_{mass}, whereas the line connecting data points shows its maximum at T_{cr}. The sharpness of T_{cr} transition is smeared out with higher magnetic fields, which is evident from different slopes of the curves in Figure 38a-c. Magnetic field strength influences the accuracy of T_{cr} determination, which was found to be 80 K for 5 Oe, 88 K for 100 Oe and 82 K for 10000 Oe. With a higher magnetic field, T_{cr} shifts towards lower temperatures, implying that less thermal fluctuations are needed to initiate magnetic ordering. Due to its highest sharpness, the χ_{mass} curve at 5 Oe is selected for further interpretation. With a decrease in temperature below ≈40 K (for the curves in Figure 38), χ_{mass} starts to rapidly fall, which, on the ZFC curve, is preceded by an edge in χ_{mass}, marked as the transition temperature T_b. From PM state at RT, alloy transforms into AFM state at T_b, which, for the curve at 5 Oe of an external field, occurs at 40 K. Another evidence of ordering towards AFM state is a decrease of T_{cr} with the higher magnetic field.

In addition to the rapid fall of χ_{mass} below T_b, a difference between ZFC and FC curves (at 5 Oe) arises and becomes more pronounced with lower temperature. While χ_{mass} of FC curve is only slightly reduced, ZFC features a significant drop in χ_{mass}, which approaches 0.4 emu/g Oe at 2 K. Splitting between ZFC and FC curves can also be observed for 100 Oe field (while data for ZFC at 10000 Oe is missing), however, it is less pronounced due to higher field. The branching of ZFC-FC and the departure of ZFC curve towards lower χ_{mass} could be a fingerprint of glass's complex structure, indicating a spin-glass-like state, although the sharpness of T_b peak is lesser than that of typical spin-glasses [228].

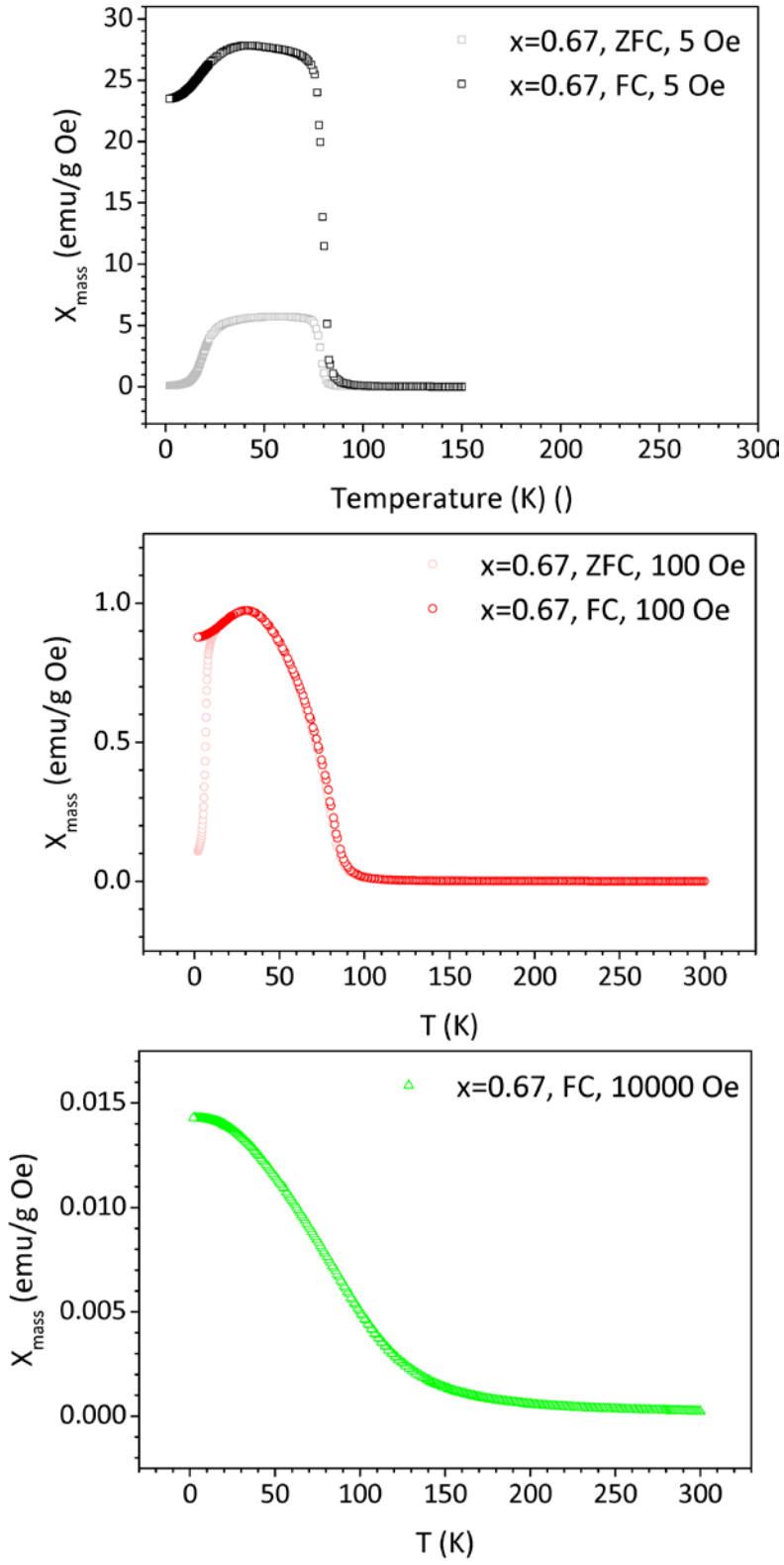

Figure 38: ZFC-FC χ_{mass}(T) curves for sample x=0.67 measured in magnetic fields of a) 5 Oe, b) 100 Oe and c) 10000 Oe.

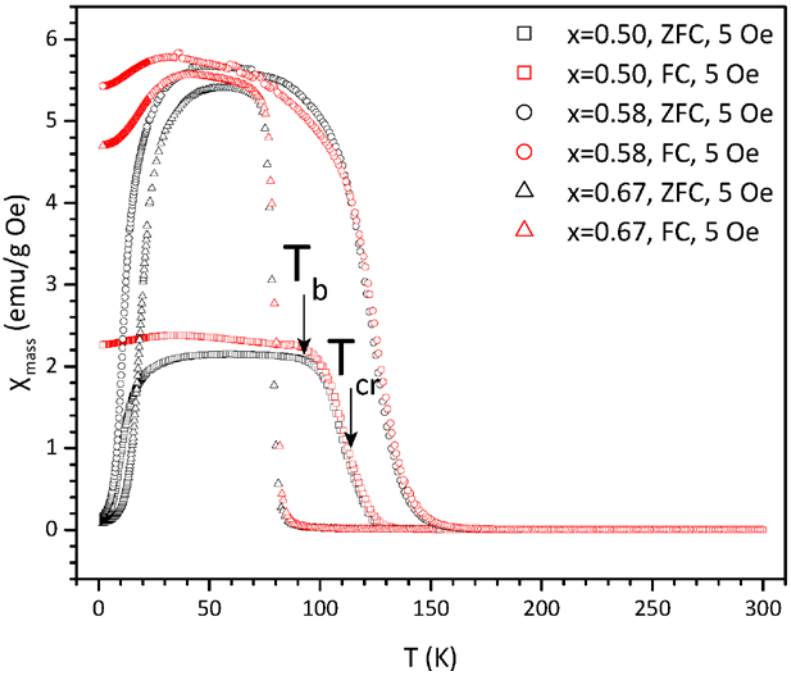

Figure 39: ZFC-FC $\chi_{mass}(T)$ curves of three different samples where $0.5 \leq x \leq 0.67$ measured in the magnetic field of 5 Oe.

Plots depicting the ZFC-FC $\chi_{mass}(T)$ curves of different sample compositions are given in Figure 39. It is observed that all three samples exhibit PM behaviour at RT, with χ_{mass} in the vicinity of zero emu/g Oe. As the temperature decreases, χ_{mass} features a rapid increase, marked with the T_{cr}. With the use of a differential method (as illustrated in Figure 31b) T_{cr} values were determined. They strongly depend on composition, whereas for x=0.5 T_{cr}=110 K, for x=0.58 T_{cr}=123 K and for x=0.67 T_{cr}=80 K. The variation of T_{cr} does not show a linear correspondence with the amount of Gd. The sharpness of T_{cr} also differs by composition, featuring its maximum at x=0.67 and then decreases for specimens x=0.58 and x=0.5. Another difference between the samples is in the achieved χ_{mass} at low temperature. At 50 K, χ_{mass} of FC curve of x=0.5 equals 2 emu/g Oe, while for x=0.58 and x=0.67 it climbs up to 5.8 emu/g Oe and 5.5 emu/g Oe, respectively. Correlation of higher χ_{mass} with a higher quantity of Gd is positive, although the increase is not linear, suggesting additional reasons for the observed difference. One of these could be the heterogeneous structure of the ribbons on WS and FS, as depicted by the XRD results.

In the 2-50 K low-temperature region, χ_{mass} of the three alloys does not differ significantly. FC curve remains at similar χ_{mass} values (for x=0.5) as for T>50 K or features a minor decrease in χ_{mass} towards 2 K (x=0.58 and x=0.67). ZFC curves tend to converge to ≈0 emu/g Oe, when the temperature is decreased to 2 K, complicating the explanation of magnetic ordering in the low-temperature region of 2-50 K.

Splitting between the ZFC and FC curves, described in the previous paragraph, is similar for all three alloys, deducing that the magnetic state of the alloys is similar as well. However, the latter cannot be described by a simple PM to FM change, as is the case for some Gd-based metallic glasses [229]. After crossing the T_{cr}, χ_{mass} of ZFC curves saturates and starts to decrease with the additional decrease of temperature. This behaviour is partly reminiscent of SGs, except for a wide cusp, without sharply defined peak [230]. Blocking temperature T_b (shown in Figure 39) is marked as the point before the first derivative of $\chi_{mass}(T)$ departs from the baseline, preceding an abrupt increase in χ_{mass} with its maximum

in T_{cr}. A transition from PM to AFM-like state occurs at T_b and amounts to 90 K, 102 K, and 64 K for x=0.5, x=0.58 and x=0.67, respectively. With the decrease of temperature below T_b, the orientation of magnetic moments is becoming frozen in random directions and is unable to rotate freely [230]. In ZFC curve, this eventually results in a decrease of χ_{mass}, rapidly declining from 35 K, 35 K, and 40 K for x=0.5, x=0.58 and x=0.67, respectively. For the ZFC curve above T_b, thermal fluctuations unfreeze the magnetic moments and χ_{mass} increases. Therefore, it is difficult to give an unambiguous interpretation of the splitting in ZFC-FC curves, the width of the peak and the exact state of MG at a specific temperature. Similar effects, found in Gd- and Dy-based MGs as well as TbDyFe glassy films, however, were shown to be a consequence of magnetic frustration due to RMA [231], [232] and SG state [230], respectively.

ZFC-FC measurements were conducted also on Gd-rich alloy x=1. No unusual phase changes have been observed in the temperature range 2-300 K. A break in χ_{mass} at T_{cr}=194 K was observed suggesting a transition from PM to FM state [229] and with it less complex magnetic behaviour of specimen x=1.

4.3 Ce- and Gd-Based Composite Bulk Metallic Glass

In order to study the combination of Ce- and Gd-based glassy ribbons in a BMG, we used a method of PECS to consolidate the glassy ribbons. The two MG powders were simultaneously heated in its SCL range and pressed to allow the viscous flow of powders and formation of a solid, disc-shaped bulk.

The compositions of Ce- and Gd-based ribbons were chosen so as to have a compatible T_g, T_x and SCL range. Regarding the Ce-based ribbon of stoichiometry $(Al_{1-x}Ce_x)_{62}Fe_{13}Cu_{25}$, a ratio of x=0.75 was selected, while for the Gd-based counterpart $(Al_{1-x}Gd_x)_{62}Fe_{13}Cu_{25}$, a ratio of x=1 was taken. In order to obtain MG powders, suitable for PECS consolidation, the ribbons were crushed with a mortar and sieved to <250 μm in size. Next, Ce- and Gd-based MG powders were homogenized with the use of rotation, translation, and inversion motion, according to the geometric theory of Schatz [233]. Then, lower and upper faces of the cylindrical WC-Co mould with 10 mm in diameter (for clarity please see Figure 26) were covered with graphite paper to prevent the adhesion of metallic powder to the mould. The cavity was then filled with 1g of powder mix. The chamber of the PECS instrument was evacuated to a vacuum $\approx 10^{-3}$ mbar, the pressure of 500 MPa was applied and the temperature was elevated. The powder's characteristic temperatures important for determining the consolidation temperature are given in Table 1. The consolidation temperature of 473 K was chosen, since it lies within the SCL region of both ribbons, while simultaneously being lesser than the T_x of both powders. A 3 min heat-up programme was used to reach 473 K with the uncertainty of end temperature $\approx \pm 10$ K, followed by 10-15 min until the temperature dropped to the vicinity of RT. Finally, the upper and the lower faces of MG cylinder were polished with SiC paper grade 1200 to remove the graphite paper.

Table 1: Characteristic temperatures of Ce- and Gd-based ribbons, along with those of the consolidated composite BMG.

Characteristic temperatures	$(Al_{1-x}Ce_x)_{62}Fe_{13}Cu_{25}$; x=0.75	$(Al_{1-x}Gd_x)_{62}Fe_{13}Cu_{25}$; x=1	50 wt% of Ce-based x=0.75, 50 wt% of Gd-based x=1
T_g(K)	433	467	463
T_x(K)	477	483	483
SCL (K)	44	16	20

4.3.1 XRD measurements

Structure of the powders and consolidated discs was verified with XRD measurements. For the characterisation of powders, the latter were spread on the surface of Si zero background holder. In the case of bulk piece, structural information is obtained from a circular face with the diameter of ≈10 mm, being perpendicular to the pressing direction. Since the powders manifest shape anisotropy with thickness (z-axis of the ribbon) of ≈30 μm and sizes in x- and y-axis (notations delineated in Figure 13b) of up to 250 μm, they stack preferentially in the mould. This was confirmed with optical microscopy, which was carried out on the sample, prepared in cross section, i.e. cut parallel with the direction of pressing. Therefore, X-rays penetrate through the bulk in the direction normal to FS or WS of the ribbon.

Figure 40 shows the diffraction patterns of the initial Ce-based x=0.75 powder and Gd-based x=1 powder as well as the pattern of a composite BMG containing 50 wt% of Ce-based x=0.75 and 50 wt% of Gd-based x=1 ribbons. Glassy structure can be ascribed to all of the samples, characterized by its diffuse halos. In addition to the most intense humps at ≈34° of 2θ, secondary humps also appear at ≈57° of 2θ for all the patterns. This observation delineates the local structure of the glassy state, but its details are generally only accessible via PDF analysis, which is not performed here.

For the Ce-based glass x=0.75, first and second humps have maximums at 33.8° and 56.6° of 2θ, respectively. The first and second hump of Gd-based MG x=1 are located at 33.5° and 56.6° of 2θ, respectively. The positions of diffuse humps in the composite BMG are shifted towards higher values of 2θ compared to both constituents. Positions of the two strongest humps are located at 34.9° and 57.5° of 2θ, meaning that they are ≈1° shifted towards higher 2θ values and made of individual humps in Ce- and Gd-based powders. Some overlapping is present since the shape of the most intense hump (Figure 40) in a composite BMG is smeared over the larger 2θ range, compared to individual powders. By conversion to Q-space, where $Q=4\pi\sin\theta/\lambda$, whereas λ is the wavelength of the X-ray radiation used (CuKα=0.15406 nm), the Q-values of the maximums of the most intense humps are retrieved. In reciprocal space, they appear at $Q_1=23.7$ nm^{-1} for Ce-based x=0.75 and $Q_2=23.5$ nm^{-1} for Gd-based x=1, while the composite BMG exhibits $Q_3=24.4$ nm^{-1}. This suggests that the SRO of the composite BMG is not solely a combination of both ribbons. Consolidation with PECS brings the glasses in their SCL regions, where the atomic mobility is increased [234] and the structure of the glass relaxes [235], which can change the SRO structure. The shift of the most intense hump towards higher Q implies that the average interatomic distances in the SRO cluster decrease, not least due to structural rearrangements in MG ribbons.

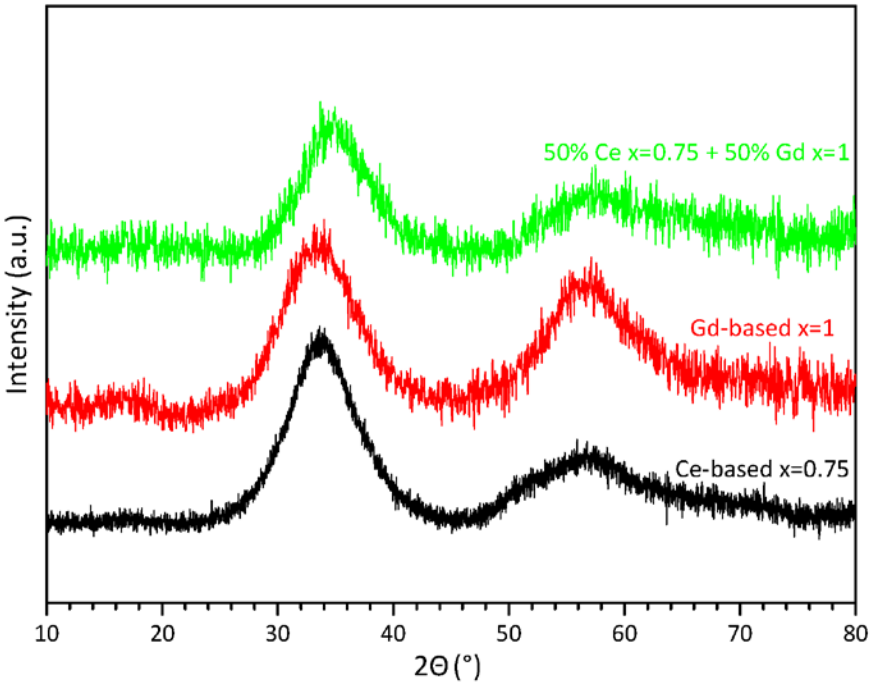

Figure 40: XRD patterns (using CuKα anode with the wavelength λ=0.15406 nm) of Ce-based x=0.75 ($(Al_{1-x}Ce_x)_{62}Fe_{13}Cu_{25}$) ribbons (black line), Gd-based x=1 ($(Al_{1-x}Gd_x)_{62}Fe_{13}Cu_{25}$) ribbons (red line) and composite BMG, made of 50:50 wt% of both ribbons (green line).

4.3.2 Thermal analysis

DSC scans in Figure 41 show the thermal behaviour of Ce- and Gd-based powders along with the scan of the composite BMG. As shown in the plot, T_g and T_x of Ce- and Gd-based powders are compatible, simultaneously enabling the consolidation of BMG and preservation of the glassy structure. The latter temperatures amount to 433 K and 477 K for Ce-based powder and 467 K and 483 K for Gd-based powder. The widths of SCL regions equal 44 K and 16 K for Ce- and Gd-based powders, respectively. Such overlap was sufficient to facilitate thermoplastic forming of the ribbons at a processing temperature of 473 K. Regarding other events in the DSC scans, there is another exothermal peak, which occurs in both RE-based powders and it is associated with secondary crystallisation. With the continuous rise in temperature, we arrive at solidus temperature-T_m, which exhibits multiple endothermal peaks in the case of Ce-based x=0.75, but only one single endothermal peak (with a relatively short tail) in the case of the Gd-based x=1 MG. However, these events are not crucial in terms of preparing the BMG specimen.

In a DSC scan of the composite BMG (green curve in Figure 41), T_g and T_x are located at 463 K and 483 K, which more closely resembles the nature of Gd-based powders than it does the Ce-based ones. This result is interesting since it indicates that T_g of a Ce-based constituent in BMG into the viscous state is retarded by ≈30 K. In addition, it is unusual that there is only one T_g peak, whereas one could expect that T_g from Ce-and Gd-based ribbons would yield a two-step kink in the heat flow signal. In spite of that, the last observations are in accordance with similar reports on the thermal behaviour of consolidated BMG made of two different ribbons [236]. Regarding the shift in T_x, the onset

moves from 477 K for the Ce-based glass to 483 K for a composite BMG, which again is found to follow preferentially the behaviour of a Gd-based constituent.

Relative intensities of exothermic peaks are more-or-less equal in the case of a composite BMG, whereas their relative intensities in the case of RE-based powders vary. In both, the first exothermic peak is more intense than the second one. The occurrence of at least four distinct exothermal peaks in the composite BMG suggests that the specimen is made of different kinds of glasses. Their positions in general match those of Ce- and Gd-based powders, except for the peak at ≈578 K, which cannot be observed in any of the two ribbons.

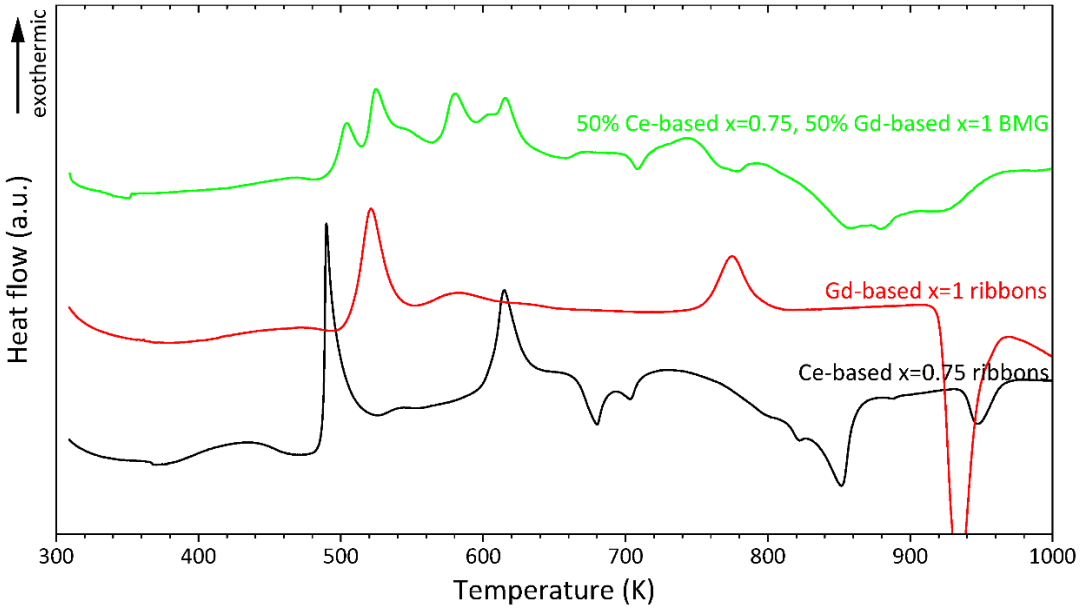

Figure 41: DSC scans of Ce-based x=0.75 powder ($(Al_{1-x}Ce_x)_{62}Fe_{13}Cu_{25}$), Gd-based x=1 powder ($(Al_{1-x}Gd_x)_{62}Fe_{13}Cu_{25}$) and a composite BMG, made of 50 wt% of Ce-based and 50 wt% of Gd-based ribbons.

4.3.3 TEM characterisation

To analyse the microstructure of composite BMG, TEM investigation of the interface between Ce- and Gd-based sample regions was performed. HAADF micrograph and EDS analyses are shown in Figure 42. EDS mapping in Figure 42b reveals the RE constituents in the adjacent ribbons, whereas blue and yellow dots represent Ce and Gd, respectively. From this elemental map, a clear threshold between the ribbons can be observed.

Green marker in Figure 42a shows a linear analysis of the interface between the two parts of the specimen. The region, from which the data was retrieved, is shown with the green transparent rectangle, superimposed on top of the micrograph, measuring ≈ 0.5 μm^2 in the area. The results of this line scan are visualized in Figure 42c, where the concentrations of elements are plotted against the position. The intensity of the HAADF signal has a dedicated scale on the right-hand side in order to enable better visualization for the rest of the data. The variation of HAADF signal intensity is connected with a varying thickness on the edge of the ribbon.

As we approach the end of the Ce-based region (Figure 42c), the concentration of Ce rapidly declines. The same is valid for Cu, Fe, and Al, although their counts differ due to different composition and different energy-scattering properties of the atomic species. In the EDS line profile, the central point, i.e. the boundary between the ribbons, where the concentration of the majority of the elements features a minimum is found at approximately 500 pixels. Further on, elements of Gd, Fe and Cu feature a rising trend (with different slopes), while Ce and Al are constant. The latter two are absent in the composition of Gd-based ribbon, which justifies their steadiness. A detail that needs to be mentioned is that the concentration of Gd starts increasing even before the central point at 500 pixels. Reason for this is tilted interface, which hides a part of Gd-based ribbon below the Ce-based one. This results in a higher signal of Gd, when still in the region of Ce-based ribbons.

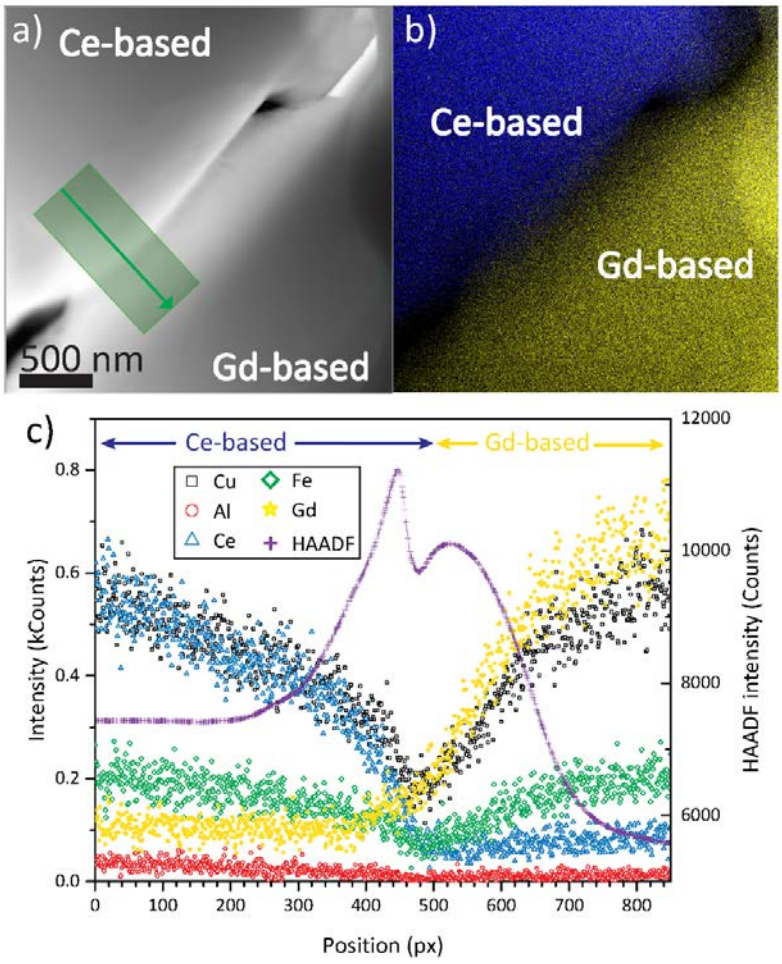

Figure 42: a) Linear EDS analysis of the interface between Ce- and Gd-based ribbons. The marker shows the area of data acquisition. b) EDS maps of Ce (blue dots) and Gd (yellow dots). c) Line profile of the area marked in a), HAADF data is shown with the scale on the right, whereas other data is viewed with an intensity scale on the left side of the diagram.

4.3.4 Magnetic properties of the composite BMG

Magnetic properties measured with VSM are conducted in a similar way to previous investigations, i.e. XRD and DSC. The characterisation is made on Ce- and Gd-based ribbons and also on the consolidated BMG. Magnetic hysteresis loops are shown in Figure 43. Ce-based x=0.75 ribbons feature PM behaviour distinguished by the linear dependence of magnetisation with changing magnetic field (inset of Figure 43) and the lack of coercivity. Maximum magnetisation at 18 kOe of an external field, M_{18kOe}, reaches 0.8 emu/g. Gd-based MG x=1, in contrast, exhibits FM-like or SPM-like behaviour, due to S-shaped hysteresis loop. M_{18kOe} of 15.8 emu/g is obtained, a value almost 20 times higher than that of Ce-based glass. Composite BMG is a mix of both kinds of magnetic behaviours. Its M_{18kOe} is measured to be 8.7 emu/g, and the hysteresis loop preserves the FM-like response of Gd-based ribbons. The theoretical mean magnetisation of a composite with exactly 50:50 wt% of Ce- and Gd-based ribbons is 8.3 emu/g, which is not significantly different from the measured value of 8.7 emu/g. The coercivity of the samples is lower than 100 Oe, indicating soft FM-like behaviour for Gd-based ribbons and composite BMG. These results are consistent with different fundamental nature of Ce- and Gd-based ribbons, which stems from different magnetic properties of Ce and Gd.

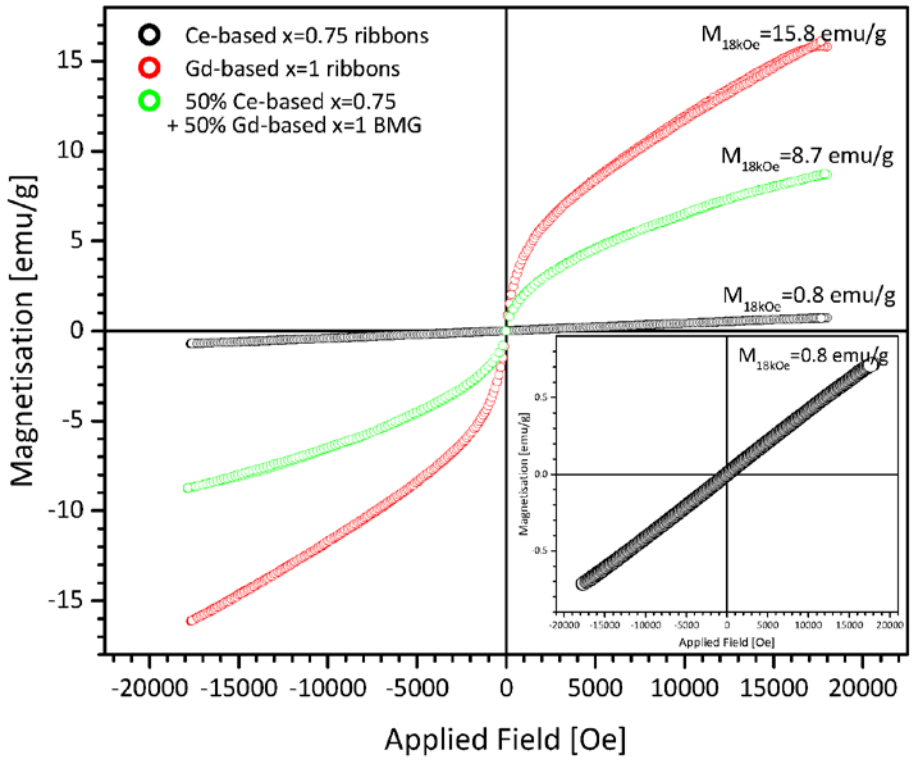

Figure 43: Magnetic hysteresis loops of Ce-based x=0.75 ($(Al_{1-x}Ce_x)_{62}Fe_{13}Cu_{25}$) ribbons, Gd-based x=1 ($(Al_{1-x}Gd_x)_{62}Fe_{13}Cu_{25}$) ribbons and a composite bulk MG, made of 50 wt% of Ce-based and 50 wt% of Gd-based ribbons. The inset shows the M(H) curve of Ce-based x=0.75 ribbons on a magnified scale.

4.4 Discussion of the Properties of Ce- and Gd-Based Alloys

Ce and Gd REs differ most prominently by their contrasting magnetic moments, amounting to 2.54 μ_B for fcc 3^+ Ce and three times higher for that of hcp Gd, at 7.63 μ_B. Their crystalline structures differ as well, which brings about the question of how these fundamental properties adapt in a multicomponent alloy. The families of alloys studied within this doctoral work are designed so as to contain variable fractions of the two REs, with respect to Al metal. Two additional elements that constitute the quaternary alloys are Fe and Cu.

Structure of Ce-based alloys exhibits a ratio x=RE/(RE+Al), where RE=Ce. When the ratio x lies near x=0.75, alloy vitrification is favoured over crystallisation. This coincides with the occurrence of low-temperature eutectic in Al-Ce system at 72.5 at% ref. [75], justifying the improved glass formability for x=0.75. In a series of Gd-based alloys exists a similar ratio x, for RE=Gd, where alloys hinder crystallisation for certain x ratios. It is found that the ratio x of the strongest glass formers appears in the vicinity of x=0.67. The explanation of superior GFA near this composition is the vicinity of binary eutectic in Al-Gd diagram, which is located at 77 at% Gd [224]. Both REs exhibit a similar ratio of x for the formation of strong glass, whereas the strongest Ce-based glass is shifted for 6 at% and Gd-based glass for 10 at% from the eutectic compositions in respective Al-RE binary diagrams. This discrepancy arises due to the compositional complexity of the quaternary systems and step-wise variation of ratio x, which equals 8-9 at%. For x values lower and higher than $0.58 \leq x \leq 0.75$, alloys tend to form crystallites (as deduced from XRD patterns) along with the glassy matrix. These results can be interpreted with the observation of the liquidus line in both Al-Ce and Al-Gd binary diagrams. Whereas it is lowered to 900 K and 1100 K for near-eutectic compositions, it can increase up to 1500 K and 1600 K for 50 at% and 1100 K and 1600 K for 100 at% of Ce and Gd, respectively. Bearing in mind that quenching temperature is approximately equivalent for all compositions ($\approx$1600 K), the temperature span of the liquid is much smaller for alloys closer to x=0.5 and x=1.

For both Ce- and Gd-based ribbons it is found that the structure on the WS differs from the one on the ribbons' FS. It is due to the fact that WS is in direct contact with the wheel, where the cooling rate is greater compared to FS. Hence, more crystalline reflections are observed in the patterns from FS, since this data originates from PD of 14 μm and 10 μm for the alloys with x=0.5 (having the highest PD of X-rays) in Ce- and Gd-based systems, respectively. XRD patterns of powder are a combination of WS and FS contributions, due to random orientations of the powder particles, and as such, they display the average structure.

The crystallisation of Ce-based x=0.75 glass results in the formation of a hexagonal $AlCe_3$ phase, whose stoichiometry corresponds to the same, nominal ratio x, between Ce/(Ce+Al). A small quantity of cubic Fe_2Ce reflections and several unidentified peaks appear in the pattern, implying a complex solidification sequence of the quaternary alloy.

SRO atomic arrangements in Gd-based alloys show a decrease in Q_M with higher amounts of Gd. Since Q space represents the inverse of real space, the average interatomic distance in the glassy phase, however, increases with more Gd. Considering the size of Gd atom (0.1795 nm), which is considerably larger than that of Al (0.1429 nm), Fe (0.1260 nm) and Cu (0.1276 nm) [111], a reasonable explanation can be given. The incorporation of a bigger atom, such as Gd in the quaternary alloy, causes a rearrangement of the atomic positions in SRO clusters in order to maintain the structure. Since the amount of Gd in MG increases significantly, from 31 at% to 62 at%, and its atomic radius is 25-40 % larger compared to the neighbouring atomic species, it is reasonable to anticipate an increase in the average interatomic distance within the SRO cluster [237].

Consolidation of BMG in the case of Ce-based x=0.75 is eased by the large-enough SCL range, which in conjunction with rapid processing in PECS hinder the crystallisation and preserve the glassy structure. A threshold temperature for the consolidation in PECS to bypass the formation of crystallites is in line with T_x as found by the DSC scan. Material characteristics of Ce-based x=0.75 in the process of thermoplastic deformation in its SCL region are appropriate to allow densification of the ribbons into cylindrical compacts. Meanwhile, the same does not apply for Gd-based glass x=0.75 where the behaviour of the material in its SCL range does not facilitate strong-enough cohesion between the ribbons in PECS processing and the fabrication of BMG is not possible. Reasons for this difference could not be elucidated, however, they could originate in the dissimilar plasticity of the glasses in their SCL regions, resulting in higher brittleness of Gd-based glasses [238].

Formation of the glassy phase in alloys with variable amounts of immiscible Fe and Cu depends on the ratio y. Higher additions of Fe decrease the GFA, which is reflected in the appearance of crystallites within the glassy matrix. The understanding of a decrease in GFA can be obtained from binary Fe-Cu diagram [239], where higher concentrations of Fe result in ≈100 K higher T_l compared to Cu-rich binary compositions. If this situation is transferred to the series of quaternary alloys within $0 \leq y \leq 1$, a similar trend is observed. T_l of Fe-rich alloys near y=1 is ≈200 K higher than that of Cu rich alloys in the vicinity of y=0. For the family of alloys within $0 \leq y \leq 1$, lower T_l thus correlates with the ease of glass formation.

Thermal analysis depicts the transition of alloys from the metastable glassy state to the crystalline state. Temperature T_g is reduced when adding more RE, from 200 K to 100 K for Ce- and Gd-based alloys, respectively. These findings are in agreement with similar reports on Ce- [214] and Gd-containing [240] glasses. Although it was proposed that T_g decreases with having the alloy-composition near the eutectic region [241], this rule does not apply to the families of RE-containing alloys, studied herein. The predominant factor for the decrease of T_g in MGs studied within this work is the increase in RE content, an observation in line with the reports of other researchers [214]. The reasons for such behaviour are not well understood yet, however, they may originate in the peculiar electronic structure of RE. MGs tend to crystallise in close proximity to T_g, which sets them apart from common oxide glasses. In this respect, it is of no surprise to encounter T_x in the vicinity of T_g [242]. In the studied series of RE-based alloys, the T_x precedes T_g by 10-50 K, whereas the amorphous solids without the observable T_g, have T_x below that of T_g or in close nearness so that the transformation is much faster than the accessible tracing of ϕ in a DSC measurement. A decrease of T_x with higher additions of RE is in line with the similar trend for T_x. Variations of T_m and T_l are not consistent with the change in Ce and Gd contents. On the other hand, the increase of ratio y towards the higher amount of Fe yields higher T_x, T_m, and T_l. The latter is due to the higher melting point of Fe, whose content increases.

Magnetic properties, which present the core difference between Ce and Gd metals, are found to be connected with the nature of RE itself, nevertheless, the role of RE hybridisation is important in the occurrence of different magnetic states. The magnetisation of Ce-based alloys within the composition landscape, where $0.5 \leq x \leq 1$, fluctuates in the range 0.3-0.5 emu/g without direct correlation to the amount of Al and Ce, nor to the occurrence of crystallites. The coupling of magnetic moment-carrying atoms Fe and Ce in the SRO clusters is not significant enough to increase the magnetic anisotropy of the MG substantially. Low-temperature behaviour of the Ce-based specimen x=0.75 features a transition to AFM-like and spin-glass-like state. At T_b, magnetic spins freeze in an antiparallel arrangement, which results in the AFM-like state. The support of spin glass behaviour originates from a cusp at T_b, as well as ZFC and FC branches departing towards zero emu/g Oe and a steady increase of χ_{mass}, respectively.

On the contrary, Gd-based alloys demonstrate about two orders of magnitude higher M compared to Ce-based equivalents. Magnetisation increases in the range ≈4-16 emu/g with higher content of Gd. M(H) behaviour of the loops turns from PM to FM-like, visualised through a change of the hysteresis loop's shape from linear to S-shaped. The threshold stoichiometry where this transition occurs at RT is between x=0.67, exhibiting PM behaviour and x=0.75, which shows FM-like behaviour.

Low-temperature $\chi_{mass}(T)$ measurements on Gd-based alloys demonstrate that transition temperature T_{cr}, in fact, lies at temperature, significantly lower than that of RT. It is observed at 80-120 K, which is some 200 K lower than RT. Increase in χ_{mass} up to T_b is in line with the appearance of RMA in the glassy microstructure [219], when thermal fluctuations allow reorientations of the spins, so as to result in higher susceptibility. Due to SRO and MRO structure of the glass, there is no long-range magnetic order [243]. After the Gd-based alloys pass below the threshold T_b temperature, thermal fluctuations are stopped, and the magnetic spins in the AFM state are locked-in, which continues with a decrease in χ_{mass}.

Investigation of the microstructure with TEM shows that Ce-based alloy x=0.75 is able to completely hinder the crystallisation. TEM micrograph without any sign of LRO and SAED containing only the diffuse ring witness the completely glassy structure of this MG. Gd-based glasses x=0.75 or x=0.67, meanwhile, cannot fully bypass crystallisation using a comparable set of experimental parameters. A thin layer of crystals forms on the FS of the ribbon. In the TEM micrograph, some regions exhibit a fully glassy phase, while other regions contain crystallites within the glassy matrix. SAED patterns of the latter region confirm this through multiple sets of diffraction spots, along with the diffuse rings of the glassy region. Interplanar values in SAED indicate that the occurring precipitates are cubic Gd_2O_3 crystallites, most likely formed during sample preparation.

A composite BMG was fabricated using the PECS technique through thermoplastic consolidation of two comparable Ce- and Gd-based glasses, with x=0.75 and x=1, respectively. The similar temperature of the SCL region represents a pre-requisite for obtaining a dense compact with retained glassy structure, as it is confirmed through XRD measurements. In a DSC scan, the composite preferentially follows the behaviour of Gd-based alloys, since T_g and T_x of the composite display a lag of ≈30 K, compared to the Ce-based glass. This is the consequence of a mixed composition, which averages out the individual effects, resulting in less sharp and less intense peaks. The quantity of the peaks in a composite BMG, though, is a summation of both RE-based systems. Magnetic properties-wise, BMG is an average of both systems. The magnetisation is just slightly above the calculated value of 8.3 emu/g, whereas the nature of the magnetic system is FM, deduced according to the Gd-based component. A study that was not conducted but whose results would be fundamentally interesting is the characterisation of low-temperature ZFC-FC curves in order to elucidate whether the cryogenic behaviour is related to one particular RE or the behaviour is more complex.

Chapter 5

Conclusions

In the alloys where Al and Ce are varied with ratio x=Ce/(Ce+Al), it can be observed that the strongest glasses are formed for compositions in vicinity of x=0.75. Successful hindering of the crystallisation stems from the fact that the latter compositions lie near the binary eutectic in the Al-Ce phase diagram and feature T_l as low as 900 K. Compositions with more or less Ce exhibit crystalline reflections in the XRD patterns, suggesting the presence of crystallites in the glassy matrix. Regarding the thermal properties, Ce-rich glasses exhibit extremely low T_g, equalling 350 K for x=1, which subsequently increases with lesser amounts of Ce. Characteristic temperature T_x follows that of T_g and a similar, decreasing trend with more Ce can be observed for T_m. T_l, on the other hand, increases with higher additions of Ce.

Detailed XRD measurements of Ce-glasses on both sides, free (FS) and wheel (WS) sides, show that the tendency towards crystallisation is stronger on FS since the latter has a lower cooling rate. Synchrotron light diffraction data shows that the primary phase to crystallise from Ce-based glassy ribbons x=0.75 is a hexagonal $AlCe_3$.

Since the elastic modulus and hardness of Ce are inferior to those of Al, higher additions of Ce decrease the mechanical properties. Exception from this rule is x=1, which contains a considerable amount of Ce-rich crystallites in the glassy matrix, that act as strengthening points of the composite glass.

In contrast to Ce-based alloys, the structure of Gd-based alloys is more susceptible to crystallisation, even for the compositions, whose ratio x=Gd/(Gd+Al) belongs to the eutectic region of the Al-Gd diagram. FS of Gd-containing alloys with x near 0.67 contain a minor amount of crystallites, whereas WS is completely vitrified. Mean interatomic distance in these glasses increases with higher additions of Gd, due to the large atomic size of Gd.

Thermal measurements outline very low T_g of Ce-based alloys, amounting to a value as low as 350 K for x=1. T_g is followed by T_x, with a lag of ≈50 K, a value corresponding to the average width of the SCL region. Parameters T_g, T_x and T_m decrease with more Ce, while T_l is higher for alloys with increasing content of Ce. Compared to Ce-based alloys, Gd-based counterparts exhibit higher T_g, T_x and T_m, originating from higher liquidus line in Al-Gd diagram, set against the one from Al-Ce diagram. Analogous to Ce-based alloys is also the general decrease of T_g, T_x and T_m with more Gd. The behaviour of T_l is different, and fluctuates between 1300 K and 1375 K.

As observed from TEM micrographs and SAED patterns, the microstructure of Ce-based alloy x=0.75 is completely glassy. Meanwhile, some Ce-poor and Ce-rich specimens exhibit crystallites within the glassy matrix. In Gd-based alloys, the strongest glasses appear around x=0.67, and similarly exhibit featureless microstructure and diffuse halo on TEM micrographs and SAED patterns, respectively. A minor quantity of Gd_2O_3 crystallites, however, was found to coexist in the glassy matrix of these Gd-alloys.

Magnetic behaviour of the two series of RE-containing alloys differs due to the strength of the magnetic moment carried by the respective RE. Ce-based alloys are paramagnetic at RT, and the variation in ratio x does not significantly influence the resulting magnetisation. At low temperature, their magnetic response is complex, having a critical

temperature T_{cr} in the range 80-123 K, manifested by a rapid increase of χ_{mass}. In the range 64-102 K, a transition at T_b to AFM-like state occurs, which is followed by the divergence of ZFC-FC curves, suggesting spin-glass-like behaviour. The magnetisation of Gd-based MGs strongly depends on the concentration of Gd, whereas higher quantity of Gd elevates the magnetisation. Gd-containing samples within $0.5 \leq x \leq 0.67$ are PM, while those containing more Gd are FM-like. Low-temperature behaviour of PM alloys is not monotonic, showing a rapid increase of χ_{mass} at T_{cr} and PM-AFM transition at T_b. Additionally, the divergence of ZFC-FC curves, convergence of the ZFC branch of χ_{mass} towards zero, as well as a steady decrease of the FC branch suggest RMA behaviour in these Gd containing MG.

Ce- and Gd-based glassy ribbons are consolidated into bulk metallic glass through thermoplastic consolidation with PECS technique. The process was conducted at a joint SCL temperature of 200°C, resulting in a glassy cylinders containing both kinds of ribbons. T_g and T_x of the composite exhibit a lag of ≈30 K, compared to individual ribbons, while the overall number of thermal events is more than doubled. Magnetic properties of the composite BMG are an intermediate between the properties of Ce- and Gd-based ribbons, with M at H_{18kOe} of 8.7 emu/g. Meanwhile, the magnetic ordering resembles that of Gd-based ribbons and exhibits FM-like response.

References

[1] H. S. Chen, "Glassy metals," *Rep. Prog. Phys*, vol. 43, pp. 1–84, 1980.

[2] S. R. Elliott, *Physics of Amorphous Materials*, 1st ed. New York: Longman Inc., 1984.

[3] E. D. Zanotto and J. C. Mauro, "The glassy state of matter: Its definition and ultimate fate," *J. Non. Cryst. Solids*, vol. 471, pp. 490–495, 2017.

[4] B. E. Warren, "The basic principles involved in the glassy state," *J. Appl. Phys.*, vol. 13, no. 10, pp. 602–610, 1942.

[5] D. B. Miracle, W. S. Sanders, and O. N. Senkov, "The influence of efficient atomic packing on the constitution of metallic glasses," *Philos. Mag.*, vol. 83, no. 20, pp. 2409–2428, 2003.

[6] M. K. Miller and P. Liaw, *Bulk Metallic Glasses: An Overview*. New York, USA: Springer Science+Business Media, LLC, 2008.

[7] D. Turnbull and M. H. Cohen, "Free-volume model of the amorphous phase: Glass transition," *J. Chem. Phys.*, vol. 34, no. 1, pp. 120–125, 1961.

[8] A. L. Greer and F. Spaepen, "Creep, Diffusion, and Structural Relaxation in Metallic Glasses," *Ann. N. Y. Acad. Sci.*, vol. 371, no. 1, pp. 218–237, 1981.

[9] W. Klement, R. H. Willens, and P. Duwez, "Non-crystalline Structure in Solidified Gold–Silicon Alloys," *Nature*, vol. 187, no. 4740, pp. 869–870, 1960.

[10] H. S. Chen, "Glass Temperature, Formation and Stability of Fe, Co, Ni, Pd and Pt Based Glasses," *Mater. Sci. Eng.*, vol. 23, no. 1976, pp. 151–154, 1976.

[11] H. S. Chen, "The glass transition temperature in glassy alloys: Effects of atomic sizes and the heats of mixing," *Acta Metall.*, vol. 22, no. 7, pp. 897–900, 1974.

[12] H. W. Kui, A. L. Greer, and D. Turnbull, "Formation of bulk metallic glass by fluxing," *Appl. Phys. Lett.*, vol. 45, no. 6, pp. 615–616, 1984.

[13] A. J. Drehman, A. L. Greer, and D. Turnbull, "Bulk Formation of a Metallic Glass: Pd40Ni40P20," *Appl. Phys. Lett.*, vol. 41, no. 8, pp. 716–717, 1982.

[14] A. Inoue and A. Takeuchi, "Recent development and application products of bulk glassy alloys," *Acta Mater.*, vol. 59, no. 6, pp. 2243–2267, 2011.

[15] A. Inoue, N. Nishiyama, and H. Kimura, "Preparation and thermal stability of Bulk Amorophous Pd40Cu30Ni10P20 alloy cylinder of 72 mm in diameter," *Materials Transactions-JIM*, vol. 38. pp. 179–183, 1997.

[16] C. Suryanarayana and A. Inoue, *Bulk Metallic Glasses*, 2nd ed. Boca Raton, Florida, USA: CRC Press Taylor & Francis Group, 2017.

[17] Y. H. Liu, G. Wang, R. J. Wang, D. Q. Zhao, M. X. Pan, and W. H. Wang, "Super Plastic Bulk Metallic Glasses at Room Temperature," *Science (80-.).*, vol. 315, no.

5817, pp. 1385–1388, Mar. 2007.

[18] A. Inoue, "Stabilization of metallic supercooled liquid and bulk amorphous alloys," *Acta Mater.*, vol. 48, no. 1, pp. 279–306, 2000.

[19] M. A. Willard, J. C. Claassen, R. M. Stroud, T. L. Francavilla, and V. G. Harris, "(Ni,Fe,Co)-based nanocrystalline soft magnets with near-zero magnetostriction," *IEEE Trans. Magn.*, vol. 38, no. 5, pp. 3045–3050, 2002.

[20] A. Makino, T. Hatanai, A. Inoue, and T. Masumoto, "Nanocrystalline soft magnetic Fe-M-B (M = Zr, Hf, Nb), alloys and their applications," *Mater. Sci. Eng. A*, vol. 226–228, no. 5, pp. 594–602, Jun. 1997.

[21] G. Kumar, P. A. Staffier, J. Blawzdziewicz, U. D. Schwarz, and J. Schroers, "Atomically Smooth Surfaces through Thermoplastic Forming of Metallic Glass," *Appl. Phys. Lett.*, vol. 97, no. 10, p. 101907, 2010.

[22] W. L. Johnson, "Is metallic glass poised to come of age?," *Nature Materials*, vol. 14, no. 6. pp. 553–555, 2015.

[23] K. J. Laws, D. B. Miracle, and M. Ferry, "A predictive structural model for bulk metallic glasses.," *Nat. Commun.*, vol. 6, p. 8123, 2015.

[24] A. R. Yavari, "A new order for metallic glasses," *Nature*, vol. 439, no. 7075, pp. 405–406, 2006.

[25] H. W. Sheng, W. K. Luo, F. M. Alamgir, J. M. Bai, and E. Ma, "Atomic packing and short-to-medium-range order in metallic glasses," *Nature*, vol. 439, no. 7075, pp. 419–425, 2006.

[26] F. Zhu, A. Hirata, P. Liu, S. Song, Y. Tian, J. Han, T. Fujita, and M. Chen, "Correlation between Local Structure Order and Spatial Heterogeneity in a Metallic Glass," *Phys. Rev. Lett.*, vol. 119, no. 21, pp. 1–6, 2017.

[27] W. K. Luo, H. W. Sheng, F. M. Alamgir, J. M. Bai, J. H. He, and E. Ma, "Icosahedral short-range order in amorphous alloys," *Phys. Rev. Lett.*, vol. 92, no. 14, pp. 1–4, 2004.

[28] D. B. Miracle, D. V Louzguine-Luzgin, L. V Louzguina-Luzgina, and A. Inoue, "An assessment of binary metallic glasses: correlations between structure, glass forming ability and stability," *Int. Mater. Rev.*, vol. 55, no. 4, pp. 218–256, 2010.

[29] D. B. Miracle, "A physical model for metallic glass structures: An introduction and update," *JOM*, vol. 64, no. 7, pp. 846–855, 2012.

[30] D. B. Miracle, "The efficient cluster packing model - An atomic structural model for metallic glasses," *Acta Mater.*, vol. 54, no. 16, pp. 4317–4336, 2006.

[31] P. H. Gaskell, "Medium-range structure in glasses and low-Q structure in neutron and X-ray scattering data," *J. Non. Cryst. Solids*, vol. 351, no. 12–13, pp. 1003–1013, 2005.

[32] D. B. Miracle, "A structural model for metallic glasses," *Nat Mater*, vol. 3, no. 10, pp. 697–702, 2004.

[33] V. K. Pecharsky and P. Y. Zavalij, *Fundamentals of Powder Diffraction and Structural Characterization of Materials*, 2nd ed. New York, USA: Springer Science+Business Media, LLC, 2009.

[34] J. D. Bernal and J. Mason, "Packing of Spheres: Co-ordination of Randomly Packed Spheres," *Nature*, vol. 188, no. 4754, pp. 910–911, 1960.

[35] G. D. Scott, "Packing of Spheres: Packing of Equal Spheres," *Nature*, vol. 188, no. 4754, pp. 908–909, 1960.

[36] D. E. Polk, "The structure of glassy metallic alloys," *Acta Metall.*, vol. 20, no. 4, pp. 485–491, 1972.

[37] P. H. Gaskell, "A new structural model for transition metal–metalloid glasses," *Nature*, vol. 276, no. 5687. pp. 484–485, 1978.

[38] P. H. Gaskell, "A new structural model for amorphous transition metal silicides, borides, phosphides and carbides," *J. Non. Cryst. Solids*, vol. 32, no. 1–3, pp. 207–224, 1979.

[39] J. M. Dubois, P. H. Gaskell, and G. L. Caer, "A Model for the Structure of Metallic Glasses Based on Chemical Twinning," *Proc. R. Soc. A Math. Phys. Eng. Sci.*, vol. 402, no. 1823, pp. 323–357, 1985.

[40] D. B. Miracle, "On the universal model for medium-range order in amorphous metal structures," *J. Non. Cryst. Solids*, vol. 317, no. 1–2, pp. 40–44, 2003.

[41] N. J. A. Sloane, "Kepler's conjecture confirmed," *Nature*, vol. 395, pp. 435–436, 1998.

[42] A. R. Yavari, "Solving the puzzle of eutectic compositions with 'Miracle glasses,'" *Nat. Mater.*, vol. 4, no. 1, pp. 2–3, 2005.

[43] X. H. Lin and W. L. Johnson, "Formation of Ti-Zr-Cu-Ni bulk metallic glasses," *J. Appl. Phys.*, vol. 78, no. 11, pp. 6514–6519, 1995.

[44] Y. He, S. J. Poon, and G. J. Shiflet, "Synthesis and properties of metallic glasses that contain aluminum.," *Science*, vol. 241, no. 9, pp. 1640–1642, 1988.

[45] D. Malterre, G. Krill, J. Durand, G. Marchal, and M. F. Ravet, "Electronic configuration of cerium in amorphous alloys investigated by X-ray absorption spectroscopy," *Phys. Rev. B*, vol. 34, no. 4, pp. 2176–2181, 1986.

[46] W. Zhang, F. Jia, Q. Zhang, and A. Inoue, "Effects of additional Ag on the thermal stability and glass-forming ability of Cu-Zr binary glassy alloys," *Mater. Sci. Eng. A*, vol. 459, no. 1–2, pp. 330–336, 2007.

[47] A. I. Akira Takeuchi, "Calculations of Mixing Enthalpy and Mismatch Entropy for Ternary Amorphous Alloys," *Materials Transactions*, vol. 41, no. 11. pp. 1372–1378, 2000.

[48] A. L. Greer, "Confusion by design," *Nature*, vol. 366, no. 6453, pp. 303–304, 1993.

[49] R. J. Highmore and A. L. Greer, "Eutectics and the formation of amorphous alloys," *Nature*, vol. 339, no. 6223, pp. 363–365, 1989.

[50] R. F. Mehl, "Rates of diffusion in solid alloys," *J. Appl. Phys.*, vol. 8, no. 3, pp. 174–185, 1937.

[51] R. W. Cahn and P. Haasen, *Physical Metallurgy*, 4th ed. Amsterdam: Elsevier Science B.V, 1996.

[52] T. Egami and Y. Waseda, "Atomic size effect on the formability of metallic glasses," *J. Non. Cryst. Solids*, vol. 64, no. 1–2, pp. 113–134, 1984.

[53] D. B. Miracle and O. N. Senkov, "Topological criterion for metallic glass formation," *Mater. Sci. Eng. A*, vol. 347, no. 1–2, pp. 50–58, 2003.

[54] O. N. Senkov and D. B. Miracle, "A topological model for metallic glass formation," *J. Non. Cryst. Solids*, vol. 317, no. 1–2, pp. 34–39, 2003.

[55] O. N. Senkov, D. B. Miracle, and H. M. Mullens, "Topological criteria for amorphization based on a thermodynamic approach," *J. Appl. Phys.*, vol. 97, no. 10, pp. 1–8, 2005.

[56] M. H. Cohen and D. Turnbull, "Composition Requirements for Glass Formation in Metallic and Ionic Systems," *Nature*, vol. 189, no. 4759, pp. 131–132, 1961.

[57] W. L. Johnson, "Bulk Glass-Forming Metallic Alloys: Science and Technology," *MRS Bull.*, vol. 24, no. 10, pp. 42–56, 1999.

[58] T. B. Massalski, *Binary Alloy Phase Diagrams Volume 1*. American Society of Metals (ASM), 1986.

[59] P. Franke and D. Neuschütz, Eds., *Binary Systems. Part 5: Binary Systems Supplement 1*, vol. 19B5. Berlin, Heidelberg: Springer-Verlag, 2007.

[60] Y. P. Ma, D. D. Dong, C. Dong, L. J. Luo, Q. Wang, J. B. Qiang, and Y. M. Wang, "Composition formulas of binary eutectics," *Sci. Rep.*, vol. 5, pp. 1–16, 2015.

[61] Y. Li, "Bulk metallic glasses: Eutectic coupled zone and amorphous formation," *JOM*, vol. 57, no. 3, pp. 60–63, 2005.

[62] L. L. Shi, J. Xu, and E. Ma, "Alloy compositions of metallic glasses and eutectics from an idealized structural model," *Acta Mater.*, vol. 56, no. 14, pp. 3613–3621, 2008.

[63] D. Stockdale, "Numerical Relationships in Binary Metallic Systems," *Proc. R. Soc. A Math. Phys. Eng. Sci.*, vol. 152, no. 875, pp. 81–104, 1935.

[64] W. Hume-Rothery and E. Anderson, "Eutectic compositions and liquid immiscibility in certain binary alloys," *Philos. Mag.*, vol. 5, no. 52, pp. 383–405, 1960.

[65] H. Okamoto, "Al-Ce (Aluminum-Cerium)," *J. Phase Equilibria Diffus.*, vol. 32, no. 4, pp. 392–393, Aug. 2011.

[66] K. A. Gschneidner and F. W. Calderwood, "The Al-Gd (Aluminum-Gadolinium) system," *Bull. Alloy Phase Diagrams*, vol. 9, no. 6, pp. 680–683, 1988.

[67] A. Saccone, A. M. Cardinale, S. Delfino, and R. Ferro, "Gd-Al and Dy-Al Systems: Phase Equilibria in the 0 to 66.7 at.% Al Composition Range," *Zeitschrift für Met.*, vol. 91, pp. 17–23, 2000.

[68] Q. Chen and Z. Jin, "The Fe-Cu system: A thermodynamic evaluation," *Metall. Mater. Trans. A*, vol. 26, no. 2, pp. 417–426, Feb. 1995.

[69] S. Y. Wu, S. H. Wei, G. Q. Guo, J. G. Wang, and L. Yang, "Structural mechanism of the enhanced glass-forming ability in multicomponent alloys with positive heat of mixing," *Sci. Rep.*, vol. 6, no. November, p. 38098, 2016.

[70] S. P. Sun, D. Q. Yi, H. Q. Liu, B. Zang, and Y. Jiang, "Calculation of glass forming ranges in Al-Ni-RE (Ce, La, Y) ternary alloys and their sub-binaries based on Miedema's model," *J. Alloys Compd.*, vol. 506, no. 1, pp. 377–387, 2010.

[71] L. Battezzati, G. Borzone, and G. Cacciamani, "Thermodynamic investigation on glass forming AI-RE Systems," *J. Chim. Phys.*, vol. 90, pp. 261–268, 1993.

[72] K. A. Gschneidner and F. W. Calderwood, "The AI-RE (Aluminum-Rare Earth) Systems," *Bull. Alloy Phase Diagr.*, vol. 9, no. 6, pp. 658–668, 1988.

[73] Q. Zeng, H. Sheng, Y. Ding, L. Wang, W. Yang, J.-Z. Jiang, W. L. Mao, and H.-K. Mao, "Long-Range Topological Order in Metallic Glass," *Science (80-.).*, vol. 332, no. 6036, pp. 1404–1406, 2011.

[74] Q. S. Zeng, Y. Ding, W. L. Mao, W. Yang, S. V. Sinogeikin, J. Shu, H. K. Mao, and J. Z. Jiang, "Origin of pressure-induced polyamorphism in Ce75Al25 metallic glass," *Phys. Rev. Lett.*, vol. 104, no. 10, pp. 1–4, 2010.

[75] B. Predel, "Al – Ce (Aluminum – Cerium)," in *Landolt-Börnstein New Series IV/12A Phase Equilibria, Crystallographic and Thermodynamic Data of Binary Alloys , Ac-Ag to Au-Zr, Supplement to IV/5A*, vol. 12A, B. Predel, Ed. Springer, 2006, pp. 157–158.

[76] D. A. Atwood, *The Rare Earth Elements: Fundamentals and Applications*. Chichester, UK: Wiley, 2013.

[77] K. A. Gschneidner, L. Eyring, and G. H. Lander, *Handbook on the Physics and Chemistry of Rare Earths*, vol. 32. Elsevier Science B.V, 2001.

[78] W. Klemm and H. Bommer, "Zur Kenntnis der Metalle der seltenen Erden," *Zeitschrift fur Anorg. und Allg. Chemie*, vol. 231, no. 1–2, pp. 138–171, 1937.

[79] H. J. Nolting, C. R. Simmons, and J. J. Klingenberg, "Preparation and properties of high purity yttrium metal," *J. Inorg. Nucl. Chem.*, vol. 14, no. 3–4, pp. 208–216, 1960.

[80] J. L. Moriarty, "The Industrial Preparation of the Rare Earth Metals by Metallothermic Reduction," *J. Miner. Met. Mater. Soc.*, vol. 20, no. 11, pp. 41–45, 1968.

[81] A. H. Daxne and F. H. Spedding, "Preparation of Yttrium and Some Heavy Rare Earth Metals," *J. Electrochem. Soc.*, vol. 100, no. 10, pp. 442–444, 1953.

[82] Jefferson Lab, "It's Elemental - The Element Gadolinium." [Online]. Available: https://education.jlab.org/itselemental/ele064.html. [Accessed: 15-Mar-2018].

[83] G. B. Haxel, J. B. Hedrick, and G. J. Orris, "Rare Earth Elements — Critical Resources for High Technology," *United States Geol. Surv. Fact Sheet*, vol. 87, p. 4, 2002.

[84] M. E. Weeks, "The discovery of the elements XI. Some elements isolated with the aid of potassium and sodium: Zirconium, titanium, cerium, and thorium," *J. Chem. Educ.*, vol. 9, no. 7, p. 1231, 1932.

[85] N. Krishnamurthy and C. K. Gupta, *Extractive metallurgy of rare earths*. Boca Raton, Florida, USA: CRC Press, 2005.

[86] Hillebrand and Norton, "Ueber metallisches Cer, Lanthan und Didym," *Ann. der Phys. und Chemie*, vol. 232, no. 11, pp. 466–476, 1875.

[87] W. M. Haynes, D. R. Lide, and T. J. Bruno, *CRC handbook of chemistry and physics, 96th Edition*. Boca Raton, Florida, USA: CRC Press/Taylor and Francis, 2015.

[88] Jefferson Lab, "It's Elemental - The Element Cerium." [Online]. Available: https://education.jlab.org/itselemental/ele058.html. [Accessed: 15-Mar-2018].

[89] J. C. Slater, "Atomic radii in crystals," *J. Chem. Phys.*, vol. 41, no. 10, pp. 3199–3204, 1964.

[90] F. Decremps, L. Belhadi, D. L. Farber, K. T. Moore, F. Occelli, M. Gauthier, A. Polian, D. Antonangeli, C. M. Aracne-Ruddle, and B. Amadon, "Diffusionless phase transition in polycrystalline and single-crystal cerium," *Phys. Rev. Lett.*, vol. 106, no. 6, pp. 1–4, 2011.

[91] M. J. Lipp, D. Jackson, H. Cynn, C. Aracne, W. J. Evans, and A. K. McMahan, "Thermal Signatures of the Kondo Volume Collapse in Cerium," *Phys. Rev. Lett.*, vol. 101, no. 16, pp. 1–4, 2008.

[92] Q. S. Zeng, Y. Z. Fang, H. B. Lou, Y. Gong, X. D. Wang, K. Yang, A. G. Li, S. Yan, C. Lathe, F. M. Wu, X. H. Yu, and J. Z. Jiang, "Low-density to high-density transition in Ce75Al23Si2 metallic glass," *J. Phys. Condens. Matter*, vol. 22, no. 37, p. 375404, 2010.

[93] B. Johansson, "The - transition in cerium is a Mott transition," *Philos. Mag.*, vol. 30, no. 3, pp. 469–482, 1974.

[94] K. A. Gschneidner, R. O. Elliott, and R. R. McDonald, "Effects of alloying additions on the transformation of cerium—Part I. Pure cerium," *J. Phys. Chem. Solids*, vol. 23, no. 6, pp. 555–566, 1962.

[95] D. A. Young, *Phase diagrams of the elements*. University of California Press, 1991.

[96] D. C. Koskimaki, "Some low-temperature properties of cerium," PhD Thesis, Iowa State University, 1973.

[97] J. Jensen and A. R. Mackintosh, *Rare Earth Magnetism; Structures and Excitations*. Oxford: Clarendon Press, 1991.

[98] J. M. Lock, "The Magnetic Susceptibilities of Lanthanum, Cerium, Praseodymium, Neodymium and Samarium, from 1.5°K to 300°K," *Proc. Phys. Soc. Sect. B,* vol. 50, no. 6, pp. 566–576, 1957.

[99] L. Kelhar, J. Ferčič, M. Maček-Kržmanc, J. Zavašnik, S. Šturm, P. Koželj, S. Kobe, and J.-M. J.-M. Dubois, "The role of Fe and Cu additions on the structural, thermal and magnetic properties of amorphous Al-Ce-Fe-Cu alloys," *J. Non. Cryst. Solids*, vol. 483, pp. 70–78, 2018.

[100] C. A. Welsbach, "Pyrophoric alloy," United States Patent Office, No. 837,017, 1903.

[101] J. H. L. Voncken, *The Rare Earth Elements: An Introduction*. Springer, 2016.

[102] K. Binnemans and P. T. Jones, "Rare Earths and the Balance Problem," *J. Sustain. Metall.*, vol. 1, no. 1, pp. 29–38, 2015.

[103] Z. C. Sims, D. Weiss, S. K. McCall, M. A. McGuire, R. T. Ott, T. Geer, O. Rios, and P. A. E. Turchi, "Cerium-Based, Intermetallic-Strengthened Aluminum Casting Alloy: High-Volume Co-product Development," *JOM*, vol. 68, no. 7, pp. 1940–1947, 2016.

[104] J. Gadolin, "Undersökning af en svart tung stenart ifrån Ytterby stenbrott i Roslagen.," *K. Sven. Vetenskapsak. Handl.*, vol. 15, pp. 137–155, 1794.

[105] C. H. Evans, *Episodes from the History of the Rare Earth Elements*. Dordrecht: Springer Netherlands, 1996.

[106] "Gadolinium: the essentials," *[WebElements Periodic Table]*, 2018. [Online]. Available: https://www.webelements.com/gadolinium/. [Accessed: 24-Mar-2018].

[107] F. H. Spedding, H. A. Wilhelm, W. H. Keller, D. H. Ahmann, A. H. Daane, C. C. Hach, and R. P. Ericson, "Production of Pure Rare Earth Metals," *Ind. Eng. Chem.*, vol. 44, no. 3, pp. 553–556, 1952.

[108] F. H. Spedding and A. H. Daane, "Production of Rare Earth Metals In Quantity Allows Testing of Physical Properties," *JOM*, vol. 6, no. 5, pp. 504–510, 1954.

[109] R. G. Jordan and D. W. Jones, "The purification of the rare-earth metals: I. Solid

state electrolysis of gadolinium," *J. Less-Common Met.*, vol. 31, no. 1, pp. 125–141, 1973.

[110] D. E. Newton and K. J. Edgar, *Chemical elements*, 2nd ed. Farmington Hills: Gale, Cengage Learning, 2010.

[111] L. Pauling, "Atomic Radii and Interatomic Distances in Metals," *J. Am. Chem. Soc.*, vol. 69, no. 3, pp. 542–553, 1947.

[112] A. Jayaraman and R. C. Sherwood, "Pressure-induced phase transformation in gadolinium and its effect on the magnetic behavior," *Phys. Rev. Lett.*, vol. 12, no. 1, pp. 22–23, 1964.

[113] A. Jayaraman, "Solid-liquid and solid-solid transformations in the rare-earth metals at high pressures," *Phys. Rev.*, vol. 139, no. 3A, 1965.

[114] F. H. Spedding, J. J. Hanak, and A. H. Daane, "High temperature allotropy and thermal expansion of the rare-earth metals," *J. Less-Common Met.*, vol. 3, no. 2, pp. 110–124, 1961.

[115] J. Akella, G. S. Smith, and A. P. Jephcoat, "High-pressure phase transformation studies in gadolinium to 106 GPa," *J. Phys. Chem. Solids*, vol. 49, no. 5, pp. 573–576, 1988.

[116] D. Errandonea, R. Boehler, B. Schwager, and M. Mezouar, "Structural studies of gadolinium at high pressure and temperature," *Phys. Rev. B*, vol. 75, no. 1, p. 014103, 2007.

[117] W. A. Grosshans and W. B. Holzapfel, "Atomic volumes of rare-earth metals under pressures to 40 GPa and above," *Phys. Rev. B*, vol. 45, no. 10, pp. 5171–5178, 1992.

[118] W. B. Holzapfel, "Structural systematics of 4f and 5f elements under pressure," *J. Alloys Compd.*, vol. 223, no. 2, pp. 170–173, 1995.

[119] W. Nolting, T. Dambeck, and G. Borstel, "Temperature-dependent electronic structure of gadolinium," *Zeitschrift für Phys. B Condens. Matter*, vol. 94, no. 4, pp. 409–421, 1994.

[120] S. Y. Dan'kov, A. M. Tishin, V. K. Pecharsky, and K. A. Gschneidner Jr, "Magnetic phase transitions and the magnetothermal properties of gadolinium," *Phys. Rev. B*, vol. 57, no. 6, pp. 3478–3490, 1998.

[121] H. W. White, B. J. Beaudry, P. Burgardt, S. Legvold, and B. N. Harmon, "Magnetic moments of ferromagnetic gadolinium alloys," *AIP Conf. Proc.*, vol. 29, no. 1, pp. 329–330, 1976.

[122] J. Cable and E. Wollan, "Neutron Diffraction Study of the Magnetic Behavior of Gadolinium," *Phys. Rev.*, vol. 165, no. 2, pp. 733–734, 1968.

[123] G. V. Brown, "Magnetic heat pumping near room temperature," *J. Appl. Phys.*, vol. 47, no. 8, pp. 3673–3680, 1976.

[124] V. K. Pecharsky and K. A. Gschneidner Jr, "Advanced Materials for Magnetic Cooling." Sigma-Aldrich Corporation, Milwaukee, Wisconsin, USA, pp. 4–8, 2007.

[125] Cooltech Applications, "Market opportunities," 2017. [Online]. Available: http://www.cooltech-applications.com/market-opportunities.html. [Accessed: 03-Apr-2018].

[126] The NEWS, "Magnetic Refrigeration Market Worth $315.7 Million by 2022," 2015. [Online]. Available: https://www.achrnews.com/articles/130376-magnetic-

refrigeration-market-worth-3157-million-by-2022. [Accessed: 03-Apr-2018].

[127] H. D. Choi, R. B. Firestone, M. S. Basunia, A. Hurst, B. Sleaford, N. Summers, J. E. Escher, Z. Révay, L. Szentmiklósi, T. Belgya, and M. Krtička, "Radiative Capture Cross Sections of 155,157 Gd for Thermal Neutrons," *Nucl. Sci. Eng.*, vol. 177, no. 2, pp. 219–232, 2014.

[128] C. F. G. C. Geraldes and S. Laurent, "Classification and basic properties of contrast agents for magnetic resonance imaging," *Contrast Media Mol. Imaging*, vol. 4, no. 1, pp. 1–23, 2009.

[129] J. M. D. Coey, *Magnetism and Magnetic Materials*, 1st ed. Cambridge: Cambridge University Press, 2009.

[130] André-Marie Ampère, *Théorie des phénomènes électro-dynamiques, uniquement déduite de l'expérience*. Paris: Méquignon-Marvis, 1826.

[131] M. Doppelbauer, "The invention of the electric motor 1800-1854," 2014. [Online]. Available: http://www.sze.hu/~szenasy/VILLVONT/vill vont bevezhez/History - The invention of the electric motor 1800-1854.html. [Accessed: 06-Jul-2018].

[132] S. Tumanski, *Handbook of Magnetic Measurements*, vol. 96, no. 2395. Boca Raton, Florida, USA: CRC Press Taylor & Francis Group, 2011.

[133] David Jiles, *Introduction to the Electronic Properties of Materials*, First Edit. Springer-Science+Business Media, B.V., 1994.

[134] D. Jiles, *Introduction to Magnetism and Magnetic Materials*, 1st ed. New Delhi: Springer-Science+Business Media B.V., 1991.

[135] Y. Liu, D. J. Sellmyer, and D. Shindo, *Handbook of Advanced Magnetic Materials*, vol. 1. New York: Springer-Science+Business Media, B.V., 2005.

[136] E. J. Lavernia and T. S. Srivatsan, "The rapid solidification processing of materials: Science, principles, technology, advances, and applications," *J. Mater. Sci.*, vol. 45, pp. 287–325, 2010.

[137] M. Ferry, *Direct strip casting of metals and alloys : processing, microstructure and properties*. Cambridge, UK: Woodhead Publishing Limited, 2006.

[138] Hazelett Corporation, "History — Hazelett Corporation," 2017. [Online]. Available: https://www.hazelett.com/history/. [Accessed: 06-Jul-2018].

[139] E. H. Strange and C. A. Pim, "Process of manufacturing thin sheets, foil, strips, or ribbons of zinc, lead, or other metal or alloy," United States Patent Office, No. 905,758, 1908.

[140] R. E. Napolitano and H. Meco, "The role of melt pool behavior in free-jet melt spinning," *Metall. Mater. Trans. A*, vol. 35, no. 5, pp. 1539–1553, 2004.

[141] P. D. Wilde and E. F. Matthys, "Experimental investigation of the planar flow casting process: development and free surface characteristics of the solidification puddle," *Materials Science and Engineering A*, vol. 150, no. 2. pp. 237–247, 1992.

[142] H. H. Liebermann, "Rapidly solidified alloys made by chill block melt-spinning processes," *Journal of Crystal Growth*, vol. 70, no. 1–2. pp. 497–506, 1984.

[143] J. K. Carpenter and P. H. Steen, "Planar-flow spin-casting of molten metals: process behaviour," *J. Mater. Sci.*, vol. 27, no. 1, pp. 215–225, 1992.

[144] M. Baricco, E. Bosco, E. Olivetti, M. Palumbo, P. Rizzi, A. Stantero, and L. Battezzati, "Rapid solidification of alloys," *Int. J. Mater. Prod. Technol.*, vol. 20,

no. 5–6, pp. 358–376, 2004.

[145] N. Decristofaro, "Amorphous Metals in Electric-Power Distribution Applications," *MRS Bull.*, vol. 23, no. 5, pp. 50–56, 1998.

[146] R. W. Jech, T. J. Moore, T. K. Glasgow, and N. W. Orth, "Rapid solidification via melt spinning - Equipment and techniques," *JOM*, vol. 36, no. April, pp. 41–45, 1984.

[147] M. Ferry, *Direct Strip Casting of Metals and Alloys*. Cambridge, UK: Woodhead Publishing Limited, 2006.

[148] D. N. Brown, Z. Wu, F. He, D. J. Miller, and J. W. Herchenroeder, "Dysprosium-free melt-spun permanent magnets," *J. Phys. Condens. Matter*, vol. 26, pp. 064202, 1–8, 2014.

[149] B. D. Cullity and S. R. Stock, *Pearson New International Edition: Elements of X-Ray Diffraction*, 3rd ed. Essex, UK: Pearson Education Limited, 2014.

[150] M. Eckert, "Max von Laue and the discovery of X-ray diffraction in 1912," *Ann. Phys.*, vol. 524, no. 5, pp. 83–85, 2012.

[151] Nobel Media AB 2014, "Nobel Prize in Physics 1914 - Presentation," 2014. [Online]. Available: https://www.nobelprize.org/nobel_prizes/physics/laureates/1914/present.html. [Accessed: 31-Jan-2018].

[152] J. A. Kaduk, "Chemical Accuracy and Precision in Structural Refinements From Powder Diffraction Data," *Adv. X-ray Anal.*, vol. 40, no. C, pp. 352–371, 1997.

[153] W. L. Bragg, "The Diffraction of Short Electromagnetic Waves by a Crystal," in *Proceedings of the Cambridge Philosophical Society Vol. XVII*, Cambridge, UK: Cambridge University Press, 1912, pp. 43–57.

[154] T. Volker, D. Schatzlein, and D. Mercuro, "Tutorial: Attenuation of X-Rays By Matter," *Spectroscopy*, vol. 20, no. 9, pp. 22–25, 2005.

[155] P. Scherrer, "Bestimmung der Grösse und der inneren Struktur von Kolloidteilchen mittels Röntgenstrahlen," *Nachrichten von der Gesellschaft der Wissenschaften zu Göttingen, Math. Klasse*, vol. 1918, no. 1916, pp. 98–100, 1918.

[156] J. Bednarcik, S. Michalik, V. Kolesar, U. Rütt, and H. Franz, "In situ XRD studies of nanocrystallization of Fe-based metallic glass: A comparative study by reciprocal and direct space methods," *Phys. Chem. Chem. Phys.*, vol. 15, no. 22, pp. 8470–8479, 2013.

[157] U. Holzwarth and N. Gibson, "The Scherrer equation versus the 'Debye-Scherrer equation,'" *Nat. Nanotechnol.*, vol. 6, no. 9, pp. 534–534, 2011.

[158] J. I. Langford and A. J. C. Wilson, "Scherrer after sixty years: A survey and some new results in the determination of crystallite size," *J. Appl. Crystallogr.*, vol. 11, no. 2, pp. 102–113, 1978.

[159] E. Ma, "Tuning order in disorder," *Nat. Mater.*, vol. 14, no. 6, pp. 547–552, 2015.

[160] T. Egami and S. J. L. Billinge, *Underneath the Bragg Peaks : Structural Analysis of Complex Materials.*, 2nd ed. Oxford: Elsevier Science, 2003.

[161] P. Haines, *Principles of Thermal Analysis and Calorimetry*. Cambridge: Royal Society of Chemistry, 2002.

[162] G. W. H. Höhne, W. F. Hemminger, and H. J. Flammersheim, *Differential Scanning*

Calorimetry, 2nd ed. Berlin: Springer-Verlag, 2003.

[163] W. J. Boettinger, U. R. Kattner, K.-W. Moon, and J. H. Perepezko, *DTA and Heat-flux DSC Measurements of Alloy Melting and Freezing*. Washington, USA: National Institute of Standards and Technology, 2006.

[164] NETZSCH GmbH & Co, "Principle of a heat-flux DSC." [Online]. Available: https://www.netzsch-thermal-analysis.com/en/landing-pages/principle-of-a-heat-flux-dsc/. [Accessed: 29-May-2018].

[165] W. W. Wendlandt, *Thermal Analysis*, 3rd ed. New York, USA: John Wiley & Sons, Inc, 1986.

[166] R. F. Speyer, *Thermal Analysis of Materials*. New York, USA: Marcel Dekker, Inc, 1994.

[167] J. H. Gibbs and E. A. Dimarzio, "The glass transition and the nature of the glassy state," *J. Chem. Phys.*, vol. 28, no. 3, pp. 373–383, 1958.

[168] G. Tarjus, S. A. Kivelson, Z. Nussinov, and P. Viot, "The frustration-based approach of supercooled liquids and the glass transition: A review and critical assessment," *J. Phys. Condens. Matter*, vol. 17, no. 50, 2005.

[169] R. Busch, E. Bakke, and W. L. Johnson, "Viscosity of the supercooled liquid and relaxation at the glass transition of the Zr46.75Ti8.25Cu7.5Ni10Be27.5 bulk metallic glass forming alloy," *Acta Mater.*, vol. 46, no. 13, pp. 4725–4732, 1998.

[170] Y. C. Chang, T. H. Hung, H. M. Chen, J. C. Huang, T. G. Nieh, and C. J. Lee, "Viscous flow behavior and thermal properties of bulk amorphous Mg58Cu31Y11 alloy," *Intermetallics*, vol. 15, no. 10, pp. 1303–1308, 2007.

[171] J. Schroers, "Processing of bulk metallic glass," *Adv. Mater.*, vol. 22, no. 14, pp. 1566–1597, 2010.

[172] P. Zhang, H. Wei, X. Wei, Z. Long, and X. Su, "Evaluation of glass-forming ability for bulk metallic glasses based on characteristic temperatures," *J. Non. Cryst. Solids*, vol. 355, no. 43–44, pp. 2183–2189, 2009.

[173] E. S. Park, D. H. Kim, and W. T. Kim, "Parameter for glass forming ability of ternary alloy systems," *Appl. Phys. Lett.*, vol. 86, no. 6, pp. 1–3, 2005.

[174] Z. P. Lu, Y. Li, and S. C. Ng, "Reduced glass transition temperature and glass forming ability of bulk glass forming alloys," *J. Non. Cryst. Solids*, vol. 270, no. 1–3, pp. 103–114, May 2000.

[175] Z. Bian and A. Inoue, "High glass-forming CeCuFeAlSi bulk metallic glass alloys," *Mater. Sci. Eng. A*, vol. 449–451, pp. 114–117, 2007.

[176] S. Guo, Z. P. Lu, and C. T. Liu, "Identify the best glass forming ability criterion," *Intermetallics*, vol. 18, no. 5, pp. 883–888, 2010.

[177] X. H. Du, J. C. Huang, C. T. Liu, and Z. P. Lu, "New criterion of glass forming ability for bulk metallic glasses," *J. Appl. Phys.*, vol. 101, no. 8, pp. 1–4, 2007.

[178] B. Fultz and J. Howe, *Transmission Electron Microscopy and Diffractometry of Materials*, 4th ed. Berlin, Germany: Springer-Verlag, 2013.

[179] T. L. Daulton, K. S. Bondi, and K. F. Kelton, "Nanobeam diffraction fluctuation electron microscopy technique for structural characterization of disordered materials-Application to Al88-xY7Fe5Tix metallic glasses," *Ultramicroscopy*, vol. 110, no. 10, pp. 1279–1289, 2010.

[180] P. Voyles and J. Hwang, "Fluctuation Electron Microscopy," *Charact. Mater.*, 2012.

[181] L. Reimer, *Transmission Electron Microscopy, Physics of Image Formation and Microanalysis*, 4th ed. Berlin, Germany: Springer-Verlag, 1997.

[182] R. F. Egerton, *Physical Principles of Electron Microscopy: An Introduction to TEM, SEM, and AEM*, vol. 8, no. 12. Springer Science+Business Media, 2005.

[183] E. Z. F. Krumeich, "Electron Microscopy Methods," 2015. [Online]. Available: http://www.microscopy.ethz.ch/methods.htm. [Accessed: 25-May-2018].

[184] J. F. Keithley, *The Story of Electrical and Magnetic Measurements: : from 500 B.C. to the 1940s*. New York, USA: IEEE, 1999.

[185] S. Foner, "Versatile and sensitive vibrating-sample magnetometer," *Rev. Sci. Instrum.*, vol. 30, no. 7, pp. 548–557, 1959.

[186] S. Foner, "The vibrating sample magnetometer: Experiences of a volunteer (invited)," *J. Appl. Phys.*, vol. 79, no. 8, pp. 4740–4745, 1996.

[187] F. Fiorillo, *Measurement and Characterization of Magnetic Materials*, 1st ed. Amsterdam: Elsevier, 2004.

[188] A. Zieba and S. Foner, "Detection coil, sensitivity function, and sample geometry effects for vibrating sample magnetometers," *Rev. Sci. Instrum.*, vol. 53, no. 9, pp. 1344–1354, 1982.

[189] J. P. C. Bernards, "Design of a detection coil system for a biaxial vibrating sample magnetometer and some applications," *Rev. Sci. Instrum.*, vol. 64, no. 7, pp. 1918–1930, 1993.

[190] J. Sievert, H. Ahlers, J. Ludke, S. Siebert, L. Pareti, and M. Solzi, "European intercomparison of measurements on permanent magnets," *IEEE Trans. Magn.*, vol. 29, no. 6 pt 1, pp. 2887–2889, 1993.

[191] K. Gramm and L. Lundgren, "SQUID Magnetometer for Magnetization Measurements," *Phys. Scr.*, vol. 13, pp. 93–95, 1976.

[192] B. D. Josephson, "Possible new effects in superconductive tunnelling," *Phys. Lett.*, vol. 1, no. 7, pp. 251–253, 1962.

[193] J. E. Lenz, "A Review of Magnetic Sensors," *Proc. IEEE*, vol. 78, no. 6, pp. 973–989, 1990.

[194] J. Clarke and A. I. Braginski, *The SQUID Handbook Vol. I Fundamentals and Technology of SQUIDs and SQUID Systems*. Weinheim, Germany: Wiley-VCH Verlag GmbH & Co KGaA, 2005.

[195] P. W. Anderson and J. M. Rowell, "Probable observation of the Josephson superconducting tunneling effect," *Phys. Rev. Lett.*, vol. 10, no. 6, pp. 230–232, 1963.

[196] J. W. Rohlf, *Modern Physics from α to Z^0*. John Wiley & Sons, Inc., 1994.

[197] J. Clarke and A. I. Braginski, *The SQUID Handbook Vol. II Applications of SQUIDs and SQUID Systems*. Weinheim, Germany: Wiley-VCH Verlag GmbH & Co KGaA, 2006.

[198] "Magnetic Property Measurement System (MPMS® 3)." [Online]. Available: https://www.qdusa.com/products/mpms3.html. [Accessed: 20-Sep-2018].

[199] S. H. Risbud and Y. H. Han, "Preface and historical perspective on spark plasma sintering," *Scr. Mater.*, vol. 69, no. 2, pp. 105–106, 2013.

[200] O. Guillon, J. Gonzalez-Julian, B. Dargatz, T. Kessel, G. Schierning, J. Räthel, and M. Herrmann, "Field-assisted sintering technology/spark plasma sintering: Mechanisms, materials, and technology developments," *Adv. Eng. Mater.*, vol. 16, pp. 830–849, 2014.

[201] D. M. Hulbert, A. Anders, D. V. Dudina, J. Andersson, D. Jiang, C. Unuvar, U. Anselmi-Tamburini, E. J. Lavernia, and A. K. Mukherjee, "The absence of plasma in 'spark plasma sintering,'" *J. Appl. Phys.*, vol. 104, no. 3, 2008.

[202] R. Marder, C. Estournès, G. Chevallier, and R. Chaim, "Plasma in spark plasma sintering of ceramic particle compacts," *Scr. Mater.*, vol. 82, pp. 57–60, 2014.

[203] U. Anselmi-Tamburini, S. Gennari, J. Garay, and Z. Munir, "Fundamental investigations on the spark plasma sintering/synthesis process II. Modeling of current and temperature distributions," *Mater. Sci. Eng. A*, vol. 394, no. 1–2, pp. 139–148, 2005.

[204] Z. A. Munir, D. V. Quach, and M. Ohyanagi, "Electric current activation of sintering: A review of the pulsed electric current sintering process," *J. Am. Ceram. Soc.*, vol. 94, no. 1, pp. 1–19, 2011.

[205] S. Grasso, Y. Sakka, and G. Maizza, "Pressure Effects on Temperature Distribution during Spark Plasma Sintering with Graphite Sample," *Mater. Trans.*, vol. 50, no. 8, pp. 2111–2114, 2009.

[206] L. Kelhar, J. Ferčič, P. Boulet, M. Maček-Kržmanc, S. Šturm, M. Lamut, B. Markoli, S. Kobe, and J.-M. Dubois, "Stabilisation of Ce-Cu-Fe amorphous alloys by addition of Al," *Philos. Mag.*, pp. 1–16, Sep. 2016.

[207] J. E. Garay, "Current-Activated, Pressure-Assisted Densification of Materials," *Annu. Rev. Mater. Res.*, vol. 40, pp. 445–468, 2010.

[208] M. Tokita, "Development of Square-Shaped Large-Size WC/Co/Ni System FGM Fabricated by Spark Plasma Sintering (SPS) Method and Its Industrial Applications," *Mater. Sci. Forum*, vol. 492–493, pp. 711–718, 2005.

[209] B. McWilliams, A. Zavaliangos, K. Cho, and R. Dowding, "The modeling of electric-current-assisted sintering to produce bulk nanocrystalline tungsten," *JOM*, vol. 58, no. 4, pp. 67–71, 2006.

[210] L. Zhang and R. Luck, "Phase diagram of the Al-Cu-Fe quasicrystal-forming alloy system I. Liquidus surface and phase equilibria with liquid," *Zeitschrift für Met.*, vol. 94, no. 2, pp. 91–97, 2003.

[211] B. Coqblin and A. Blandin, "Stabilité des Moments Magnétiques Localisés dans les Métaux," *Adv. Phys.*, vol. 17, no. 67, pp. 281–366, 1968.

[212] J. G. Speight, *Lange's Handbook of Chemistry*, 16th ed. New York, USA: McGraw-Hill, 2005.

[213] K. A. Gschneidner and F. W. Calderwood, "The Al-Ce (Aluminum-Cerium) System," *Bull. Alloy Phase Diagr.*, vol. 9, no. 6, pp. 669–672, 1988.

[214] Z. Bian and A. Inoue, "Ultra-low glass transition temperatures in Ce-based bulk metallic glasses," *Mater. Trans.*, vol. 46, no. 8, pp. 1857–1860, 2005.

[215] I. V. Nikolaenko and M. A. Turchanin, "Enthalpies of formation of liquid binary (copper + iron, cobalt, and nickel) alloys," *Metall. Mater. Trans. B*, vol. 28, no. 6, pp. 1119–1130, 1997.

[216] D. Chen, A. Takeuchi, and A. Inoue, "Gd-Co-Al and Gd-Ni-Al bulk metallic glasses with high glass forming ability and good mechanical properties," *Mater. Sci. Eng. A*, vol. 457, no. 1–2, pp. 226–230, 2007.

[217] K. Baberschke, P. Pureur, A. Fert, R. Wendler, and S. Senoussi, "Rare-earth spin-glasses with uniaxial anisotropy," *Phys. Rev. B*, vol. 29, no. 9, pp. 4999–5006, 1984.

[218] J. L. Tholence and R. Tournier, "Magnetization of very dilute Au-Fe alloys," *J. Phys. Colloq.*, vol. 32, no. C1, pp. 211–212, 1971.

[219] Q. Luo and W. H. Wang, "Rare earth based bulk metallic glasses," *J. Non. Cryst. Solids*, vol. 355, no. 13, pp. 759–775, 2009.

[220] R. R. Galazka, S. Nagata, and P. H. Keesom, "Paramagnetic-spin-glass-antiferromagnetic phase transitions in Cd1-xMnxTe from specific heat and magnetic susceptibility measurements," *Phys. Rev. B*, vol. 22, no. 7, p. 3344, 1980.

[221] D. C. Hofmann, G. Duan, and W. L. Johnson, "TEM study of structural evolution in a copper mold cast Cu46Zr54bulk metallic glass," *Scr. Mater.*, vol. 54, no. 6, pp. 1117–1122, 2006.

[222] C. A. Schneider, W. S. Rasband, and K. W. Eliceiri, "NIH Image to ImageJ: 25 years of image analysis," *Nat. Methods*, vol. 9, no. 7, pp. 671–675, 2012.

[223] "PDF card number 00-012-0797, PDF4+ database." The International Centre for Diffraction Data, Newtown Square, USA.

[224] Scientific Group Thermodata Europe (SGTE), *Al – Gd (Aluminium – Gadolinium), Landolt-Bornstein, New Series, Group IV: Physical Chemistry, Part 19B.* Berlin, Germany: Springer-Verlag, 2007.

[225] Z. P. Lu, H. Tan, S. C. Ng, and Y. Li, "The correlation between reduced glass transition temperature and glass forming ability of bulk metallic glasses," *Scr. Mater.*, vol. 42, no. 7, pp. 667–673, 2000.

[226] R. Harris, M. Plischke, and M. J. Zuckermann, "New Model for Amorphous Magnetism," *Phys. Rev. Lett.*, vol. 31, no. 3, pp. 160–162, 1973.

[227] H. Z. Kong, L. Wang, Y. P. Feng, Y. Li, and J. Ding, "Monte Carlo simulation of a cluster system with strong interaction and random anisotropy," *Phys. Rev. B - Condens. Matter Mater. Phys.*, vol. 64, no. 21, pp. 1–10, 2001.

[228] D. L. Stein and C. M. Newman, "Spin Glasses: Old and New Complexity," *Complex Syst.*, vol. 20, pp. 115–126, May 2011.

[229] B. Schwarz, B. Podmilsak, N. Mattern, and J. Eckert, "Magnetocaloric effect in Gd-based Gd60FexCo30-xAl10 metallic glasses," *J. Magn. Magn. Mater.*, vol. 322, no. 16, pp. 2298–2303, 2010.

[230] T. Speliotis and D. Niarchos, "Extraordinary magnetization of amorphous TbDyFe films," *Microelectron. Eng.*, vol. 112, pp. 183–187, 2013.

[231] Q. Luo, P. N. Dinh, X. Kou, and J. Shen, "Controllable ferromagnetic/re-entrant spin glass state and magnetocaloric response of Gd-Er-Al-Co metallic glasses," *J. Alloys Compd.*, vol. 725, pp. 835–839, 2017.

[232] L. Y. Ma, B. Z. Tang, K. C. Chan, L. Zhao, M. B. Tang, D. Ding, and L. Xia, "Formability and magnetic properties of Dy-Co binary amorphous alloys," *AIP Adv.*, vol. 8, no. 7, p. 075215, 2018.

[233] Paul Schatz Stiftung, *The Study of Rhythms and Technology: The Evertible Cube.*

Polysomatic Form-Finding, 4th ed. Niggli Verlag, 2013.

[234] A. van den Beukel, "On the Parameters Governing Atomic Mobility in Metallic Glasses," *Phys. Status Solidi*, vol. 128, no. 2, pp. 285–293, 1991.

[235] W. Gotze and L. Sjogren, "Relaxation processes in supercooled liquids," *Rep. Prog. Phys*, vol. 55, pp. 241–376, 1992.

[236] G. Xie, D. V. Louzguine-Luzgin, L. Song, H. Kimura, and A. Inoue, "Dual phase metallic glassy composites with large-size and ultra-high strength fabricated by spark plasma sintering," *Intermetallics*, vol. 17, no. 7, pp. 512–516, 2009.

[237] D. V. Louzguine-Luzgin, K. Georgarakis, A. R. Yavari, G. Vaughan, G. Xie, and A. Inoue, "Effect of Ag addition on local structure of Cu-Zr glassy alloy," *J. Mater. Res.*, vol. 24, no. 1, pp. 274–278, 2009.

[238] E. S. Park, J. Y. Lee, D. H. Kim, A. Gebert, and L. Schultz, "Correlation between plasticity and fragility in Mg-based bulk metallic glasses with modulated heterogeneity," *J. Appl. Phys.*, vol. 104, no. 2, 2008.

[239] O. Kubaschewski, *Iron—binary phase diagrams*. Düsseldorf, Germany: Springer-Verlag, 1982.

[240] E. S. Park, W. T. Kim, and D. H. Kim, "Bulk Glass Formation in Mg-Cu-Ag-Y-Gd Alloy," *Mater. Trans.*, vol. 45, no. 7, pp. 2474–2477, 2004.

[241] C. R. Cao, D. W. Ding, D. Q. Zhao, E. Axinte, H. Y. Bai, and W. H. Wang, "Correlation between glass transition temperature and melting temperature in metallic glasses," *Mater. Des.*, vol. 60, pp. 576–579, 2014.

[242] U. Köster and J. Meinhardt, "Crystallization of highly undercooled metallic melts and metallic glasses around the glass transition temperature," *Mater. Sci. Eng. A*, vol. 178, no. 1–2, pp. 271–278, 1994.

[243] E. M. Chudnovsky, W. M. Saslow, and R. A. Serota, "Ordering in ferromagnets with random anisotropy," *Phys. Rev. B*, vol. 33, no. 1, pp. 251–261, 1986.

Bibliography

Journal Articles

L. Kelhar, J. Ferčič, P. Boulet, M. Maček-Kržmanc, S. Šturm, M. Lamut, B. Markoli, S. Kobe, and J.-M. Dubois, "Stabilisation of Ce-Cu-Fe amorphous alloys by addition of Al," Philos. Mag., vol. 96, no. 30, 2016.

L. Kelhar, J. Ferčič, M. Maček-Kržmanc, J. Zavašnik, S. Šturm, P. Koželj, S. Kobe, and J.-M. J.-M. Dubois, "The role of Fe and Cu additions on the structural, thermal and magnetic properties of amorphous Al-Ce-Fe-Cu alloys," J. Non. Cryst. Solids, vol. 483, pp. 70–78, 2018.

A. Kocjan, L. Kelhar, A. Gradišek, B. Likozar, K. Žagar, J. Ghanbaja, S. Kobe, and J.-M. Dubois, "Solid Solubility in Cu5Gd1-xCax System: Structure, Stability, and Hydrogenation," Adv. Mater. Sci. Eng., vol. 2017, 2017.

Conference Paper

Kelhar L, Kobe S, Dubois J-M. Amorphous alloys in the system Al-Ce-Fe-Cu. In: 10th Young Researchers' Day CMBE. Ljubljana, Slovenia: Jožef Stefan Institute; 2016.

Kelhar L, Kobe S, Dubois J-M. Characterization of structure and magnetic properties in Ce-based bulk amorphous glass. In: Godec M, Donik Č, Hočevar M, Kocijan A, eds. 24th International Conference on Materials and Technology. Portorož, Slovenia: Inštitut za kovinske materiale in tehnologije; 2016.

Kelhar L, Kobe S, Dubois J-M. Stability of amorphous alloys in the system Ce-Cu-Fe with additions of Al. In: Holland-Moritz DD, Kargl PDF, eds. 16th International Conference on Liquid and Amorphous Metals (LAM-16). Bonn - Bad Godesberg, Germany: German Aerospace Center (DLR); 2016:31.

Kelhar L, Kobe S, Dubois J-M. Amorphous alloys with variable amounts of immiscible Fe and Cu metals. In: Matjaž Godec, Črtomir Donik, Matej Hočevar AK, ed. 25th International Conference on Materials and Technology. Portorož, Slovenia: Inštitut za kovinske materiale in tehnologije; 2017.

Biography

The author of this thesis Luka Kelhar was born on 9th March 1990 in Ljubljana, Slovenia. He finished his B.Sc. study of Materials Engineering in 2012 at the Faculty of Natural Sciences and Engineering, Ljubljana, Slovenia. Under the supervision of Prof. Dr. Boštjan Markoli he completed his B.Sc. thesis entitled "Ni-Mn-Ga alloys with memory-shape effect.

For the M.Sc study, he enrolled at the Jožef Stefan International Postgraduate School, where he studied metal-bonded $Nd_2Fe_{14}B$ magnets as a potential replacement of polymer bonded magnets. Research work has been carried out under the supervision of Prof. Dr. Spomenka Kobe and Asst. Prof. Paul J. McGuiness. From this investigation, a patent has been filed and in 2015 the thesis entitled: "Metal-bonded Nd-Fe-B magnets" was successfully defended.

Author's education was continued with a PhD at the Department for Nanostructured Materials K7, a part of JSI, under the guidance of Professor Jean-Marie Dubois and Professor Spomenka Kobe. A fundamental study of cerium- and gadolinium-containing glassy metallic glasses was conducted by investigating the structure, microstructure, thermal and magnetic properties of the glassy alloys. In this time, he spent three months at Institut Jean Lamour in Nancy, France, where he was working on the growth of $AlCe_3$ monocrystals and the characterisation of their properties.

Another field, which he was pursuing in parallel since 2017, was the additive manufacturing of magnetic materials. A fused filament fabrication (FFF) of polymer matrix wire loaded with magnetic filler was used to produce magnets layer-by-layer. In this process, he constructed a 3D printer adapted for FFF of a composite wire and experimented with additive production of magnets.